

THE PIERRE AUGER OBSERVATORY DESIGN REPORT

Second Edition

The Auger Collaboration

14 March 1997

Acknowledgements

The Auger Collaboration gratefully acknowledges the following institutions, whose support made possible the preparation of this Design Report:

University of Chicago,

University of Michigan,

Fermi National Accelerator Laboratory,

Grainger Foundation,

National Science Foundation,

Universities Research Association,

and an anonymous corporate donor.

We especially thank *UNESCO*, whose generous and ongoing support has been vital to the work of the Auger Project Design Group.

Foreword to the Revised Edition

The Auger Project is a broad-based international effort to make a detailed study of cosmic rays at the highest energies. Two established air shower detector techniques – a surface array of particle detectors coupled with an air fluorescence detector – form a powerful instrument for the proposed research. The objectives of the Auger Observatory are to measure the arrival direction, energy, and mass composition of cosmic rays above 10^{19} eV.

The Auger Project had its conception in a series of workshops in Paris (1992), Adelaide (1993), Tokyo (1993), and finally at Fermilab in 1995. The Design Group for the Auger Project, hosted by Fermilab, met from January 30 through July 31, 1995. More than 140 scientists from 17 countries attended one or more of the conferences and topical workshops. The Design Group produced a Design Report in November 1995 containing a reference design and a cost estimate for the proposed Auger Observatory.

This document is a second edition of the Auger Design Report. It contains additional and enhanced discussion of many of the topics in the first edition. The additions resulted from discussions with many interested scientists from around the world as well as formal reviews of the Auger Project by distinguished panels convened at Fermilab and in Paris.

This edition of the Report is organized as follows: Chapter 1 is an Executive Summary of the Report; Chapter 2 presents the scientific motivation together with a program of observations that would illuminate the theoretical picture; Chapter 3 contains the historical background of air shower studies, current and expected results, and the role of the Auger project; Chapter 4 describes how the parameters of high energy cosmic ray air showers are measured and interpreted; Chapter 5 gives results of a detailed simulation of the Auger detector and its expected performance; Chapters 6 through 8 describe the reference design for the detectors, communication, and data acquisition system; Chapter 9 describes the survey of candidate sites. The central station is treated in Chapter 10. The organization, cost, and schedule are outlined in Chapter 11.

The Auger Collaboration membership list as of January 1997, as well as a list of other individuals who have authored parts of the Design Report, participated in the workshops, or significantly contributed to this Design Report in other ways are given in an Appendix.

This Report, the library of GAP Technical Notes, and other information on the Auger Project are available via the world wide web by accessing the Astrophysics pages at Fermilab: <http://www-td-auger.fnal.gov:82>.

14 March 1997

Contents

1	Executive Summary	9
2	Science	14
2.1	Introduction	14
2.2	Acceleration and propagation of cosmic rays	17
2.2.1	Acceleration	17
2.2.2	Propagation and the GZK Cutoff	21
2.3	Recent theoretical work	26
2.3.1	Shock acceleration in extended sources	27
2.3.2	Association with gamma-ray bursts	30
2.3.3	Exotic sources	32
2.3.4	Astrophysical Neutrinos	35
2.3.5	Summary Comments on Source Models	36
2.4	Observational capabilities needed for the Auger Observatory	37
2.4.1	Composition resolution.	37
2.4.2	Energy resolution	39
2.4.3	Arrival direction resolution	40
2.4.4	Neutrino Astronomy	45
3	Observations of the Highest Energy Cosmic Rays	49
3.1	Background	49
3.2	Energy measurements	52
3.2.1	Energy spectrum	53

3.2.2	The highest energy events	56
3.3	Direction measurements	61
3.3.1	Anisotropy	61
3.3.2	Point sources	63
3.3.3	Magnetic spectrometry with event pairs	64
3.4	The Immediate Future	67
3.5	The Physics and Astrophysics Potential of the Auger Project	68
4	Air Shower Measurement Techniques	70
4.1	Properties and Development of Air Showers	70
4.1.1	The Electromagnetic and Muon Components	71
4.1.2	Spatial Structure of the Shower	71
4.1.3	Time Structure of the Shower Front	74
4.1.4	Fluctuations in Shower Development	75
4.2	Determination of Shower Parameters	76
4.2.1	The Shower Direction and Axis	76
4.2.2	Energy	77
4.2.3	Primary Mass	78
4.2.4	New Particle Physics	80
4.3	Surface Array Methods	82
4.3.1	Water Čerenkov lateral distribution function	83
4.3.2	Event Reconstruction	86
4.3.3	Energy Assignment Parameter	86
4.4	Fluorescence Detection	89
4.4.1	Air Fluorescence	90
4.4.2	Čerenkov production and scattering	91
4.4.3	Detection Technique	94
4.4.4	Finding Shower Trajectories	97
4.4.5	Shower Shape and Energy	99
5	Simulated Performance of the Reference Design	102

5.1	Numerical simulations	102
5.1.1	The MOCCA Simulation Program	103
5.1.2	The SIBYLL Interaction Generator	104
5.1.3	Nucleus-Nucleus Interactions	106
5.1.4	Comparison to Data	106
5.1.5	Ongoing studies	108
5.2	Surface Detector Simulation	109
5.2.1	Detector description	110
5.2.2	Air Shower Structure	110
5.2.3	Detector Simulation	113
5.2.4	Comparison of Simulation and Data	118
5.2.5	Reconstruction of simulated events	126
5.3	Hybrid Detector Simulation	133
5.3.1	Methods	133
5.3.2	Simulation of Fluorescence Detector Response	134
5.3.3	Simulation of Ground Array Response	136
5.3.4	Hybrid Geometric Reconstruction Method	137
5.3.5	Energy and X_{max} Resolution	140
5.3.6	Results	141
5.4	Summary of Reconstruction Resolution	144
6	Surface Detector Array Design	151
6.1	The reference design	152
6.2	Detector geometry and array spacing	152
6.3	PMT positioning and detector uniformity	154
6.4	Mechanical realization and prototypes	157
6.5	Water purification and stability	160
7	Fluorescence Detector Design	163
7.1	The site layout	164
7.2	The telescope design	166

7.3	Alternative Designs	168
7.3.1	The Dual Mirror Concept	168
7.3.2	Wide angle Schmidt telescopes	168
8	Electronics Systems and Software	170
8.1	Station Electronics Packaging	170
8.2	Front End Electronics	171
8.3	Station Controller	175
8.4	Timing	176
8.5	Communications	178
8.5.1	Licensing Issues	179
8.5.2	Propagation	179
8.5.3	Performance Analysis of Frequency-Hopped Spread Spectrum.	182
8.5.4	Link Budget	184
8.5.5	Network Topology	186
8.6	Solar Power	187
8.7	Data Acquisition and Archives	189
8.8	Trigger	190
9	Site Survey	193
9.1	Introduction	193
9.2	Site Requirements	194
9.3	Site Visits and Relevant Data	194
9.4	Argentina	195
9.4.1	Laguna Blanca:	195
9.4.2	La Humada:	197
9.4.3	Monte Coman:	197
9.4.4	Nihuil:	198
9.4.5	Somuncura:	199
9.5	South Africa	200
9.5.1	Vaalputs:	200

9.6	Australia	201
9.6.1	Woomera	201
9.7	Spain	202
9.7.1	Tierra de Campos	203
9.8	Mexico	204
9.8.1	El Barreal	204
9.9	United States of America	205
9.9.1	Engle, NM:	205
9.9.2	Grand Canyon, AZ:	206
9.9.3	Lamar, CO:	207
9.9.4	Millard, UT:	208
10	Central Station	210
10.1	Central Station	210
10.1.1	The Office Building	210
10.1.2	The Dormitory	211
10.1.3	The Shed	211
10.2	Civil Engineering	211
11	Organization, Cost, and Schedule	213
11.1	Introduction	213
11.2	Organization	213
11.3	Construction Cost Estimate	216
11.4	Operating Cost	217
11.4.1	Project Schedule	222
A	Auger Project Participants	224
A.1	Auger Collaboration Membership	224
A.2	Auger Project Contributors	233

Chapter 1

Executive Summary

One of the foremost issues in astrophysics today is that of the origin of the most energetic cosmic rays. Eighty years ago in a series of pioneering balloon flights Victor Hess discovered that the earth was bathed in a sea of ionizing “cosmic” radiation. Three decades later Pierre Auger observed showers of secondary particles at ground level produced by energetic cosmic rays interacting high in the atmosphere[2]. Based on the size of these “air showers” Auger concluded that the spectrum of primary particle energies extended up to and perhaps beyond 10^{15} eV. More recently, in 1962, an air shower event was observed with an energy approaching 10^{20} eV, one-hundred million times more energetic than the highest energy attained by terrestrial accelerators[3]. Since that time only a handful of similarly energetic events have been detected, the maximum to date reported at 3×10^{20} eV([4]-[7]).

Today substantial progress has been made in understanding the nature of cosmic rays of relatively modest energy (those greater than about 10^{15} eV). Indeed, our understanding is now such that we are forced to consider the possibility that the highest energy primary particles, those with energies above about 10^{19} eV, have an entirely different origin than lower energy cosmic rays. Unfortunately, the nature of these remains as enigmatic today as when they were first observed. The failure to solve this puzzle despite three decades of effort stems both from practical and theoretical difficulties.

The flux of cosmic rays above 10^{19} eV is extraordinarily low: on the order of one per square-kilometer per year. Only detectors of exceptional size, thousands of square-kilometers, can hope to acquire a significant number of events. The nature of the primary particles must be inferred from properties of the associated air showers. Two techniques are used: surface arrays sample the lateral density profile of the muon and electromagnetic components in the shower front; atmospheric fluorescence detectors observe the evolution of air showers — their growth and subsequent attenuation — as they develop.

Addressing the theoretical issues surrounding the production and propagation of 10^{20} eV primaries is problematic as well. At these energies, cosmic rays typically have a mean free path less than 50 Mpc (~ 150 million light-years) — a short distance on a cosmological scale. Cosmic rays, regardless of their nature, lose energy in their interaction with the 2.7K cosmic microwave background radiation: protons photo-produce pions, nuclei photodisintegrate via

the giant dipole resonance, photons produce e^+e^- pairs. Only neutrinos propagate freely. Thus, the source or sources must be relatively nearby, within 50 - 100 Mpc. But models of the acceleration of protons or nuclei to these extreme energies have proven very difficult to construct. Few sufficiently energetic astrophysical environments lie within the requisite distance. The existence of these extraordinarily energetic cosmic rays is a puzzle, the solution of which must lead to new discoveries in astrophysics, fundamental physics, or both.

In this Report, we present a design for the Auger Observatory whose primary goal is to solve this mystery. Separate, identical sites in the Northern and Southern Hemispheres will measure the arrival direction and energy of the primary particle, the muon content of the extensive air shower it induces, and for a subset of events, the longitudinal development of the shower in the atmosphere.

Analysis of these shower parameters, guided by Monte Carlo simulations, can be used to select event samples enriched in either light ($A \leq 16$) or heavy ($A \geq 16$) primaries. Correlations among the various parameters — energy, arrival direction, and mass — may reveal a number of components contributing to the total observed cosmic ray flux. For example, it is possible that a significant fraction of heavy primaries around 10^{19} eV are produced in our galaxy. If so, their arrival directions ought to be correlated with the mass distribution in our own galaxy (i.e. they should appear to come from the direction of the *plane*, as opposed to the *poles*, of the galaxy). This component, nearly unaffected by the cosmic microwave background radiation, would exhibit an energy spectrum directly reflecting the production mechanism within galactic accelerators. If the lighter sample (including protons) is isotropic and exhibits a cut-off near 10^{20} eV, then we may conclude that it represents a universal extragalactic component which has suffered attenuation due to its interaction with the cosmic microwave background.

However, it is the origin and nature of the cosmic rays which have been observed with the highest energies ($E \geq 10^{20}$ eV) which is most perplexing. We have virtually no information as to their fundamental nature. Are they protons? Nuclei? Or perhaps something exotic? How and where do they acquire such enormous energies? Do their arrival directions cluster about any known, particularly energetic astrophysical objects? Or about any extended mass distribution such as the super-galactic plane? Do they exhibit any directional anisotropy? If not, then perhaps they are among the products created in the decay of topological defects. Their energy distribution should then be characteristic of a “top down” source: the product of a cascade from still higher energies. In the absence of greatly increased statistics even the wildest speculation can hardly be ruled out.

The Auger Observatory is to be a *hybrid* detector, employing two complementary techniques to observe extensive air showers. A giant array of particle counters will measure the lateral and temporal distribution of shower particles at ground level. An optical air-fluorescence detector will measure the air shower development in the atmosphere above the surface array. Operating together, the surface array and fluorescence detector characterize showers to a greater degree than either technique alone. Both methods are well established by prior experiments. The surface array resembles the array successfully employed by the Haverah Park group for over twenty years[7], although on a much larger scale. The optical device uses the *fluorescence* technique pioneered by the University of Utah’s Fly’s Eye[8].

Measurement of atmospheric fluorescence is possible only on clear, dark nights. About 10% (possibly more) of all Auger showers will be measured by both techniques.

The decision to use the two techniques together is based upon the following considerations:

Intercalibration: The two methods measure shower energy, direction, and primary particle type in independent, complementary ways, providing invaluable redundancy and cross checks. The two kinds of detector have not yet been operated in coincidence on a large scale. A hybrid device will reveal any systematic effects which might be inherent to either method alone.

Enhanced composition sensitivity: Both kinds of detector have sensitivity to primary particle type, but the two techniques together provide a much clearer picture. Each method obtains information about the nuclear type of the primary cosmic ray by measuring air shower quantities which correlate with it. Together, these data are much less susceptible to fluctuations leading to misidentification.

Hadronic interactions: Measurement of both the muon and electromagnetic particle densities together with the shower's longitudinal development profile imposes tighter constraints on hadronic interaction models than either technique can provide by itself. The interaction energies of Auger events is well beyond the reach of accelerator based experiments.

Uniform exposure: Patterns of cosmic ray arrival directions, whether isotropic or not, provide the most compelling evidence for their sources. Surface arrays in both hemispheres, operating 24 hours per day year-round, provide data with nearly uniform celestial exposure. This enables a straightforward search for excesses from discrete sources and also a sensitive large scale anisotropy analysis.

Cost: The cost per event for the Auger surface array, operating continuously, is substantially less than for a *stereo* fluorescence detector with its small duty cycle. For a cosmic ray experiment based solely on fluorescence detectors, stereo detection (the shower recorded simultaneously by at least two separated installations or “Eyes”) is required for accurate shower direction reconstruction. In contrast, data from only one of the Eyes (*monocular* detection), when combined with that from the surface array, gives equivalently good direction resolution. For a given acceptance, a fluorescence design based on monocular reconstruction is less expensive than stereo, because each of the Eyes is not required to “see” as far.

Auger's hybrid configuration is the most economical and robust way to obtain the necessary data, including a subset with especially high reconstruction resolution and independent cross checks.

Each of the two surface arrays of the Auger Observatory will consist of about 1600 detectors spaced on a grid with about 1.5 km separation between individual detectors. Each array encompasses an area of 3000 km². The angular and energy resolution of a ground array (without coincident fluorescence data) are typically less than 1.5° and less than 20%, respectively. If an event trigger is assumed to require five detectors above threshold, the array is fully efficient at 10¹⁹ eV. New technologies are employed, making it practical to

operate thousands of detectors spread over such an area. Each detector will be solar powered (consuming less than 10 watts) and will communicate via modern wireless techniques. Inter-detector relative timing is accomplished by individual Global Positioning Satellite (GPS) receivers.

A number of options for the surface detectors (e.g., water Čerenkov, scintillator-lead sandwich) were explored during a six month design study held at the Fermi National Accelerator Laboratory. Their performance was investigated using Monte Carlo techniques; prototypes were constructed at various laboratories around the world. Care was taken to ensure that these results agreed with experimental data available from existing cosmic ray detectors. Based on a combination of cost, simplicity, and performance, the Water Čerenkov Detector (WCD) was selected. Such a detector is relatively simple, consisting of a water tank of 10 m² area and 1.2 m depth with an efficient, diffusely reflective lining. The Čerenkov light produced by the shower particles is viewed by three downward facing photomultipliers. WCD, in comparison to scintillation detectors or gas chambers, are simple, stable, inexpensive, and, perhaps most important, have significantly better sensitivity to showers at large zenith angles. Twenty years of WCD experience of the Haverah Park experiment provides an important check of the design work.

Air showers at 10¹⁹ eV may contain 10¹⁰ charged particles and extend over an area of twenty square kilometers. Due to the 1.5 km detector separation in Auger, the properties of showers at a distance of a kilometer or more from the core are the most relevant to the detector design. Here, the particle density has fallen to a few per square meter. The “thickness” of the shower front — the time it takes to pass through the detector — is several microseconds. The electromagnetic components (electrons, positrons, and photons) are some 100 times more numerous than are the muons. However, their mean energy is only 10 MeV while that of the muons is about 1 GeV. The former produce a large number of relatively small Čerenkov pulses whereas muons produce a small number of large pulses. Given the breadth of the arrival time distribution, it is feasible, using only moderately fast flash-ADCs, to estimate the muonic and electromagnetic components of the showers independently. Similarly, the *rise-time* of the shower front is related to the relative proportion of muons in the shower (muons are typically “leading” particles within the shower front). The ratio of muons to the electromagnetic component is sensitive to the nuclear type of the primary cosmic ray particle.

The Auger fluorescence detector consists of many meter-sized mirrors, each of which is equipped with a cluster of a hundred or more photomultipliers. Each mirror and associated cluster will view its own segment of the sky. Together, the system of mirrors observes most of the sky above the surface array. The magnitude of the photomultiplier signals gives the number of electromagnetic particles in the shower, and hence the energy. Fast timing of the sequence of signals yield the trajectory of air showers passing in the field of view of the detector. In the hybrid mode of operation, the surface and fluorescence detectors together have a directional reconstruction resolution of about 0.3° for events near 10²⁰ eV.

Events which are observed by both the fluorescence and the surface detectors can be effectively reconstructed even if only two surface detectors are registered. Thus, the event trigger for the hybrid arrangement will permit “sub-threshold” surface array triggers (i.e.,

less than five stations), provided that the fluorescence detector also reports its own event trigger. The Auger hybrid threshold therefore extends down to about 10^{18} eV. These events, at lower energy than the targeted energy range of Auger, provide a valuable set with which to compare to the extensive data of previous (and current) cosmic ray experiments.

The most significant uncertainty in air shower simulations used to guide the design arises from variations in the models for the first few interactions in the developing shower. These occur at energies well beyond the range of accelerator measurements. The uncertainties do not significantly affect the shower properties relevant to the overall design of the detector. For example, reasonable variations in the physics of the first few interactions lead to a 60% variation in the measured ratio of muon to electromagnetic energy deposition in the water tank. The absolute value of this ratio will not uniquely identify a particular primary with certainty. Nevertheless, the difference between heavy primaries and light ones, the width of the distribution, and its correlation with the depth of shower maximum are less sensitive to the physics assumptions. The latter two measures will reveal whether the primary flux is composed of a single or multiple species, with very little model dependence.

The Auger Observatory sites require a great deal of accessible, yet lightly populated land. The altitude above sea level is not of paramount importance in the study of air showers at such high energy, but the skies must be astronomically clear. A survey team has evaluated twenty candidate sites worldwide; a dozen sites have been visited and studied in detail. Beyond the physical attributes of the sites, selection criteria include the anticipated scientific and infrastructure support.

The survey team identified three finalist countries in each hemisphere: in the Southern Hemisphere, excellent candidates were nominated in Argentina, South Africa, and Australia; in the Northern Hemisphere, the United States, Mexico, and Spain were presented to the international collaboration as acceptable possibilities. A site in the Province of Mendoza, Argentina, was selected as the southern location of the Auger Observatory in November 1995. The collaboration voted in September 1996 to select the Northern Hemisphere location to be in Millard County, Utah, in the United States.

Chapter 2

Science

The Auger Project will explore the cosmic ray energy spectrum and arrival direction distribution above 10^{19} eV as a function of the mass of the primaries. Such data will shed light on the origin of these cosmic rays, on the distance of the sources, and on the magnetic field structure and strength between the sources and the earth. Further, for the subset of particles whose types have been identified, it may be possible to obtain information of relevance to particle physics at energies well beyond those ever attainable in terrestrial accelerators.

This chapter surveys the astrophysics and cosmology which underlies current thinking on the origin of the highest energy cosmic rays. It has proven difficult to construct a satisfactory theory. The fundamental obstacle to understanding the nature of these particles is the lack of data; the next chapter summarizes the present observational status. Here, we begin by discussing general principles of acceleration and propagation of extremely energetic particles, highlighting significant constraints on the possible sources. Next, we review some recent theoretical work. We conclude the chapter by describing the kind of measurements which are required to test theories.

2.1 Introduction

A detailed measurement of the energy spectrum will yield a wealth of important information on the nature of the highest energy cosmic rays. Soon after the discovery by Penzias and Wilson [11] of the cosmic microwave background radiation (CMBR), Greisen [12] and Zatsepin and Kuz'min [13] independently pointed out that this radiation would make the universe opaque to cosmic rays of sufficiently high energy. This occurs, for example, for protons when their energy exceeds the threshold for pion photoproduction (via the Δ^+ resonance) in an encounter with a photon of the CMBR. The reaction sequence $p\gamma \rightarrow \Delta^+ \rightarrow \pi^0 p$ effectively degrades the energy of the proton. The characteristic attenuation length is less than 50 Mpc¹ when the proton's energy is greater than 10^{20} eV. A similar phenomenon of

¹50 megaparsecs (Mpc) is the distance light travels in 150 million years. The center of the Virgo cluster of galaxies, of which our own Milky Way is a member, is approximately 20 Mpc away.

energy degradation also occurs for nuclei due to processes of photodisintegration. This is a small fraction of the size of the Universe and has the following implications:

- If the highest energy cosmic rays are universal in origin, then the observed energy spectrum should not extend, except at greatly reduced intensity, beyond about 5×10^{19} eV, a phenomenon known as the Greisen-Zatsepin-Kuz'min (GZK) cut-off.
- Particles with energy above the GZK cut-off must come from nearby, cosmologically speaking. Over modest distances, charged particles of such high energy would traverse cosmic magnetic fields with little deviation. Their observed trajectories would thus indicate the direction to their sources. It may therefore be possible to identify the sources of these particles with previously known astrophysical objects, or else to establish the existence of new sources which are not visible at lower energies. Identification of such sources requires that many cosmic ray events are detected from each one.

Due to their extremely low flux, the study of cosmic rays above 10^{19} eV requires extremely large detectors. This is illustrated in Figure 2.1, which shows a recent compilation[14] of measurements of the cosmic ray differential energy spectrum. The dotted line represents an E^{-3} spectrum for comparison. Also indicated are approximate integral fluxes (per steradian) above certain energies where the spectrum shows changes in its power law behavior. The observed rate of events above 10^{19} eV is about 0.5 events/km²/year/steradian; above 10^{20} eV, the rate has diminished by roughly a factor of 100.

Such large areas are, for the foreseeable future, only possible with ground-based air shower detectors. Current experiments, with areas of order 100 km², are limited in the number of events they can collect in the crucial energy region above 10^{19} eV. While there is insufficient data to answer the fundamental questions, present results hint at several interesting and important phenomena. For example, a recent analysis of a subset of the available data[15] noted that there were 7 events observed with energies exceeding 10^{20} eV, while a simple power-law extrapolation of the experiments' observed spectra at lower energy predicts more than 20. Since there is also the suggestion of a slight flattening of the spectrum above 10^{19} eV, these observations may be indicating interesting spectral structure. Could this be evidence for the GZK cut-off? On the other hand, there definitely are several events with $E > 10^{20}$ eV, which must originate from relatively nearby. What are their sources?

These questions will be discussed in more detail in the next chapter. To summarize, there simply are not enough data above 10^{20} eV to draw definitive conclusions. The Auger Project is designed to remedy this problem.

Much new theoretical work has already been stimulated by the recent observation of two events with estimated energies $E \geq 2 \times 10^{20}$ eV [4, 6] and also by the series of workshops on the Auger Project. None of the theories proposed to date accounts for all the facts in a really satisfactory way. The present data raise questions of great importance for astrophysics, cosmology, and fundamental physics.

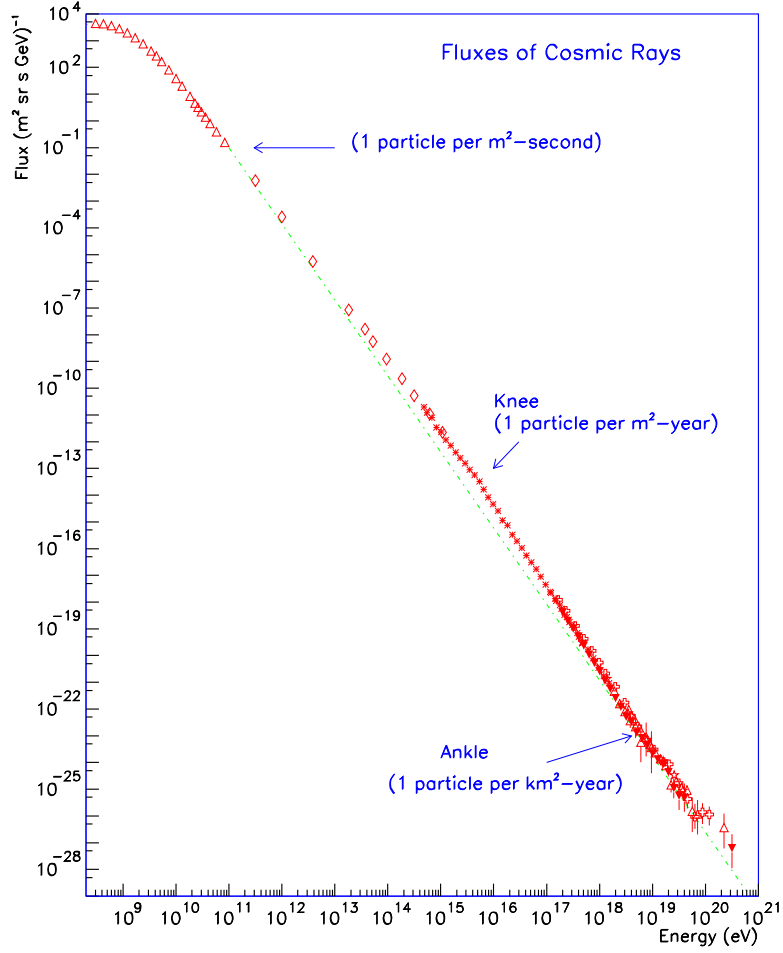


Figure 2.1: Compilation[14] of measurements of the differential energy spectrum of cosmic rays. The dotted line shows an E^{-3} power-law for comparison. Approximate integral fluxes (per steradian) are also shown.

2.2 Acceleration and propagation of cosmic rays

The two central questions about the highest energy cosmic rays are how, and where, they are accelerated. The most energetic particle yet detected, presumably a single proton or a nucleus, had a macroscopic energy of 50 joules — roughly the kinetic energy of a tennis ball at 100 mph! Its energy, 3×10^{20} eV, is more than eight orders of magnitude higher than can be achieved by the most powerful man-made accelerator. Over the years a few events with energies near 10^{20} eV have been recorded. More recently two events have been observed with energies well above the GZK cut-off and have, as a result, attracted significant attention and scrutiny. Each of the groups involved has devoted a paper to a critical review of the events and the analysis leading to their energy assignment [4, 6]. As will be shown, because of the limited range and high magnetic rigidity of such particles, a detector with sufficient collecting power will be able to determine their sources.

2.2.1 Acceleration

Acceleration in astrophysical settings occurs when energy in large-scale macroscopic motion is transferred to individual particles[17]. The macroscopic motion could, for example, be associated with turbulence or shock waves in plasmas. Another scenario is the environment near a rapidly spinning, magnetized compact object. There are also more speculative models invoking exotic mechanisms, such as topological defects.

Fermi acceleration

In 1949, Fermi[18] developed a model where particles can achieve high energies through repeated encounters with moving, magnetized plasmas. This process (“Fermi acceleration”) is often referred to as stochastic or diffusive acceleration, since high energies result from particles randomly scattering many times within a confined region, with some chance of escaping the region permanently. The magnetic field, B , embedded in the plasma plays a crucial role.

Fermi demonstrated that the geometry of moving plasma clouds is such that the *average* energy change per encounter is positive and proportional to the particle’s energy: $\Delta E = \alpha E$. After k encounters, a particle initially with energy E_0 will achieve an energy $E = E_0(1 + \alpha)^k$. Suppose P_{esc} is the probability per encounter that the particle escapes the containment region and is no longer accelerated. The number of particles which survive long enough to reach some energy E is given, by summing over k , to be $N(> E) \propto E^{-\gamma}$, where $\gamma \approx P_{esc}/\alpha$, if P_{esc} and α are each small. Thus, Fermi acceleration naturally produces a power-law spectrum of particle energies.

Fermi acceleration by astrophysical shock waves is an attractive paradigm with which to construct models of cosmic rays. As shown in Figure 2.1, cosmic rays exhibit a non-thermal power law energy spectrum. It can be shown [17] that the spectral index γ of the Fermi acceleration integral energy spectrum, in the limit of strong shocks, has a value

slightly greater than $\gamma \approx 1$, and is not very dependent upon the details of the environment. Because the particles will undergo energy dependent processes during transport to Earth, the observed spectrum is expected to be steeper than that at production. The experimentally observed integral spectrum varies from $E^{-1.1}$ to $E^{-2.1}$ in various energy regimes, so the predictions of Fermi acceleration are in reasonable accord with data. In situations where Fermi acceleration may occur from plasma motions which are not strong shocks, the spectral index is very sensitive to geometric details and can be quite large.

Perhaps most importantly, Fermi acceleration has actually been observed to occur in the heliosphere (although at much lower energy). One example is the direct observation by the *ISEE* satellite of the acceleration of $\sim 10 - 100$ keV protons by shocks in the solar wind. The data agree in detail with the predictions of Fermi acceleration theory[19].

In general, the maximum possible energy is determined by the length of time over which the particles are able to interact with the plasma. In some cases, the accelerating region itself only exists for a limited time, such as in the case of supernovae shock waves which dissipate after about 10^3 years. Otherwise, if the plasma disturbances persist for much longer periods, the maximum energy may be limited by an increased likelihood of escape from the region. The latter case is relevant to the extreme energies seen in cosmic rays. As particles reach extreme energy, it becomes very difficult to confine them magnetically to the acceleration region.

The simplest modeling[17, 20, 21] of Fermi acceleration by shock waves gives the maximum energy acquired by a particle of charge Ze :

$$E_{max} \approx \beta c \times Ze \times B \times L, \quad (2.1)$$

where L is the characteristic size of the acceleration region and βc is the shock velocity ($\beta \approx 0.01$ for supernovae). However, under certain configurations of the shock and the embedded magnetic field, β is replaced by a much larger factor, of order 1-3 [17, 22]. Equation 2.1 essentially states that the gyro-radius of the particle being accelerated must be contained within the acceleration region, as in a terrestrial accelerator. Realistically, it is unreasonable to assume that astrophysical accelerators will have the nearly 100% efficiency required to achieve energies like those in Eq. 2.1; it is more likely that the above value of E_{max} should be reduced by perhaps a factor of ten, depending on the details of the shock and its environment[20].

Figure 2.2 shows where some potential astrophysical accelerators lie in the B - L plane [23]. Objects below the diagonal lines derived from Eq. 2.1 cannot accelerate particles to 10^{20} eV by shock acceleration. The dashed line is for iron nuclei and the solid line for protons, each case for $\beta = 1$. A value of $\beta = 1$ is unrealistically extreme. The top of the shaded region is for protons assuming $\beta = 1/300$, a more typical value for many astrophysical shocks.

It is striking that the most energetic accelerators in the figure appear to have a maximum energy just in the range where the GZK cut-off comes into play. In addition, since for any given configuration of magnetic fields and plasma motion, the maximum total energy for nuclei is approximately Z times higher than that for protons, we expect the observed mass spectrum to have interesting and revealing structure in the energy range above 10^{19} eV.

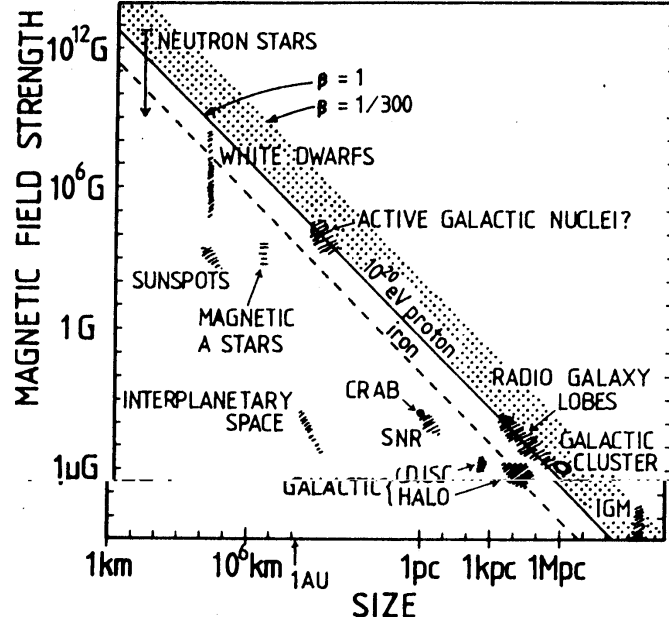


Figure 2.2: Size and magnetic field strength of possible sites of particle acceleration [23]. Objects below the diagonal lines cannot accelerate particles to 10^{20} eV by shock acceleration. Dashed line is for iron nuclei, solid for protons, each with $\beta = 1$. The top of the shaded region is for protons and $\beta = 1/300$. IGM refers to the intergalactic medium; Galactic Cluster refers to accretion shocks in clusters.

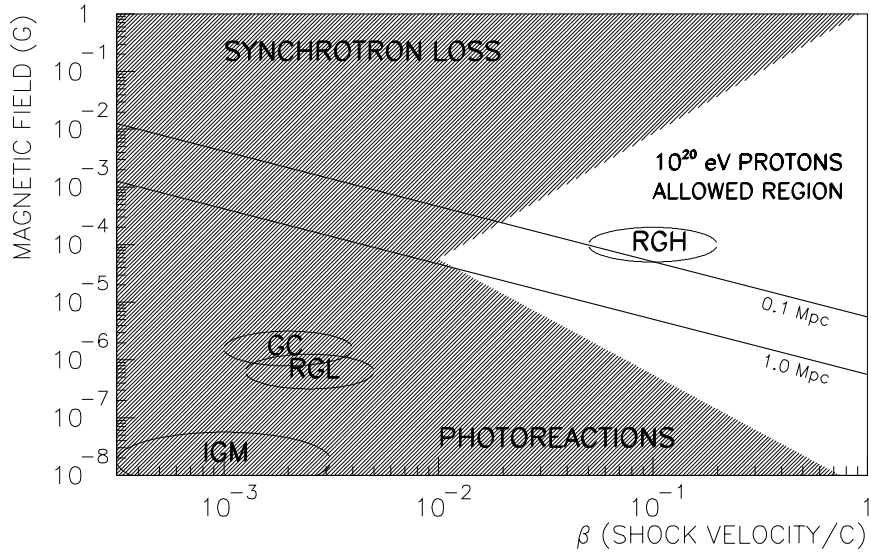


Figure 2.3: Magnetic field strength and shock velocity of possible sites of acceleration (adapted from [23, 24]). Only the unshaded region allows acceleration of protons to 10^{20} eV. Candidate accelerators must also lie above lines appropriate to their characteristic size. Notations are as in the last figure: GC is Galactic Cluster, RGL is Radio Galaxy Lobes. RGH is a subclass of radio-lobe sites added here, denoting radio galaxy hot-spots.

Good energy resolution and sensitivity to the mass of the initiating primary will be required in order, for example, to distinguish between a GZK cut-off for a proton source and the maximum energy of an accelerator for which $E_{max} \propto Z \times e$.

Only a few of the objects in Figure 2.2 appear able to generate particle energies above 10^{20} eV. Generally, large structures associated with galaxies or groups of galaxies seem to have sufficient size and field strength to merit consideration as acceleration sites. Not shown in this figure is a recent suggestion by Cesarsky[25, 26] that the environs of colliding galaxies might also have the appropriate conditions to accelerate particles beyond 10^{20} eV through diffusive shock processes. The magnetic fields will be amplified during the collision above the single galaxy value.

It is often impossible to achieve the maximum energy suggested by Eq. 2.1 and Fig. 2.2. This occurs when conditions are such that the energy loss rate exceeds the acceleration rate. One source of losses is synchrotron radiation, which can become important even for protons at very high energy in regions of extreme magnetic fields. Other loss processes include photoproduction interactions (e.g., $p\gamma \rightarrow \pi^+n$). These loss rates can dominate all others in compact volumes with intense thermal radiation. It can also be important in large regions of space if the acceleration occurs over long time scales. In the latter case it is the cosmic microwave background radiation that provides the target photon field; indeed, this is the mechanism of the GZK cut-off mentioned earlier.

The effects of synchrotron radiation or interactions with the cosmic background radiation were not included in Figure 2.2. Acceleration ceases when the rate of such losses exceeds the rate at which energy is gained through shock encounters. Figure 2.3 illustrates an estimate of this effect[23, 24], showing that certain combinations of shock velocity and magnetic field strength can prevent the acceleration process from achieving energies as high as 10^{20} eV. An estimate of the allowed region of $B - \beta$ space was made as follows. The rate of energy gain from shock acceleration is parametrized as $dE/dt \propto \beta^2 B$, by replacing L in Eq. 2.1 by βcT (with T some characteristic time over which the shock acceleration process works), and differentiating. Equating this rate with that of losses from synchrotron radiation ($dE/dt \propto B^2$) or photoreactions ($dE/dt \approx \text{constant}$), one obtains the diagonal boundaries of the disallowed regions in the Figure 2.3. Note that this calculation was done for photoreactions on the cosmic background radiation; even more of $B - \beta$ space would be excluded if the target radiation field was the intense, higher energy environment near an AGN. It can be seen here that the rate of energy gain from most of the potential accelerators in the Figure 2.2 is too slow to overcome losses due to photoreactions.

Compact objects

Compact objects with very large magnetic fields, such as neutron stars or Active Galactic Nuclei (AGNs), also appear in Figure 2.2 near the diagonal lines which indicate the requirements for shock acceleration to 10^{20} eV. However, in these compact systems, shock acceleration (perhaps in accretion flows) is not the only means to accelerate particles. The rapid rotation of small, highly magnetized objects generates enormous electric fields. These fields might then accelerate particles in so-called “one-shot” mechanisms. It turns out that

the upper limit on the energy in such models is given by a formula quite similar to the shock acceleration case in Equation 2.1 [27]. For example, the maximum energy available from a rotating neutron star can be obtained by dimensional analysis as $E_{max} = eZ\omega B_s R_s^2/c$ where ω is the pulsar angular velocity, B_s a surface magnetic field and R_s the neutron star radius. Representative values of $B = B_s$ and $L = R_s$ for neutron stars were shown in Fig. 2.2, and the combinations required to achieve 10^{20} eV energies would lie on a line very similar to that shown for the shock wave case.

When realistic models of acceleration are constructed, however, this ideal dimensional limit for neutron stars is not realized [27]. For example, in an aligned rotator, the maximum potential available is the integral of the electric field from the pole to the last open field line which extends beyond the light cylinder. In this case the dimensional estimate of E_{max} is reduced by an additional factor of $\omega R_s/c \leq 0.1$. Further, it is generally true that the energetic particles which may be produced will suffer significant degradation of their energy in the intense local radiation fields. Examples include curvature radiation near neutron stars or photodisintegration of nuclei and photopion production by protons near the cores of AGN.

Nevertheless, it may be possible to have field geometries associated with compact objects which are able to accelerate particles to extreme energy. Colgate has described one scenario where electrostatic fields are aligned with magnetic flux surfaces[28]. This configuration arises during reconnection of magnetic fields in plasmas. Pulsars or AGN at the cores of quasars may be examples. In Colgate's model, a single traversal by a charged particle of a reconnection surface associated with the twisted flux surfaces extending from a quasar accretion disk to the radio lobes can lead to particle energies well above those presently observed.

Exotic accelerators

Inspection of Figures 2.2 and 2.3 suggests that few of the proposed astrophysical accelerators can easily account for energies as high as 10^{20} eV. Indeed, the possibility exists that the very highest energy particles come not from these "conventional" objects but are produced directly by some exotic mechanism (e.g. the so-called "topological defects"). Such sources could produce jets of hadrons and photons with energies well above 10^{20} eV that would then cascade down to lower energy. This particular scenario has its own potential difficulties, which will be mentioned in a later section. Nevertheless it is clear that cosmic rays in this energy range have the potential to teach us about particle physics far beyond the reach of even dreamt-of accelerators.

2.2.2 Propagation and the GZK Cutoff

Cosmic ray particles do not travel unhindered through space. They are subject to various interactions and their trajectories may be curved by magnetic fields. The result of these effects will characteristically alter the observed energy spectrum and arrival directions at earth.

For a cosmic ray nucleus of charge Ze in a magnetic field $B_{\mu G}$ in μGauss , the Larmor radius in kiloparsecs (kpc) is

$$R_{kpc} \approx E_{18}/(Z B_{\mu G}), \quad (2.2)$$

where E_{18} is the total energy of the particle in units of 10^{18} eV. Since the disk of the Galaxy is significantly thinner than 1 kpc, and magnetic fields there are on the order of a few μGauss , if all cosmic rays are from sources in the disk, they must exhibit a tendency to come from the galactic plane at higher energies. At present there is no statistically significant evidence for cosmic ray arrival directions to cluster along the Galactic plane. It is therefore reasonable to assume that particles with $E > 10^{19}$ eV are extragalactic in origin, even for heavy particles such as Iron nuclei ($Z = 26$). (Indeed, it has been proposed that if nuclei can be identified with a specific source direction, then it may be possible to use the large-scale magnetic field in the disk of the Galaxy as a magnetic analyzer, correlating deflections with energy and charge. This will be discussed in the next chapter.)

If cosmic rays seen at earth have an extragalactic origin then they have survived a very long time. There are several processes that can degrade the energy of particles as they propagate through the cosmos [17]. We have already mentioned one mechanism whereby protons produce secondary hadrons in interactions with the microwave background. They may also lose energy through the production of electron-positron pairs in the background radiation. After pion photoproduction, the proton (or perhaps, instead, a neutron) emerges with a reduced but still very large energy. Further interactions occur until its energy is below the GZK cut off[29].

Nuclei also undergo photo-disintegration in the CMBR and infrared radiations[30], losing about 3-4 nucleons per Mpc traveled when their energy exceeds about 2×10^{19} eV[31]. Although the latter process occurs at a lower energy per nucleon than pion photoproduction by protons, the thresholds for the two processes are nearly the same when expressed in terms of the total energy of the nucleus. Hence, no nucleus can be observed at earth with such energy if the source is more than about 20 Mpc distant.

The attenuation lengths for these processes are shown in Figure 2.4. Also shown is the interaction length of high energy photons which interact with various background radiations and produce electron-positron pairs[29]. In this case we show separately the attenuation of photons in diffuse infra-red radiation, the radio background, and the CMBR. The radio and infra-red backgrounds are, however, much less well determined than the microwave radiation.

Note the line in Figure 2.4 marked “red shift limit”. All particles lose energy over time due to the general expansion of the universe. The time scale over which a particle would suffer complete energy loss from this effect is of order

$$\tau_H = \left(\frac{1}{E} \frac{dE}{dt}\right)^{-1} \approx H^{-1},$$

where H is the Hubble constant. The constant $c\tau_H$ is plotted in this figure, representing an absolute upper limit on the distance a particle can travel before expiring.

As a consequence of the various background radiation fields, there are limits to how far away the sources of extremely energetic particles can be, no matter how high their initial

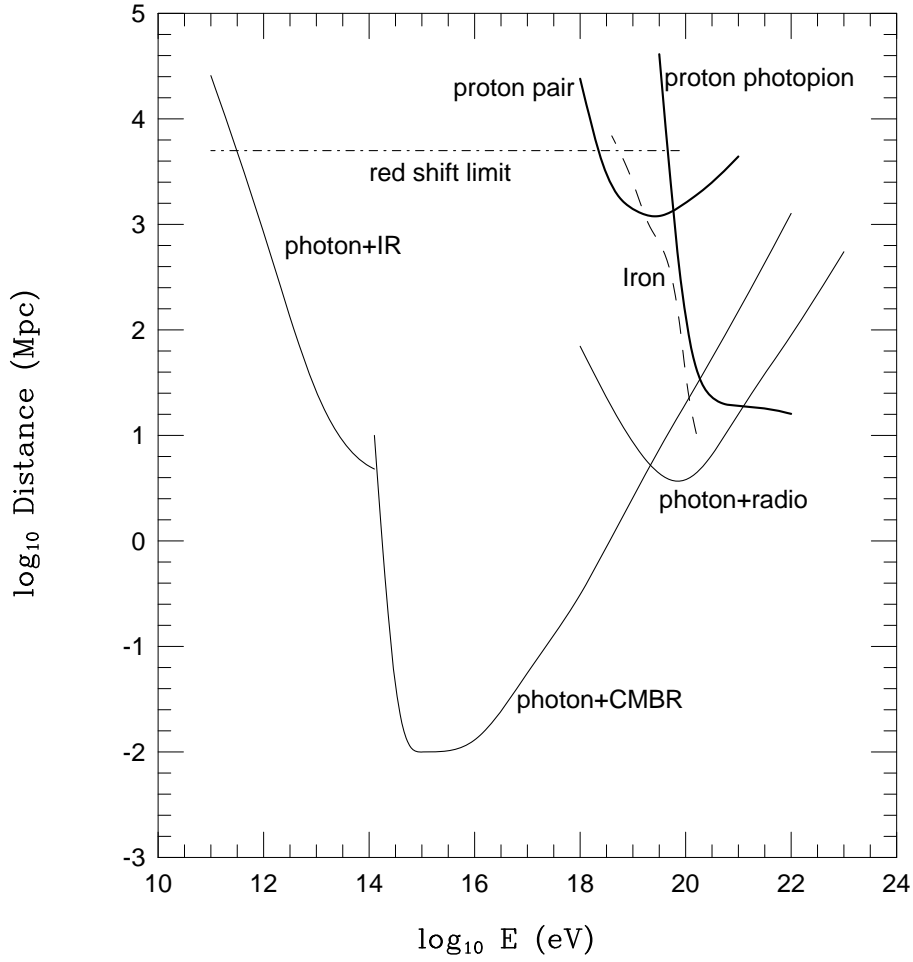


Figure 2.4: Attenuation length of photons, protons and iron in various background radiations as a function of energy. The three lowest and left-most curves refer to photons, showing the attenuation by infra-red, microwave background and radio [29]. The upper, right-most solid curves refer to propagation of protons in the microwave background, showing separately the effect of pair production and photo-pion production [29]. The dashed curve illustrates the attenuation of iron nuclei [30].

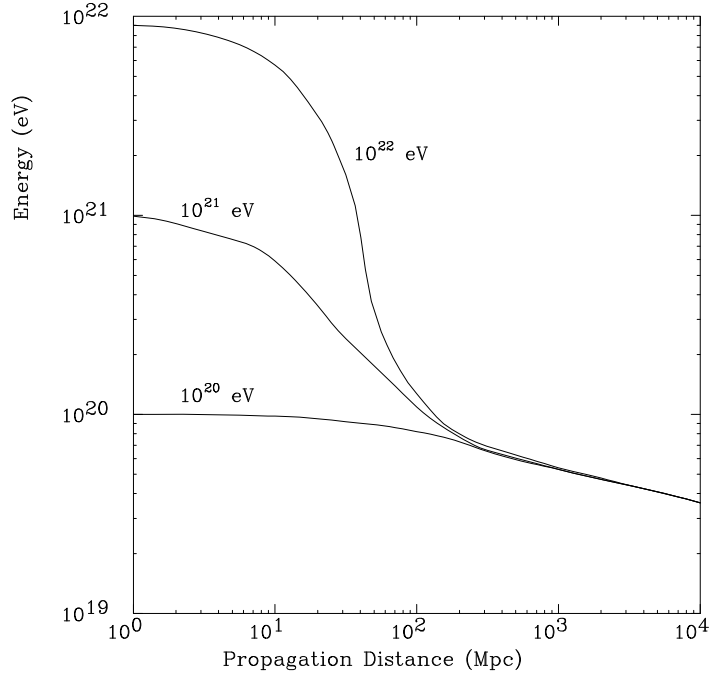


Figure 2.5: Energy of a proton as a function of propagation distance through the 2.7 K cosmic background radiation for various initial energies [31, 32].

energy. This is illustrated for protons in Figure 2.5 [31, 32]. This figure shows how, as described above, the energy of a proton effectively degrades due to successive photopion interactions with the CMBR. The GZK limit is evident, i.e., the flux of protons observed with energies exceeding about 10^{20} eV, regardless of their initial energy, is sharply reduced if they have traveled more than 100 Mpc.

Stated more generally, the attenuation length of protons and nuclei in the microwave background depends strongly on energy, especially in the region of the threshold for photopion production. As a result, the *observed* shape of the spectrum will depend strongly on the distribution in time and space of the sources, as well as the initial energy spectrum of the particles. Some examples are illustrated in Figures 2.6 and 2.7 [33]. Figure 2.6 shows the energy spectrum observed at earth if protons originate from a single source with an initial differential energy spectrum proportional to E^{-2} . The observed spectrum is very sensitive to the distance of the source, showing a sharp GZK cutoff when the source exceeds a distance corresponding to a redshift² of $z = 0.01$ (≈ 50 Mpc).

Figure 2.7 gives the observed spectrum for a different situation, where there are many sources of cosmic rays, distributed uniformly in space (“cosmologically”). Again, the spectrum is complex and sensitive to details of the production process. The five curves correspond to models in which cosmic ray production is increasingly important in the past and for which the cut-off effect is therefore more severe. For example, the curve labeled 1 corresponds to a

²Redshift z is the fractional wavelength change in radiation from distant sources due to the expansion of the universe. To first order, z is proportional to the source distance: $d \approx zc/H \approx z \times 5000$ Mpc, where H is the Hubble constant.

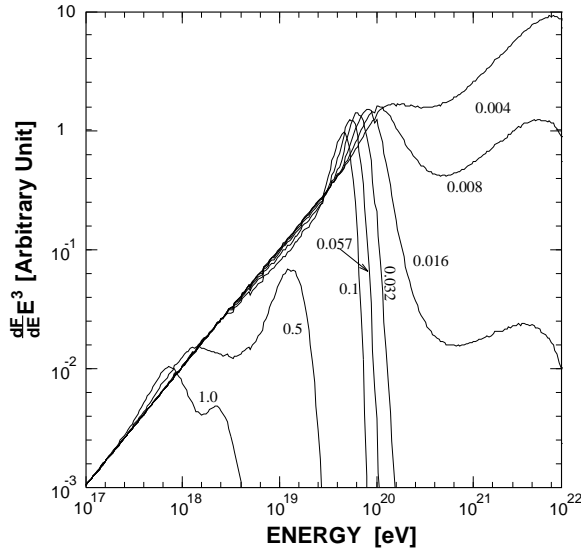


Figure 2.6: The observed energy spectra assuming a single source of protons with an E^{-2} injection spectra[33]. Spectra are shown for various fixed source distances corresponding to redshifts $z = 0.004$ to 1 (i.e., from about 2 Mpc to 5 Gpc).

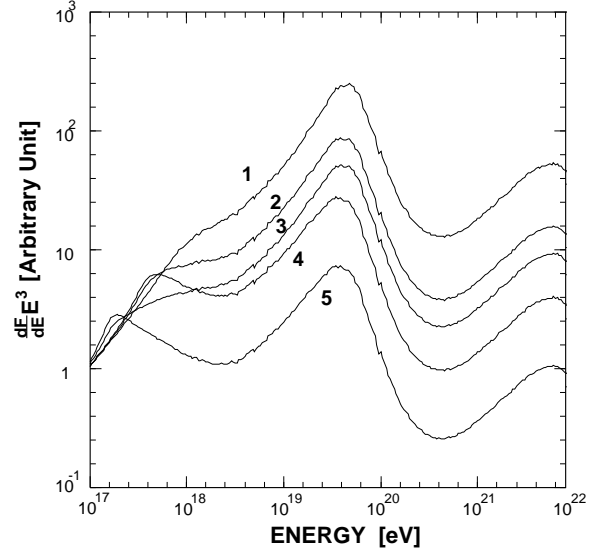


Figure 2.7: Observed spectra from several cosmological distributions of sources [33], leading to a strong cut-off below 10^{20} eV. The five curves correspond to models in which the cosmic ray production is increasingly important in the past and for which the cut-off effect is therefore more severe.

uniform distribution of sources up to a red-shift of $z = 2$ but with no cosmological evolution. Curve 5 is a model in which the sources extend back to red-shift $z = 4$ and the sources are assumed to be significantly more active in the past than at present.

Figure 2.7 also indicates another general feature of the GZK effect, that of a slight recovery of spectra if they extend to energies of $10^{21} - 10^{22}$ eV or higher. The interactions which cause losses are primarily resonance phenomena (e.g., Δ^+ production). The “dip” in the spectra seen in Fig. 2.7 near 10^{21} eV reflects this. Most of the acceleration models described earlier are clearly unable to generate particles at such extreme energy, but some of the exotic scenarios predict fluxes possibly observable in very large detectors such as the Auger Observatory. There has also been recent work which points out that the energy of the GZK cutoff might be significantly higher if the cosmic rays are light (~ 1 GeV) SUSY particles[34], because the interaction threshold is higher. Such speculation is interesting in light of the fact that cosmic rays are now known to exist above 10^{20} eV.

It is not easy to fit the experimental observations with combinations of the spectra of Figure 2.6. These data are discussed more fully in the next chapter, but note, for example, that a source sufficiently nearby to account for two events observed above 2×10^{20} eV tends to yield more particles than are actually observed just below this energy. The data may actually indicate an anomalously low flux or “gap” in the spectrum around 10^{20} eV, perhaps indicating a transition where one source’s spectrum overtakes another. Unfortunately, existing detectors have insufficient exposure for this feature around 10^{20} eV to be considered to be statistically

significant.

Thus, particles with $E > 10^{20}$ eV must come from relatively nearby (Figure 2.5). Because extragalactic fields are expected to be weak (probably $< 10^{-9}$ G [35]), the particle trajectories will be only slightly deflected. We can expect to do particle astronomy with these particles. A major goal of the Auger Project is to accumulate enough particles above 10^{20} eV to identify source locations based upon arrival directions.

The observation of extragalactic sources of ultra high energy cosmic rays by the Auger Project will establish important constraints on the poorly known structure and strength of extragalactic magnetic fields. The study of the spectrum, composition, and directional distribution of cosmic rays with energies above $\sim 10^{19}$ eV will probe extragalactic magnetic fields below the present observational upper limit of $\sim 10^{-9}$ G [35]. The angular distribution of the arrival directions of charged cosmic rays with respect to their source(s) conveys information about extragalactic fields. In addition, ultra high energy photons interact with magnetic fields, and so will exhibit an alteration in their observed spectrum around $\sim 10^{19}$ eV for extragalactic magnetic fields in the range $10^{-9} - 10^{-11}$ G [36]. Probing extragalactic fields will help answer the question of how they originated and whether the galactic magnetic field is purely a primordial relic or was dynamically enhanced from a much smaller cosmological seed field. Either case will have important consequences which extend from understanding galaxy formation to the study of processes in the early universe (e.g., phase transitions) which generate magnetic fields.

2.3 Recent theoretical work

We have mentioned above general principles of and constraints on mechanisms of particle acceleration. Spurred by recent detection of cosmic ray events apparently exceeding the GZK cutoff, there has been much recent work on detailed models. This section highlights some of this work, emphasizing how different models may have signatures discernable by the Auger Observatory. Three kinds of models are considered:

- Gradual acceleration in large objects, such as radio galaxies;
- Acceleration in catastrophic events, e.g. in association with gamma-ray bursts;
- Exotic sources, e.g. topological defects or monopoles

There are also some remarks on the inevitable production of astrophysical neutrinos associated with the cosmic rays.

None of the models described here can be considered complete. We conclude the section with comments on the considerable work which remains, with emphasis on the need for more and better data at the highest energies. The Auger Project aims to provide the data which is necessary for further progress.

2.3.1 Shock acceleration in extended sources

In the preceding section, broad arguments were presented which showed that if the highest energy cosmic rays were produced through Fermi acceleration associated with strong shock waves, then the most likely sources were extragalactic. That the highest energy particles require extragalactic sources has long been recognized [37]. There are a variety of scenarios for accelerating particles in large-scale astrophysical structures. The following are examples which have been recently investigated in detail:

- Large scale structure formation in the universe could lead to very large scale shocks and associated particle acceleration [38].
- Shocks in the accretion flows in clusters of galaxies, possibly already observed in an absorption feature in the Perseus cluster. If the magnetic fields are strong enough, particles can be accelerated to high energy [39].
- Collisions of galaxies, fairly common in dense clusters, are expected to generate shock waves [26].
- Shocks in the lobes at the ends of the high speed jets observed in some powerful radio galaxies may be sites of particle acceleration. Some are sufficiently nearby to supply events above 10^{20} eV [40].

Detailed discussion of all of these mechanisms is beyond the scope of this Report. However, as an illustration of the issues involved, we discuss the last scenario in more detail.

It is natural to consider radio galaxy jets as possible accelerators since they are among the few structures in the cosmos with sufficient size and magnetic field strength to support shock acceleration to 10^{20} eV (recall Figure 2.2). Many objects with strong radio jets have been observed to be emitters of GeV gamma-rays by the Compton Gamma Ray Observatory[41]. There is also convincing evidence that the gamma ray spectrum from two AGNs (Markarian 421 and 501, whose jets are pointing toward earth) continues into the TeV energy range [42]. These high energy gamma rays are produced by electrons or protons of still higher energy. In either case, they indicate the tremendous energy flow in the jets.

Localized regions of especially intense radio emission, so-called “hot spots”, are sometimes seen within the lobes at the ends of the jets of high power radio galaxies. These features are usually interpreted as large scale plasma shock waves in the jets, possibly weakly relativistic [40, 43]. Objects which exhibit hot spots are a small sub-class of all radio sources called Fanaroff-Riley Class II (FR-II) galaxies.

It is important to recognize that models of acceleration to extreme energy will also have consequences at much lower energy. Particles will “react” on fields which have been influenced by the shocks responsible for the highest energies. When constructing models to explain 10^{20} eV particles, one must simultaneously respect constraints imposed by other observations. Consider, for example, that it has been empirically known that certain otherwise

very different objects have some puzzlingly similar properties of their optical radiation. Radio quasars with strong red optical emission, the jets in M87, and optical emission from FR-II radio galaxy hot spots all share two common properties: i) The emission is polarized, and is therefore almost certainly synchrotron emission from very energetic electrons/positrons and ii) the emission cuts off sharply near 3×10^{14} Hz. The generality of such a finding in both compact and extended objects, and sources as different as the M87 jet and radio galaxy hot spots, suggest rather simple underlying physics. A comprehensive model, addressing a very wide range of energy, is required.

In 1987, Biermann and Strittmatter proposed [40] that Fermi acceleration of protons at shock fronts could provide a basis for a physical interpretation of the preceding observations. As described earlier, protons are accelerated near shock waves until they reach a sufficiently high energy where losses in their interaction with the ambient magnetic and photon fields compensate for any further gains. The highest energy protons in turn initiate turbulence in the thermal plasma, which can be described as a superposition of component “waves” whose wave-numbers have a power-law distribution. The turbulence spectrum power-law can be related to the synchrotron emission spectrum integrated over the emission region. Indeed the same standard power-law is found in almost all systems, including the solar wind and in the interstellar medium. In this resulting wave field, electrons are also accelerated by the shock wave. The maximum synchrotron emission frequency is nearly independent of the magnetic field strength, depending weakly on the ratio of the energy density of photon and magnetic fields, and strongly on the shock velocity. The highest emission frequency possible in the rest frame of the shock is approximately 2×10^{15} Hz, assuming a rather simple shock geometry and non-relativistic flow. Recent optical observations in fact support such a number for the cut-off frequency of the synchrotron emission [44] .

A key feature of the model is that the acceleration to the highest energies occurs far from the central engine where the intense radiation would cause severe energy losses to cosmic ray particles. An important result was the prediction that radio galaxy hot spots could accelerate protons to 10^{21} eV [45, 46]. Indeed, the model *required* that protons be accelerated to extreme energy in order to explain the lower energy observations.

A relativistic flow could obviously increase both the maximum cut-off frequency and the maximum proton energy. The ultimate power source for the plasma shock waves in the jets of strong radio sources is the compact object at the center. One can scale the properties of radio jets and hot spots with the power of the central engine and estimate the maximum proton energy possible in any of the known radio galaxies. The maximum energy derived from this limiting argument is about 4×10^{21} eV [47].

Romero and coworkers [48] have also recently employed the “hot-spot” model to the nearby radio source Cen-A, predicting that it is capable of accelerating protons to a maximum energy of 2×10^{21} eV. If this analysis is correct, then because Cen-A is extremely close (3.5 Mpc), it would surely have been “seen” as a point-source had there been any cosmic ray experiments in the Southern Hemisphere with the collecting power and angular resolution enjoyed by the Northern Hemisphere’s Akeno/AGASA or Haverah Park arrays.

If powerful radio galaxies are in fact the source of extremely energetic cosmic rays, then certain signatures should be evident:

- The arrival directions of individual events above 10^{20} eV — which are, it is supposed, only weakly deflected by intergalactic magnetic fields — should cluster about the direction of nearby strong radio galaxies, especially FR-II galaxies or those with highly asymmetric structures.
- The distribution of arrival directions of events above a few times 10^{19} eV should exhibit anisotropy which increases with energy. The preferred directions should correlate with the distribution of nearby strong radio galaxies. These galaxies tend to lie along a broad swath of the sky known as the “supergalactic plane”.
- Radio galaxy sources of the events above 10^{20} eV should also produce an excess of particles of somewhat lower energy from those same general directions.
- The cosmic rays are almost certainly protons or perhaps gamma-rays, since heavier nuclei are unlikely to survive transport from the central AGN through to the hot spots at the end of the jets.

The directions of extremely energetic cosmic rays events have been studied to see if they correlate with any known objects. There are interesting hints:

- The two highest energy events (a 3×10^{20} eV event from the Fly’s Eye, and the 2×10^{20} eV event from Akeno) appear to come from the general locations of FR-II galaxies, probably nearby ones[49]. The likelihood of a random association of the event directions with FR-II galaxies is small, since there are very few such sources in the sky within modest distances.
- Evidence for a directional clustering along the supergalactic plane has recently been published, for cosmic rays whose energies exceed 4×10^{19} eV[50, 51, 52]. The statistical significance of these observations is rather small, however.

Pending the collection and analysis of a far larger body of data, it is premature to draw strong conclusions from either of the above observations. Each will be discussed more fully in the next chapter (Sections 3.3.1 and 3.3.2).

The association of event directions with the supergalactic plane is an example of a more general situation discussed by Berezhinsky et al.[27] in which there is an excess of sources in the local supercluster. The prediction of clustering in the supergalactic plane would hold for any mechanism associated with mass concentrations in our part of the Universe.

The shape of the cosmic ray energy spectrum near the expected cut-off may tell us about the relative density enhancement of nearby sources. This is particularly true if all sources are of a similar nature. However, if it is impossible to distinguish one source from another based on the arrival directions or if different source types are involved, the situation

is considerably more complicated. Even if the sources are of a similar type, such as the lobes of radio galaxies, each system would be expected to have somewhat different parameters and correspondingly different values of E_{max} , some above and some below the GZK cut-off.

Better angular resolution, a sensitivity to the nuclear type of the primary cosmic ray particle, and many more events above 10^{20} eV are needed to resolve the situation. The Auger Project aims to meet these needs.

2.3.2 Association with gamma-ray bursts

Gamma-ray bursts (GRBs) are observed (by satellites) as short, intense bursts of keV-GeV gamma rays. Despite hundreds having been detected (at a rate of about one per day), their origin and nature are unknown. It is possible that GRBs are indicators of some catastrophic event during which cosmic ray particles are shock-accelerated to extreme energies.

Recent observations give increasing evidence that the sources of GRBs are distributed throughout the entire universe (a “cosmological” origin)[53]. If GRBs are indeed so very far away then they must be very powerful. It is interesting that the power needed to account for the energy flux of the highest energy cosmic rays is comparable to the average rate (over volume and time) at which energy is emitted as γ -rays by GRBs in the cosmological scenario. These facts invite the suggestion that GRBs and high-energy cosmic rays have a common origin.

Aspects of the data (such as millisecond variability, a hard spectrum sometimes extending to GeV energies, etc.) impose strong constraints on the physical conditions in the γ -ray emitting region[54]. It has been suggested that protons may be Fermi accelerated in this region to $10^{20} - 10^{21}$ eV [55, 56]. Waxman has argued[57] that the cosmic ray spectrum above 10^{19} eV is consistent with a cosmological distribution of sources of protons having a power law generation spectrum $dN/dE \propto E^{-x}$, with $x = 2.3 \pm 0.5$ (consistent with the universal value characteristic of Fermi acceleration by strong shocks).

An essential ingredient of a cosmological GRB model for high energy cosmic rays is a time delay due to inter-galactic magnetic fields (IGMF). Consider the two most energetic cosmic ray events yet recorded, from the Fly’s Eye and the Akeno experiments. The energy of the most energetic cosmic ray detected by the Fly’s Eye experiment was 3×10^{20} eV, and that of the most energetic AGASA event was 2×10^{20} eV. As was shown in Figure 2.5, the distance such energetic particles could travel before becoming victims of the GZK cutoff is < 100 Mpc. The arrival directions of the two events are sufficiently separated that we will assume that they did not originate from the same GRB event within such a distance. Furthermore, the two events were recorded within 26 months of each other. Assuming GRBs have a cosmological origin, the rate of relevant “nearby” GRBs is rather small. Based on the GRB observations from BATSE, there is about one GRB per 50 years in the field of view of the cosmic ray experiments and within 100 Mpc [58]. The observed short time difference between the Fly’s Eye and AGASA events can be reconciled with the typical rate of GRBs if the dispersion in the arrival times of protons produced in a single burst is longer than a time on the order of the average time difference between GRBs. Therefore, 10^{20} eV protons produced in a distant

GRB must arrive at earth dispersed in time over ≥ 50 years. Dispersions of this magnitude are quite plausible, produced by the combined effects of deflection by random magnetic fields and energy dispersion of the particles, provided that the IGMF is $\geq 10^{-12}$ G ([55, 59]; see also Figure 2.9 later in this chapter).

An arrival time dispersion exceeding 50 yr implies that no correlation between the arrival directions of cosmic rays and gamma-rays should be expected on a much smaller time scale, unless the GRBs are very nearby. Since the BATSE observations started only about 5 years ago, it is not possible to conduct an extensive search for correlations between extreme-energy cosmic ray events and older GRBs. Nevertheless, it was pointed out [60], that the arrival direction error box of the most energetic Fly’s Eye event is consistent (within errors) with that of the strongest GRB recorded in the first two BATSE catalogues (still among the highest 1% of all BATSE events collected). Similarly, the most energetic AGASA event is within 5° of another strong GRB. There are many BATSE events, so it is not unlikely to find one near either the Fly’s Eye or Akeno events. It is nevertheless noteworthy that these GRBs are so strong.

Clearly, many more cosmic ray events at the highest energies must be collected in order to test the hypothesis of an association with GRBs. If the possible correlation between the arrival directions of either the Fly’s Eye or Akeno event with strong GRBs is confirmed (by observing new events above 2×10^{20} eV to be correlated with GRBs on time scales of a year or so), this would imply that the rate per unit volume of nearby GRB events is much higher than that expected from a cosmological distribution. Such a finding would strongly suggest that the (common) sources of GRBs and of high energy cosmic rays are Galactic [61, 59].

If the highest energy cosmic rays are associated with nearby GRBs (e.g., in the Galactic halo), one expects: (i) new $> 10^{20}$ eV events to be correlated with GRBs; (ii) no GZK cutoff; (iii) highly isotropic cosmic ray distribution, due to the observed isotropy of GRBs. If, on the other hand, the high energy cosmic rays are associated with cosmological GRBs, one expects a GZK cutoff, and, if GRB sources are associated with luminous matter, anisotropy related to the large-scale structure of the local ($< 100\text{Mpc}$) universe, since cosmic rays cannot travel far.

In addition to the latter signatures, which are common to any model with cosmological distribution of cosmic ray sources, the cosmological GRB model for high energy cosmic rays predicts several unique signatures [62]. The energy dependent delays in the cosmic ray arrival times, induced by the IGMF, result in individual cosmic ray sources having narrow observed spectra, since at any given time only those cosmic rays having a fixed time delay are observed. Thus, the brightest cosmic ray sources may be different at different energies.

Another possible signature is a delayed flux of moderately high energy photons[59]. The energy lost by the cosmic rays as they propagate and interact with the microwave background is transformed by cascading into secondary GeV-TeV photons. A significant fraction of these photons can arrive with delays much smaller than the cosmic ray delay if much of inter-galactic space is occupied by large-scale magnetic “voids”, regions of size $\sim 5\text{Mpc}$ or larger and field weaker than 10^{-15}G . Such voids might be expected, for example, in models where a weak primordial field is amplified in shocked, turbulent regions of the intergalactic

medium during the formation of large-scale structure. For a field strength $\sim 4 \times 10^{-11} \text{G}$ in the high field regions, the value required to account for observed Galactic fields if the IGMF were frozen in the protogalactic plasma, the delay of cosmic rays produced by a burst at a distance of 100Mpc is $\sim 100 \text{yr}$, and the fluence of secondary photons above 10 GeV on hour-day time scales is $I(> E) \sim 10^{-6} E_{\text{TeV}}^{-1} \text{cm}^{-2}$. This fluence is close to the detection threshold of current high-energy γ -ray experiments. It will be described later how the Auger Observatory ought to be sensitive as well, by observing enhanced individual detector singles rates over the entire array.

If the suggested association of the highest energy cosmic rays with cosmological GRBs is true, then the expected signatures should be identifiable once the number of events observed above 10^{19}eV is increased by a factor of several tens [57, 62]. This would require ~ 50 observation-years with existing experiments, but only a few years operation of the Auger Observatory. Confirming an association of the highest energy cosmic rays with GRBs (either Galactic or cosmological) would have profound influence on our understanding of both phenomena, and would also provide information on the poorly known IGMF.

2.3.3 Exotic sources

The difficulties so far encountered in modelling the production of extremely high energy cosmic rays arise from the need to identify an astrophysical environment capable of raising low energy particles to extreme energy. In contrast to “bottom-up” acceleration of charged particles in active galactic nuclei or other astronomical objects, there could be a “top-down” (TD) mechanism where the (charged and/or neutral) primaries are produced at extreme energies in the first place.

Topological Defects

One example invokes the decay of supermassive “X” particles. These particles may be radiated from *topological defects* formed during phase transitions as the early universe cooled, a product of spontaneous symmetry breaking implicit in some Grand Unified Theories (GUTs)[63, 64]. Relic topological defects, such as ordinary and superconducting cosmic strings, domain walls, and magnetic monopoles, are relatively stable topologically, but can release part of their energy in the form of X particles, if they collapse or annihilate.

The X particles, with typical GUT scale masses on the order of 10^{24} eV , subsequently decay into leptons and quarks. The strongly interacting quarks fragment into jets of hadrons resulting in typically $10^4 - 10^5$ mesons and baryons. Certain TD scenarios (e.g., annihilation of bound states of magnetic monopoles) are capable of producing extremely energetic cosmic rays at the observed level [65]. There is, then, the exciting possibility of connecting cosmic rays to new fundamental physics. Since the predicted density of topological defects is very model dependent [66], measurements of the highest energy cosmic rays may impose tight constraints on the theory.

The shapes of the nucleon and γ -ray spectra produced in TD models are expected to be

universal (i.e., independent of the any specific TD scenario) above 10^{20} eV, depending only on the physics of X particle decay. This is because at these energies, nucleons and γ -rays have attenuation lengths in the cosmic microwave background radiation (CMBR) which are small compared to the Hubble scale (the “red shift limit” in Fig. 2.4). Cosmological evolutionary effects which depend on the specific TD model are therefore negligible. Since the resulting spectra tend to be considerably harder than acceleration spectra, TD mechanisms could contribute to the flux dominantly above $\simeq 10^{20}$ eV, but negligibly in the range 10^{14} eV – 10^{19} eV.

TD models of the origin of the highest energy cosmic rays are subject to a variety of constraints which are mostly of cosmological nature. For example, the predicted neutrino flux and the γ -ray flux below $\sim 10^{14}$ eV depend on the energy release integrated over redshift and thus on the specific TD model. Compared to acceleration scenarios, this energy release can be substantial, especially at high redshifts where there is no contribution from conventional sources like galaxies. Electromagnetic energy injected into the universe above the pair production threshold on the CMBR is recycled into a generic cascade spectrum below this threshold on a time scale short compared to one Hubble time. This can have several potentially observable effects, such as modified light element abundances due to ^4He photodisintegration, distortions of the CMBR, and neutrino fluxes at earth. Comparison with observational data already rules out a certain class of TD models related to superconducting cosmic strings [67].

If a TD model is to explain the origin of the highest energy cosmic rays, its predicted spectrum must be normalized to account for the events observed above 10^{20} eV without violating any observational flux measurements and limits at higher and lower energies. Observational data on the universal γ -ray background in the 100 MeV region [68, 69, 70] to which the generic cascade spectrum would contribute directly turn out to play an important role in that respect. Since especially the extreme energy γ -ray flux depends sensitively on some astrophysical parameters like the extragalactic magnetic field, a reliable calculation of the predicted spectral shapes requires numerical methods [71]. Interestingly, in the case of TD scenarios with uniform injection (as expected, for example, in case of monopole annihilation [65]) the resulting constraints are somewhat modified compared to earlier analytical estimates [67]. For certain extragalactic magnetic fields, X particle masses as high as 10^{25} eV are quite viable [72]. An earlier claim that TD models might already be ruled out altogether [29] can only be substantiated for the case of discrete sources with monoenergetic injection [71], but there is still concern that the predicted gamma ray emission at 3×10^{20} eV and above is too large.

Since it is currently not possible to determine unambiguously the composition of extremely energetic cosmic rays, the normalization procedure has to involve the sum of the nucleon and γ -ray fluxes. This, in turn, predicts the spectrum and composition at other energies and offers certain signatures typical for the TD scenario: a hard TD component could produce a pronounced recovery in the form of a flattening beyond the GZK cutoff. This might become an important signature for TD scenarios in case a considerable rate of superhigh energy events above 2×10^{20} eV is found and if the “gap” in the cosmic ray spectrum between these events and the lower energy data should prove to be real [73]. Acceleration

models cannot account for a gap due to their softer spectra. Furthermore, within TD scenarios, the flux above 10^{20} eV would be dominated by γ -rays, as opposed to the case of an acceleration origin [74]. In addition, an isotropic γ -ray component at the 10% level of the total flux at 10^{19} eV would hint at the presence of a TD mechanism and a large scale magnetic field weaker than about 10^{-11} G [72]. Another indicator for new physics would be the detection of a substantial neutrino flux above 10^{18} eV. Combined with bounds on contributions to the low energy γ -ray background, its magnitude would yield important information on the decay mechanism operating in a possible TD scenario [75].

In summary, the signature of TD models is a very hard cosmic ray spectrum ($\sim E^{-1.5}$) dominated by neutrinos, gamma rays, and protons. The proton component comprises only a few percent of the total flux. The majority of the particles are light and uncharged, and would presumably include any exotic varieties that might exist (e.g., photinos). Overall, the spectrum extends to extraordinarily high energy, near the X -particle mass of perhaps 10^{24} eV. The hardness and high energy of the spectrum may provide events whose energies are well beyond the GZK cutoff.

These distinctive characteristics arise because the particles are produced in the decay of massive X bosons. Observation of such a spectrum would be extremely interesting because theories with a real grand unification simple group will have such heavy particles, while most classes of string theories do not. For them, $SU(3) \times SU(2) \times U(1)$ directly unify at the string scale, without a larger group entering. String theories can produce topological defects [76], but the mechanisms for producing cosmic rays are different. Cosmic ray data that implied the existence of heavy bosons would have a major impact on efforts to formulate a fundamental theory.

Confirmation of the existence of an “exotic” component of cosmic rays, such as produced by topological defects, would potentially provide insight into the conditions in the early universe, as well as into particle physics beyond the “Standard Model”.

Magnetic monopoles

Another idea utilizing topological defects is one where relic magnetic monopoles themselves constitute the highest energy primary cosmic rays. This possibility was first raised in 1960 by Porter [77]. We discuss here a more recent investigation of this idea by Kephart and Weiler [78].

As in the earlier discussion of GRBs, the consideration of relic monopoles as an explanation of cosmic rays is motivated by two interesting facts:

- The observed cosmic ray flux above 10^{20} eV is similar to the theoretically allowed *Parker bound* [79] (the maximum flux of relic monopoles which would not destroy the observed interstellar magnetic field).
- Under reasonable assumptions about field strengths and field coherence lengths, Dirac monopoles can be accelerated to energies beyond 10^{20} eV.

If the highest energy cosmic rays are indeed magnetic monopoles, they must be relativistic to transfer enough energy to the atmosphere to initiate air showers and thus they must have masses less than 10^{19} eV. Because there is a monotonic relationship between the allowed monopole flux and mass in cosmological models of monopole origin, this provides another limit on the density of monopoles which is consistent with the Parker bound. It may also lead to an energy threshold for the initiation of observable air showers, an important prediction if indeed the apparent “gap” in the energy spectrum of cosmic rays around 10^{20} eV is confirmed by further data.

The monopole hypothesis has observational consequences. One is that energetic monopoles may be expected to be distributed preferentially in the direction of the local galactic magnetic field. Another may be that air showers produced by monopoles have distinctive characteristics.

Detailed modelling of the interactions of magnetic monopoles in the upper atmosphere has not been carried out to date. The electromagnetic component is not difficult to calculate and should resemble the interactions of a particle of charge $137/2$, but the hadronic component is likely to be complicated. For monopoles of mass greater than 10^{15} eV, the energy loss per scatter is expected to be rather small, leading to a shower that is initiated over a longer distance, and the scattering angle per collision is expected to be larger, scaling as $1/\gamma$. It is not yet known whether a monopole can produce an air shower which would mimic what is expected for a hadron primary and in particular the rather “normal” looking cascade development which was observed directly with the Fly’s Eye (see the next chapter, section 3.2.2).

The detectors of the Auger Observatory are designed to be sensitive to air shower structure in order to study effects related to the nuclear composition of the primary particles.

2.3.4 Astrophysical Neutrinos

A common feature of most of the models of cosmic ray sources discussed above is the production of extremely high energy neutrinos. The detection of neutrino fluxes would provide valuable additional experimental signatures to distinguish different models. The Auger Observatory will be able to detect and identify extremely energetic neutrinos, if their flux is high enough.

Neutrinos provide a unique opportunity to explore regions of the Universe that are otherwise obscured by either large depths of matter or by the attenuating effects of intense radiation fields (recall Figure 2.4). Neutrinos are uncharged and have a very small interaction cross section, so they emerge unscathed from even the most active locations. Neutrinos are undeflected and virtually unattenuated while traversing very long cosmic trajectories, thus providing a way to study the possible sites of cosmic ray origin in a manner complementary to that using other particles.

The recent discoveries of GeV and TeV γ -ray sources seemingly necessitates the production of neutrinos within AGN, radiogalaxies, blazars, and quasars [80]. Charged pions are

produced in these astrophysical beam dumps and decay into neutrinos. The mechanism of the GZK cutoff itself is also a source of high energy neutrinos through the $\Delta^+ \rightarrow \pi^+ + \dots \rightarrow \nu + \dots$ decay sequence[81]. Neutrinos are also one of the main expected byproducts of two possible cosmic ray production mechanisms described above: the decay of topological defects [63, 64], and GRB's [82].

In summary, all proposed cosmic sources of extremely energetic cosmic rays seem inevitably to produce energetic neutrinos in numbers possibly large enough to be observable. Their detection would provide independent support for these models. Moreover, the relative fluxes of neutrinos and cosmic rays should give extremely valuable information on the distance at which they are produced because of the difference in their interaction lengths in intergalactic space. The ability of the Auger Observatory to detect high energy cosmic neutrinos will be discussed in the next chapter.

2.3.5 Summary Comments on Source Models

Our survey of recent theoretical work has just shown several very interesting alternatives to the problem of the origin of the highest energy cosmic rays. All of these models begin to penetrate the fundamental mystery: how can such extraordinary energies be achieved? Yet none of the ideas is yet completely satisfactory. Here are some the important issues which need to be clarified:

- An approximately homogeneous distribution of radio galaxy sources predicts that the cosmic ray energy spectrum observed at earth will show the GZK cutoff. It would not permit many particles well above 10^{20} eV and yet there are now several such candidates observed. Are there too many?
- The GZK cutoff is avoided only if the sources are nearby. That is, all observed cosmic rays are *young*. For radio galaxy sources, a strong preponderance of such young particles might be plausible if we lived in a rich cluster, or if the radio sky were dominated by a single brilliant source. But neither is the case. There is no independent reason to suppose that there is such a strong local overdensity of radio galaxy sources.
- With the exception of radio galaxy hot spots, the cited models of shock acceleration in extended sources would appear to be too slow to work (recall Figure 2.3). The energy losses associated with interactions on the cosmic background radiation exceed the acceleration gains by the time the particles approach 10^{20} eV. Thus no particles exceeding about 10^{20} eV appear able to emerge from most sources.
- Likewise, GRB sources of cosmic rays, if they are distributed homogeneously throughout the universe, should exhibit the GZK cutoff. This or any homogeneous model is not viable if very many events are observed well above 10^{20} eV.
- Nearby GRB sources (i.e., in our Galaxy or its corona) would avoid the GZK cutoff, but no theory for acceleration to extreme energy has been proposed. It is certainly not expected in any of the popular models of Galactic GRBs involving neutron stars.

- Topological defect models predict a cosmic ray spectral *shape* similar to that which is being observed at the highest energies. However, its normalization is not calculated from first principles. When set to agree with the rate at which events above 10^{20} eV have been observed, it may predict too many particles at even higher energies. This possible conflict is very uncertain due to the lack of data at such high energy. However, this normalization may also have problems at lower energies. Some TD scenarios may be ruled out by measured upper limits on 100 MeV diffuse gamma-ray fluxes if the mean intergalactic field strength exceeds 10^{-11} G or if the TD annihilation rate evolved early in the universe as strongly as the theoretically favored time dependence (t^{-3}).

It is clear that the most important things needed to further our physical understanding are more, and better, data. An accurate, high-statistics measurement of the energy spectrum, arrival directions, and particle identity of the highest energy cosmic rays will be provided by the Auger Observatory's detectors. While these data may not conclusively establish any of the models as they now stand, it is an absolutely necessary part of the effort to achieve the final goal of understanding the origin of the highest energy cosmic rays.

2.4 Observational capabilities needed for the Auger Observatory

As discussed above, models of acceleration and propagation do not satisfactorily account for all the observations of cosmic rays at the highest energies. This is an assurance that either new fundamental physics or unanticipated astrophysics will result from solving this mystery. With only incremental increases in detector aperture, however, the discoveries will be a long time coming. The promise of new physics is ample motivation to increase the collecting power now by a large factor. The largest current surface array (AGASA) has an area of 100 km². The Auger Project will achieve a 60-fold increase in collecting power with an area of 6000 km². Complete sky coverage with fairly uniform celestial exposure is essential for a sensitive search for arrival direction anisotropy. The detector must also measure cosmic ray directions, energies, and identify the types of particles accurately.

2.4.1 Composition resolution.

The mass composition of cosmic rays is a powerful constraint on theories. Highly charged nuclei are easier to accelerate to high energies than protons, although they are susceptible to photodisintegration at the source and during propagation. Gamma-rays and neutrinos are potentially unique signatures of exotic models. The mass composition should be determined at all energies. It is especially important to identify the particle type(s) arriving with energies above the expected GZK cut-off (which occurs at different energies for protons and heavy nuclei). The goal is to achieve sufficient energy and mass resolution to resolve the situation above 10^{19} eV in which all of the following effects might be manifest:

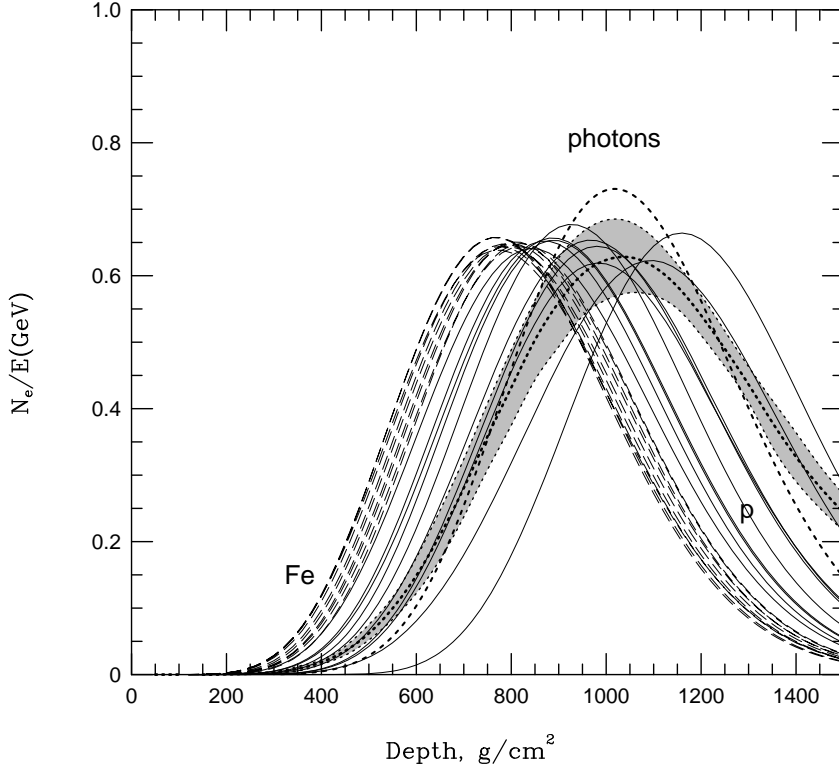


Figure 2.8: Longitudinal development of air showers with energies near 10^{20} eV produced by protons, iron nuclei, or photons. Ten showers each are individually shown for protons (thin solid lines) and iron nuclei (thin dashed lines). The calculation for photons was performed two ways: the shaded band includes the LPM effect and interactions with the geomagnetic field, while the thick dashed is simple electromagnetic cascading only.

- A GZK cut-off.
- Events beyond the GZK cut-off, contributed by nearby sources. The energy spectrum might exhibit a characteristic dip-bump structure if there are new and/or exotic source for the highest energy particles.
- Energy-dependent composition associated with the upper limiting energies of different contributing sources.
- Energy-dependent composition associated with differential attenuation in the intergalactic medium.

To accomplish this goal it will be necessary to be able to distinguish among the three major groups of potential primaries: primordial nuclei (protons and helium), products of stellar nucleosynthesis (carbon and heavier), and photons (expected in some models of exotic sources).

One way to distinguish primary particle types is by measuring the way the extensive air shower develops. Figure 2.8 shows a comparison of the longitudinal shower profiles for

different types of primaries, from a one dimensional monte-carlo simulation. The curves show the growth and attenuation of air showers in terms of the number of electrons N_e present at various atmospheric depths.

Average shower development curves for photon induced air showers are also shown in Figure 2.8. The banded curve for photons includes the cascading in the geomagnetic field as well as the LPM effect³. The thick dashed line shows the profile that would be expected for a simple (Bethe-Heitler) electromagnetic cascade only.

It must be noted that current uncertainty in knowledge of hadronic interactions at such high energy leads to uncertainties in the expected X_{max} – the depth in the atmosphere where the shower reaches the maximum number of particles – for iron and proton showers, although their *difference* is not strongly model dependent[84]. The calculated profiles for protons (and to a lesser extent heavy nuclei) also have inherent systematic uncertainties as a consequence of the need to extrapolate hadronic interactions many orders of magnitude beyond accelerator energies. The main effect of these uncertainties would be to shift the entire profile to the right or left by amounts possibly as much as 100 g/cm², since only the first few interactions occur at such unexplored energy regimes.

The calculation used to estimate the air shower development curves in Figure 2.8 was a simplified one-dimensional simulation. A more sophisticated and detailed simulation (described in Chapter 4) confirms the features shown here, predicting the mean X_{max} difference between iron and proton showers is about 70 g/cm².

The numbers of muons and electrons in air showers also differ between events initiated by protons, gamma rays, and heavier nuclei. Gamma-ray showers have far fewer muons than hadron showers. Heavy nuclei at the same total energy as a proton will yield showers with more muons. These effects are discussed in more detail in Chapter 4 (section 4.2.3), where simulation of air shower physics is discussed. The Auger Observatory’s ground detectors will have good ability to distinguish primary mass groups based on muon and electron measurements. When combined with measurements of the shower longitudinal development by the fluorescence detector of Auger, the power of the experiment is further increased.

2.4.2 Energy resolution

An accurate measurement of the spectrum requires both adequate statistics and good energy resolution. Energy measurement errors distort a steeply falling spectrum because each energy bin gains many more mismeasured showers from lower energies than it does from higher energy. It will be shown later (Chapter 5, section 5.2.5) that structures in the shape of the cosmic ray energy spectrum (like the GZK cutoff) can be clearly resolved if the experimental $\delta E/E$ resolution is less than about 20%.

³The Landau-Pomeranchuk-Migdal (LPM) effect is a quantum mechanical alteration of electromagnetic showers at very high energy. Roughly put, bremsstrahlung has a “formation length”, governed by the uncertainty principle, which grows with the electron’s energy. Radiation begins to be suppressed when this length becomes comparable to the distance between scatterings[83].

By designing the detector to have good mass resolution, it will necessarily have good energy resolution. The Auger Observatory fluorescence detector should measure the atmospheric depth of shower maximum (X_{max}) to an accuracy of 20 g/cm² (as mentioned above, the mean X_{max} for iron showers is about 70 g/cm² higher in the atmosphere than that from protons of equal energy). As will be seen in a later chapter, a 20 g/cm² X_{max} resolution implies that the integral of the longitudinal profile (i.e., the total energy) can be fitted with less than 10% uncertainty. Systematic uncertainties from modeling the atmosphere may also be present. Similarly, the ground array should have sensitivity to composition by measuring separately the muon and electromagnetic ($e + \gamma$) particle fluxes. By achieving adequate accuracy in the muon/electromagnetic ratio, particle density measurements will necessarily provide good energy resolution.

2.4.3 Arrival direction resolution

Detector requirements for anisotropy studies depend on the particular energy range of interest. For energies above 10²⁰ eV, magnetic deflection of protons by Galactic or extragalactic magnetic fields is expected to be so small that detector angular resolution is an issue. For charged particles of lower energy, point source resolution is limited by magnetic scattering – detector angular resolution is important only if there is a flux of neutral particles. A very large exposure is then needed in order to detect any anisotropy or clustering of arrival directions. At the detector's energy threshold, scattering by magnetic fields may be so severe that the distribution of arrival directions differs from isotropy in only a subtle way: in addition to large numbers of events, a fairly uniform exposure will be vital for sensitive detection of such patterns.

For a source at distance L_{kpc} , the trajectory of a charged particle in a uniform magnetic field is curved such that the observed angular deviation of its arrival direction with respect to the straight line of sight to its source is:

$$\theta \approx 0.3^\circ \frac{L_{kpc} Z B_{\mu G}}{E_{20}} = 0.3^\circ \frac{L_{Mpc} Z B_{nG}}{E_{20}}, \quad (2.3)$$

if the deflection is reasonably small (i.e., $\sin \theta \approx \theta$). This expression is an immediate result of Equation 2.2 using $L = R\theta$. The particle energy E_{20} is in units of 10²⁰ eV, the field strength B transverse to the particle motion is in μG when L is in kpc or nG when L is in Mpc. The former case is typical of Galactic dimensions and fields, the latter for extragalactic paths. Z is the charge of the particle in units of e .

The left side of Figure 2.9 displays the observed angular deflection from Eq. 2.3 as a function of energy for protons. One line is calculated for a source distance of 0.5 kpc and an intervening transverse magnetic field of 2 μG (typical of the Galaxy's disk thickness and field intensity). The same line in the figure happens also to pertain to a distance of 1 Mpc through a transverse extragalactic field of 1 nG.

The assumption of a value of order nG for extragalactic magnetic fields is not supported by observations (see the discussion at the end of the first section of this chapter). Intergalactic

field strengths and coherence lengths are not well established, but it is plausible to assume that fields have coherent directions on scales of about 1 Mpc. A long trajectory is multiply deflected, each “scatter” contributing an independent angular deviation whose magnitude is roughly given by Eq. 2.3. The number of scatterings is given by the path length divided by a *step size*. The step size l is taken here as the coherence length, so the number of scatterings is equivalent to the source distance in units of Mpc. The average total angular deviation of the arrival direction from the line of sight to the source can then be approximated as $\sqrt{L_{Mpc}}$ times the angular deviation over 1 Mpc. The left side of Figure 2.9 exhibits the result for a linear distance to the source of 30 Mpc (a typical distance to other galaxies in our local cluster). These assumptions about extragalactic field strength and coherence length are not verifiable, but they provide a specific model for examining the energy dependence of magnetic deflections.

Magnetic bending of particle trajectories causes them to arrive later than photons emitted simultaneously from the same source. For a simple circular arc path, the expected delay is given by

$$\Delta t \approx 0.012 \text{ yrs} \times L_{kpc}^3 Z^2 B_{\mu G}^2 / E_{20}^2 = 12.0 \text{ yrs} \times L_{Mpc}^3 Z^2 B_{nG}^2 / E_{20}^2,$$

with L the straight-line distance to the source. For multiple scattering with step size l_{Mpc} , the delay is

$$\Delta t \approx 6.0 \text{ yrs} \times L_{Mpc}^2 l_{Mpc} Z^2 B_{nG}^2 / E_{20}^2.$$

The right side of Figure 2.9 shows the expected proton time delay as a function of energy for Galactic and extragalactic path lengths. The Galactic path is taken, as before, to be a circular arc originating from a source 0.5 kpc distant and $B = 2\mu G$. The extragalactic path length is again taken for a source distance of 30 Mpc, $B = 1 \text{ nG}$, and with a step size $l_{Mpc} = 1$. It is notable that the time delays expected for extragalactic sources can be very large, preventing the association of charged cosmic ray arrival times with astrophysical events at the source observed in photons or other neutral particles.

The search for point sources or an anisotropic cosmic ray arrival direction distribution will have energy dependent requirements. We discuss below three energy ranges pertinent to Auger observations.

$E > 10^{20} \text{ eV}$

The estimated angular deflection of a 10^{20} eV proton over Galactic distances is 0.3° , as shown in Figure 2.9. If extragalactic deflections are negligible, then charged particle astronomy is certainly possible and a detector angular resolution which is small compared to 0.3° would be desirable in order to locate the sources as precisely as possible. However, extragalactic deflections are likely to exceed the Galactic deflection, even though pion photoproduction limits the path lengths to about 50 Mpc. According to the model of multiple scattering outlined above, the arrival directions from a single source would be dispersed by $(\sqrt{50}) \times 0.3^\circ = 2.1^\circ$. It is important that the detector angular resolution be better than this in order to take full advantage of the high magnetic rigidity. Based on the present uncertain intensity

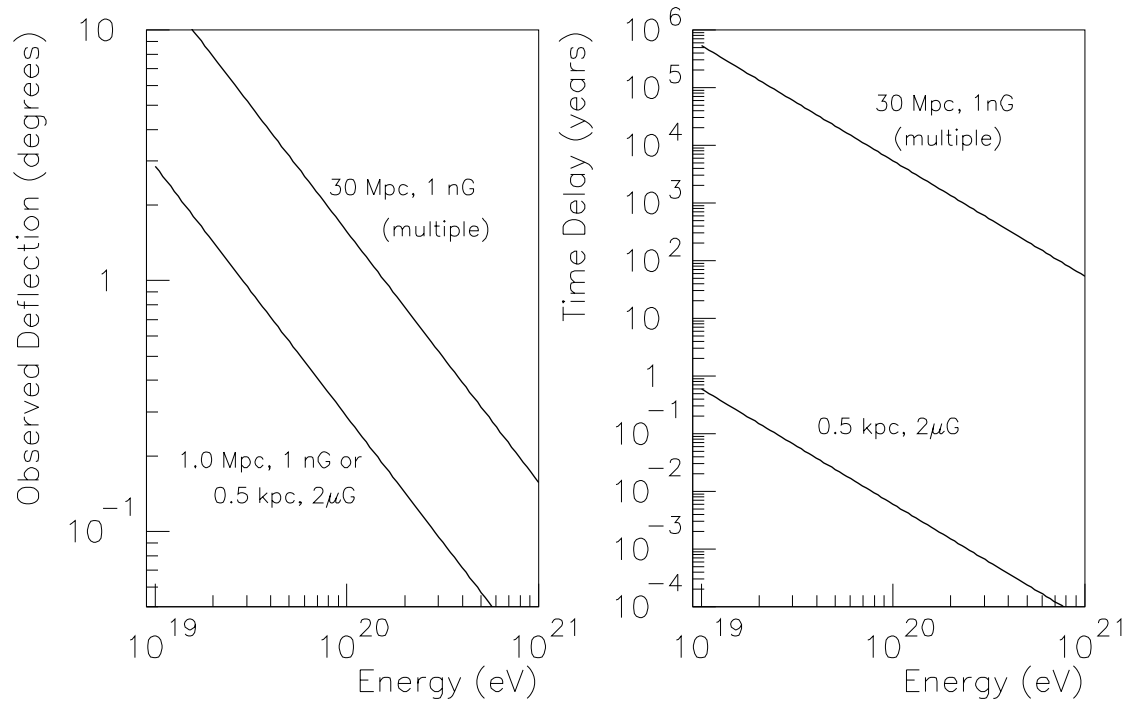


Figure 2.9: Magnetic bending of protons. On the left, the observed deflection from a straight-line path for several cases: travel through the Galactic disk or a path of 1 Mpc through extragalactic space, and multiple scattering over 30 Mpc (assuming a field coherence length of 1 Mpc). On the right side, the time delay relative to a straight line trajectory for two of these cases.

determinations, the Auger Observatory may detect about 180 such particles in three years. It may then be obvious if the number of contributing sources is much less than 180, based on the presence of tight clusters. Sensitivity to “repeaters” depends on angular resolution. If the angular resolution is limited only by this 2.1° magnetic deflection, the expected number of error circles overlapping by chance if randomly distributed on the sky would be about 20. If degraded further by a 3° detector angular resolution, for example, the number of chance overlaps would be about 70. Detector resolution better than 2° is desirable in case extragalactic magnetic deflections are less than estimated here and in case there is a flux of neutrons (whose decay length $\gamma c\tau$ is about 1 Mpc at 10^{20} eV) or γ -rays.

$$E > 4 \times 10^{19} \text{ eV}$$

Recent analysis of Haverah Park [50] and AGASA data [52] suggests that there is an excess of arrival directions associated with the “supergalactic plane”⁴. The observed anisotropy begins to be seen at about 4×10^{19} eV. If confirmed, this is an exciting result because it would verify a variety of expectations. The first expectation is that particles of such high energy should be magnetically rigid enough to point back to their sources with only small deflection, even for rather large source distances. Another expectation is that particles at these energies have not traveled more than a few hundred Mpc, since attenuation from the GZK effect would become severe (recall Figure 2.4). Within that nearby volume of space, the mass density of the universe is biased toward the supergalactic plane. Any theory of energetic particle production would predict the source locations to be correlated with the mass distribution. The importance for this discussion is the observational evidence that the cosmic ray population above 4×10^{19} eV is not isotropic, implying that the shower directions do indeed carry information about source locations.

In three years of running, the Auger Observatory will collect more than 1000 showers above 4×10^{19} eV with approximately uniform sky exposure. Figure 2.9 gave the expected angular deflection for protons as 0.7° at 4×10^{19} eV. Assuming a typical source distance of 200 Mpc, then the multiply-scattered arrival directions should be distributed about the source directions by $(\sqrt{200}) \times 0.7^\circ = 10^\circ$. Unless there are very many sources, clusters from individual sources should be evident. Figure 2.10 shows a simulation of the Auger sky at energies above 4×10^{19} eV after 3 years if all the cosmic rays come from 15 sources of approximately equal flux. Each source is smeared by sampling its arrival directions from a 10° Gaussian. The source locations are easily seen by eye and their coordinates can be localized to within $10^\circ/\sqrt{N}$ for N events from each. A realistic map would have a variety of source fluxes and magnetic dispersions. Higher flux and smaller dispersion makes a discrete source easier to detect.

Note that the orientations of the arrival directions around the sources in Figure 2.10 were simulated by *uniformly* placing them around the source direction. Each cluster thus has a circular appearance on the sky map. In reality the clusters will have more complex shapes which depend upon the magnetic fields and the energy spectrum of the particles[86].

⁴Recall that the supergalactic plane is a swath of sky which includes the locations of most of the nearest galaxies. The evidence for an excess of events from this direction is discussed in Section 3.3.1.

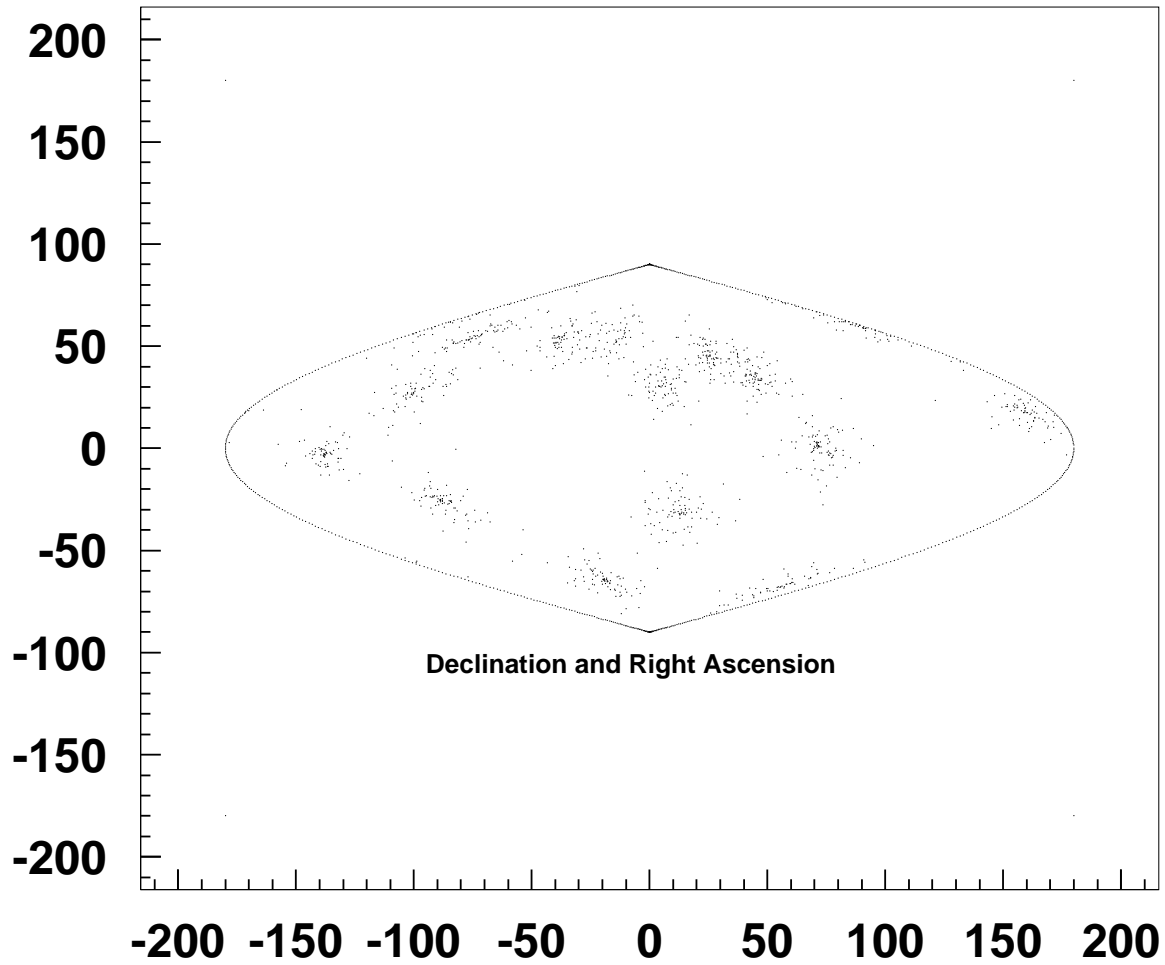


Figure 2.10: Simulation of the Auger sky for showers with energy greater than 4×10^{19} eV after 3 years (1165 showers expected). Positions for 15 point sources of approximately equal flux were chosen randomly. Each simulated source is smeared by sampling a Gaussian of 10° width.

For example, the arrival directions might form thin arcs on the map, passing through the source locations. In any case there will likely be a correlation of displacement with energy. Thus, anisotropy analysis benefits greatly from both good direction reconstruction accuracy and good energy resolution.

$E > 10^{19}$ eV

The anisotropy analysis is expected to be more complicated using all the Auger Observatory showers above 10^{19} eV. The problem is not lack of statistics, as 18,000 showers should be collected in three years. The difficulty is due in part to the fact that the GZK effect does not significantly attenuate these particles, and so there is no effective distance limit imposed on the possible source locations. Thus, the detected particles may have suffered magnetic scrambling over cosmological times, perhaps having originated from a source distribution which reflects the large scale homogeneity of the universe. There may also be a

non-negligible contribution from our Galaxy at 10^{19} eV. If the cosmic rays of galactic origin are all heavy nuclei at this energy (due to preferential acceleration and confinement), an analysis excluding small mass primaries could reveal a pattern produced by sources in the galactic disk compounded by propagation through the Galaxy’s magnetic field.

A sensitive anisotropy analysis is greatly facilitated by uniform sky exposure. This is a primary reason for building identical detectors in both the northern and southern hemispheres. Previous experiments have had highly non-uniform exposure, including large areas with no exposure whatsoever. A search for arrival direction anisotropies under those conditions is extremely difficult, and analysis by spherical harmonics is not feasible. Even the simplest search for a dipole harmonic cannot be conclusive. This point was emphasized in the 1980s when an apparent negative gradient was reported in galactic latitude [87, 88, 89]. The initial interpretation was that the intensity of cosmic rays is greater from southern latitudes than from the galactic northern hemisphere. Wolfendale and Wdowczyk [90] pointed out, however, that for a detector with a north-dominated exposure, such a gradient could also be construed as evidence for an excess from galactic *equatorial* regions, without any actual north-south asymmetry in the cosmic ray intensity. With poor exposure to south galactic latitudes, two radically different interpretations were viable.

Identical installations in both the northern and southern hemispheres will ensure that the Auger Observatory has nearly uniform exposure to the entire sky. A small exposure dependence on declination will remain, but it is well known and can easily be corrected for. The Auger Observatory will be the first opportunity to study cosmic ray arrival directions over the full celestial sphere with good efficiency.

2.4.4 Neutrino Astronomy

It was noted in the last section that most proposed cosmic sources of extremely energetic cosmic rays seem surely to lead to associated neutrino fluxes. Their detection would provide independent and complementary information to discriminate between models. Here, we describe the sensitivity of a general purpose cosmic ray detector to extremely energetic neutrinos. The main method to differentiate neutrino-induced air showers from ordinary cosmic rays is to use their very low interaction cross section to advantage: neutrinos will produce *horizontal* air showers (“HAS”) over the Auger Observatory far more easily than ordinary hadronic cosmic rays can.

The first requirement of any neutrino detector is a large target mass. Several experiments are currently under development to instrument large volumes of water or ice with photomultipliers and detect the Čerenkov light from neutrino interactions [80]. These detectors sense the Čerenkov light produced either by muons (from charged current ν_μ interactions) or electromagnetic cascades (ν_e interactions). Theoretical estimates of TeV and PeV neutrino fluxes from quasars and radiogalaxies have motivated recent interest in $1 \text{ km}^3 \text{ H}_2\text{O}$ detectors.

It has also been known for a long time that deeply penetrating high energy particles such as muons and neutrinos initiate horizontal air showers that can be detected at ground level [91]. Since the mean free path for muons and neutrinos in the atmosphere is larger than

the whole atmospheric depth, they have roughly equal probability to interact at any point in the atmosphere. The rate of air showers due to the hadronic cosmic rays decreases very rapidly with zenith angle as the atmospheric depth rises from about 1000 g/cm^2 vertically to nearly $4 \times 10^4 \text{ g/cm}^2$ horizontally. The electromagnetic component of air showers is absorbed well before reaching the Earth's surface, leaving only muons for events at sufficiently large zenith angles. An air shower array that is sensitive to muons, like that planned for Auger, is then also sensitive to penetrating neutrino events.

Large zenith angle events were first observed in the 1960's [92] for moderately large air showers (10^3 to 10^5 particles). They have been interpreted as electromagnetic showers induced by hard bremsstrahlung events from the conventional atmospheric muon flux (π and K decays) alone [93]. Such events, whether induced by muons or neutrinos, have inspired a range of theoretical and experimental interest. It has been recently stressed that HAS of higher energy can be related to the charm production cross section [94] and to composition [95]. The power of the HAS technique is evident in recent results which ruled out one prediction of neutrino fluxes from AGN [96]. For all these reasons, HAS are currently being studied by several particle array groups [97], [98].

To estimate the sensitivity of a ground array to neutrino induced events, it is useful to compute the effective *volume* of the detector. This measure is most easily compared among different kinds of experiments. The effective volume for neutrino detection through HAS is calculated as the product of its projected area and the range of depths within which the shower must originate in order to trigger the device. It is necessary at this point to assume some detector details, in accord with the proposed configuration for the Auger detectors which is described later in this Report. We shall assume that the ground array consists of individual stations, spaced 1.5 km from one another, each registering a "hit" if the air shower particle density exceeds some assumed value ρ_e^{th} . The boundary of the array encloses a total area of about 3000 km^2 . A calculation has been done using parametrizations of particle lateral distributions for showers, and demanding that three stations in a row have electron number density above ρ_e^{th} [99]. The results are illustrated in Figure 2.11.

Note that the effective volume of a device like that described here exceeds 10^4 km^3 of air for large showers. Despite the low density of air, the effective target mass is comparable to a 1 km^3 water detector. Lower energy showers may also be detected if they are aligned with rows of detectors in the array, but the effective volume is greatly reduced.

Also note that we have not included an optical detector in the computation leading to the results in Figure 2.11. An air fluorescence device, like the one described later in this Report, gives additional information which may increase the acceptance of the experiment and will certainly improve the reconstruction of HAS over that which could be done by a ground array alone.

When the effective volume as computed above is convolved with predictions of the neutrino flux from topological defect decay [64, 100] or from the GZK cutoff reactions [81], it reveals that measurable rates are within reach of the Auger Observatory. In Table 2.1 we give the yearly event rates expected under two extreme extrapolations of the neutrino cross section to these energies: the parton distributions of Martin, Stirling, and Roberts are denoted MRS

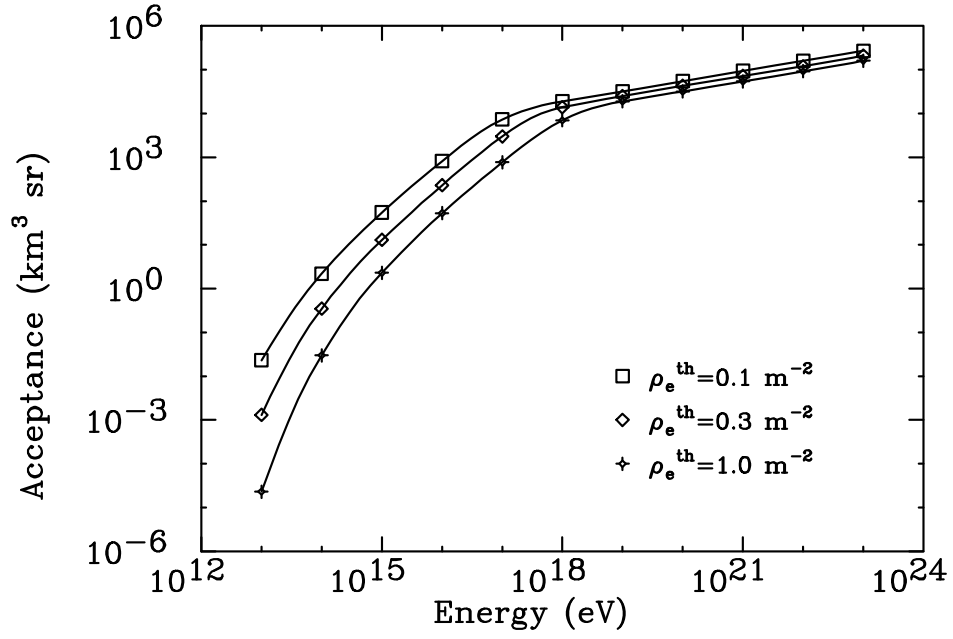


Figure 2.11: Acceptance of a large ground array to neutrino induced air showers, expressed in terms of its effective volume (km^3 of air) and field of view (steradians). The configuration and triggering of a ground array has been modeled as described in the text. Results of separate calculations assuming three different thresholds for individual surface stations to participate in a trigger are indicated.

Table 2.1: Neutrino event rates (per year)

$\rho_e^{th} (m^{-2})$	MRS	GRV
	Interactions with Cosmic Microwave Background	
1	1	0.5
0.1	3	1
	Topological Defects	
1	27	8
0.1	51	17

[101], those of Glück, Reya, and Vogt as GRV [102]. (A recent analysis suggests that the true value of the cross section is likely close to that found using the MRS assumptions[103]). It can be seen that the results are not very sensitive to the assumed threshold ρ_e^{th} of individual detectors because most of the events are due to very large showers.

The size of the Auger Observatory, which will use both a fluorescence detector and a ground array, provide a unique opportunity to study HAS of greater energy than before. The sensitivity is optimal for showers of energy above 10^{19} eV, as is the case for ground detectors measuring more vertical events. This is one of the most interesting energy ranges for neutrino astronomy. Sources include the GZK cutoff interactions, from which neutrinos are produced as byproducts. Others may include the large neutrino fluxes expected from the decays of topological defects.

The interaction cross section of the photinos or the lightest SUSY particles is expected to be comparable to that of neutrinos. If the highest energy cosmic rays are produced by topological defects, and supersymmetric ideas are correct, some of any observed HAS should be photinos. Demonstrating this would not be easy, but they would appear as a component of the data with anomalous interaction cross sections.

Chapter 3

Observations of the Highest Energy Cosmic Rays

3.1 Background

The aim of this chapter is to introduce the observations of the highest energy cosmic rays and to describe the conclusions drawn about the energy of the events detected above 10^{18} eV. In the 1920s and 1930s studies of the trajectories of cosmic ray particles in the Earth's magnetic field demonstrated that some had energies in excess of 20 GeV, more than 2,000 times that of the most energetic particles from radioactive sources[118]. In the 1930s Auger and his group discovered[2] the phenomenon now known as “extensive air showers”, EAS, and soon showed that the energy spectrum of cosmic rays extends beyond 10^{15} eV - a jump of five orders of magnitude from the previous highest energy particles. The estimates of energy made by Auger were based on the understanding of electromagnetic cascades at that time; in hindsight the estimates were probably quite conservative. It is now possible to use massive emulsion chambers, flown to high altitude by balloons, to detect individual cosmic rays of nearly 10^{15} eV and to identify, from their ionization trails, the charges of the individual particles. Relatively conventional calorimetric techniques, using emulsions interleaved with lead, permit estimates of the primary energy; an example of this work is the JACEE project[104], funded by American, Japanese and Polish agencies.

Above a few $\times 10^{15}$ eV, the cosmic ray flux decreases more rapidly with energy than at lower energies (recall Figure 2.1 in the last chapter). The rate is so low that individual events can no longer be detected efficiently by aircraft or balloon-borne calorimeters at a useful rate and one relies instead on developments of the technique pioneered by Auger. The post-war availability of large area scintillation counters led to a series of important experimental advances, particularly by the MIT group under Rossi. A detailed understanding of the shower phenomenon was acquired, and the ability to measure both the size of the shower and its arrival direction with considerable accuracy was developed. The regular registration of events having energies greater than 1 Joule (6.24×10^{18} eV) resulted from the construction of the first giant shower array, by Linsley's MIT group [3, 105] at Volcano Ranch, New

Mexico, during the late 1950s. This work was innovative and the experiment was the first to claim the detection of an event with an energy of about 10^{20} eV.

The Volcano Ranch work, and all other work carried out in this field until 1966, was motivated largely by the recognition that a proton of 10^{18} eV in a magnetic field of $2\mu\text{G}$ (typical of our Galaxy) has a Larmor radius of about 0.5 kpc, somewhat greater than the thickness of the disc of the galaxy. It was thus a reasonable expectation that study of the arrival directions of cosmic rays above 10^{18} eV would reveal, at least, large scale anisotropies, the amplitudes of which were expected to increase with energy. Point sources, perhaps associated with neutrons which have a mean free path before decay of about 10 kpc at 10^{18} eV, were also anticipated and there was considerable interest in what the ultimate energy of detectable cosmic rays might be. Following the recognition by Greisen[12] and by Zatsepin and Kuzmin[13] in 1966 that cosmic rays above 4×10^{19} eV would be exceedingly rare if the cosmic ray sources were at cosmological distances (> 100 Mpc or so) attention focussed more and more strongly on searching for an end to the cosmic ray spectrum. At the same time it was recognized (see [23] for a detailed review) that 10^{20} eV was rather close to the limit of acceleration by known mechanisms.

It is now known that the rate of cosmic rays above 10^{19} eV is about $0.5 \text{ km}^{-2}\text{sr}^{-1}\text{yr}^{-1}$. How that energy scale is established will be discussed below and in the following chapters but it is clear from this rate that one requires a large collecting area ($\gg 10 \text{ km}^2$) to obtain a useful sample of events. With one exception, the approach adopted has been to cover the monitoring area, more or less uniformly, with a relatively small number (a few tens) of detectors, each having an area greater than about one square meter. The original configuration of the Volcano Ranch array is shown in Figure 3.1; here the spacing between the 3.3 m^2 scintillators was 884 meters. At each detector of such an array the particle density - more strictly the energy loss - is measured together with the arrival time of the signal at the detector relative to the other detectors. The event shown in Figure 3.1 was initially ascribed an energy of 10^{20} eV: this was subsequently revised upwards to 1.3×10^{20} eV[106]. No Monte Carlo calculations were used to make these estimates but rather a detailed analytical understanding of the physics of electromagnetic cascades was invoked.

The shower particles travel in a thin disc or “pancake” which moves, essentially at the speed of light, in the direction of the incoming primary cosmic ray particle. The relative arrival times at separated detectors allow reconstruction of the primary’s direction to 2° or better, this accuracy being a strong function of the number of detectors hit and of the area of each detector.

Other arrays at Yakutsk (Russia), Akeno (Japan), and Narrabri (Australia) were also constructed using scintillation detectors. At Haverah Park (UK) the detectors were water Čerenkov detectors (1.2 m deep and of various areas from 1 m^2 to 34 m^2) spread over 12 km^2 ; the array ran more or less continuously for twenty years. Much of the design information from the Monte Carlo calculations used by the Auger collaboration has been checked against results from this experiment (described in Chapters 4 and 5). A particular advantage of the deep water Čerenkov detectors lies in their ability to respond to the large number of photons of relatively low energy (less than 10 MeV) present in the shower.

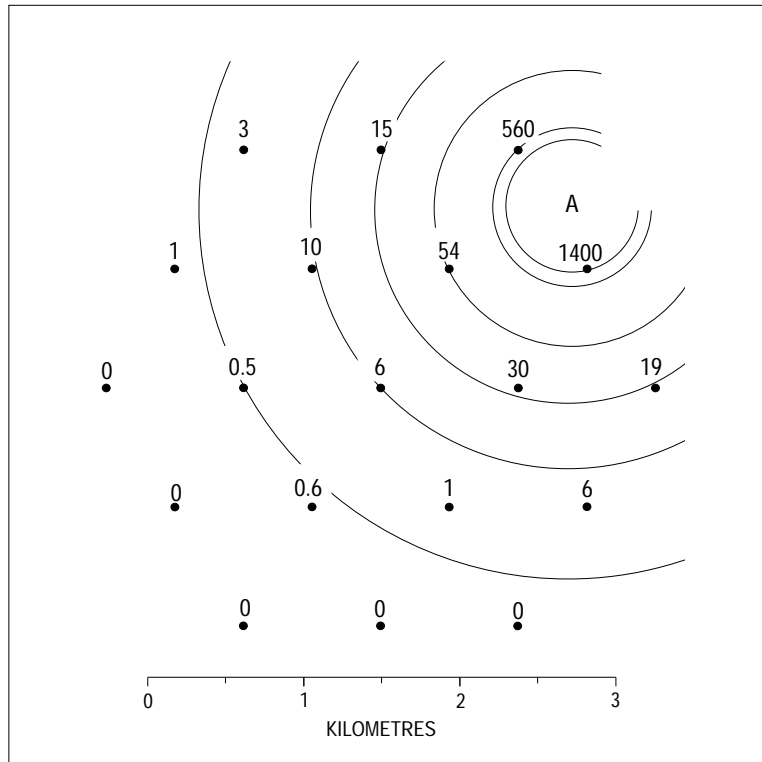


Figure 3.1: An extensive air shower recorded by the Volcano Ranch array with energy above 10^{20} eV. The numbers indicate the observed particle densities (m^{-2}).

A completely different method of recording the extensive air showers relies upon the fluorescence light produced through interactions of the charged particles with atmospheric nitrogen molecules. The light is produced predominantly in the 300-400 nm band and although the fluorescent yield is small (typically 4.5 photons are emitted isotropically per meter of electron track) a detector has been built to observe the emission. The light can be seen above the sky background on clear, dark nights. This feat was achieved by the University of Utah group who have built a device containing two separated “Fly’s Eyes” made up of 880 and 460 photomultiplier tubes respectively, 3.3 km apart[8]. With these units it was possible to map out the longitudinal development of individual shower events for the first time.

3.2 Energy measurements

The unique feature of a fluorescence detector is that it allows direct measurements of the depth in the atmosphere of the maximum numerical size of the shower (X_{max}), as well as of the shape of the cascade curve. The energy of the particle which initiates each cascade is obtained from the track length integral of the shower-development curve, i.e.,

$$E_{em} = \frac{E_c}{\lambda_r} \int N_e(x) dx$$

where E_{em} is the total energy dissipated in the electromagnetic channel, E_c/λ_r is the ratio of the critical energy of electrons to the radiation length, and $N_e(x)$ is the observed number of electrons in the shower as a function of atmospheric depth, x . Strictly speaking, the integration sums the total number of charged particles in the shower, but electrons vastly outnumber other particles. The amount of fluorescence light observed is determined by the number of particles. In terms of how the total energy is apportioned among shower particles however, a significant fraction is carried by other particles. An upward correction of about 10% must be made to E_{em} as computed above in order to obtain the energy of the primary cosmic ray particle, to account for the energy which goes into muon, neutrino and hadronic channels.

The inference of N_e from the amount of detected fluorescence light depends on accurate knowledge of the factors responsible for light production and transmission through the air, calibration of the optical detection system and determination of the shower trajectory. Over the years of operation of the Fly’s Eye experiment an ongoing program of study of atmospheric effects has evolved. Allowances for these factors have been discussed in detail by the Fly’s Eye group [10, 107]. Recent laboratory measurements[108] of the fluorescence efficiency of gaseous nitrogen have confirmed these calibration factors.

In both the Fly’s Eye detector and ground arrays, analogies can be seen with the calorimeters used in accelerator based high energy physics experiments. In the former case the atmosphere acts as a calorimeter just as would a block of scintillator, but on a vastly different scale, and the shower is observed by a large number of photomultipliers to give spatial information. The ground array is a sampling calorimeter, by far the most common type in accelerator experiments, but with a single detector layer located near X_{max} that is

only sparsely implemented. In this case the atmosphere is analogous to the absorber of the calorimeter, usually lead or iron plates.

In a sampling calorimeter, even though only a small fraction of the energy is actually detected, the principle of calorimetry is that the detected energy is proportional to the incident particle energy. In the ground array, the relationship of signal to primary energy is calculated by Monte Carlo simulations, many features of which (such as the transverse shower shape) can be checked against real showers. Still, this calorimeter cannot be calibrated in a well defined beam. Nevertheless, measurements of the same cosmic ray events by both the ground array and the fluorescence detector provide crucial cross calibrations. This is a strength of the hybrid design of the Auger Observatory. Any systematic energy differences will be studied and understood.

There are differences in the character of measurements made in high energy physics experiments and those by air-shower experiments. Air showers have enormous numbers of particles so fluctuations contribute negligibly to the fractional errors in energy. The variation of the depth in the atmosphere where the shower begins is the dominant source of variation in shower size at the ground. Ground arrays measure the lateral density profile, which exhibits minimal fluctuation at a certain intermediate core distance (600 m for the Haverah Park analysis, including dependences on array spacing), ultimately permitting energy resolution $\delta E/E$ of about 10%, based upon calibrating the observed density with primary energy via simulations. This effect is not significant in fluorescence detectors which measure the shower profile, but errors in characterizing the scattering properties of the atmosphere for distant events can introduce energy reconstruction errors of similar magnitude.

If showers are measured by *both* a ground array and a fluorescence detector, both problems are greatly reduced and the resulting energy calculation correspondingly improved. The Auger Observatory will use both techniques, ensuring the most robust and cost-effective reconstruction of events.

3.2.1 Energy spectrum

Determination of the cosmic ray energy spectrum from ground-based arrays, and primary energy computation generally, are closely tied to Monte Carlo model calculations. Ingenious methods have been devised to reduce this dependence but, until the calorimetric measurements of the Fly's Eye device were finalized, considerable doubt existed about the validity and systematic errors associated with the various approaches. This was despite efforts at cross-calibration made, for example, by operating independent arrays within the Haverah Park facility.

The proof of the efficacy of these efforts lies in the excellent agreement between the spectral shapes and absolute intensities deduced by Akeno and AGASA, Fly's Eye, Haverah Park and Yakutsk. All groups [15, 106, 109] are agreed that:

- The shape of the differential energy spectrum from 10^{17} to $\sim 6 \times 10^{17}$ eV is a power law $E^{-\gamma}$ with $\gamma = 3.0 \pm 0.05$.

Array	$\text{m}^{-2} \text{ s}^{-1} \text{ sr}^{-1} \text{ eV}^{-1}$
AGASA	2.91×10^{-33}
Fly's Eye	2.38×10^{-33}
Haverah Park	2.22×10^{-33}
Yakutsk	3.39×10^{-33}

Table 3.1: Cosmic ray intensity measurements at 10^{19} eV from several experiments. In each case, the experimental uncertainty is about $\pm 20\%$.

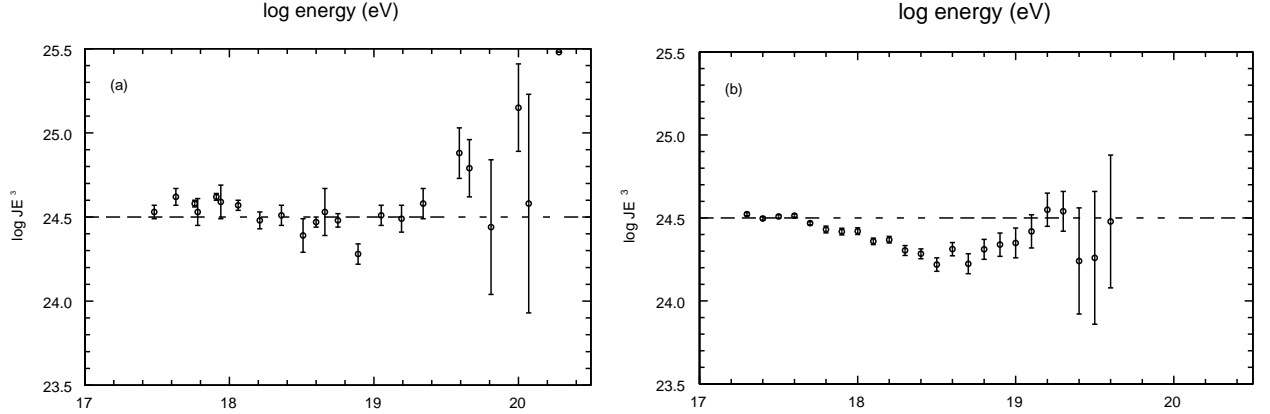


Figure 3.2: Differential energy spectrum ($\times E^3$) as observed by, (a) the Haverah Park array, (b) the Fly's Eye experiment. Note that the exhibited spectrum for the Fly's Eye is for events recorded by more than one of the Eyes ("stereo" events), and so does not include their largest event at $E = 3 \times 10^{20}$ eV).

- Above about 6×10^{17} eV the energy spectrum steepens ($\gamma = 3.2 \pm 0.1$) before recovering at about 5×10^{18} eV to a slope of $\gamma = 2.7 \pm 0.2$ (flatter than the slope near 10^{17} eV). The differential intensities at 10^{19} eV are in excellent agreement and within the experimental uncertainties (see Table 3.1 and discussion below), demonstrating that the processes of energy derivation and the systematic errors are well understood.

The spectra from the Haverah Park, Fly's Eye and AGASA work are shown separately in Figures 3.2a, 3.2b and 3.3. Figure 3.4 combines the spectra from these three experiments along with the Yakutsk data[15]. The slope changes just described are clearly seen in these figures. Note also that the Haverah Park and AGASA plots each exhibit combined points from different analyses of their data. In each case, less restrictive criteria were imposed on events in higher energy data sets than in lower energy ones, in order to obtain sufficient numbers of events at the high energy (low flux) end of the spectrum.

In order to compare the *shapes* (without regard to the absolute scales) of the energy spectra of the different experiments, the data are plotted together in Figure 3.4. The energy scale of each experiment has been separately adjusted[15] in order that all match the AGASA measurement near 10^{18} eV. The scale factors used were 1.0 (Haverah Park), 1.1 (Fly's Eye),

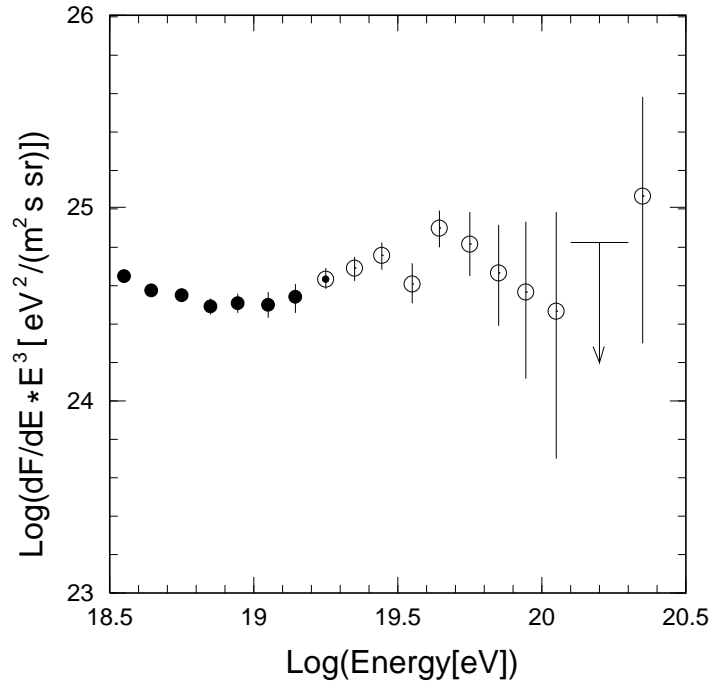


Figure 3.3: Differential energy spectrum ($\times E^3$) as observed by the AGASA experiment, for an integrated exposure of $630 \text{ km}^2 \text{ yr sr}$. The upper limit shown is at 90% confidence. (This figure is an updated version of a plot originally given in reference [15]).

and 0.9 (Yakutsk). These factors are within the quoted systematic energy uncertainty of each experiment. Thus, the four results clearly are in good agreement on the shape of the energy spectrum. It is encouraging that these experiments, employing very different techniques to estimate the energy, arrive at the same qualitative result. It is to be emphasized that this exercise can *not* be used to quantitatively evaluate the energies at which any possible spectral features may be occurring.

At 10^{20} eV the flux is $\sim 0.5 \text{ km}^{-2} \text{ century}^{-1} \text{ sr}^{-1}$ and with the present exposures it is not surprising that there are uncertainties. A recent analysis of a subset of available data [15] noted a total of 7 events exceeding 10^{20} eV . An extrapolation of the experiments' $E^{-2.7}$ differential power-law observed at lower energy predicts that about 20 should have been seen. But the slope of the power laws is also uncertain, so the significance of any deficit is difficult to assess. With the present limited statistical power of the available data, significant “cutoffs” or “gaps” in the cosmic ray energy spectrum are not observed. Still, it is interesting to compare the measurements in Figure 3.4 with the spectral structure expected from the GZK effect as was shown, for example, in last Chapter's Figures 2.6 and 2.7.

The purpose of the Auger Observatory is to study the origin and nature of cosmic rays with energies above 10^{19} eV . The integrated exposures of past and present experiments achieved so far at $5 \times 10^{19} \text{ eV}$ are shown in Table 3.2. For the particle detector arrays, these exposures correspond to showers detected within 45° of the zenith. Even at 10^{20} eV the maximum of the shower is above the level of the detectors, and its amplitude is attenuated at a rate which depends on the shower components detected. For scintillators the attenuation

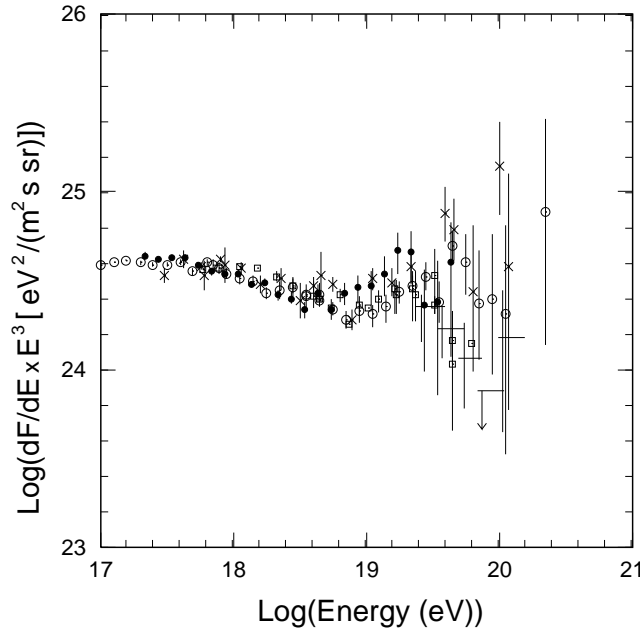


Figure 3.4: Combined differential energy spectra ($\times E^3$) from the Haverah Park (\times), Fly's Eye (stereo, \bullet), Yakutsk (\square), and Akeno/AGASA (\odot) experiments. The energy scale of each experiment has been slightly shifted to match the AGASA result around 10^{18} eV. (This figure is an updated version of a plot originally given in reference [15]).

length is ~ 320 g/cm 2 . For water Čerenkov detectors, which are relatively more sensitive to muons in air showers, the corresponding figure is 750 g/cm 2 , so that showers can be detected at a useful rate at even larger angles. This is most clearly seen by comparing the declination distributions registered by Volcano Ranch (all zenith angles) and Haverah Park (zenith angle $< 60^\circ$) shown in Figure 3.5. The combined acceptance of the two separated sites of the Auger Observatory can be estimated based on the Haverah Park data; this is shown in Figure 3.6. It is evident that having sites in the Northern and Southern Hemisphere will give coverage (with some overlap) of the entire celestial sphere. The current total exposure of 1000 km 2 y sr will thus be exceeded by one of the two 3000 km 2 detectors of the Auger project in about 100 days.

3.2.2 The highest energy events

The limited data available above 5×10^{19} eV have, until recently, made it difficult to answer unequivocally the question of whether or not events exist above the GZK cut-off. However the early claims by Volcano Ranch[3] and Haverah Park[7] that events with energies close to 10^{20} eV do exist have recently been supported by results from the other groups. In 1990 the Yakutsk group described[5] an event with an energy of $(1.1 \pm 0.4) \times 10^{20}$ eV. While this is undoubtedly an event which has been produced by a very energetic primary, the almost completely muonic nature of the particles detected and its relatively large zenith angle (58.7°) make it hard to be definite about the energy assignment.

Array	km ² yr sr
AGASA (100 km ²)	630
Fly's Eye (stereo)	151
Fly's Eye (monocular)	930
Haverah Park (12 km ²)	270
Yakutsk (25 km ²)	490
Total	2471
Total (Exc. FE mono)	1541

Table 3.2: Comparison of integrated exposure at $\sim 5 \times 10^{19}$ eV for different experiments. Only the AGASA experiment is still operating.

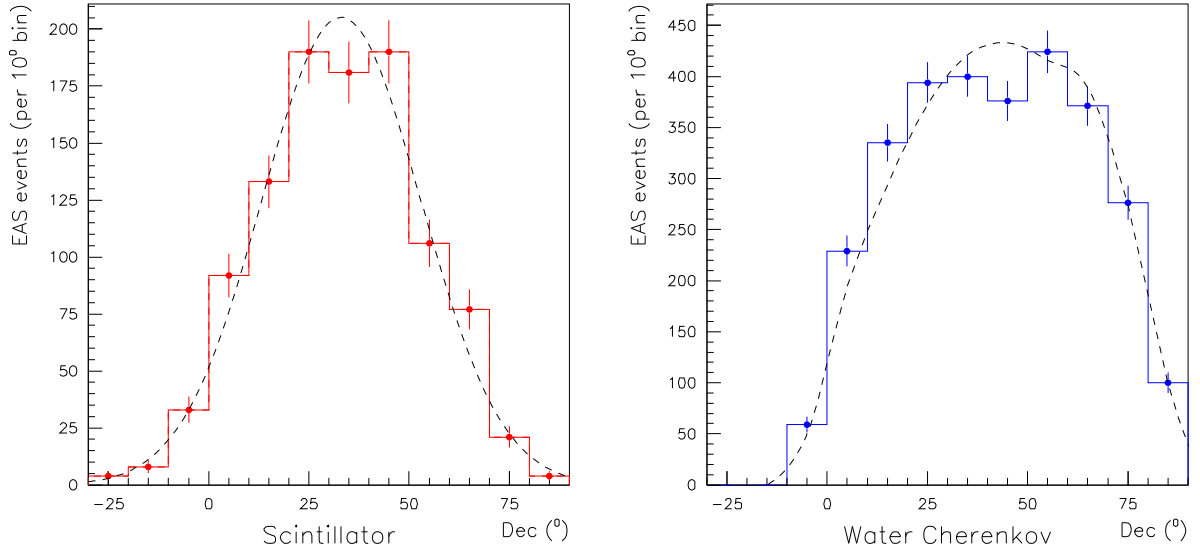


Figure 3.5: A comparison of the declination distributions of showers recorded by large water Čerenkov and scintillator EAS arrays. The water Čerenkov data is taken from the Haverah Park array at an atmospheric depth of 1020 g cm^{-2} and latitude of 54° N , and the scintillator data from the Volcano Ranch array at an atmospheric depth of 834 g cm^{-2} and latitude of 35° N . Shower size is $1 \times 10^{18} < E < 4 \times 10^{18} \text{ eV}$. Haverah Park data are restricted to zenith angles $< 60^\circ$, whilst the Volcano Ranch data are for all zenith angles. The FWHM of the Haverah Park distribution is $\approx 75^\circ$ as opposed to $\approx 40^\circ$ for Volcano Ranch. The water Čerenkov array has approximately twice the solid angle sky coverage.

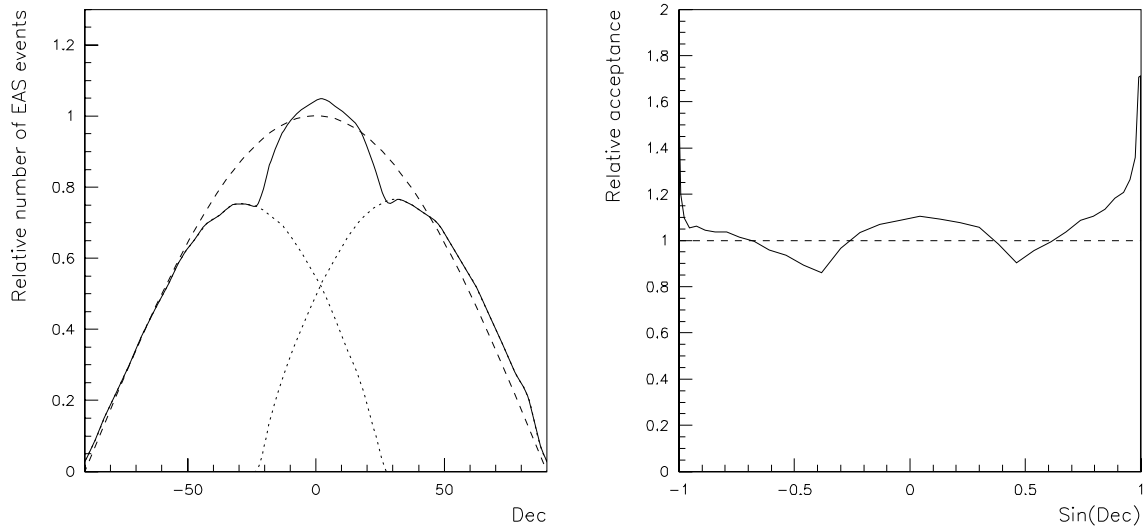


Figure 3.6: Left, solid line is the expected declination distribution of events from the combination of the two Auger ground arrays (at latitudes 39.1° N and 35.25° S). Dotted lines show the separate contributions of the each site. The calculation assumes events are accepted within 60° of the zenith, and uses the shape of the Haverah Park experiment’s declination distribution (shown in the previous Figure). The dashed curve is the distribution which would be obtained from an “ideal” detector with uniform solid angle acceptance (i.e., $\cos(\text{Dec})$). On the right, the ratio of the predicted to the ideal is plotted against $\sin(\text{Dec})$. In this form the area below the curve is proportional to the product of acceptance and available solid angle. It is seen that although there is relative over-exposure at the celestial poles and equator, the acceptance of the two water Čerenkov arrays is good over the whole sky.

In 1993 the Fly's Eye group reported[4] a monocular event for which the assigned energy is $(3.2 \pm 0.9) \times 10^{20}$ eV. This is the highest energy event ever recorded and its reconstructed cascade curve is shown in Figure 3.7. Although the shower size at maximum is extraordinary, there is nothing unusual about the shape of the longitudinal profile. The amplitude rises and falls with the characteristic smooth functional form of air showers predicted by Monte Carlo simulations. This event was not measured stereoscopically, so there is some uncertainty in the geometric reconstruction. If the shower were closer to the detector, the inferred size would be smaller, so the geometric uncertainty implies an energy uncertainty also. The shower depths would also be different, however, if the shower were closer. Changing the geometry to bring the energy down below 10^{20} eV would require the primary particle to have penetrated more than 800 g/cm^2 before interacting. That would mean an incredible penetration of more than 20 mean free paths as well as an implausibly large error in the geometry. Another source of energy uncertainty is atmospheric attenuation of the fluorescence light. If the light suffered less attenuation than calculated, then the true light production and shower size would have been smaller than estimated. However, even using a perfectly clear atmosphere (Rayleigh scattering only), the energy is still calculated to be 2.2×10^{20} eV. It should also be noted that the fluorescence energy measurement is a calorimetric measure of the electromagnetic cascade. The electromagnetic cascade energy measurement for this event was 2.9×10^{20} eV, and it was assumed that 10% additional energy is in muons and neutrinos. Although some systematic error in energy calculations can be attributed to uncertainty in the atmospheric fluorescence efficiency, this uncertainty is not greater than 20%, having been measured in accelerator beam experiments [108]. The lower bound on this particle's energy is still above 10^{20} eV.

Using their 100 km^2 array of 111 2.2 m^2 scintillators, the AGASA group have observed a particularly clean event, at a zenith angle of 23° , for which the primary energy is measured [6] to be in the range of 1.7 to 2.6×10^{20} eV. This event fell in such a position that the core of the shower is in a part of the array which is relatively densely populated with detectors. The largest recorded particle density is $\sim 25,000 \text{ m}^{-2}$ and is only about 250 m from the core. The primary energy is derived by first obtaining the area density of particles at 600 m, $S(600)$, from the density data, normalizing this to what would have been observed had the event come from the zenith rather than from 23° and then converting this number to primary energy using a Monte Carlo calculation. There are thus three sources of uncertainty in the energy estimate. These will be discussed briefly in turn. For this event $S(600)$ is measured as 892 m^{-2} .

The use of $S(600)$ as an energy estimator is a standard technique with long history. It is a development of an earlier idea of Hillas's first applied extensively to the Haverah Park water Čerenkov array. Extensive model calculations by him and others have shown that variations in shower models and mass composition affect the primary energy estimates only weakly. $S(600)$ can be found rather accurately from the data: Monte Carlo studies of the analysis techniques give the uncertainty as +21% and -6.6%. The normalization from 23° to the vertical depends upon empirical information about the attenuation length (see above). The vertical value of $S(600)$ is between 892 and 1065 m^{-2} , where the smaller value would apply if there was no attenuation correction to be made. Taking the smaller figure and subtracting 6.6%, gives a lower bound (68% confidence) limit of 833 m^{-2} . The conversion of

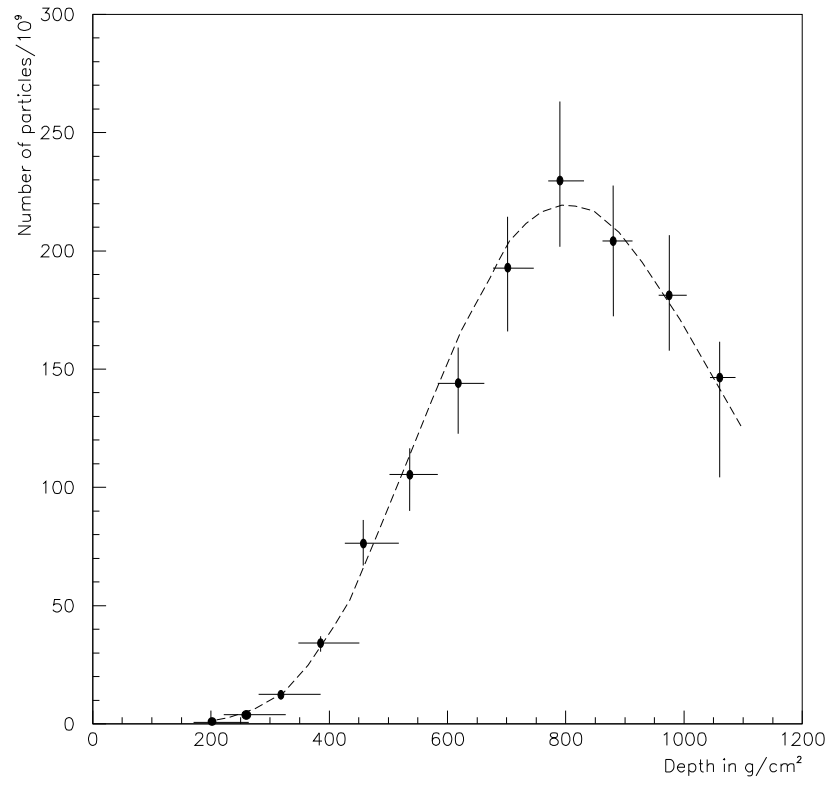


Figure 3.7: Longitudinal cascade development profile for the Fly's Eye 3×10^{20} eV event, the largest cosmic ray air shower ever recorded.

the vertical $S(600)$ value to primary energy is model dependent; that used by the AGASA group is a QCD model which gives $E = 2.0 \times 10^{17} \text{ eV} \times (S(600)/1 \text{ m}^{-2})$. The systematic error which may be present can be estimated by comparison of the 10^{19} eV differential intensities measured by AGASA and Fly's Eye (see Table 3.1 or discussion in text for Figure 3.4). This would suggest that the two quite different approaches to energy estimation agree within 10%, with the published AGASA energies being systematically greater than the Fly's Eye estimates at 10^{19} eV .

The extrapolation by a further order of magnitude is, of course, uncertain. However, the fall off with distance of the unshielded scintillator signals is not anomalous by comparison with expectation from lower energies. Furthermore muons are detected in seven detectors at a normal density level. The temporal distribution of the signal in the 30 m^2 scintillation counter at 1920 m from the shower axis is also consistent with expectation. There is thus high confidence that the AGASA event is above 10^{20} eV and well above the GZK cut-off.

The energy estimates for the largest events are subject to still uncertain systematic errors, such as the unknown particle types of the primaries. Nevertheless, the very good agreement between the intensity measurements at extreme energy, from four rather different experiments (Table 3.1 and Figure 3.4), argues strongly that there is a proper understanding of the uncertainties at the 20% level near 10^{19} eV . Furthermore, the characteristics of the showers recorded by Fly's Eye and by AGASA are consistent with what is expected from ordinary hadronic cosmic ray primaries by straightforward extrapolation from well-studied behavior near 10^{19} eV . The agreement of the different methods makes it quite convincing that the discovery of these two well-measured events, at least two or three times more energetic than any other prior cosmic ray, clearly settles the question of the existence of cosmic rays above the GZK cutoff. What is not yet decided is the particle type, the spectral shape, and, of course, the fundamental question of the limit to the energy reached by cosmic rays. These are further problems which the Auger Observatory is designed to answer.

3.3 Direction measurements

3.3.1 Anisotropy

Most theories of energetic particle production predict that the source locations are correlated with the cosmic matter distribution. Extremely energetic particles are magnetically rigid enough to point back to their sources with only small deflection, even for rather large source distances (recall Figure 2.9 in the last chapter). It is also true that such particles have not traveled more than $\sim 200 \text{ Mpc}$ (or much less, depending on energy) since attenuation from the GZK effect would become severe. Within this volume of space, the mass density is dominated by the so-called *supergalactic plane*.

The supergalactic plane appears as a line on the sky, intersecting the Milky Way at nearly a right angle. It was defined through the observation that the nearest optically bright galaxies lie not far from and on either side of this line. Radio-galaxies closer than $z \approx 0.02$

Energy(10^{20} eV)	HP	All	AGASA
> 0.2	0.68	0.31	0.52
> 0.4	0.013	0.012	0.30
> 0.6	0.038	0.027	0.83
> 1.0		0.058	

Table 3.3: Probability, for several experiments, that an isotropic source distribution of cosmic ray arrival directions fluctuates randomly to exhibit clustering with respect to the supergalactic plane to the degree each observes.

(about 100 Mpc) also tend to concentrate along this band. This appearance is what is expected if the large scale structure of the universe has a mass distribution arranged in bubble-like geometries.

Recent analyses of the data sets of both Haverah Park[50, 51] and AGASA[52] have suggested that the highest energy cosmic ray arrival directions appear to cluster near the supergalactic plane. The enhancements in the data sets are apparent for energies greater than 4×10^{19} eV. An energy-dependent anisotropy can result from the increasing magnetic rigidity of particles or if the highest energy cosmic rays have a different source than lower energy particles.

The degree of anisotropy is measured by computing the “latitude” b^{SG} of the arrival directions of cosmic rays with respect to the supergalactic plane.¹ Table 3.3 gives the results of these analyses. Shown is the probability that a uniform arrival direction distribution fluctuates to give a value of $\langle |b^{SG}| \rangle$ as small or smaller than what was observed. The columns marked “HP” and “All” are from reference [50] and refer respectively to the Haverah Park data alone (73 events above 2×10^{19} eV) or to a combined set of Haverah Park, AGASA, Volcano Ranch, and Yakutsk (143 events above 2×10^{19} eV). The column for “AGASA” is from a more recent analysis[52] which includes a larger data set from this experiment (149 events above 2×10^{19} eV) than those used in Ref.[50]. In each analysis, the r.m.s. fluctuation of b^{SG} was also studied and the results were similar.

It can be seen from Table 3.3 that the Haverah Park data shows a clustering along the supergalactic plane with a chance probability of only a few percent. The AGASA result appears inconsistent with this, although the celestial acceptance of the two experiments are different. Furthermore, the AGASA group reports[52] that the data show an anomalous distribution of the parameter b^{SG} , shown in Figure 3.8. It is observed that about 30% of the AGASA data above 4×10^{19} eV are contained within 10° of the supergalactic plane. However, the significance of this excess is only about 1.6σ .

The evidence for anisotropy of cosmic ray arrival directions is suggestive but statistically very weak. Clearly, if the effect is real, it will become very apparent with the increased collecting power and excellent angular resolution of the Auger Observatory.

¹The latitude b^{SG} is the angular displacement from the supergalactic plane, analogous to our earthly latitude which measures angular distance from the equator.

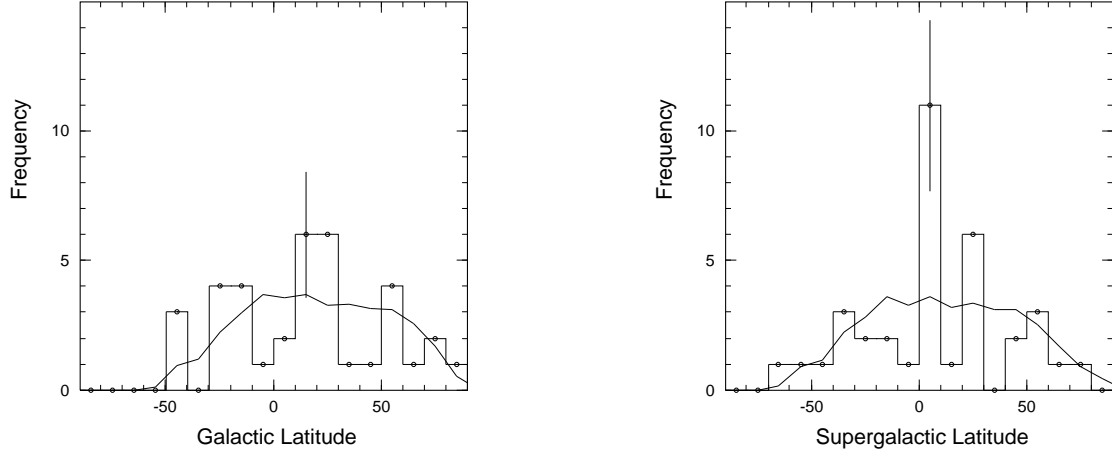


Figure 3.8: Distribution of angular deviation of cosmic ray arrival directions from (a) the Galactic plane and (b) the supergalactic plane, from the AGASA experiment. Lines in each case give the distribution expected if the arrival directions are isotropic.

3.3.2 Point sources

In addition to statistical associations with the mass distribution, the arrival directions of individual cosmic rays ought to correlate with their source locations, if the particle energies (rigidities) are high and the sources nearby. There is some evidence in this regard for the highest energy events. It was noted in the previous chapter that galaxies with powerful radio jets, especially FR-II objects with “hot-spots”, are excellent candidate accelerators of 10^{20} eV particles([40]-[47]). There are very few such objects within 100 Mpc, so the likelihood of a chance association is small. It is therefore interesting that:

- The FR-II galaxy 3C134 is within the error box of the reconstructed direction of the 3×10^{20} eV Fly’s Eye event. The distance (redshift) of 3C134 is not yet measured, having only recently been detected in the optical continuum. However, based on crude distance estimates, 3C134 is likely to be among the closest of all FR-II galaxies[49].
- Similarly, NGC315 is 10° from the Akeno event at 2×10^{20} eV. NGC315 is powerful, asymmetric source only about 50 Mpc distant. (An asymmetric appearance is expected when the axis of the jets is oriented along or near our line of sight).

It has also been pointed out recently[110] that the direction of a close pair of energetic AGASA events is near to the location of the colliding galaxy system VV338. As noted in the last chapter, Cesarsky [25, 26] has identified such systems as good candidate accelerators. However, the angular distance (about 10°) between the AGASA pair and VV338 may be too large for the association to be real. As is also the case for the single event near NGC315 described above, the intervening magnetic field would have to be much larger than the upper limit on the *average* field (10^{-9} G), at least in some part of the trajectory of the particles.

It is best to be circumspect about attempting to evaluate the statistical significance of the above associations. The only convincing proof of their reality will be through the

Energy(10^{20} eV)	l^G	b^G	$\rho_\mu(1000)/S(1000)$
2.10	131.2°	-41.1°	0.08 ± 0.04
0.51	130.2°	-42.3°	0.14 ± 0.07

Table 3.4: Properties of an AGASA Event Pair (see text)

confirmation of the effect with many more events.

3.3.3 Magnetic spectrometry with event pairs

Recently, the AGASA array in Japan has reported[52] three separate cases of two cosmic rays coming from the same direction within its angular resolution of 1.6° . The events in the pairs have different energies, so they undergo correspondingly different deflections if they are charged particles. Under this assumption a number of significant conclusions can be drawn, provided the magnetic field of the galaxy is known with modest precision ($\sim 50\%$). For one specific case reported by AGASA, it can be concluded that the cosmic rays are likely to be protons, and one can place limits on the fluctuating component of the extra-galactic magnetic field.

The event pairs were obtained during 5 years of operation of the AGASA 100 km² array. There are a total of 36 events above 4×10^{19} eV and 20 events above 5×10^{19} eV in this data set. Two of the three pairs occur within the sample of 20 events and a third appears if the sample is extended to the 36 events. The probability that these pairs occurred by chance from an isotropic distribution of cosmic rays is 0.01 for the two higher energy pairs each falling within a space angle of 2.5° of one another. Finding three such cases among 36 events has a probability of 0.02. In what follows it is *assumed* that these pairs are *not* accidental and explore the consequences.

The most interesting case is the pair which includes the highest energy event observed with AGASA. The energy and direction (in Galactic latitude b^G and longitude l^G) of each event in this pair are listed in Table 3.4.

Note that the energies of the two cosmic rays differ by a factor of four. If the cosmic rays are neutral the difference in energy has no consequence. The last column of Table 3.4 gives the ratio of the observed muon density to the charged particle density measured at 1000m. The values quoted are typical of all the showers in the AGASA sample and are expected for hadronic primaries (the measured values are about three times larger than that expected for a γ -ray primary). If the source of the cosmic rays is extra-galactic, they are unlikely to be neutrons since the decay length of a 10^{20} eV neutron is only 1 Mpc. It is therefore assumed that both cosmic rays are charged, and hence will be affected by Galactic and/or intergalactic magnetic fields. If the magnetic rigidity of the two cosmic rays were equal then there would be no magnetic effects on the relative trajectories. This would be the case, for example, if the higher energy cosmic ray was a Be nucleus while the lower energy particle was a proton. If the two cosmic rays are the same species, then the effect of the galactic

Primaries	Separation
Protons	0.88°
Helium	3.29°
Carbon	16.1°
Observed:	1.41°

Table 3.5: Computed and Observed angular separation of an AGASA pair.

magnetic field can be used as an analytical tool.

The Galactic magnetic field is parametrized as given by Vallée [111]. The field lies in the plane of the galaxy and follows the spiral arms. An approximation places the direction of the magnetic field along concentric circles about the galactic center. In this parameterization the field shows a reversal between 6 and 8 kpc. For the directions of the AGASA events it is only the magnetic field ($\sim 2\mu\text{G}$) towards the galactic anticenter that is traversed. Field fluctuations on a sub-kpc scale will be averaged out for cosmic rays with energy $\geq 10^{19}$ eV.

It is also necessary to know how the magnetic field drops off above and below the galactic plane. Parker[112] has suggested a Gaussian fall off:

$$B(h) = B(0) \times \exp(-(h/0.8)^2),$$

with h the distance out of the galactic plane in kpc.

The trajectories of these two cosmic rays are traced backwards out of the galaxy. If the directions beyond the galactic magnetic field differ by an amount outside the angular resolution of the AGASA detector then it is not possible that the two cosmic rays have the same origin, and their overlap is by chance. The observed space angle difference between the two cosmic rays is 1.41°. The space angle differences calculated under various assumptions about the primary particles' charges are listed in Table 3.5.

Thus, if the two cosmic rays are the same species, it is most likely that they are protons. If the integrated magnetic field were a factor of two weaker then helium would be a possibility. It is more likely that the integrated magnetic field is stronger because of a more extended halo [112]. In this case the argument for proton primaries is strengthened.

This particular pair of events lies close to a cluster of events from prior experiments identified by Chi and Wolfendale [113], who examined the historical data set from previous experiments and identified a cluster of older events whose arrival directions are near the AGASA pair listed in Table 3.4. These two events are also within 3.0° of a Haverah Park event at 6.9×10^{19} eV. If the AGASA pair indeed represents a point source there should be additional events at lower energy, which should have arrival directions dispersed in a line roughly perpendicular to the galactic plane. A significant enlargement of the world data set at these energies, such as will be provided by the Auger Observatory, will reveal such a correlation if it exists, strongly supporting the conclusion that protons are the primaries.

Having established that two cosmic rays with energies different by a factor of four come

from the same direction within the resolution of the detector implies that the highest energy partner points to its source with negligible magnetic deflection. Then the uncertainty of the source direction is limited by the resolution. It will be shown in later chapters that the detector systems of the Auger Observatory will have good accuracy: at 10^{20} eV, the surface array will reconstruct directions within $\sim 1.0^\circ$, while events recorded by both the surface array and the fluorescence detector will have an angular resolution of $\sim 0.4^\circ$.

This particular pair of AGASA events (Table 3.4) was observed in about five years of operation of an array with an area of 100 km^2 . Assuming a common source, in one Auger installation of 3000 km^2 , we expect more than 50 events from this source above 5×10^{19} eV in the same length of time. With such a richness of data, the Auger Observatory can:

- establish whether the primaries are protons;
- measure the magnitude of the integrated transverse magnetic field along the trajectory, if the particles are protons or nuclei of known charge, and so decrease the uncertainty in the galactic magnetic field;
- determine the source location to within 0.1° ;
- measure the muon content and the depth of maximum of the showers. This latter measurement will serve as a constraint on the interactions of protons with matter at energies well beyond those that will be accessible at the colliders. If there is a qualitative change in the nature of the strong interaction, it should be evident;

If indeed this AGASA pair originated from a single point source, then there is no doubt that there are other such sources. The AGASA analysis of arrival directions with respect to the supergalactic plane suggests that perhaps a third of all events above 5×10^{19} eV are from point sources. An estimated 1200 events will be collected above that energy in 5 years by the Auger Observatory, so about 400 would be associated with point sources.

Much can be learned about extragalactic magnetic fields with an independent identification of the primaries from point sources, and a measurement of their energy. For example, the r.m.s. magnetic field can be estimated using Eq. 2.3 in the last chapter (section 2.4.3). Assuming in this case that the magnetic multiple scattering difference between the two cosmic rays is of the order of the 1.6° resolution, then $B \leq 0.5 \times 10^{-9}$ gauss. This is comparable to the upper limit on the average field strength of $\sim 10^{-9}$ gauss given by radio astronomy studies for the intergalactic medium (i.e., for directions away from our local cluster)[35].

Even an approximate knowledge of the magnetic field should permit the determination of the charge of the primary cosmic rays as the example discussed here suggests. With much more data this procedure can work effectively with checks that it is self consistent. The Galactic magnetic field is used in a similar way that the Earth's magnetic field was used to learn many things about Galactic cosmic rays.

3.4 The Immediate Future

The only high energy cosmic ray surface array currently taking data is the 100 km² scintillator arrays at AGASA. It is planned to continue operating this device until the year 2000, by which time the integrated exposure will have reached about 2000 km²·sr·year. A further 10-20 events might be expected above 10²⁰ eV, though with only limited information about mass composition. The Yakutsk array has been contracted in size and will focus on specific features of shower properties near 10¹⁹ eV.

Two new projects are under development:

The HiRes Project

The University of Utah Fly's Eye group has entered into collaboration with the University of Adelaide and Columbia University to construct a next-generation air-fluorescence detector, the High Resolution Fly's Eye or HiRes. The first stage of construction of this detector has been completed. Two sites, twelve kilometers apart, have been chosen at which a total of 56 two meter diameter mirrors will be installed. The mirrors are arranged in rings, each ring subtending 14° of elevation. Two complete rings at one site and one partial ring at the second site will be built. Each mirror will have a 256 phototube array at its focal plane. Each phototube will view a 1° × 1° section of the sky. The signals from the phototubes will be digitized using FADC electronics so that both the amplitude and the detailed pulse shape will be available for later analysis. All events will be recorded by both sites ("stereo") for good control of experimental uncertainties and redundancy of measurement.

The aperture for this Stage I detector is optimized for events greater than 10¹⁹ eV, and approaches 10⁴ km²sr at 10²⁰ eV. Assuming a 10% duty factor, this detector should record of order 10 events per year above 10²⁰ eV, and 200 events per year above 10¹⁹ eV, based on scaling the flux observed by previous experiments. This is an order of magnitude increase in statistics over the monocular Fly's Eye. The resolution in energy and X_{max} is also much improved over the Fly's Eye detector, approaching 10% statistical uncertainty in energy and 15 gm/cm² mean uncertainty in X_{max} . This detector can also search for a possible gamma ray and neutrino flux.

Many aspects of the HiRes technical design and data from the prototype have guided our thinking in the development of the fluorescence detector of the Auger Observatory. These will be discussed in later chapters.

The Telescope Array Project

Another fluorescence detector is at the prototype stage. Known as the Telescope Array, it is proposed by a consortium of Japanese universities and the University of Utah, led by the University of Tokyo. The goal is to build an air fluorescence detector with a pixel size of 0.25° by 0.25° using multi-anode photomultiplier tubes. With this small pixel size, sky noise

is essentially negligible. The array is designed to be sensitive also to low energy gamma rays above 100 GeV by detecting Čerenkov light from these showers. It includes 120 fixed and 120 steerable altitude-azimuth, 3 m diameter mirror dishes positioned at two stations 40 km apart. The aperture of such an array at 10^{20} eV, excluding the duty cycle, is estimated to be approximately 40,000 km²sr. The energy resolution is 10% and the resolution in X_{max} is 10 gm/cm². Prototype mirror and PMT clusters are being tested at Dugway and AGASA.

The Japanese groups have indicated their willingness to provide a fully developed version of this detector for one of the sites of the Auger project. The goals of the Telescope Array Project differ somewhat from those of Auger, in that the study of Čerenkov radiation from 10^{12} eV showers is as important as the study of the highest energy events. Consequently, this device is not being considered as the main fluorescence component of the Auger Observatory, but rather as a valuable complementary detector.

3.5 The Physics and Astrophysics Potential of the Auger Project

The unambiguous discovery of cosmic rays above 10^{20} eV is of exceptional astrophysical interest as judged by the recent flood of theoretical papers. The sources of the most energetic events are required, by the GZK cut-off, to be rather close (less than ~ 100 Mpc). Energy arguments [115, 116, 23, 25] imply that these locations must have some of the most extreme physical conditions in the cosmos. The Auger Observatory is planned to provide a high statistics measurement of the energy spectrum (with resolution better than 20%) and arrival direction (with a typical error of $< 1^\circ$) distribution of the highest energy events. At the same time inferences about the mass composition will be drawn from a careful study of detailed shower properties, as well as from differences in the arrival direction patterns of sub-sets of “heavy” and “light” nuclei. There is no doubt that there are events to observe beyond 10^{20} eV. In ten years of operation of the two detectors, each of 3000 km², between 600-1000 events above 10^{20} eV are expected from the whole sky. If the E^{-2} integral power law spectrum measured at 10^{19} eV continues to 10^{21} eV about 5 events will be observed above that energy.

It is important to recognise that detectors in both the Northern and Southern Hemispheres are essential, as the radio galaxies (one of the possible “conventional” sources of the highest energy cosmic rays) close enough to be the sources of such particles are anisotropically distributed around the supergalactic plane, and thus across the two hemispheres. A detector at a single site cannot properly address the arrival direction problem.

The use of a hybrid device, with a fluorescent detector and a ground particle detector combined, offers unique opportunities to study many parameters in the same event. In particular, one will be able to obtain the depth of maximum, the muon-electromagnetic ratio and the spread of the particle arrival times, all of which are crucial parameters in attempting to measure the primary mass composition. Independent measurements of shower energy by the fluorescence detector and ground array give necessary redundancy and crucial

cross checks of the assumptions made in the calibration.

High statistics observations of cosmic rays beyond 10^{20} eV will increasingly constrain theories of cosmic ray origin whatever the outcome of the observations. Most clear cut would be the identification of specific sources by the observation of clusters of the most energetic events from a few regions of the sky. These regions may correspond with objects known to be powerful in other parts of the spectrum. A spin-off from such an outcome would be much needed information on the magnetic field structure in the region out to 50 Mpc from our galaxy. At the other end of the scale, isotropy at ever increasing energy might favor the exotic models which associate the most energetic events with topological defects or gamma ray bursts. The higher the energy of the most energetic event recorded, the more intriguing the theoretical problems become. The wealth of data to be obtained promises new insights into particle physics, astrophysics, and cosmology.

Chapter 4

Air Shower Measurement Techniques

The Auger Observatory will employ methods of analysis of air showers which have been developed by prior experiments. The results from past and present surface arrays and air fluorescence detectors were reviewed in the last chapter. Here we describe the details of the methods of these experiments. The next chapter will give detailed expectations for the performance of the Auger systems.

The manner in which the essential physics of air showers affects the data is discussed first, with emphasis on how the direction, energy, and nature of the primary particle are obtained from analysis both of the particles at the ground and of the air fluorescence or scintillation. Next, details of surface array methods is given. We conclude with an examination of the basis and implementation of the air fluorescence technique.

4.1 Properties and Development of Air Showers

The goal of the Auger Observatory is to study the arrival direction, energy, and primary mass composition of cosmic rays. The fluorescence detector and surface array provide complementary methods of extracting this information from the showers. Each relies on a combination of signal timing and amplitude measurements to characterize the geometry of the shower. Energy is measured calorimetrically in the fluorescence detector, and by sampling the particle density at ground level in the surface detector. The depth of shower maximum and the shape of the longitudinal profile provide composition diagnostics for the fluorescence data. In the surface detector, composition information is extracted from a number of shower characteristics which reflect the depth of shower maximum and the muon content of the shower.

Before proceeding to discuss in greater detail how each of these quantities is determined, it is useful to review key characteristics of air showers with emphasis on those aspects which impact the measured quantities most directly. When it is relevant, special emphasis is placed on ground array measurements made using water Čerenkov detectors, these having been selected for the Auger Observatory.

4.1.1 The Electromagnetic and Muon Components

An air shower is a particle cascade initiated by the interaction of an energetic cosmic ray high in the atmosphere. If the primary cosmic ray particle is a nucleon or nucleus, the cascade begins with a hadronic interaction. The number of hadrons increases through subsequent generations of particle interactions. In each generation, however, about 30% of the energy is transferred to an electromagnetic cascade by the rapid decays of π^0 mesons. Ultimately, the electromagnetic cascade dissipates roughly 90% of the primary particle's energy through ionization. The remaining energy is carried by muons and neutrinos from charged pion decays. Figure 4.1 illustrates the development of an air shower in schematic form.

The energy dissipated by the electromagnetic component of the shower, and hence the total number of low energy electromagnetic particles in the cascade, is very nearly proportional to the shower energy. However, the total number of muons reaching the ground grows more slowly with primary energy, mainly because of the transferral of energy from the hadronic interaction channels into electromagnetic showering. This effect is important for distinguishing air showers produced by heavy nuclear primaries from those of protons or light nuclei. Simulations predict [127] that the total number of muons reaching the ground in a proton induced air shower increases with primary energy as $E^{0.85}$. As a consequence, viewing a nucleus with atomic number A as a collection of individual nucleons each with energy E/A , the number of muons in a shower induced by that nucleus is related to the number of muons in a proton shower (of the same total energy) by

$$N_\mu^A = A^{0.15} N_\mu^p.$$

Thus, an iron shower ($A=56$) will have about 80% more muons than a proton shower with the same E . These effects will be described more fully below (section 4.2.3).

Because fluorescence is essentially a calorimetric technique, it is primarily sensitive to the electromagnetic component of the shower. On the other hand, signals from water Čerenkov detectors, such as those planned for use in the Auger Observatory surface array, have comparable contributions from the muon and electromagnetic components.

4.1.2 Spatial Structure of the Shower

An air shower is a broad, thin disc of particles moving at the speed of light through the atmosphere. The particles ionize and excite N_2 molecules in the air, causing radiation of near-UV photons. From a distance, the fluorescence detector sees the shower as a spot of light whose motion is along the *shower axis* or *core*. The intensity of the light, corrected for geometrical and atmospheric effects, reflects the longitudinal development of the shower, and its integral is proportional to the energy deposited in the atmosphere.

An air shower's *depth of maximum* (X_{max}) is the location in the atmosphere where the shower has developed the largest number of particles. X_{max} depends on both the total energy and the mass of the primary nucleus. At the same total energy, an air shower from a heavy nucleus is expected to develop faster than a shower initiated by a proton. This is

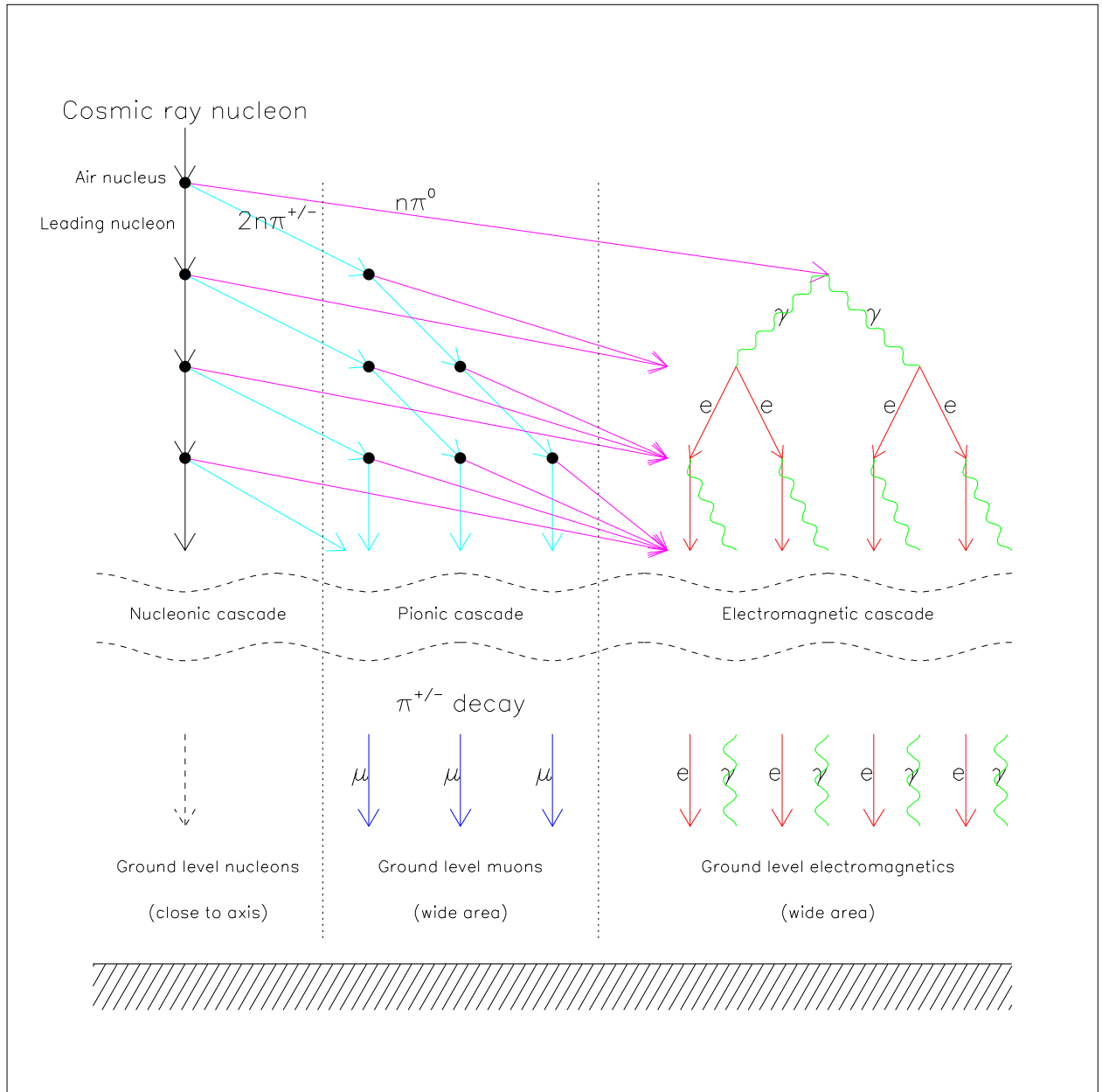


Figure 4.1: Schematic diagram showing the principal EAS cascade processes. An incident cosmic ray nucleon is assumed, and the resulting shower divided into three categories; the nucleonic cascade consisting of the surviving primary itself in the guise of a “leading-nucleon”, the pionic cascade, and the electromagnetic cascade which is fed by neutral pion decay. This picture is, of course, highly simplified.

partly because a heavy nucleus has a larger cross section, so it tends to interact sooner than a proton. More importantly, however, the heavy nucleus behaves much like a superposition of its constituent nucleons. The *superposition model* is a simple and very good estimator of the average behavior of many shower properties. An iron nucleus produces an air shower which can be approximated as the superposition of 56 nucleon showers, each with $1/56$ th of the iron nucleus' energy. X_{max} for proton showers increases by at least 55 g/cm^2 for each decade of energy, so reducing the energy by $1/56$ decreases the expected X_{max} by approximately 100 g/cm^2 . An iron shower therefore has an expected X_{max} about 100 g/cm^2 less than the expected X_{max} for a proton shower of the same energy.

The particle swarm is spread away from the shower axis due to the combined effects of multiple Coulomb scattering and the transverse momentum in interactions and decays. The particles spread out laterally from the shower axis in a pancake-like shower front which can be detected over a large area when it strikes the ground. The highest particle density is near the axis, falling off with distance on a scale determined by the Moliere radius in air (80 m at ground level). Outside the core region the distribution of particles is axially symmetric about the core. This is an experimental fact, confirmed over a wide range of energies (see Figure 3.1 in the last chapter, and Section 4.3.1 below). It is also predicted to be the case by shower simulations. The density of particles falls off rapidly with increasing core distance. It is customary to characterize the observed lateral distribution of showers at ground level by a *lateral distribution function*. A modified power law is normally used; the exact form and slope which is appropriate depends on the type of ground array detector which is employed, and the atmospheric depth at which observations are made.

The longitudinal profile of the most energetic air shower yet observed was shown in the last chapter as Figure 3.7. The left part of Figure 4.2 shows the lateral distributions of ground particles in a giant shower as predicted by simulation. (Details of the simulation procedures are given in the next chapter.) Close to the axis, low energy electrons and photons outnumber muons by several orders of magnitude. However, the muons have a flatter lateral distribution, and at large core distances carry significantly more energy per particle ($\sim \text{GeV}$ as opposed to $\sim 10 \text{ MeV}$ for gammas and electrons). Also note that far from the core the electromagnetic cascade is dominated by photons.

Thin scintillators essentially measure charged particle density. Deep water Čerenkov detectors have a strong sensitivity to the more penetrating muons, and also convert most of the gamma rays into observable signal. To predict the actual lateral distribution which will be observed it is necessary to convolve the ground particle energy spectra at given core distance with the appropriate response curves for the detectors being used. This process is illustrated in the right part of Figure 4.2, where the signal observed in 1.2 m deep water detectors is plotted for each shower component together with the total. Notice that at large core distances ($> 1 \text{ km}$), the muons and electromagnetic particles make approximately equal contributions to the total signal from a water Čerenkov detector.

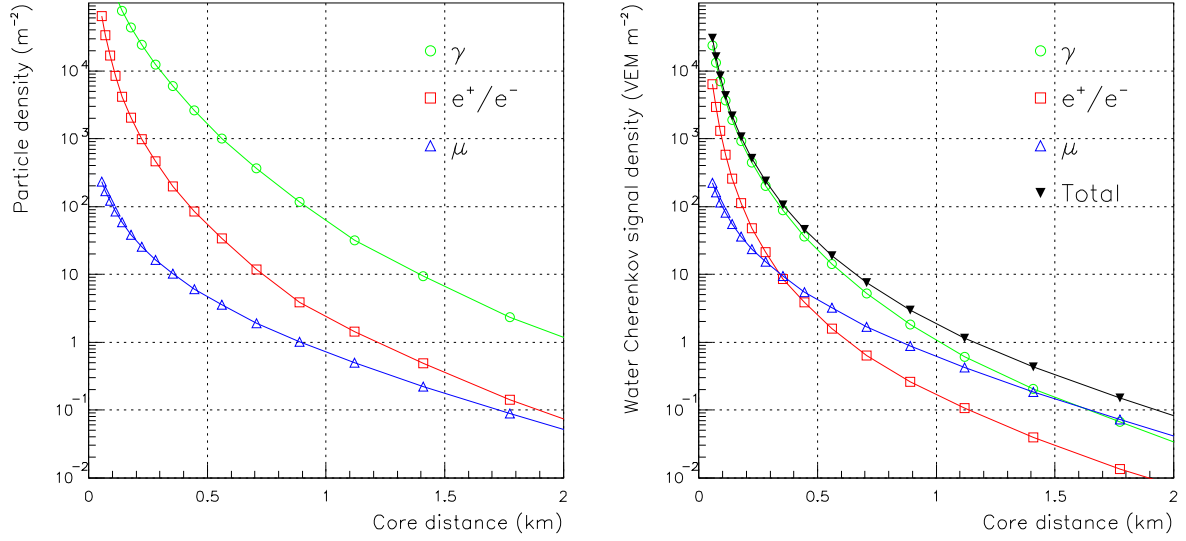


Figure 4.2: The left plot shows the simulated lateral distributions of the three main shower components at ground level for a 10^{19} eV proton shower. In the right frame the particles have been convolved with the response of a 1.2 m deep water Čerenkov detector, such as that proposed for the Auger Observatory.

4.1.3 Time Structure of the Shower Front

Particles scatter from the region of the shower axis throughout its development. The shower core effectively acts as a moving point source of both fluorescence photons and particles, which make their way to detectors far from the core. The plane tangent to the shower front at the axis is the *shower plane*. The shower front itself is slightly curved, resembling a cone. Particles far from the core will arrive behind the shower plane due to simple geometry.

Generally speaking, those particles arriving at the ground first at point some given distance from the core originated higher, and thus earlier, in the cascade (this can be simply seen by considering the geometry of path-length differences). Electrons and photons diffuse away from the shower axis throughout the shower development. Thus, far from the core particles are spread in time, with the time spread roughly proportional to the distance from the axis. This time spread helps to distinguish distant large showers from nearby small showers, and is thus useful in triggering the surface array. The time spread becomes greater as the depth of shower maximum increases.

Muons tend to arrive earlier than electrons and photons, because they suffer much less scattering and so have more direct paths to the ground. Iron showers, which are both muon-rich and have developed higher in the atmosphere relative to proton showers, thus have a signal which arrives over a shorter time than that from a proton shower with the same total energy. “Rise-time” measures based on this effect are among the most robust diagnostics of composition for the surface array.

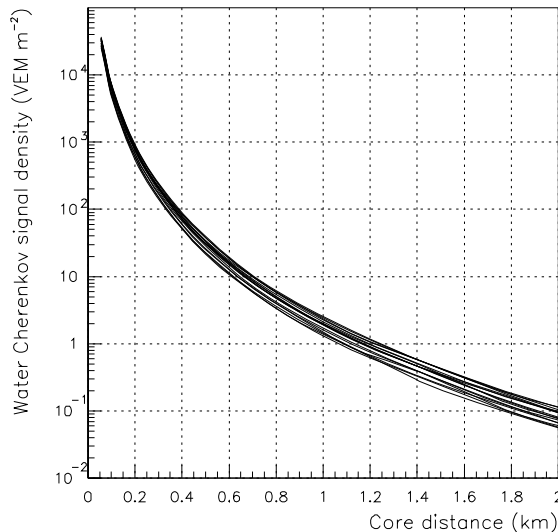


Figure 4.3: Lateral distributions of individually simulated proton air showers as observed in 1.2 m deep water Čerenkov detectors. A range of zenith angles ($\theta < 30^\circ$), and energies ($10^{19} < E < 10^{20}$ eV) are included. Signal density is normalized by energy to 10^{19} eV.

4.1.4 Fluctuations in Shower Development

The most important source of fluctuations in shower development are the depth and characteristics of the first few interactions. Fluctuations in later interactions are averaged over a large number of particles and are not important. The depth of first interaction has a direct effect on the depth of shower maximum. Recalling Figure 2.8 in Chapter 2, variations in the total shower size at the ground result from roughly shifting the entire average profile higher or lower, depending on the depth of the starting point. In addition, fluctuations in the relative number of charged versus neutral pions in the first few generations of the cascade affect both the rate of development of the electromagnetic cascade and the muon content of the shower.

These physical fluctuations in the shower as observed at ground level have been estimated using MOCCA simulations. At the high energies of interest here, fluctuation in the muon component is approximately 15%, while the fluctuation in the electromagnetic component is only about 5% [124]. The fractional fluctuation in the ground particle density is roughly independent of radius beyond a few 100 m from the core. In water Čerenkov detectors, where the muon and electromagnetic components make comparable contributions to the signal, the physical fluctuation in the total signal is about 10%. Figure 4.3 shows the lateral distributions of a number of individually simulated showers over a range of zenith angles and energies, and with physical fluctuations included as presently understood.

4.2 Determination of Shower Parameters

4.2.1 The Shower Direction and Axis

“Geometrical reconstruction” is the important procedure of determining the shower axis and core location at the ground. The direction of the shower axis is the cosmic ray’s arrival direction. If three ground stations record the shower, the shower direction can be computed by triangulation, finding the unique downward going speed-of-light shower front which accounts for the three positions and arrival times. When more than three stations trigger, a least squares method is used to find the plane front which fits best.

The position of the shower axis in space is located by exploiting the circular symmetry of particle densities in the shower plane (a plane perpendicular to the axis). This assumption of axial symmetry was mentioned in Section 4.1.2 above, and is the fundamental principle on which ground array analysis is based. For showers arriving close to the vertical the symmetry in the plane of the ground is of course circular; away from the zenith it becomes elliptical. A crude initial estimate of the position where the shower core impacts the ground is the “center of gravity” of the density measurements. Using the shower direction determined previously, and a given core impact position, the lateral distance of a detector can be calculated. Reconstruction proceeds by fitting the detector densities at their computed axial distances to an empirical *lateral distribution function*, the most probable core impact position and shower size being sought.

Once the core impact position has been determined it is possible to re-fit the detector times allowing for curvature of the shower front. This provides a refined shower direction, and the whole process can be repeated. After a small number of iterations (≤ 3) convergence is achieved. It is clearly key to this process that the lateral distribution function be well known. This is the case from previous experiments, whose results are also well reproduced by current Monte Carlo calculations — see Sections 4.3.1 and 5.2.4 for detailed discussion.

A better determination of the axis is achieved if the shower is also measured by the fluorescence detector. The axis is then constrained to lie in the plane containing the fluorescence detector and the viewing directions of the illuminated pixels. Locating the shower axis within that shower-detector plane is achieved using timing, both of the ground station detectors and of the spot of fluorescence light as it passes the various pixels. In this case the core impact position is located with minimal use of ground detector density information, and the lateral distribution can be studied in an essentially independent manner.

With or without the fluorescence detector, determination of the shower axis improves with the size of the shower. This is because greater numbers of particles (or UV photons for the fluorescence detector pixels) give a better measure of the passing shower front, and because more ground stations can be used in the fit. For measurements by the ground array alone, the typical angular resolution for vertical showers at 10^{19} eV is about 2° , improving to $< 1^\circ$ at 10^{20} eV. The error in the core impact position decreases from 80 m to 50 m. For hybrid measurements (fluorescence detector with ground array), the angular resolution improves from 0.25° to 0.20° over the same energy. The core position uncertainty decreases

from 35 m to 20 m. (See the next chapter for details of these methods and results.)

4.2.2 Energy

The cascade of ionizing particles is monitored in the atmosphere via nitrogen fluorescence. The amount of light produced at each atmospheric depth is proportional to the shower *size*, i.e., the number of charged particles N_e . By measuring the light produced at many depths, the fluorescence detector determines the shower's longitudinal profile $N_e(X)$. The atmospheric depth X is measured in units of g/cm² along the shower axis. As the shower size increases, the original energy gets divided among more and more particles. The average energy eventually becomes low enough that ionizing particles are removed from the cascade, by ionization energy losses, at a rate exceeding their production rate by bremsstrahlung and pair production. The shower size therefore reaches its maximum size N_{max} at some atmospheric depth X_{max} (its *depth of maximum*), and the size decreases beyond that depth.

The integral of the longitudinal profile is a calorimetric measure of the total electromagnetic shower energy,

$$E_{em} = 2.2 \text{ MeV/g/cm}^2 \times \int N_e(X) dX,$$

since a charged particle in the cascade deposits an average of 2.2 MeV into the atmosphere in each depth interval of 1 g/cm² [118]. The portion of the electromagnetic cascade reaching the ground is included by fitting a functional form to the observed longitudinal profile and integrating that function past the surface depth.

This electromagnetic cascade energy is a lower bound for the energy of the primary cosmic ray. The amount of unmeasured energy which goes into the ground as muons and neutrinos depends on the shower development and is subject to fluctuations. For protons, the unmeasured energy is about 5% on average. For iron primaries, the mean is about 15%. The Fly's Eye analysis assumed a uniform 10% unmeasured energy. That gives no more than a 5% expected error for any nucleus and a 10% error for γ -rays. The energy not measured by the fluorescence detector can be estimated using the measured muon densities. (The measured X_{max} provides correlated information. Larger X_{max} at fixed electromagnetic energy implies less energy in muons and neutrinos, as will be discussed below with composition issues.) The fraction of primary energy not dissipated by the electromagnetic cascade can be estimated shower by shower by exploiting the ground array's muon information and the X_{max} measurement.

Ground arrays have traditionally determined the shower energy by interpolating and/or extrapolating the measurements to a single quantity which is known from shower simulations to correlate well with total energy for all primary particle types. The Haverah Park energies are based on energy correlation with $\rho(600)$, which is the signal density per square meter in water tanks at a distance of 600m from the shower core. The AGASA detector uses $S(600)$, the energy deposition density in plastic scintillators at 600 m from the core. The use of these energy estimators are well established. Extensive modeling by Hillas[114] and others[122] have shown that variations in shower physics models and mass composition affect the energy

estimates only weakly. For the Haverah Park and AGASA arrays $\rho(600)$ and $S(600)$ can be found rather accurately, with uncertainties less than 20% (this includes roughly 10% physical fluctuation and 10% reconstruction uncertainty).

Because of the larger spacing between particle counters in the Auger ground array, it is more reliable to determine densities at 1.0 to 1.5 km from the core, rather than at 600 m. An important advantage of the Auger detector will be the separate measurements of muon density (mu) and the electromagnetic particle density (em) when measurements are made at sufficiently large distances from core that the individual muon pulses can be discerned. Algorithms to optimally identify these muon pulses as near to the core as possible are currently under development. The pair (mu,em) should be a more powerful indicator of energy than either density by itself or a combination of them such as $\rho(600)$. In addition, the ground array measures quantities such as the time distribution of the incoming particles, slope of the lateral distribution, and curvature of the shower front. These quantities are sensitive both to the muon fraction and to the depth of shower maximum, and will aid in both energy and primary mass reconstruction.

The hybrid data set will provide a distribution function in the multidimensional parameter space consisting of the fluorescence detector parameters E and X_{max} , and of the parameters measured by the ground array discussed above. Here E is the fluorescence detector's energy measurement (corrected for unmeasured energy based on its measured X_{max}). This allows the ground array to be inter-calibrated with the fluorescence detector, and enables the ground array to measure shower energy without reference to any hadronic interaction model or cascade simulation.

In the determination of shower energy, there are numerous advantages in the Auger detector's hybrid configuration. A shower measured in hybrid mode has an internal consistency check on the energy, since the ground array and the fluorescence detector independently measure the shower size at ground level. The fluorescence detector "trains" the ground array as explained in the previous paragraph, so the ground array can determine a shower's energy without the fluorescence detector and without reliance on any air shower development simulation. The ground array will also assist the fluorescence measurements. Many showers will be detected at large distances where atmospheric attenuation uncertainty can cause uncertainty in the longitudinal profile normalization. The array's measurement of shower size at ground level will provide the crucial normalization for those longitudinal profiles.

4.2.3 Primary Mass

The muon content of air showers is a powerful indicator of primary mass. The superposition model of a heavy nucleus can be invoked to explain why an iron shower produces more muons than a proton shower. The energy is divided among the constituent nucleons, so it takes fewer generations to distribute the hadronic energy into low energy pions which can decay before interacting. That means less energy is lost to the electromagnetic cascade, which results in more low energy pions than in a proton shower of the same energy. This is a general argument which pertains to all hadronic interaction models.

To evaluate quantitatively the relative muon production in heavy nucleus showers *vs.* proton showers, first note that muon production in proton showers increases with energy as $E^{0.85}$ [127]. The number of muons does not increase linearly with energy because more generations are required at higher energy to reduce the average pion energy down to where decay becomes likely. The extra generations mean a larger fraction of the energy is lost to the electromagnetic cascade, so a smaller fraction of the original energy gets delivered to those low energy pions which decay. Considering a nucleus-initiated shower as a superposition of A showers, each with energy E/A , we find that the total number of muons is

$$N_{\mu}^A \propto A(E/A)^{0.85},$$

or, comparing to proton showers,

$$N_{\mu}^A = A^{0.15} N_{\mu}^p.$$

Thus we expect that an iron shower ($A = 56$) will produce about 80% more muons than a proton shower of the same total energy.

The foregoing explanations for why X_{max} and muon number both correlate with primary mass may suggest that X_{max} and muon production are both controlled by the same shower development feature, so measuring both is redundant. To some extent that is the case. If a proton's primary collision were somehow to yield 56 equal-energy hadrons which all go on to interact, then its longitudinal profile should resemble the expected iron profile for the same total energy, and its muon content should be consistent with what is expected in an iron shower. In shower simulations, X_{max} and muon number are indeed correlated. But the correlation is far from perfect because of additional fluctuations which do not produce strongly correlated effects. For example, fluctuations in the number of charged *vs.* neutral pions in the first generation affect the number of low energy pions – hence muons – more than the shape of the electromagnetic longitudinal profile (e.g. X_{max}). While not independent, X_{max} and muon density are separate handles on composition. Moreover, they are measured with essentially independent instruments.

Similar remarks pertain to a third measurable quantity which correlates with the primary mass, the *rise-time* of the particle pulse far from the shower core. One practical example would be the time interval between the arrival of the 10% and 50% points of the integrated signal ($t_{10/50}$); other similar quantities are also used. Like X_{max} and muon density, its correlation with mass can be understood in terms of the shower development. Earlier shower development means more nearly equal paths for detected particles, so they arrive more tightly bunched in time. The effect is accentuated for water detectors by the larger fraction of muon signal in the pulse since the muons undergo less scattering and arrive earlier, on average, than electromagnetic particles.

These three quantities – depth of maximum, muon density, and rise-time – are used in concert to determine the cosmic ray nuclear composition and to find the most likely mass for each primary particle. The hybrid data set will provide a distribution function on the 3-dimensional space (mu:em, $t_{10/50}$, \hat{X}_{max}). Here mu:em is the muon to electromagnetic density ratio at 1 km from the core, $t_{10/50}$ is the rise-time for pulses at that distance, and

$$\hat{X}_{max} \equiv X_{max} - \frac{d \langle X_{max} \rangle}{d \log E} (\log E - \log E_0)$$

is the measured X_{max} corrected to a convenient reference energy E_0 using the observed *elongation rate* ($d < X_{max} > / d \log E$). Because the three measured parameters are correlated, the distribution function will be concentrated around a 1-dimensional curve in this space, where the curve can be parameterized by shower development speed. The observed distribution function on $(\mu:\text{em}, t_{10/50}, \hat{X}_{max})$ -space will be compared with the expected distribution function for alternative composition hypotheses.

A potential difficulty is that the expected distribution function may also depend on untestable properties of hadronic interactions at the highest energies. It is conceivable that the composition determination could be hindered by inadequate knowledge of the first generations of hadronic interactions. It is likely, however, that the relevant interaction model parameters (e.g. energy dependence of cross section, inelasticity, and multiplicity) will be well enough constrained that ambiguities due to the model freedom will be small compared to differences expected from different composition hypotheses. Significant constraints on the hadronic model have been imposed by the Fly’s Eye data[84]. HiRes and AGASA data can be expected to provide further constraints. By combining muon and electromagnetic particle measurements with X_{max} measurements, shower by shower, the Auger Observatory will provide valuable additional constraints. The Fly’s Eye analyses have demonstrated that such data can be used both to constrain the interaction model and also to make composition inferences. In the Fly’s Eye case, the model constraints derived from the need to explain the full range of the X_{max} distribution with nuclei of $1 \leq A \leq 56$. The energy dependence of the mean X_{max} was then used to infer a composition changing from heavy nuclei dominated to light nuclei dominated in the energy decade from $10^{18} - 10^{19}$ eV.

Above 10^{19} eV, γ -rays produce a characteristic signature due to the LPM effect [83]. This effect reduces the high energy electromagnetic cross sections, so the longitudinal profile becomes longer than that obtained using Bethe-Heitler cross sections. At Auger Observatory shower energies, a γ -ray shower is expected to have a significantly broader profile than any hadron-induced shower of equal energy, and the γ -ray showers should exhibit large fluctuations in X_{max} . The LPM effect grows with the γ -ray primary energy. The fluorescence detector’s longitudinal profile measurements will enable a sensitive search for any γ -ray population.

At the time of writing, work on the multi-parameter composition sensitivity is still in progress. The composition resolution based on $\mu:\text{em}$ alone is exhibited in Figure 4.4. The resolution based on \hat{X}_{max} alone is shown in Figure 4.5. Note that, in both cases, the air shower and detector response have been simulated with most relevant fluctuations. Changing the hadronic interaction model at the highest energies could change the locations of the peaks in those plots, but their separations should have little dependence on model variations[84].

4.2.4 New Particle Physics

Almost all the physics of air showers is well established. Electromagnetic sub-showers can be modeled with confidence. The majority of hadronic interactions in a shower can also be confidently modeled, since most interactions occur after many “branchings” of the shower,

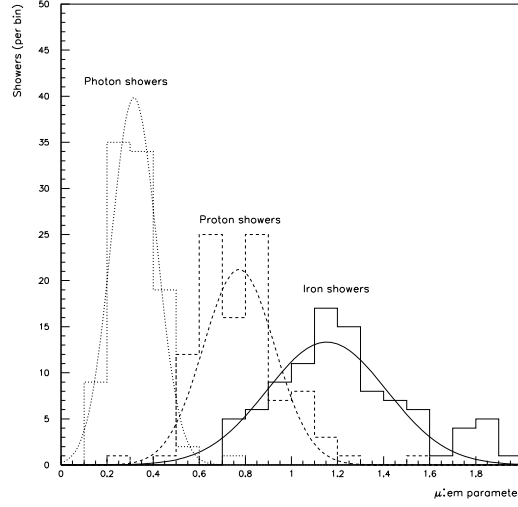


Figure 4.4: Predicted primary particle separation for the Auger surface array. Each distribution is from 100 showers at 5×10^{19} eV incident at 30° . The μ_{em} parameter is from reconstruction of realistically simulated detector signals.

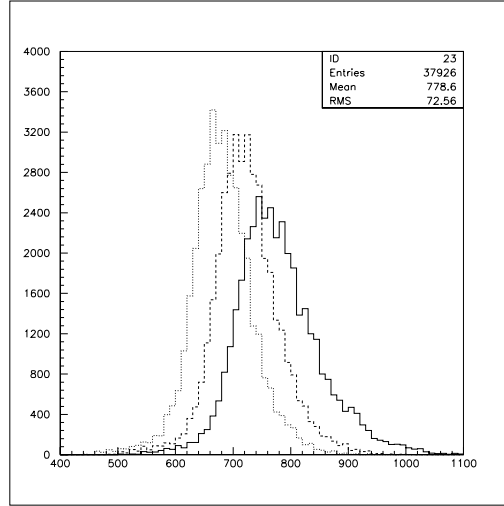


Figure 4.5: Reconstructed depth of maximum distributions from simulated iron (dotted histogram), carbon (dashed), and proton (solid) events. Showers up to 3×10^{19} eV are included, and all X_{max} values have been corrected by the elongation rate to a reference energy of 10^{18} eV. There are equal numbers of events in each histogram.

so individual particle energies are much reduced from that of the primary particle. Only the first few generations of interactions have center-of-mass energies greatly exceeding those of collisions studied in accelerator experiments. Collider experiments have explored hadronic interactions up to $\sqrt{s} = 2$ TeV. The Auger Observatory focuses on cosmic rays with energies above 10^{19} eV, for which the (nucleon-nucleon) center-of-mass energy is $\sqrt{s} = 140$ TeV.

Cosmic ray studies have a tradition of augmenting basic knowledge of particle physics. The Auger Observatory can expect to provide valuable information about particle interactions at a new frontier of energy. As happened with the Fly's Eye X_{max} distribution, combined measurements of $\mu:em$, $t_{10/50}$, and \hat{X}_{max} can be expected to constrain the interaction model even without independent knowledge of the composition. Measuring air showers provides not only information about the cosmic ray population (arrival direction patterns, energy spectrum, and composition), but offers a window to study new particle physics, if present.

Lack of complete *a priori* knowledge of hadronic interactions at the highest energies has only a limited impact on the Auger cosmic ray studies. The arrival directions can be measured completely independently of any model ambiguity. The electromagnetic shower energy is also measured without any reference to the hadronic model. It provides a solid lower bound for the cosmic ray's energy. The unmeasured energy is expected to correlate with shower development in a manner which is easily modeled. Composition studies cannot be totally divorced from models of the hadronic cascades' first few generations, but the relevant model parameters should be determined well enough to allow analysis of the mass distribution.

Systematic energy underestimation is possible if, for example, there is an unmodeled enhanced production of prompt muons which divert some of the total energy in the first interaction. Other uncertainty might arise due to the nonlinear behavior of QCD, which may cause intrinsic fluctuations in the numbers of particles produced in interactions ("intermittency") [85]. If either of these effects becomes very important at the highest energies, they may leave characteristic signatures in extensive air showers.

Learning how to model the highest energy interactions is vital for a comprehensive composition determination with the Auger data set. Developing and testing the interaction model will be a high priority of the Project. A meeting in conjunction with the Design Group Workshop was held at Fermilab in April 1995 to discuss the issues and set a course for future work. Efficient numerical simulation of air showers is an essential tool for designing the detector and evaluating its performance. The programs used for Auger are described in the next chapter.

4.3 Surface Array Methods

As described in the last chapter, most air shower experimental work has used surface arrays. Because of the low flux of extremely energetic cosmic rays, arrays require a very large collecting area (> 10 km²) to collect a useful sample of events. The approach has historically been

to cover the monitoring area, more or less uniformly, with a relatively small number (a few tens) of detectors, each having areas greater than about one square meter. A good example was shown in the last chapter, the Volcano Ranch array (Figure 3.1). In that experiment, the spacing between the 3.3 m^2 scintillators was 884 meters. At each detector of such an array the particle density is measured together with the arrival time of the signal at the detector relative to the other detectors. The geometry of the air shower is reconstructed from this data, the location of the densest part or “core” of the shower being determined under the assumption of circular symmetry (again, see Figure 3.1).

In the Volcano Ranch experiment the total number of particles in the shower was used to obtain the energy of the event. This total was estimated by integrating an empirically determined lateral distribution function (density *vs.* distance). The relationship between the number of particles and the primary energy was determined by invoking a detailed understanding of the physics of electromagnetic cascades. Modern air shower arrays use Monte Carlo calculations to relate the observed number of particles at ground level with the energy of the shower. The Auger ground arrays will use the inferred signal density at a specific core distance as their basic energy parameter. The reasoning behind this technique is described in sections 4.3.2 and 4.3.3 below.

The Volcano Ranch event also shows some other important features. Although the core of the shower impacts outside the geometrical boundary of the array it is well located by symmetry. Note also that significant signals are seen as far as 2.5 km from the shower axis. In the case of the Auger Observatory, due to its large size, it will not be necessary to use events which are not well contained within the array boundary.

4.3.1 Water Čerenkov lateral distribution function

Like the arrays planned for the Auger Observatories, the detectors of the Haverah Park experiment were water Čerenkov tanks (1.2 m deep and of various areas from 1 m^2 to 34 m^2) spread over 12 km^2 : the array ran more or less continuously for twenty years. Much of the design information from the Monte Carlo calculations used by the Auger collaboration have been checked against results from this experiment (see section 5.2.4). A particular advantage of the deep water Čerenkov detectors lies in their ability to respond to the large number of photons of relatively low energy (less than 10 MeV) present in the shower. Empirical studies using unshielded and lead-covered scintillators and the water Čerenkov detectors, now confirmed by the Monte Carlo calculations, demonstrated that photons outnumbered electrons by about a factor 10 at the large distances of interest. The depth of the tanks, 3.4 radiation lengths, allowed conversion of the bulk of the photons so that electrons, photons and muons were recorded with high efficiency. The large area ($4 \times 13.5 \text{ m}^2$) of the detectors at the periphery of the array permitted densities to be measured as far as 3 km from the core in the largest events. The rise-times (10-50%) of the water Čerenkov signals were measured at four 34 m^2 detectors which were on a 500 m grid at the center of the array.

The central element of the reconstruction and analysis of air showers using surface arrays involves fitting the lateral distribution function of particle densities. At Haverah

Park a good fit to the water Čerenkov lateral distribution was found to be the modified power law function:

$$\rho(r) = kr^{-(\eta + \frac{r}{4000})}, \quad (4.1)$$

where shower core distance r is in meters, k is a normalization parameter, and η is given by

$$\eta = 3.49 - 1.29 \sec \theta + 0.165 \log \left(\frac{E}{10^{17} \text{ eV}} \right), \quad (4.2)$$

with θ the shower zenith angle, and E the shower energy.

The parameters η and k control the shape and normalization respectively. Representative values are $\eta \approx 2.5$ and $k \approx 3.5 \times 10^8$ for vertical 10^{19} eV showers. The signal density $\rho(r)$ is expressed here in units of vertical equivalent muons per square meter (VEM m^{-2}), obtained by dividing the total observed signal by the average value from a vertical through-going muon. Use of this density unit allows simple calibration of water Čerenkov detectors using background muons.

As shown by Equation 4.2 the slope parameter η is a function of zenith angle θ and, to a minor extent, shower energy. Both of these effects reflect the “aging” of a shower as it penetrates through the atmosphere. For four years 30 smaller water Čerenkov detector units also 1.2 m deep were operated in the central part of the Haverah Park array allowing detailed study of these effects and leading to Equation 4.2.

The lateral distribution shape given by Equations 4.1 and 4.2 is known to be valid for $50 < r < 800$ m, $\theta < 45^\circ$ and $1 \times 10^{17} < E < 5 \times 10^{18}$. It was noticed that in the biggest showers, where measurements were recorded well beyond 800 m, there was a significant departure from this parametrization, the measured values of $\rho(r)$ being consistently higher. A special study of showers with $E \geq 1 \times 10^{19}$ eV indicated that these data were well represented by flattening the lateral distribution for $r > 800$ m. Thus, for the highest energy showers, Equation 4.1 is replaced at $r > 800$ m by the modified expression

$$\rho(r) = kr^{-(\eta + \frac{r}{4000})} \left(\frac{r}{800} \right)^{1.03}. \quad (4.3)$$

Figure 4.6 shows four examples of actual Haverah Park data in this energy regime. Equations 4.1–4.3 are seen to do an excellent job of describing these data over the entire measurement range. These events were experimentally very well measured. They fell close to an infilled part of the array so their cores are reliably located. This allows the lateral distribution at large distances to be observed with minimal reconstruction bias.

The flattening of the lateral distribution at large core distances seen in Figure 4.6 and expressed in Equation 4.3 can be understood in terms of a shift from an electromagnetic to a muon-dominated signal. It is a consequence of the broader muon lateral distribution which is predicted from simulation. The effect is enhanced in water Čerenkov detectors, where the higher energy muons release much more Čerenkov light per particle (recall Figure 4.2).

In Section 5.2.4 it is shown that current simulations do an excellent job of reproducing the empirical Haverah Park results. Since the Auger arrays are to be built at higher altitude than Haverah Park (870 g/cm^2 as opposed to 1020 g/cm^2) it will be necessary to

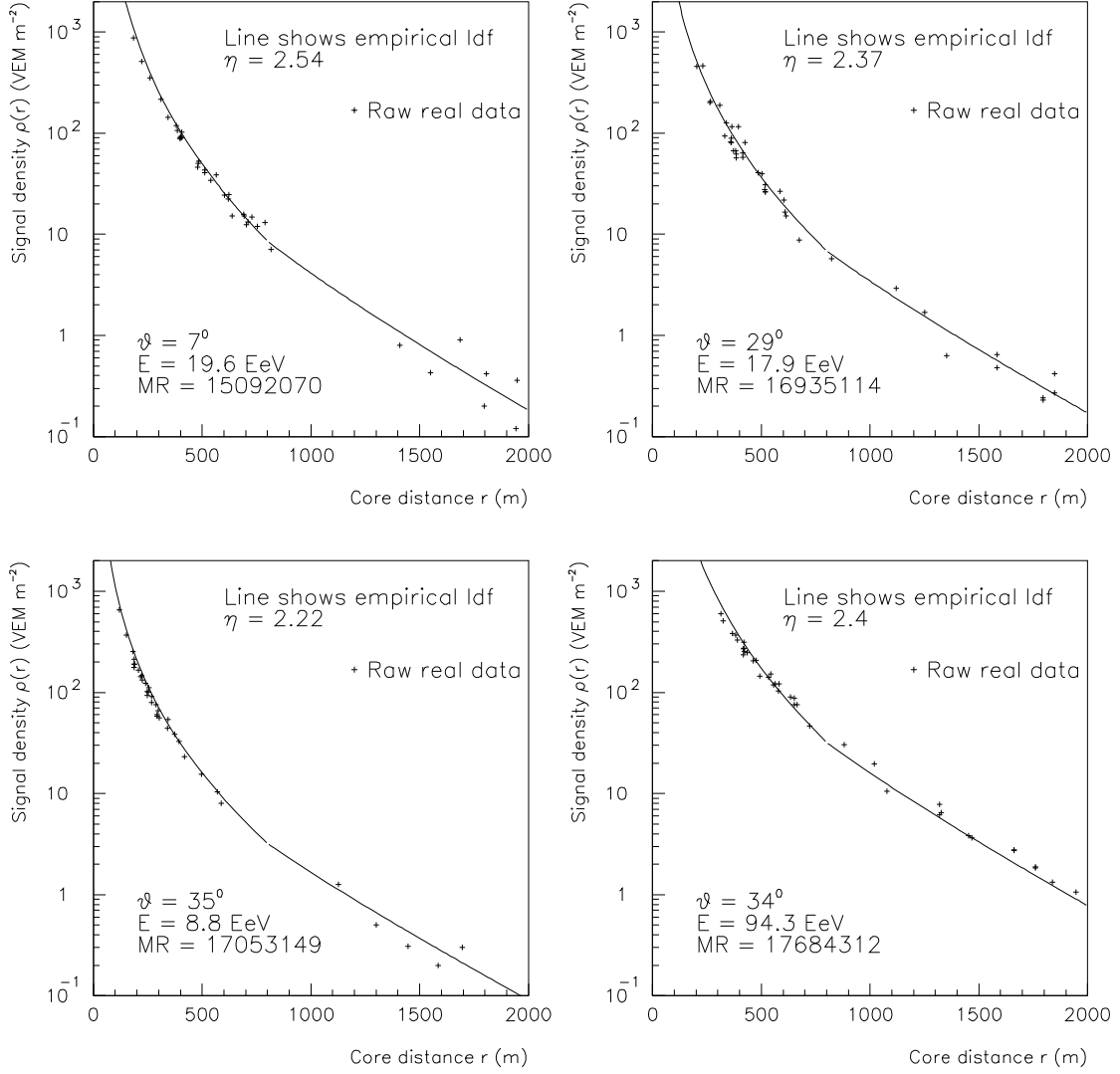


Figure 4.6: Haverah Park data showing four exceptionally well measured events at very high energy. The solid line is the lateral distribution function from Equations 4.1–4.3. The value of the slope parameter η is shown for each event, along with the best-fit values for energy and zenith angle; MR is an event identification code. Energy is expressed in units of EeV, where $1 \text{ EeV} = 10^{18} \text{ eV}$.

extrapolate the Haverah Park results, or more probably, to use an initial lateral distribution function derived from simulations validated using the Haverah Park results. Also, as mentioned in section 4.2.1, the Auger hybrid data set will allow independent investigation of the lateral distribution function.

4.3.2 Event Reconstruction

The structure of air showers was described in Section 4.1.2 above, and the reconstruction process briefly introduced in Section 4.2.1.

Figure 4.7 shows the reconstruction of an individual simulated event. The Haverah Park lateral distribution function was fit to the detector density measurements allowing the slope parameter η to go free in the last iteration. The 10% signal arrival time of the shower front (t_{10}) was fit assuming it to have a spherical shape in space; the radius of curvature was also allowed to go free at the last iteration. In time fits the observations are normally weighted by the corresponding detector densities. These two fits yield the shower incidence angles θ and ϕ , the core impact position, and the energy of the shower as inferred from the reconstructed signal at 1000 m from the core (see next section).

A final fit is illustrated; the shower front time dispersion ($t_{10/50}$) is analyzed on the assumption that it varies linearly with core distance. The slope of this fit, together with the lateral distribution slope parameter η , and the radius of curvature of t_{10} are sensitive to the mass of the primary particle.

It turns out that for a given array layout there is a distance at which the signal density is most accurately reconstructed. This results from a geometric effect whereby the errors in the determination of the lateral distribution slope and shower core position conspire to cancel at a given distance. The specific distance varies with shower impact position relative to the array grid, but it is on average somewhat less than the array spacing. For the Auger arrays it will be at ≈ 1 km. (For the Haverah Park array it was ≈ 600 m.) In the next section the proportionality between $\rho(1000)$ and the energy of the primary cosmic ray particle is investigated.

4.3.3 Energy Assignment Parameter

Air shower parameters scale in a well behaved manner with increasing primary energy. The best experimental demonstration of this has been provided by the series of arrays constructed at Akeno in Japan [123, 16]. Simulations also predict smooth scaling; Figure 4.8 shows the evolution of the lateral distribution over a broad range of energies.

The proportionality between the density observed at a given core distance and the energy of the shower changes with shower energy. This occurs because the shower is observed at differing stages of development as the depth of maximum increases with energy. In addition, the water Čerenkov detector's comparable sensitivity to muons and the electromagnetic component affects the proportionality of response as a function of radius. However, the evo-

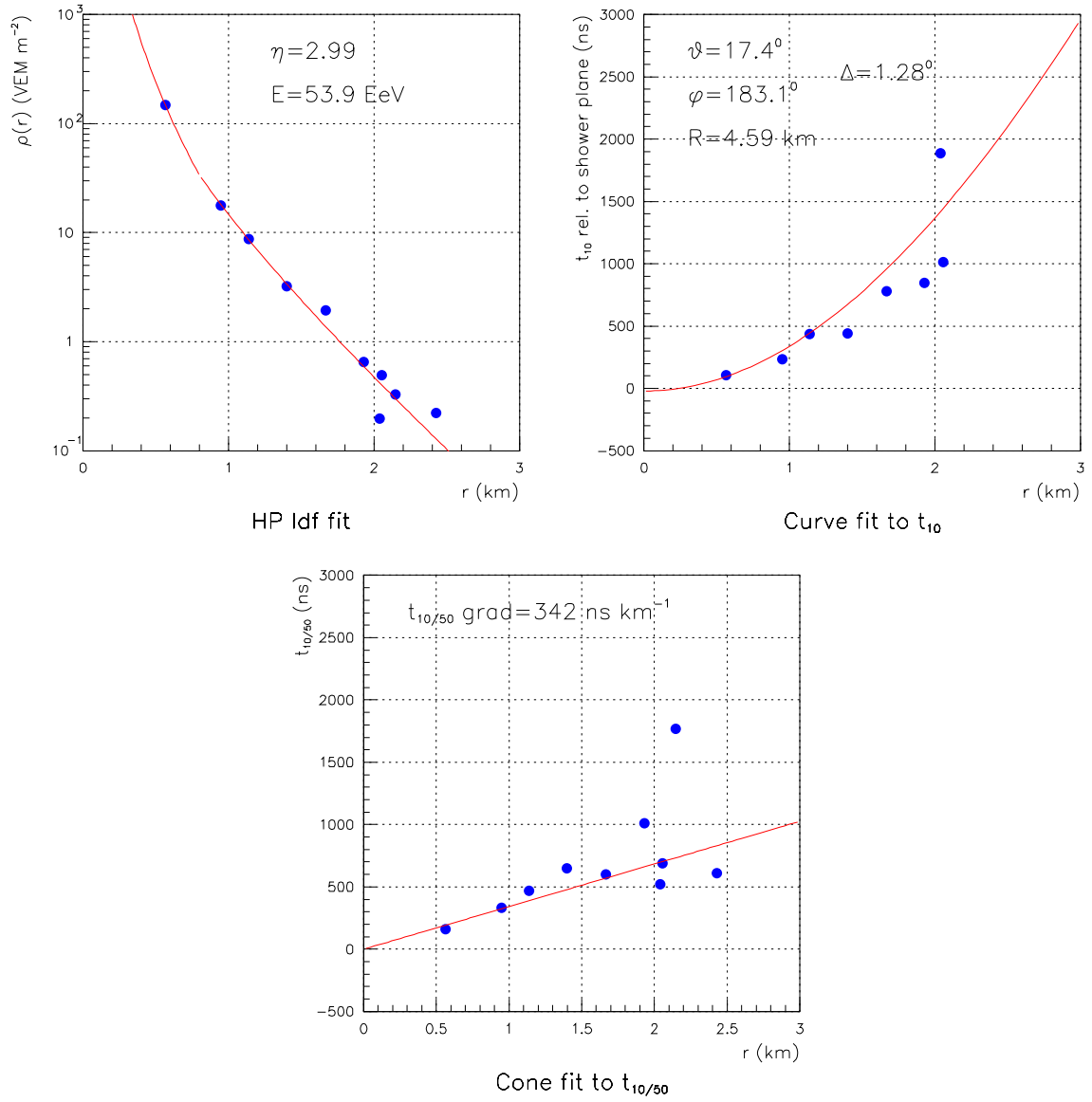


Figure 4.7: Reconstruction of a simulated Auger ground array event. At top right a lateral distribution fit to the Haverah Park functional form is shown; at upper right a fit to the 10% arrival time of the detector signals. The lower plot shows a fit to the shower front time dispersion.

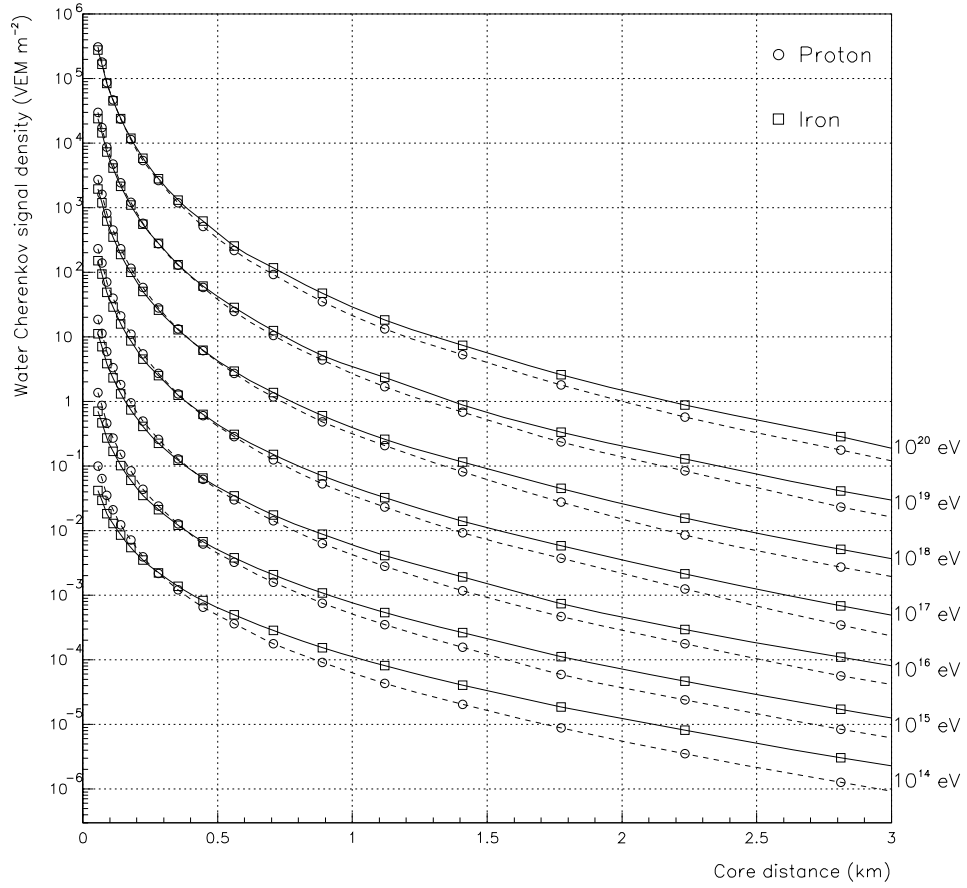


Figure 4.8: Simulated lateral distribution of air showers for a wide range of primary energies. The signal as observed in water Čerenkov detectors 1.2 m deep is plotted; calculation parameters are atmospheric depth of 850 g/cm^2 , and zenith angle of 20° .

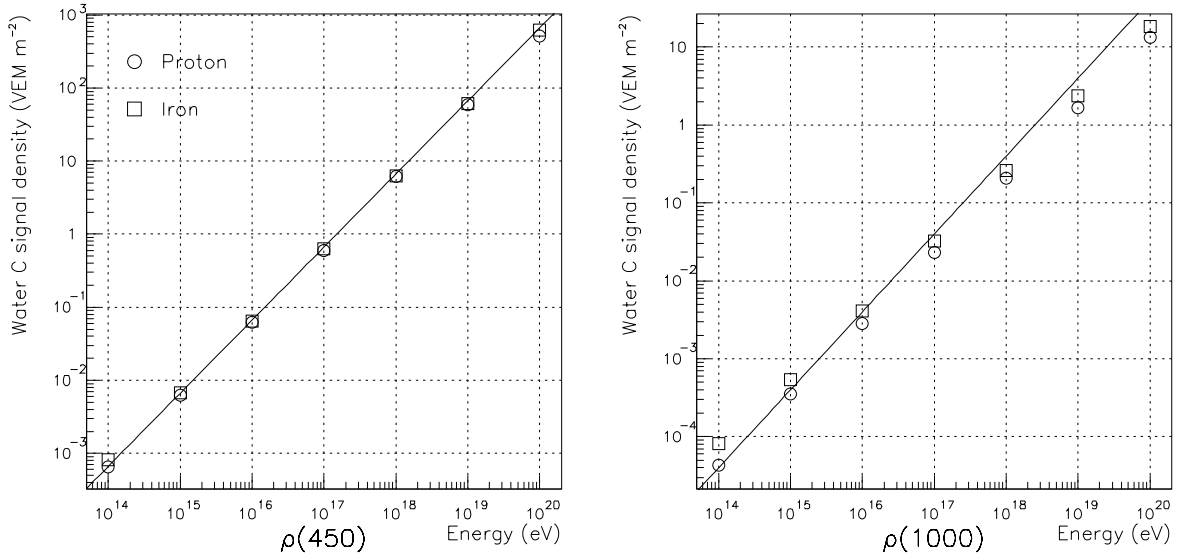


Figure 4.9: The signal density at two core distances plotted against air shower energy, and as observed by 1.2 m deep water Čerenkov detectors. Calculation parameters are atmospheric depth of 850 g/cm², and zenith angle of 20°. The solid lines show direct proportionality with the constant set such that the line passes through the proton point at 10¹⁴ eV.

lution of the lateral distribution with changing depth of maximum and muon content leads to very nearly proportional response at a particular core distance. Figure 4.9 shows the density versus energy at 450 m and 1 km. At 450 m the various factors give a density proportional to energy and nearly independent of composition. (Previous calculations by Hillas [114] found the same result at ≈ 500 m.)

Near 1 km there is both a slight deviation from proportionality and a modest dependence on composition. However, the Auger observatories will operate over a much narrower range of energies than shown in the figure; in the range 10^{18.5} eV to 10²⁰ eV proportionality is good near 1 km. As discussed in the last section practicalities of ground array reconstruction dictate the use of the inferred signal density at ≈ 1 km as the minimum variance energy estimator. This implies some composition dependence for the energy assignment. However, as mentioned in section 4.2.2 above, it is expected that such dependence can be studied and reduced using the hybrid subset of the Auger data, and by separating the detector signal into electromagnetic and muonic components. More sophisticated methods than the simple energy parameter discussed here are under consideration.

4.4 Fluorescence Detection

The Auger Observatory is to be a hybrid detector. A giant array of particle counters will measure the lateral distribution of air shower particles at ground level. An optical component will measure the air shower longitudinal development in the atmosphere, using the technique established by the University of Utah's Fly's Eye detector. These atmospheric fluorescence

measurements, although only available on clear, dark nights, will play an essential role by providing a subset of showers measured both laterally and longitudinally. This special subset will form the basis of the cosmic ray mass composition determination, as well as providing crucial cross-checks on the ground array's geometric reconstructions and energy determinations.

The primary role of the fluorescence detector is to measure the longitudinal profile of each shower. The integral of that profile is a direct measure of the shower's energy deposited in the atmosphere. The measured profile also yields information such as the atmospheric depth X_{max} at which the shower reaches its maximum number of secondary particles. For showers of fixed energy, X_{max} correlates with the mass of the primary particle.

It should be emphasized that the optical detector envisioned in this report has been designed to use ground array timing information to get good shower reconstruction capabilities. A fluorescence detector without a ground array, but with similar acceptance and reconstruction quality requirements, is considerably more expensive to build. Such a stand-alone fluorescence detector would need to view each shower simultaneously with two or more of its several eyes (i.e., in “stereo”). The intersection of the shower-detector planes from the different eyes gives the shower axis. To achieve two views of every shower for which we now plan one view would require either building twice as many separate eyes, or making each eye see twice as far. The cost of the fluorescence detector would be significantly increased, compared to the “monocular” design selected for the Auger Observatory.

4.4.1 Air Fluorescence

As a cosmic ray-induced particle cascade develops in the atmosphere it dissipates much of its energy by exciting and ionizing air molecules along its path. Excited nitrogen molecules fluoresce, producing near-UV radiation with an emission line spectrum as displayed in Figure 4.10. The efficiency of the process, defined as the radiated energy divided by the energy loss in the observed medium, is only $\sim 5 \times 10^{-5}$, but the vast number of emitting particles in a 10^{19} eV shower makes this source of radiation significant.

Fluorescence light is emitted isotropically with an intensity which is proportional to the number of charged particles in the shower. The number of fluorescence photons produced by N_e charged particles as they traverse a distance dl is expressed by

$$\frac{dN_\gamma}{dl} = N_f N_e,$$

where N_f is the fluorescent yield in photons/charged particle/meter. Strictly speaking, N_e should correspond to the total number of charged particles, but in practice it is often simply used to express the number of electrons and positrons since they so dominate the total number of charged air shower particles.

In practice N_f is very nearly a constant for most observational situations. As the pressure and temperature of the atmosphere is increased the excitation of molecular nitrogen is enhanced, but so is the probability of collisional de-excitation by oxygen molecules. The

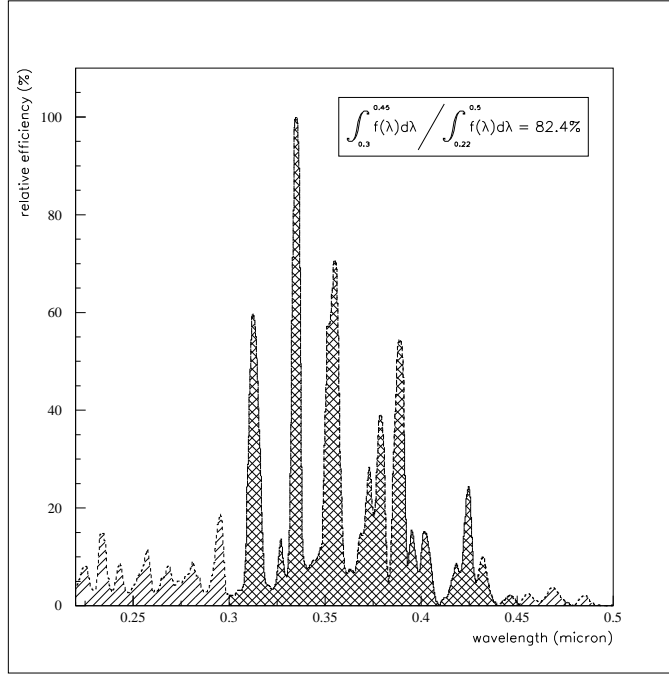


Figure 4.10: Emission spectrum of fluorescence light from the 2P band of molecular nitrogen and the 1N band of the N_2^+ molecular ion. Approximately 80% of the light is emitted between 300 and 450 nm.

two processes balance in such a manner that the variation in N_f as a function of altitude is quite small. Shown in Figure 4.11 are the results (for 80 MeV electrons) of an experiment in which a beam of electrons was sent through a chamber containing air at various pressures. The equivalent altitude is obtained using two standard atmospheric models. The observed fluorescence yield per meter of track length varies by less than 12% about an average of 4.8 photons/electron over a range of 20 km in effective altitude[108].

The relative constancy of the fluorescence yield greatly facilitates the use of this technique in which the number of particles at a given atmospheric depth is estimated via the amount of observed fluorescence light.

4.4.2 Čerenkov production and scattering

In addition to fluorescence light, showers produce prodigious numbers of Čerenkov photons which are primarily beamed in the forward direction. (The Čerenkov emission angle in the atmosphere is of order 1° , varying with altitude). The amount of Čerenkov light at a given point along the shower track depends upon the previous history of shower, and is thus not strictly proportional to the local shower size as is the fluorescent light. It is therefore necessary to estimate the amount of Čerenkov light in order to subtract its contribution to the observed signal. The number and angular distribution of Čerenkov photons over a

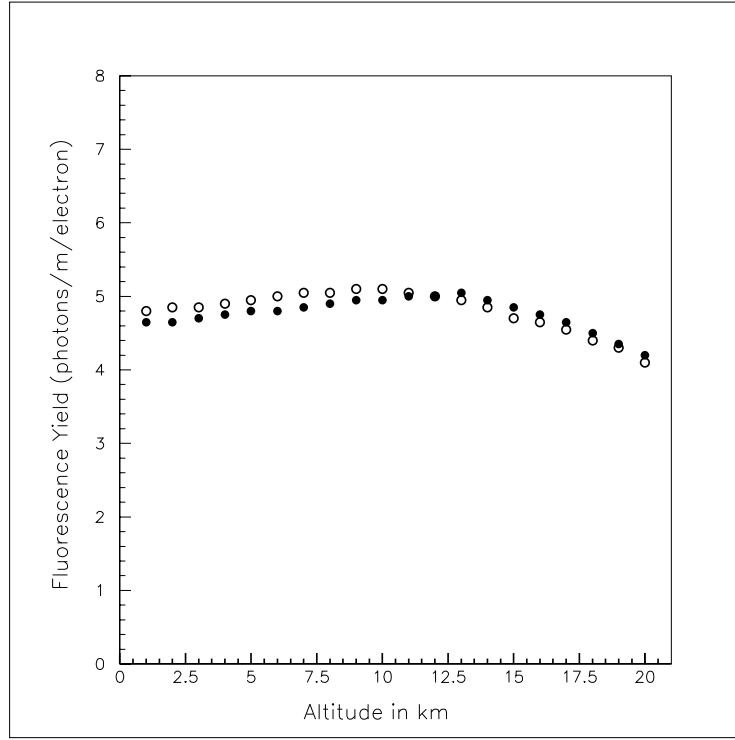


Figure 4.11: Air Fluorescence yields as a function of altitude. Open circles are for standard summer atmosphere while filled are for standard winter atmosphere[108].

distance dl of air can be approximated by :

$$\frac{d^2 N_\gamma}{dl d\Omega} = \frac{dN_\gamma}{dl} \frac{e^{-\frac{\theta}{\theta_0}}}{2\pi \sin(\theta)}$$

where dN_γ/dl is the Čerenkov photon yield per meter of air, θ is the emission angle (in radians), $\theta_0 = 0.83E_t^{-0.67}$, with E_t is the Čerenkov threshold energy in air in MeV. When a shower is viewed at small emission angles (less than 25°) with respect to the shower axis the Čerenkov signal can be many times larger than the fluorescence signal. The presence of this directly-beamed Čerenkov light often impedes the proper observation of the first stages of shower development. In addition, as the Čerenkov component builds up with the propagating shower-front, the resultant intense beam can generate enough scattered light at low altitudes such that it competes with the locally produced fluorescence light. This effect complicates the observations of the later stages of shower development.

Both fluorescence light and Čerenkov light are affected by the scattering properties of the atmosphere. The effects of scattering must be understood if one is to accurately estimate the shower size by light received from a distant section of air shower. With fluorescence light one is most concerned with the attenuation due to scattering as the light travels from the air shower to the detector. In the case of the (accumulated) Čerenkov beam, one is more concerned with the light scattered toward the detector. In both cases there are two scattering mechanisms: (1) Rayleigh (molecular) scattering and (2) Mie (aerosol) scattering.

The amount of molecular scattering at a given wavelength is proportional to the density of the air through which the beam is passing. The effect therefore tracks with the exponential

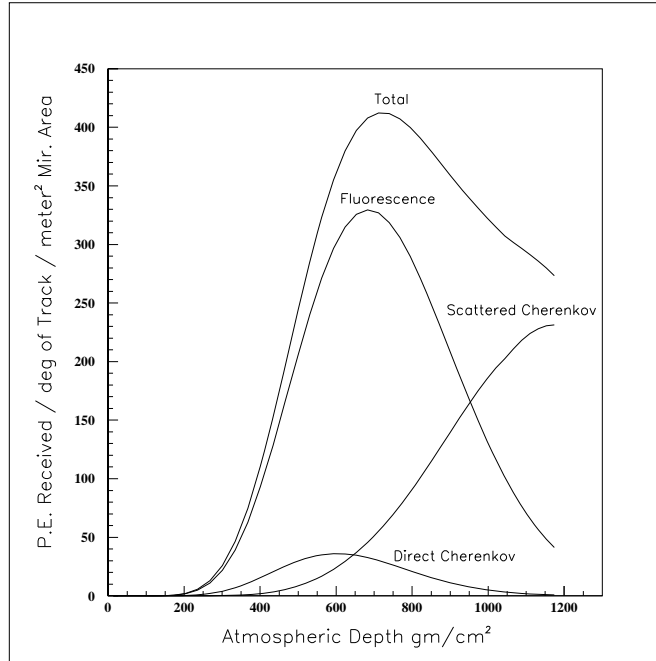


Figure 4.12: Estimated signal versus atmospheric depth of light production for a 10^{19} eV proton shower with orientation $\theta = 45^\circ, \phi = 0^\circ$ hitting the ground 10 km from the detector. The simulation included filters passing 300-400 nm light.

density profile of the atmosphere with a scale height of 7.3 km. In general the atmospheric density is well known and changes little over time. The Rayleigh scattering length at sea level is a constant 23 km at 400 nm. On the other hand, the degree of aerosol scattering depends on both the density and size distribution of particulate matter suspended in the air. These distributions are highly variable with time and location. For the desert atmosphere of the western United States the average aerosol scattering length is of order 10 km for wavelengths of interest in fluorescence detection. The vertical density distribution varies depending on weather conditions between an exponential form, similar to the molecular scattering situation and a distribution in which uniform scattering occurs beneath a fixed-height mixing layer.

Figure 4.12 illustrates the above ideas. The number of received photoelectrons versus atmospheric depth is plotted for a simulated 10^{19} eV shower at 10 km from the detector. This calculation includes the effects of 300-400 nm light filters on the apparatus. The total light, along with the contributions from fluorescence, direct Čerenkov, and scattered Čerenkov, are shown. The orientation and position of the shower has been chosen so that the contributions due to scattered and direct Čerenkov are enhanced.

This shower represents a worst-case situation for events which might be seen by the Auger Observatory near its energy threshold. The difference in the heights of peak emission of the fluorescence light and of the total light suggests that one would incur an error in energy of about 30% if the Čerenkov light contribution was ignored. The apparent shift of

50 g/cm² in X_{max} is significant however. Certainly, for highly inclined showers directed at the eye, both direct and scattered Čerenkov should be taken into account.

4.4.3 Detection Technique

An air fluorescence detector or “eye” consists of a series of large light collectors which image regions of the sky onto clusters of light sensing devices. The High Resolution Fly’s Eye (HiRes) prototype detector [120] is an example of such a detector. In the following, it will be helpful to refer to this example.

HiRes uses fourteen f/1.16, 2-meter diameter spherical mirrors to collect the light from a 0.95 sr portion of the sky. The image plane of each mirror is populated with an array of 256 1-inch diameter (hexagonal) PMTs giving the instrument a 1° angular segmentation. The integrated charge and the trigger time are recorded for each PMT through which the shower image passes. The field of view of the mirrors is centered on the Chicago Air Shower Array (CASA) and the Michigan Muon Array (MIA) [121], situated 3.3 km to the northeast. The combination of the instruments has been used as a prototype hybrid detector where HiRes records the development profile, CASA records the ground particle density and MIA detects the muonic component of a common shower.

To a distant fluorescence detector a cosmic ray cascade appears as a rapidly moving spot of ultraviolet light describing a great circle path across a night-sky background of starlight, atmospheric airglow and man-made light pollution. The angular motion of the spot depends on both the distance and the orientation of the shower axis. The apparent brightness of the spot tracks with the instantaneous number of charged particles present in the shower but is also affected by Čerenkov contamination and atmospheric scattering as discussed above. The task of the optical detector is to pick out this faint, but fast signal from the ambient background noise, measure the shower trajectory from the appearance of the track and the light arrival time as a function of the angular position, and to infer the shower development profile from the light flux from different parts of the track.

The shower track in the detector appears as long, rather narrow sequence of hit PMTs. The collection of vectors pointing from the PMTs defines a plane called the Shower Detector Plane (SDP). As the spot-like image of the shower proceeds through an individual PMT, the signal rises, levels off, and falls again. The transit time across the face of the PMT is given by

$$\Delta T = d \frac{R_p}{2c} \sec^2\left(\frac{\theta}{2}\right),$$

where R_p is the distance of closest approach between the detector and the shower track, θ (the viewing angle) is the between the PMT pointing direction and the shower axis in the SDP, and d is the angular width of the PMT’s field of view. The physical length of track viewed by the PMT is $l = c\Delta T$. If the PMT aperture is circular and the shower path doesn’t pass through the center of the pixel but misses by some fraction b of the pixel radius, then ΔT is further reduced by the factor $\sqrt{1-b^2}$. As an example, consider a vertical shower hitting the ground 10 km from the eye. A 1° pixel viewing the shower horizontally

has a signal profile which is 523 ns wide. The pixel views about 175 meters of shower track and, at an operating altitude of 860 g/cm², that observed interval of track corresponds to a atmospheric depth interval of 20 g/cm².

The magnitude S of the signal seen by a PMT depends on the size of the shower N_e , the distance R to the shower, the detector's sensitivity, and the time T over which the flux is collected. The relevant detector properties are the light collecting area A and the quantum efficiency ε . A is the effective area after correcting for mirror reflectivity and obscuration by the phototube camera at its focus. The signal S , in photoelectrons, is given by

$$S = 2.4 \frac{A\varepsilon N_e c T}{4\pi R^2} \xi(R),$$

where $\xi(R)$ characterizes the atmospheric attenuation and c is the speed of light. The fluorescence efficiency of the atmosphere in the frequency range appropriate to HiRes phototubes (with filters) gives the coefficient 2.4 photons/m per charged particle (so the above formula requires cT to be in meters).

The noise is governed by the background light from the night sky, which is approximately 40 photons/(m² deg² μ s) in the frequency range accepted by the HiRes filters and PMTs.¹ The noise is the square root of the background photoelectrons collected in T microseconds:

$$N = \sqrt{40\varepsilon A\Omega T}.$$

Here Ω is the pixel solid angle in square degrees.

The signal-to-noise ratio is therefore

$$S/N = \frac{2.4N_e c}{4\pi R^2} \sqrt{\frac{\varepsilon AT}{40\Omega}} \xi(R).$$

Suppose the maximum of a vertical 10¹⁹ eV shower at $R = 10$ km is observed using the HiRes detector. Assuming an exponential atmospheric attenuation with attenuation length 10 km, a collection time $T = 0.5\mu$ sec, and other parameters given above for the HiRes geometry, the S/N ratio for a HiRes PMT is about 9.1.

A practical detector must be able to accurately determine whether and when a shower image has passed through a given tube and thus call the tube "hit". In the case of the HiRes Prototype a tube is said to be hit when its RC filtered ($\tau_{RC} \sim 100$ ns) pulse height exceeds a voltage threshold which is continuously adjusted in response to changes in the background light level. The adjustments are made in such a way as to maintain a 200 Hz singles rate² in each tube. Signals which exceed this threshold correspond to a 4σ fluctuation in the background.

Even with this constraint, there will be tubes which report hits by chance. The detector must distinguish a random pattern of hit tubes from the pattern characteristic of a

¹This is a representative value. The actual background intensity varies with elevation angle and atmospheric conditions. In normal running conditions, the background varies by less than a factor of two.

²This rate in the HiRes is about four times larger than the original Fly's Eye rate.

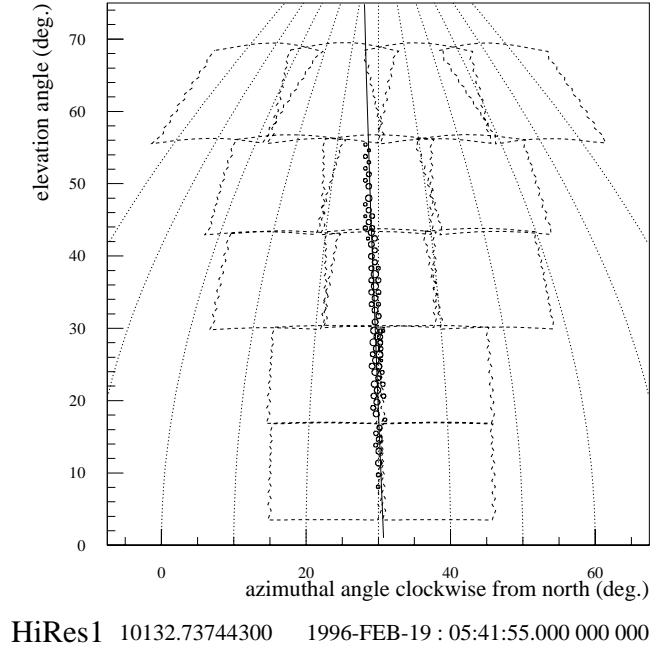


Figure 4.13: Typical HiRes shower, showing individual pixel hits and best-fit trajectory.

real shower. In addition, one must discriminate against showers that have geometries such that direct Čerenkov light dominates the fluorescence signal. Global triggering is a pattern recognition problem where the primary signature for the showers of interest is a linear pattern of hits which progresses in time. In the case of the HiRes prototype, each mirror (256 PMTs) can trigger independently. The cluster of tubes is arranged into 16 subclusters of 16 tubes (4×4). A hardware trigger occurs when at least 2 subclusters have at least 3 hit tubes, of which two of the three hit tubes are adjacent. The rate of these triggers is 0.5 - 1.0 Hz per mirror. Overall, the instrument triggers at about 10 Hz. Further discrimination criteria are implemented in software. Requiring a sensible angular velocity of the progression of hit PMTs reduces the rate of accepted (“real”) fluorescent tracks to about 0.1 Hz.

For each triggered mirror, the detector electronics record and store quantities which are representative of the light flux as a function of time. The HiRes detector records the threshold crossing time to 25 nsec for each hit tube. It also records integrals of the signal over two time scales, 1.2 μ sec and 5.0 μ sec. Another technique which is still being developed by the HiRes group involves the use of signal digitization by flash ADC (FADC). In this technique the signal pulse profile can be digitized and recorded in its entirety. Figure 4.13 shows a typical shower as detected by the HiRes instrument. A spherical projection of the viewing regions of all 14 mirrors is shown with hit PMTs displayed as circles whose sizes are proportional to the number of photoelectrons collected. Noise hits, averaging only 0.5 per mirror per event, have been removed. The CASA and MIA detectors, which also saw this event, subtend a 5° azimuthal segment centered on 30° . This particular event will be used in the following discussions as an illustration of reconstruction techniques.

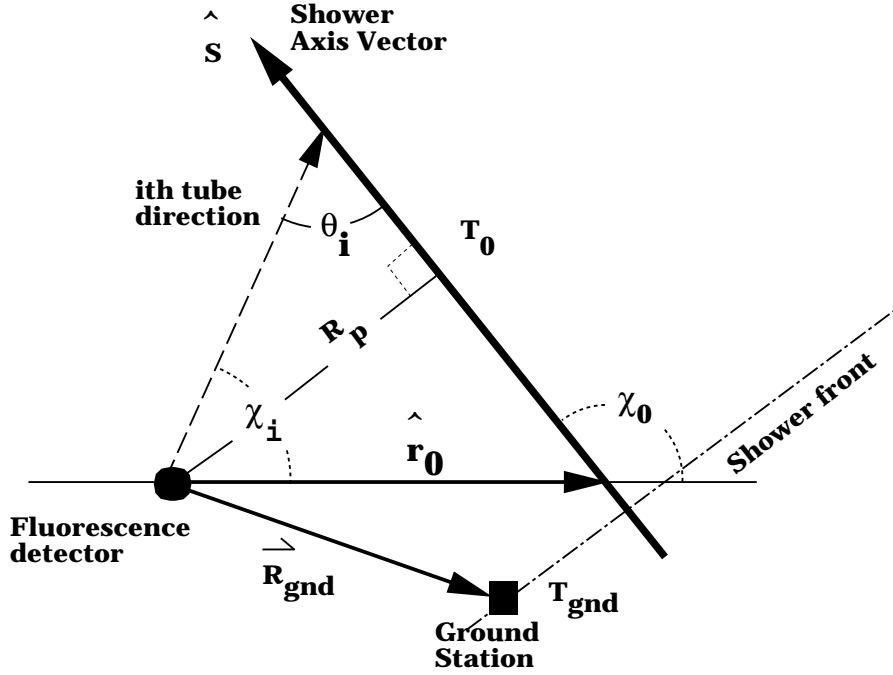


Figure 4.14: Shower/Detector Geometry.

4.4.4 Finding Shower Trajectories

The first stage in shower reconstruction is the determination of the shower trajectory. The process of trajectory finding occurs in two stages. First, the *shower-detector plane* (SDP) is determined³. The SDP is found using a fit to the eye's hit tube directions, where each point is weighted by the tube amplitude. The resulting plane normal vector can be determined in this manner with an accuracy of 0.2° [120]. The results of the SDP fit for the sample HiRes shower in Figure 4.13 is shown as a solid line through the hit tubes. The background (noise) tubes, about 0.5 per mirror, have been removed from this display.

In the second stage of track reconstruction the orientation and position of the shower axis within the SDP are determined. This amounts to finding the two quantities R_p and χ_0 as defined in Figure 4.14. R_p is the impact parameter for the collision between the optical detector and the shower and χ_0 is the angle in the SDP which the shower axis makes with the horizontal. Within the SDP the arrival time of light from the shower at each hit PMT is given by the following expression :

$$t_i = T_0 + \frac{R_p}{c} \tan\left(\frac{\chi_0 - \chi_i}{2}\right),$$

where T_0 is the time at which the shower front passes closest to the eye (i.e., at distance R_p), χ_i is the i th PMT's elevation angle in the SDP, and c is the speed of light. The desired

³Note that the SDP is not the same as the shower front plane defined earlier, in Sec 4.1.2.

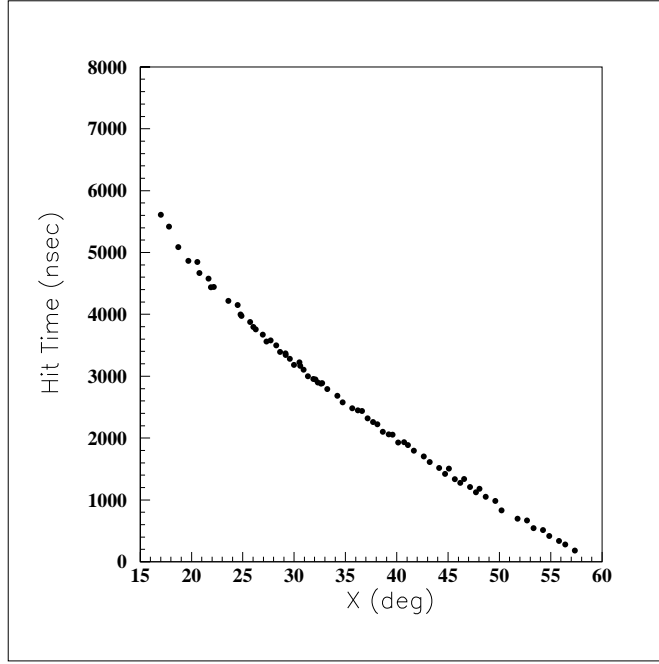


Figure 4.15: HiRes PMT hit time versus θ_i .

shower parameters may be found by minimizing :

$$\chi^2 = \sum_{i=1}^N \frac{(t_i - t_{obs_i})^2}{\sigma_i^2}$$

where t_{obs_i} is the observed tube trigger time and σ_i is the estimated measurement uncertainty in t_i .

When no ground array information is present the minimization is accomplished by varying three parameters R_p , χ_0 , and T_0 . This procedure is often called the “mono” method of track reconstruction because it uses information from a single optical detector. In general there is a problem with this method, especially for tracks of short angular extent. The degree to which one can unambiguously determine more than two parameters in the fit depends on the degree to which the function $t_i(\chi - i)$ departs from linearity over the sampled range of angles χ_i . For most showers the range of sampled angles is small and $t_i(\chi_i)$ is indeed nearly linear. The situation is illustrated in the plot of observed PMT firing time t_{obs} versus χ for our sample HiRes shower in Figure 4.15. It is clear that for segments of track shorter than 20° very little curvature is detectable in the presence of the scatter of the points. Only two parameters are needed to describe the relationship between t_{obs} and χ for such segments, thus there is an ambiguity incurred when fitting for three parameters. This ambiguity can be resolved if information from the ground array is utilized in a hybrid fitting scheme.

There are two possible hybrid fitting schemes. In the first, the mono 3-parameter fit is replaced by a 2-parameter fit by specifying the angle χ_0 in terms of the shower direction derived independently by the ground array \hat{S}_{gnd} , through

$$\chi_0 = \cos^{-1}(\hat{S}_{gnd} \cdot \hat{r}_0),$$

where \hat{r}_0 is the unit vector from the eye toward the shower impact point. In the case of our sample HiRes shower it was possible to use the shower direction, deduced from the arrival time distribution of the 665 detected muons, to constrain the fit. The shower landed 1583.7 ± 4.2 m East and 2653.9 ± 7.1 m North of the eye. The zenith angle of shower was 5.97° .

In the second hybrid fitting scheme the reduction of fit parameters is accomplished by specifying the time T_0 . T_0 can be calculated from the measured ground array trigger time T_{gnd} using

$$T_0 = T_{gnd} + \frac{\vec{R}_{gnd} \cdot \hat{S}}{c},$$

where \vec{R}_{gnd} is the vector from the eye to the ground detector and \hat{S} is the shower direction vector defined as pointing back along the shower path. In this expression it is assumed that the shower arrival front is planar. In real situations the shower front curvature must be taken into account. The hybrid Auger detector will use the latter method to determine shower trajectories.

We have reconstructed the geometry of our sample shower within the SDP in terms of R_p and χ_0 using the three methods just described. The results for each method and variable are presented along with the estimated statistical uncertainty in Table 4.1. The time T_{gnd} was obtained from a single 64-counter patch of the MIA detector which registered 56 out of a possible 61 hits. The estimated distance between this patch and the shower core is about 273 meters.

Fitting Method	R_p (meters)	χ_0 (radians)
Mono	2981.1 ± 69.8	1.540 ± 0.044
Angle-Constrained	3089.6 ± 8.2	1.4739 ± 0.0028
Time-Constrained	3117.4 ± 6.4	1.4559 ± 0.0019

Table 4.1: Trajectory comparisons for a sample event using mono, time-constrained, and angle constrained fitting methods. All methods share a common shower detector plane so comparisons are made in terms of quantities R_p and χ_0 .

4.4.5 Shower Shape and Energy

Once the trajectory has been found the next step is to use the PMT signal information to determine the shower size profile and total energy. In principle, a separate estimate of the shower size can be made by each tube seeing the track. A shower profile is then just a plot of these size determinations as a function of the particular atmospheric depth interval viewed by each tube.

If a tube views a linear interval of track l and receives N_{pe} photoelectrons while the shower was in view, then to a first approximation one can estimate the shower size N_e in

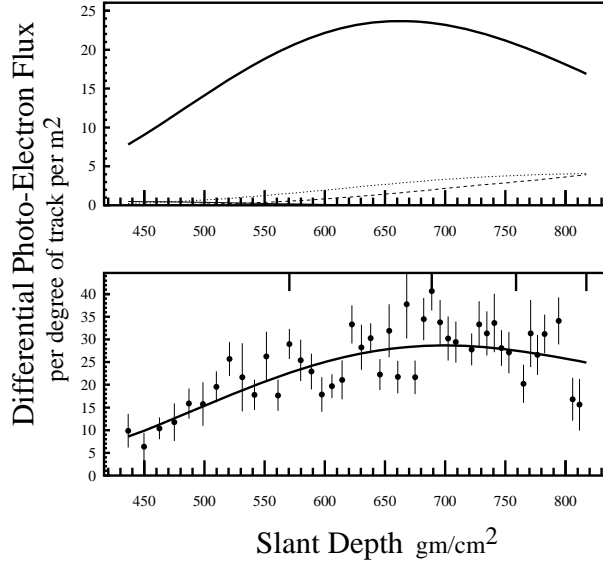


Figure 4.16: Observed light profile and the model estimate for a sample shower observed by the HiRes prototype detector. Lower plot is data with model superimposed. Upper plot is model decomposed into light production and scattering components.

the corresponding atmospheric depth interval by inverting the expression given above in section 4.4.3, to obtain

$$N_e = \frac{4\pi R^2 N_{pe}}{2.4 A \varepsilon l \xi(R)}.$$

In practice, the shower energy and size profile (and X_{max}) are found in an iterative process. First a model shower size profile is chosen, for example the Gaisser-Hillas [125] formulation

$$N_e = N_{max} \left(\frac{X - X_0}{X_{max} - X_0} \right)^{\frac{X_{max} - X_0}{70}} \exp \frac{X_{max} - X}{70},$$

where N_{max} is the size at maximum and X_0 is the depth of first interaction. An initial guess for N_{max} , X_{max} , and X_0 is made. A received light profile is generated incorporating all known light generation and scattering processes. This profile is compared with the observations. N_{max} , X_{max} , and X_0 are then adjusted until the best agreement between generated light profile and observed light profile is reached. In Figure 4.16 the received light profile is shown for our example shower. Each data point in the lower plot is a measure of total light received per degree of track per square meter of mirror area at a given atmospheric depth. The solid line is the anticipated light received for a model shower which is in best agreement with the data. The upper plot shows what the model shower predicts for the contributions from fluorescence light (upper curve), molecular-scattered Čerenkov light (middle curve), and particulate-scattered Čerenkov light (lower curve).

At this point, the best-fit X_{max} has been obtained and the energy in the electromagnetic

component is calculated by integrating the measured shower profile (as given in Sec. 3.2):

$$E_{em} = \frac{E_c}{\lambda_r} \int N_e(X) dX.$$

Our example shower has an estimated energy of $1.39 \pm 0.10 \times 10^{17}$ eV and a depth of maximum of 671 ± 16 g/cm².

Chapter 5

Simulated Performance of the Reference Design

The performance of the Auger Observatory reference design is evaluated using detailed Monte-Carlo simulations. The technical description of elements of the design will appear in later chapters. In this chapter, knowledge of the properties of air showers is applied to determine how data from the experiment will actually look and how it can be analyzed in order to achieve the stated goals of the Auger Project.

The MOCCA air shower simulation program is described first. This code is the basis for most of the predictions concerning the details of extensive air showers. Where possible, data obtained from previous observations of the highest energy cosmic rays by groups such as the Haverah Park, Akeno, and Fly's Eye Collaborations have been employed to verify the simulations.

Next, a description of the assumed parameters of the reference design is given, including both the surface and the air-fluorescence detectors. This is followed by a description of a total simulation program employing MOCCA, a detector simulation, and analysis algorithms, constructed to predict the performance of the surface array. The chapter concludes with a similar discussion of a simulation and analysis procedure for the Hybrid Detector, the integrated surface array and fluorescence detector system.

5.1 Numerical simulations

Numerical simulation of air showers is an essential tool for designing the detector and evaluating its performance. The simulation program needs to be efficient. All Auger Observatory showers produce at least 10^{10} particles. It is computationally prohibitive to simulate so many particles or to record simulated data for so many particles. A viable computer program must have an unbiased method for computing all relevant shower properties using a sampled subset of the full shower. The simulation program must also be accurate in modeling the relevant aspects of particle interactions. It must produce results which are consistent

with those properties of giant air showers which have been measured.

As mentioned in the last chapter, almost all of the relevant physics is well established. Ambiguity in modeling the highest energy hadronic interactions has little impact on evaluating detector performance. The detector resolution concerns differences in measurable quantities (e.g. particle density from a 1.5×10^{19} eV shower vs. density from a 1.0×10^{19} eV shower, or X_{max} for an iron nucleus vs. X_{max} for a proton at the same energy). Such differences in measurable quantities have less model dependence than the quantities themselves.

We have elected to use principally the MOCCA program for the design of the Auger Observatory detectors. This program is described below. We then discuss some aspects of hadronic physics which are addressed by the interaction generator SIBYLL, which can be used within the MOCCA code. Following some comments on the ways in which the nucleus-nucleus interactions are treated, we highlight important verifications of MOCCA using air shower data.

5.1.1 The MOCCA Simulation Program

This program was created by A.M. Hillas for use with the Haverah Park experiment [126]. Variations have since been successfully used by many cosmic ray experiments studying events from 10^{12} eV to 10^{20} eV. The code performs both of the main functions required of an EAS simulation: the generation of the electromagnetic cascade through the atmosphere and the details of individual hadronic interactions and decays.

At the time MOCCA was created, the speed of computers was very slow by today's standards. This program employs novel and efficient methods for generating and following the many particles in large air showers.

Particle production in hadronic collisions is simulated using a splitting technique [127]. The center-of-mass energy in the collision is apportioned between a leading particle and the production of new particles. The energy assigned to new particles is subdivided into four parts. Each part is further split in two, one of which is assigned to a single pion. The process is iterated on the unassigned energy packets until all the energy of the initial interaction is exhausted. The leading nucleon and newly produced pions are tracked until they interact again or decay, as appropriate.

This algorithm produces a spectrum of produced particles in accord with data from fixed-target accelerator experiments. This results both from the nature of the algorithm as well as *a priori* assumptions (e.g., cross sections). Specific features arising naturally from the method [127] include a flat Feynman-x distribution of the leading nucleon, Feynman scaling of resulting momentum distributions, KNO-like charged particle multiplicity distributions whose mean values increase with energy as $\ln(s)$, constant mean transverse momentum, and momentum and energy conservation.

All newly produced particles are assumed to be pions. In reality, roughly 10% of these particles would be kaons. This does not seriously alter the resulting muons, electrons, and photons of the air shower, since the interactions and decays of pions and kaons are similar.

Variations can be made in the algorithm to alter the probability distributions in the assignment of pion energies. Such changes can affect the inelasticity of the interaction and consequently the kinematics of the produced particles. The effect on air shower particles at the ground is not enormous, but it can be measurable. The effects of different variants of MOCCA are described below (cf. Figure 5.2).

It is not computationally possible to follow all the particles in an air shower. MOCCA uses a technique called “thinned sampling” to track semi-randomly selected particles. Those arriving at the ground have associated weights to indicate how many others were neglected in the procedure. For the 10^{19} eV showers used in this work, the weights may be as large as 10^5 or 10^6 . The method allows accurate computation of the total energy arriving at the ground and shower size (i.e. the total number of particles at the ground), but the study of fluctuations requires special care.

5.1.2 The SIBYLL Interaction Generator

As mentioned above, the MOCCA program uses an algorithm to generate the details of hadronic interactions which yields results that match fixed-target accelerator experiments. Certain new aspects of particle production became apparent with the advent of higher energy accelerators such as the CERN proton-antiproton Collider. SIBYLL is a hadron interaction simulator which was developed to address these developments.

SIBYLL is described fully elsewhere [128]. Pertinent to the design of EAS detectors are the following features. Hadron interactions are modeled with parton strings, similar to the algorithms in the Lund Monte Carlo extensively used in analysis of accelerator experiments. The multiplicity increases more quickly (as $\ln^2(s)$) than at lower energy and exhibits violations of the KNO distribution. The proton-proton cross section increases more quickly with energy, there are correlations of transverse momentum with multiplicity, and there is the onset of a “hard part” of the cross section (“minijets”).

These new features of particle production and kinematics match data from the CERN Collider. The onset of these features is made smoothly as the collision energy increases. Thus, SIBYLL produces hadronic interactions which are quite similar to those of MOCCA even when the particle energy approaches 100 TeV. The algorithms differ more as the energy increases. The number of pions produced in an air shower is not substantially different from what would be obtained from MOCCA in its basic form. The main effect of SIBYLL arises from the scaling violations which soften the energy distribution of pions and so ultimately alter the number of muons in the cascade.

SIBYLL can be used within MOCCA instead of the usual algorithm. The difference between the two approaches will occur mainly in the earliest interactions in the showers, after which the energies are reduced to levels where the algorithms give similar results. Figure 5.1 exhibits the distribution of the energies of hadron collisions in proton air showers. Only a small fraction of these occur in regimes where SIBYLL and basic-MOCCA differ significantly.

We thus can expect that features of air showers which do not depend on the first

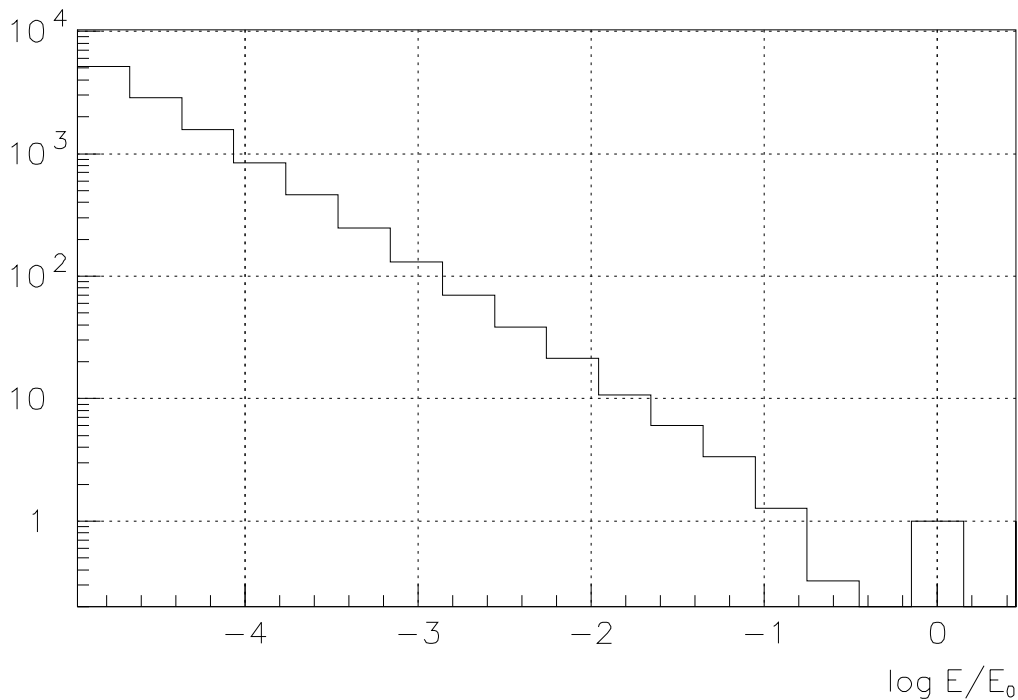


Figure 5.1: The distribution of interaction energies of hadron collisions in proton air showers, expressed as a fraction of the primary cosmic ray energy. This plot shows the highest energies of the distribution, obtained from an average of 100 showers at 10^{17} eV.

few interactions in the cascade will be relatively insensitive to whether the basic MOCCA algorithms or the more sophisticated SIBYLL approach are used. The depth of maximum of the shower is an example of a quantity which does depend on the location and features of the first interaction. X_{max} has been shown to be rather different when SIBYLL is employed. On the other hand, the total number of charged particles at the ground is not greatly changed. The number of muons at ground level shows somewhat more sensitivity to the choice of hadron interaction algorithm. (Ground particle differences are discussed further in Sec. 5.1.4 below.)

Finally, it must be considered that there is uncertainty in extrapolating the dynamics of particle interactions to the highest energies. The predictions of the MOCCA program, with or without SIBYLL, will be affected by the choice of extrapolation. Some interesting propositions can probably be tested by analysis of the structure of air showers. But it must also be stressed that only a limited set of basic shower characteristics are necessary to properly design a detector to achieve the stated goals of the Auger Project. These characteristics, such as the lateral distribution of particles and the timing structure of the shower front, derive mainly from the lower energy interactions in the shower. They are not greatly affected by reasonable alternative physics assumptions [84]. This, and the demonstrated good agreement with existing data (discussed below), leads us to conclude that the features of air showers most critical to the design of the detector can be confidently predicted using

MOCCA.

5.1.3 Nucleus-Nucleus Interactions

It is more difficult to construct algorithms which simulate the details of nucleus-nucleus collisions than it is to model proton-nucleus interactions. A simple approximation which is often used is the *superposition model*. In this approach, the interaction of a primary nucleus with A constituent nucleons and total energy E is modeled as A independent single nucleon collisions, each with energy E/A .

It has been rigorously shown [129] that this approximation will correctly produce the average values of “additive” quantities in air showers such as the total muon or electron numbers at the ground. The fluctuations in these same quantities will however be underestimated. Note that the depth of shower maximum is not an “additive” quantity in an atmospheric cascade.

The dynamical modelling of MOCCA in Auger Observatory simulations is more realistic than that of the simple superposition model. Firstly, it is to be emphasized that the SIBYLL interaction code simulates hadron interactions only. SIBYLL, whether employed in MOCCA or in the context of other air shower programs, is usually augmented with auxiliary code which generates features of nucleus-nucleus interactions in a somewhat more sophisticated manner than the simple superposition model. The fragmentation of nuclei during collisions and the cross sections of nuclei-on-nuclei are modeled after accelerator data. The interaction is thus reduced to a set of individual nucleon-air collisions which are simulated by SIBYLL.

5.1.4 Comparison to Data

The MOCCA simulation reproduces many characteristics of air showers measured by ground arrays. One very important feature of EAS is the lateral distribution of particles. Figure 5.2 shows the results of the simulation compared to data from the AGASA experiment. While the reference design of the Auger Observatory differs significantly from the hardware of the AGASA array, comparisons between the simulation and this experiment are more direct. Results of detector simulations using MOCCA air showers and the Auger Observatory reference design detector were shown in the last chapter and more will be discussed in the next.

Figure 5.2 shows several separate simulations done with MOCCA under a variety of assumptions. Results for three variants of the code are shown. One is the original MOCCA algorithm. Another is a more recent version of the code called “MOCCA92” which incorporates some slight changes in: pion transverse momentum distributions (harder), proton-air collisions elasticity (more elastic), and multiplicity of some interactions (higher). Finally, a variant using MOCCA92 and the SIBYLL interaction generator is shown, which also employs some small updates in various secondary hadron cross sections. All three simulations were done using 10^{19} eV oxygen nuclei as the primary cosmic rays in order to account for

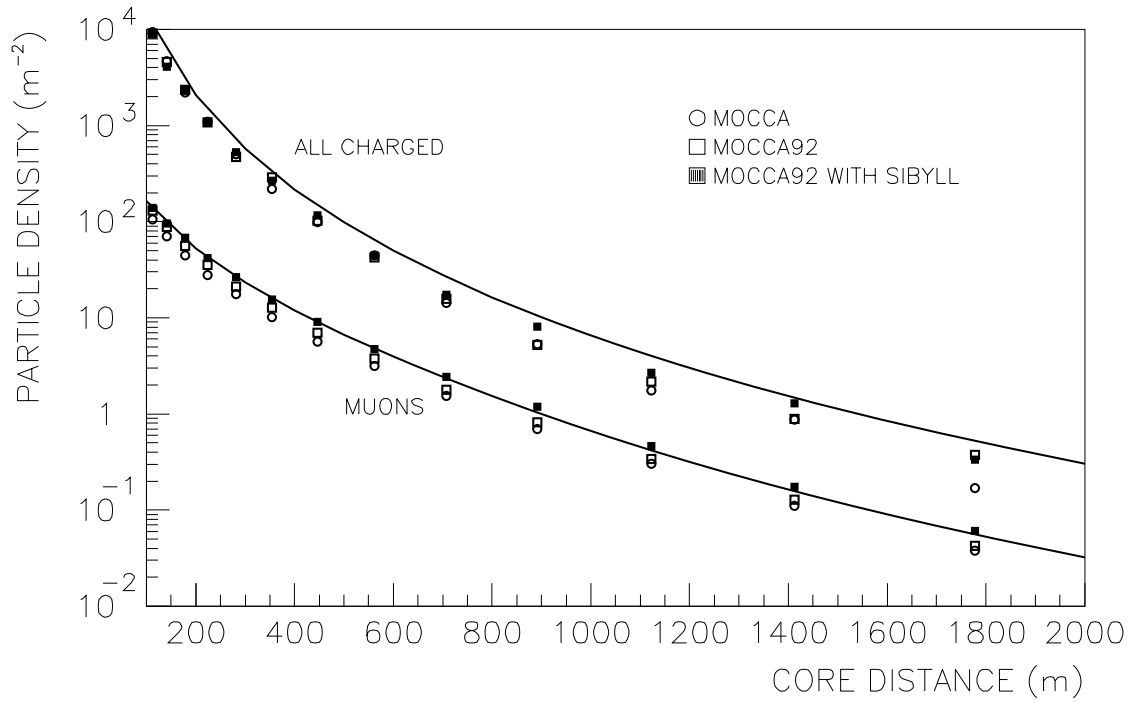


Figure 5.2: Lateral distributions of electrons and of muons from MOCCA simulations of 10^{19} eV oxygen showers. Three different interaction models are indicated: original MOCCA, the modified MOCCA92, and MOCCA92 with the SIBYLL interaction generator. Points are simulations, solid lines are published fits of the Akeno data. The upper curve and points are all charged particles, the lower for muons only.

the fact that the cosmic rays seen by Akeno are probably neither purely protons nor purely iron. While differences are evident, there is generally good agreement between data and simulation, especially for the muons.

The MOCCA92-SIBYLL version best matches the muon lateral distribution data. The different physics assumptions inherent to the three variants of the code result in systematic differences of as much as 60% in the muon densities. Given that the density itself varies over more than 5 orders of magnitude over the lateral range examined, such differences do not seriously alter the design of the array. These differing results should be interpreted as indicating the degree to which “reasonable” variations of the physics assumptions affect the predictions of the simulation programs.

The arrival time of particles at the ground is another aspect of air showers of great importance in the technical design of a detector. The shower front has a roughly conical shape. The MOCCA prediction for the delay times of particles (relative to a planar shower front) as a function of core distance is given in Figure 5.3. Also shown is a parametrization of this quantity obtained from fits to the Akeno data [130]. There is excellent agreement between the simulation and the data from 30 m to 3 km from the core (The Akeno fit is not intended to be valid at closer core distances). Similar good agreement is found when

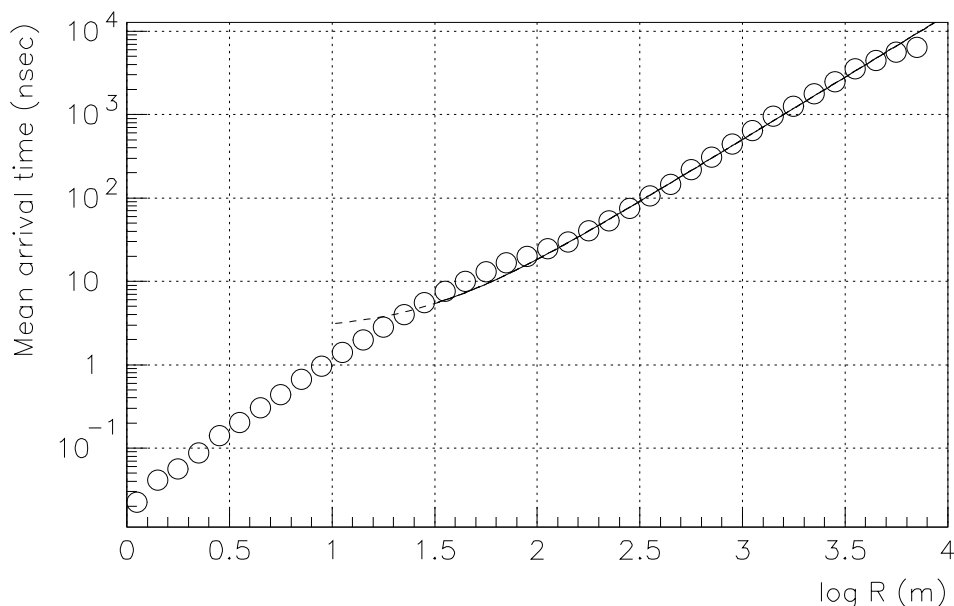


Figure 5.3: Mean arrival time of charged particles with respect to those at the core, from MOCCA simulations of 10^{19} eV proton showers. The solid line is a published fit of Akeno data.

comparing the r.m.s. spread in arrival times between MOCCA and the Akeno data.

Having confidence in the ability of MOCCA to properly represent the time structure of the shower front, we use the results of the simulation to guide the design of the detector electronics. Figure 5.4 gives information from MOCCA on the thickness of the shower front. It can be seen that particles will be arriving over a span of several μs , with the muons arriving earliest. As a more extreme example, MOCCA predicts that a $20 \mu\text{s}$ wide window contains virtually all the particles in the shower front of a 10^{21} eV event at 3.5 km from its core. The majority of the data will be at a lower primary energy and the particles will span a smaller time interval (see Fig. 5.13 in Sec. 5.2.4 below).

5.1.5 Ongoing studies

Many of the most important features of air showers relevant to the design of the Auger Observatory are insensitive to all but the most extreme variations of the details of the interaction models used in the simulations. For example, while the multiplicity of charged particles produced in hadron interactions is uncertain at the highest energies, the shower size at the ground has been found to be unchanged by “reasonable” extrapolations of lower energy data. Characteristics of the muons at ground level do show possibly measurable effects, as discussed previously, but in most cases not of a sufficient magnitude to seriously alter the conclusions arising from the simulation studies described here.

Similarly, aspects of air showers relevant to air fluorescence detection, such as X_{max} ,

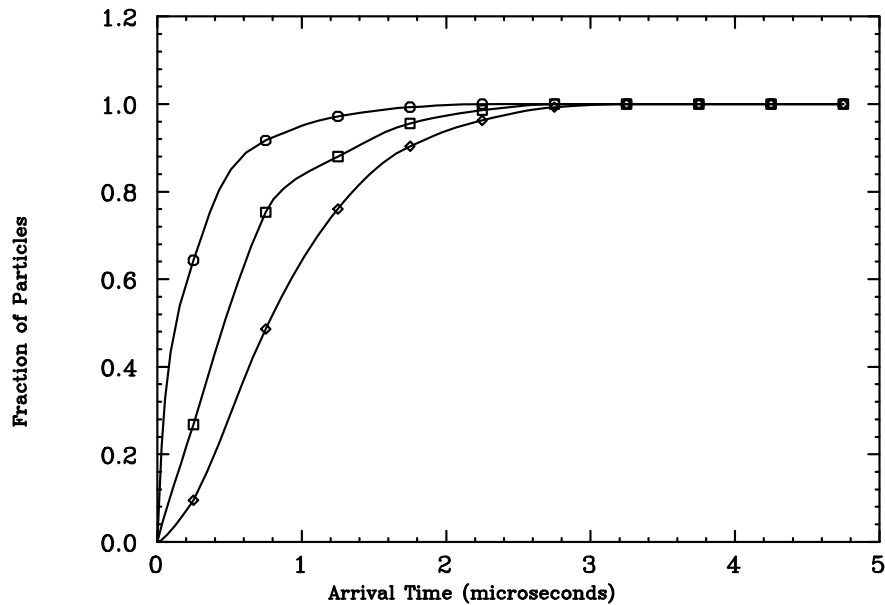


Figure 5.4: Integrated arrival times of charged particles with respect to those at the core, from MOCCA simulations of 10^{19} eV proton showers, sampled 900 m from the core. The three curves indicate respectively the muons, photons, and electrons. The muons arrive the earliest. Solid lines are to guide the eye.

have also been studied to examine their behavior under different physics scenarios [84]. Except under very extreme models, the design of the detector is not affected by such changes.

An ongoing program has been organized to compare different simulation codes, to produce more efficient drivers, and to develop the most realistic interaction models.

5.2 Surface Detector Simulation

This section describes how the ground array is expected to function and fulfill the triggering and performance requirements set forth in earlier chapters. First, we describe some elements of the Auger Observatory reference design used in the simulations which follow. Then, a summary is given of air shower characteristics which are important for our design. Next, a detailed simulation of the water Čerenkov tank system is given with attention paid to how the simulations are checked against earlier data. Finally, simulations are used to gauge the ability of the analysis algorithms to reconstruct the energy, direction, and composition of cosmic rays.

Calculations of the performance of a Hybrid detector (a surface array and fluorescence detectors as an integrated device) have been done independently of the simulations of the reference design surface array by itself. This work is given in a later separate section.

5.2.1 Detector description

Water Čerenkov detectors have been selected as the technology for the Auger Observatory surface array. This device consists of a volume of clear water acting as a Čerenkov radiator viewed by one or more photomultipliers. We have assumed a cylindrical detector 1.2 m deep with a top surface area of 10 m^2 (a radius of 1.8 m). The depth is a nominal value which allows a direct comparison with the existing experimental data from Haverah Park. We comment later (Section 5.2.5) on how a deeper tank may be useful for muon identification.

The volume of water is viewed from above by three large (200 mm diameter) photomultiplier tubes. The PMTs are placed at 120° intervals on a circle of radius 1.2 m ($2/3$ of the detector radius), looking downward from the top surface of the tank. The inner walls of the tank have a diffusively reflective white surface. The detectors are assumed to be arranged on a triangular grid with 1.5 km spacing between each station and its nearest neighbors.

5.2.2 Air Shower Structure

The performance of the detectors is sensitive to the detailed characteristics of the air shower particles. Before considering the details of a detector simulation, the air showers themselves are examined. The MOCCA simulation program which was described in the last section is used for this purpose. Good agreement was shown between the simulation and data from the Akeno experiment, demonstrating that MOCCA gives reliable predictions of air shower particles prior to their entering the detectors.

Features of the energy and arrival times of particles in the shower front are presented first, followed by discussion of the observable differences between showers initiated by protons and those from iron nuclei.

Particles in the shower front

A water Čerenkov tank differs significantly from other types of detectors (e.g. plastic scintillator or RPCs) in the way it responds to air shower particles. This kind of device will be relatively more sensitive to muons. To understand why, it is necessary to consider detailed features of the particles.

At ground level, far from the core of an EAS, the shower front consists of gammas, electrons and muons. There is also a flux of (evaporation) neutrons which are generally sub-relativistic and so are delayed with respect to the main shower front, and large numbers of atmospheric Čerenkov photons. The relativistic hadron flux is negligible beyond 50 m from the core.

The muons and electromagnetic particles have very different energies. The distributions shown in Figure 5.5 were obtained from MOCCA simulations of vertical 10^{19} eV proton showers, sampled 900 m from the shower core. A typical muon has an energy of about 1 GeV, while the majority of electrons and gammas are below 10 MeV. Note that electromagnetic

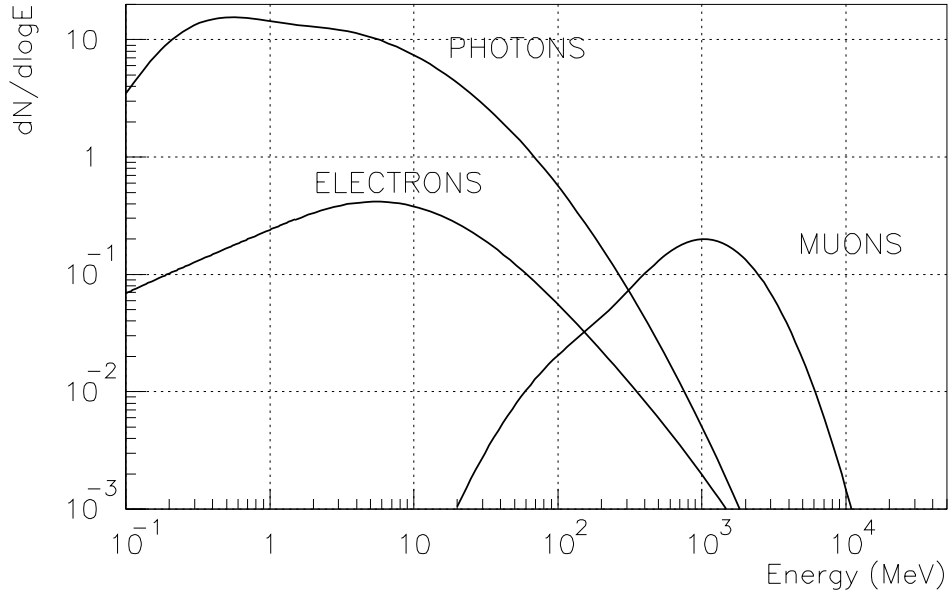


Figure 5.5: Distribution of particle kinetic energies at the ground for 10^{19} eV proton air showers, from MOCCA simulations. Ground level is taken to be 1000 g/cm^2 and particles are sampled at a core distance of 900 m.

particles greatly outnumber muons within a few kilometers of the core.

As a consequence of their higher energies (and masses), air shower muons travel much further than electrons in water. Thus, they produce a great deal more Čerenkov light in the tank. Despite their relatively small contribution to the total number of particles at the ground, muons can dominate the signals obtained from water Čerenkov detectors (recall Figure 4.2).

Figure 5.6 shows the correlation between the energy, density, and arrival times of different particle types from a set of simulated showers with the same properties as in the previous figure. Electromagnetic particles suffer significant scattering and energy loss during the course of the shower, resulting in effective “path lengths” to the ground much longer than straight line trajectories from the shower axis. Thus muons, in addition to having higher energies, also arrive earlier and over a much shorter period of time than the electromagnetic particles. These features help distinguish muons from electrons and photons, which will be useful in the study of cosmic ray composition. This is described next.

Shower features related to primary type

Muons in air showers are expected to show particular sensitivity to the nature of the primary particle. Showers initiated by iron nuclei have significantly more muons than do proton induced showers of the same energy. It is therefore useful to carefully consider the properties of air shower muons which will be relevant to their detection. The predicted numerical

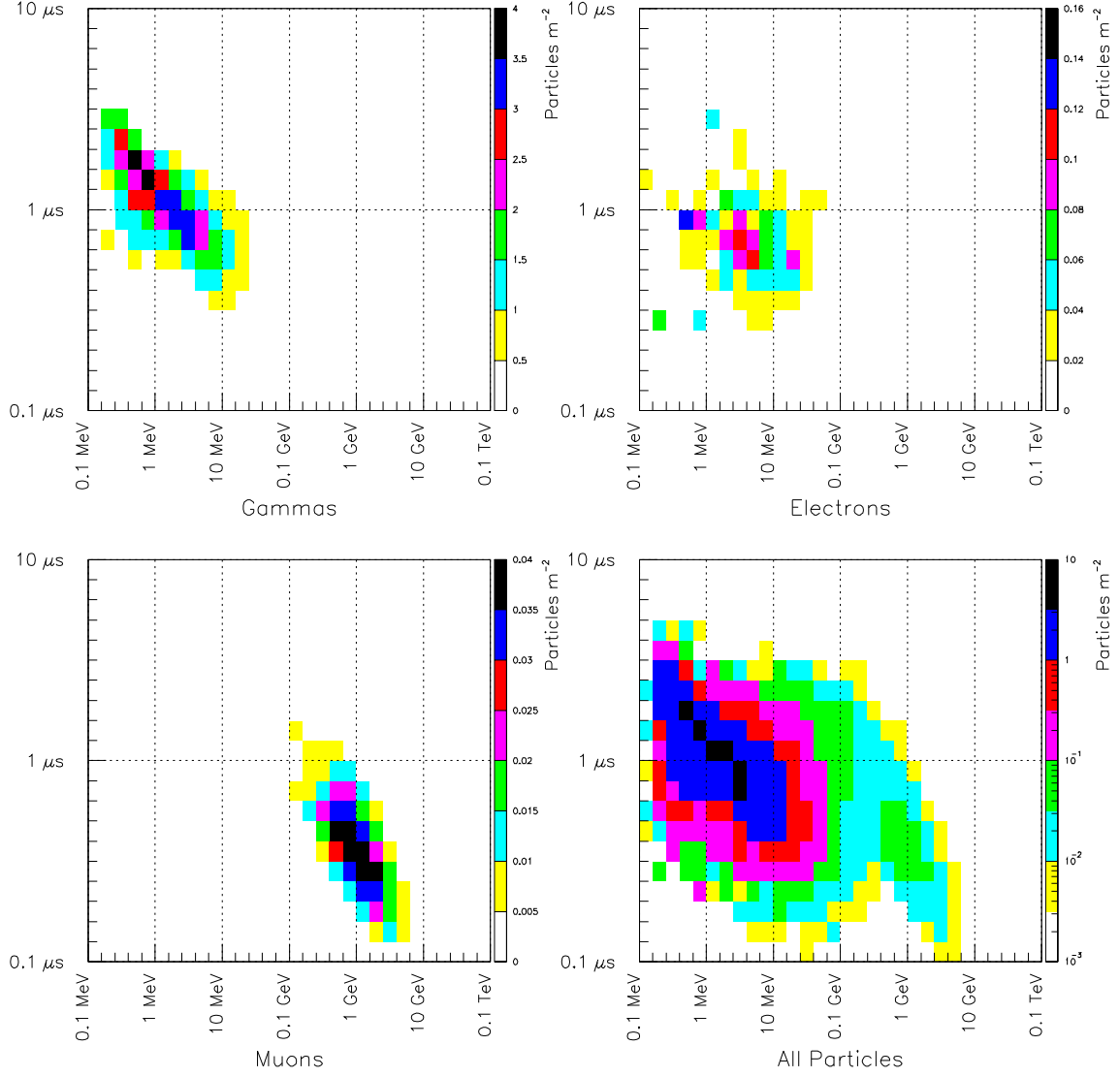


Figure 5.6: Correlations between energy, arrival time, and density for shower particles at 900 m from the core of a vertical 10^{19} eV proton initiated EAS, from a set of MOCCA simulated showers. Observation level was taken to be 1000 g/cm^2 atmospheric depth (near sea level). Note that the density scale for the all particles plot is logarithmic to allow the muons to be seen on the same scale as the electromagnetic particles.

densities of muons, electrons, and photons at sea level in 10^{19} eV proton- and iron-initiated air showers are shown in Figures 5.7(a) and 5.7(b).

At ground level the differences (other than the total number of muons) between iron and proton showers are relatively small; Figure 5.7c shows the predicted numerical density ratio of the shower component particles for iron and proton showers. The electromagnetic densities are similar, but there are $\geq 75\%$ more muons in the iron showers at the core distances of interest (≥ 1 km). Although the absolute number of muons for a shower of given energy and primary type is somewhat dependent on the details of the hadronic interaction model, the *ratio* of the densities of proton and iron showers is much less model dependent.

The amount of Čerenkov light generated per muon is very different than the amount generated per electron. In 1.2 m depth of water a large fraction of the muons will “punch through” the detector volume. However, the majority ($\geq 90\%$) of the electromagnetic energy will be absorbed (the mean free path of gammas in water is ≤ 0.5 m). Additionally, Čerenkov light yield is only proportional to energy loss for particles which are fully relativistic, which is not true for much of the total electromagnetic track length. For these reasons interpretation of the light yield recorded by a water Čerenkov array must rely on comparison with shower and detector simulations to ultimately determine the shower energy. (In fact all EAS detectors are dependent on shower and detector modeling for event energy reconstruction). Roughly speaking, the water Čerenkov signal density is proportional to the sum of muon *number* density (multiplied by the average muon energy loss) and the electromagnetic *energy* density.

Earlier (section 4.2.3), the ratio of muons when compared to electromagnetic particles was shown to be useful in the study the primary composition. Determining the fraction of the signal due to muons on the basis of pulse height will only be practical at large core distances where the density of electromagnetic particles is not so high as to overwhelm the muon signals. In a 5×10^{19} eV shower there will be ~ 5 detectors in the core distance range where the particle density is appropriate. Figure 5.7d shows the predicted proportion of electromagnetic “fake muons” – electrons or photons whose signal has fluctuated upward so as to resemble that typically expected from a muon. At core distances ≥ 1 km this fraction is $\leq 10\%$. The potential for accurately determining the fraction of muons among all the particles striking a detector is also dependent upon the proportionality of the detector response: the signal from each particle must be closely proportional to the Čerenkov light released.

5.2.3 Detector Simulation

A simple but very fast Monte Carlo simulation of the response of a cylindrical water Čerenkov detector to incident gamma, electron and muon particles has been written. Air shower particles from the MOCCA program are passed to this simulation to assess the response of the surface array. This section gives the assumptions used to model physical processes in the detector, the methodology of the procedure, and finally the results and analysis of the simulated air shower events.

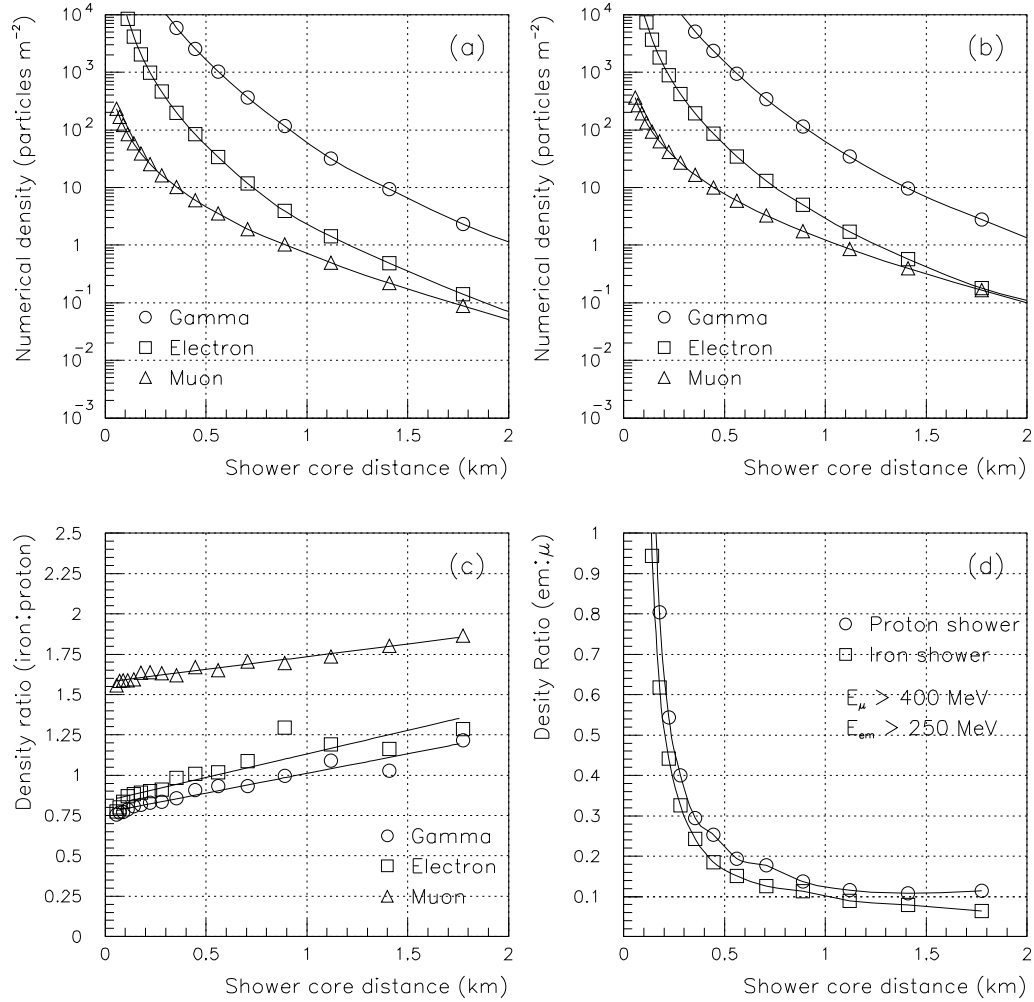


Figure 5.7: Predictions of shower front characteristics from the MOCCA EAS simulation program, without detector simulation. (a) shows the lateral distribution of an average vertical 10^{19} eV proton shower; (b) is identical but shows an average iron shower. Atmospheric depth is 1000 g/cm^2 ; (c) shows the ratio of (b) to (a) as a way of comparing properties of proton and iron showers at this energy; (d) is the number of electromagnetic particles which will produce a burst of Čerenkov light in a 1.2 m deep detector equal to that from a penetrating muon, shown as a fraction of the number of penetrating muons.

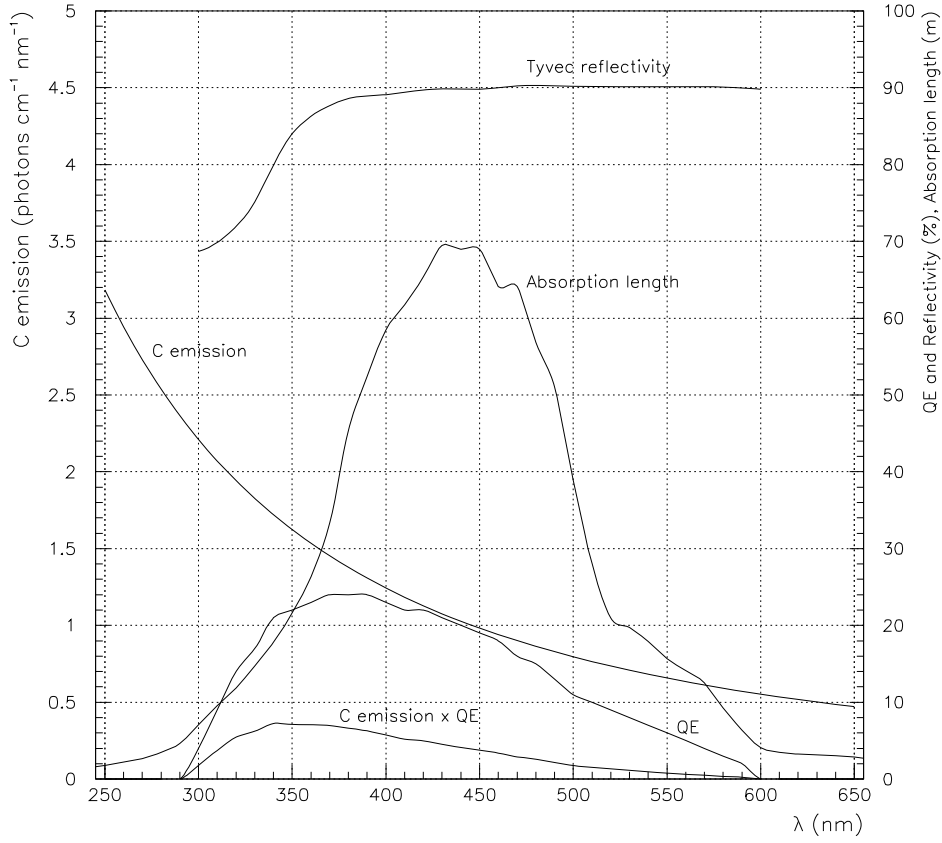


Figure 5.8: Some important spectral characteristics for a water Čerenkov detector. The quantum efficiency shown is for a bi-alkali photocathode. Absorption length is for ultra-pure water. Tyvec is a plastic material which may be used as a lining for the tank; see Chapter 7 for further details.

Čerenkov Radiation

Čerenkov light is produced by a charged particle moving through a transparent medium with velocity $\beta \geq 1/n$, where n is the refractive index ($n = 1.33$ for water). Hence a particle must have a kinetic energy greater than half its rest mass energy to radiate Čerenkov light (0.25 MeV for electrons and 73 MeV for muons). The angle of emission is $\theta = \cos^{-1}(1/\beta n)$ with respect to the particle trajectory: 41° for a fully relativistic particle in water.

The yield of Čerenkov photons with wavelengths between λ_1 and λ_2 for a small element of particle track dx is given by:

$$\frac{dN}{dx} = 2\pi\alpha \left(\frac{1}{\lambda_1} - \frac{1}{\lambda_2} \right) \left(1 - \frac{1}{\beta^2 n^2} \right),$$

where α is the fine structure constant. Figure 5.8 shows the Čerenkov emission spectrum for water calculated on the basis of the above equation.

Material Characteristics

The choices of the various elements of the reference design surface detector are described in detail in the next chapter. Reviewed here are some elements which are especially pertinent to the simulation.

In Figure 5.8 photomultiplier quantum efficiency¹ is shown as a function of photon wavelength. The convolution of quantum efficiency and the Čerenkov emission is also shown. Clearly the wavelength region between 300 and 500 nm is crucially important. The spectral diffuse reflectivity of a material called Tyvec², a possible interior lining material of the detector tank, is shown. Finally the absorption length of pure natural water is shown³, and is seen to exceed 10 m across the wavelength range of interest.

The spectral characteristics of the scattering (Mie scattering) and absorption of light in water containing particulate impurities are functions of the numerical density, size spectrum, and composition of the impurity particles. Values below the ultra-pure curve shown in Figure 5.8 are expected for water whose quality is practical for this application. Behavior varies greatly depending on the source and purification processing of a particular water sample. See Chapter 7 for further discussion, and some preliminary measurements.

The complexity of the spectral dependence of the net absorption length of water requires that it be measured specifically for any samples of water used in a detector. So details such as assigning each Čerenkov photon a wavelength sampled from the emission spectrum have not so far been explicitly included in the simulations. Instead (and also to speed up the simulation process) the number of Čerenkov photons emitted for each particle track increment is set equal to the integral of the convolution of the emission and detection characteristics. Fixed water absorption length and lining material reflectivity are assumed. The validity of this approximation depends upon the extent to which these values vary over the spectral range of interest (300 to 500 nm) in combination with the size and geometry of the detector. Further work on this point is in progress.

Other approximations regarding the physical parameters of materials have been made for the purposes of simulation. The numbers used represent average or effective values over the range 300 to 500 nm, and are believed to be realistically achievable. Here, a summary of the numerical values used in the simulation:

- 15% photocathode quantum efficiency;
- 85% reflectivity of the tank lining material;
- 7 m water absorption length;

¹Taken from the Hamamatsu R1408 data sheet. This is a hemispherical PMT 200 mm in diameter in a borosilicate glass envelope which was used in the IMB experiment.

²The curve shown is for light incident at 30° to the normal, but there is little angular dependence. Measurements made by Surface Optics Corp. for UCI School of Physical Sciences.

³Taken from a 1981 review of the available data[131]

- 10% : 90% split between perfectly specular and perfectly diffuse reflection behaviour for photons reflected from the lining material. (It turns out that the split ratio assumed has little effect on the results).

It is to be emphasized that to a very good approximation the assumed parameter values affect only the absolute photoelectron yield for a given incident particle. They do not affect the validity of the comparisons with experimental data discussed in Section 5.2.4 below, where simulated detector calibration has been carried out.

Detector Simulation Algorithm

The full simulation of the response of the Auger Observatory surface detector array has three distinct elements: production of air shower particles using MOCCA, calculation of the detailed response of the water Čerenkov detectors and electronics, and the construction of realistic event triggering.

The MOCCA program was described above. Recall that an important aspect of this code is the *thinning* of the shower in order to keep the computation time manageable. Only a very small fraction of the total number of air shower particles, each with a large weighting factor, are provided by the simulation. The number of particles provided is very small at core distances (> 1 km) typical of events in the array.

To remove such artificial fluctuations due to small numbers, individual MOCCA showers are not used to create individual events. Rather, sets of showers are run under fixed conditions, the weights summed, and then averages are taken. This has the unfortunate effect of also averaging out the physical fluctuations due to variations in the atmospheric depth of the first interaction point and shower development. (Note that a different simulation procedure will be employed in simulations of the so-called Hybrid system, a combined surface array - optical detector described later).

Batches of 100 showers have been generated for proton and iron nuclei primaries at 0° , 30° , 45° and 60° zenith angles. All the simulations are for primary energy of 1×10^{19} eV and an atmospheric depth at ground level of 1000 g/cm^2 . The energy threshold at which particle thinning commenced was 10^{-6} of the primary energy (10 TeV).

The generation of simulated experimental data is then done in the following steps:

- Output from the averaged MOCCA showers is in the form of a ground particle list giving particle type, impact coordinates, trajectory, thinning weight, and energy. Each particle is projected onto the plane perpendicular to the shower axis passing through the core impact point and then binned into a 5-dimensional array to give differential energy/time/density breakdowns for each particle type at given core distance. (Figure 5.6 was an example of the information in the annular bin centered at 0.9 km from shower core). It is not practical to further subdivide the ground particles into other categories (e.g., their trajectory angle) because of the limited computational statistics.

- To generate individual showers for a particular primary type and zenith angle a random azimuthal angle and core impact position are selected and a shower projected onto the simulated array grid. For each detector the core distance in the shower plane is calculated and the pre-determined density array re-sampled to generate a list of shower particles striking that detector, each particle being assigned impact coordinates, an energy, and an arrival time. By sampling over an area in the plane of the detector top surface (but larger), all “corner clipping” effects are automatically included.
- The detector simulation program is invoked using the lists of particles striking the detectors. Each particle is tracked through the detector volume, interacting and radiating Čerenkov light. The resulting photons are ray-traced until absorbed in the water, upon reflection, or at a PMT. A list of photoelectron release times is updated for each detector.
- The photoelectron lists are used to construct simulated amplitude versus time profiles for the summed signal from all tubes. Care is taken to represent the effects of the electronics. This profile is then scanned and an *alert* condition is imposed to simulate the lowest level (hardware) trigger of an individual detector station. A GPS event time stamp is generated which reflects the fluctuations of the trigger time relative to the shower plane arrival.

The simulation of the Čerenkov photons in the detector is illustrated in Figure 5.9. Here, the propagation of the individual photons from a single penetrating muon is shown. All the particles in the air shower which strike detectors are simulated in this manner.

Figure 5.10 shows the final output of the simulation process for a single shower. The data thus generated is then available for event reconstruction and comparison with experimental data. Note that because the shower input data from MOCCA has already been averaged, intrinsic shower-to-shower fluctuations will not be reproduced. However, all detector imposed limitations due to limited size, non-proportionality, etc., are modeled in this procedure.

Note also in the lower part of Figure 5.10 that muons give large, narrow pulses. The more numerous electrons and converted gammas tend to yield smaller pulses individually, but these overlap and add together giving a broad baseline pulse, especially near the core. The ability to distinguish muons by their signal characteristics is one component of methods to evaluate the nature of the primary particle causing the air shower.

5.2.4 Comparison of Simulation and Data

To check the validity of the shower and detector simulations, their predictions have been compared to experimental results from the Haverah Park array. Since the reconstruction of the lateral distribution of particles is central to all analyses from the surface array, substantial attention is devoted to this topic here. It will be shown that the simulation reproduces many details of the data.

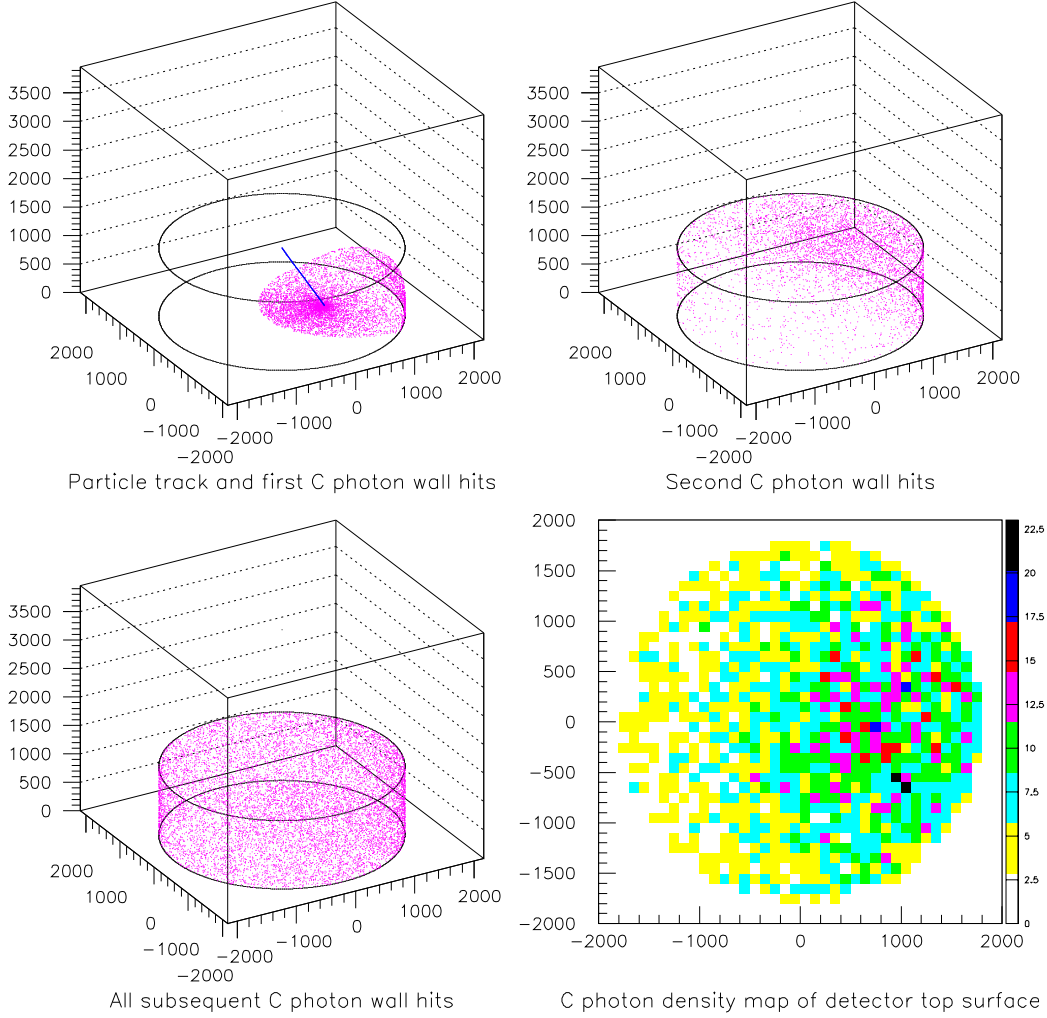


Figure 5.9: Simulation display for the reference design water Čerenkov detector unit. A single 1 GeV muon was injected at the center of the top surface traveling at 30° to the vertical. The upper left plot shows the incident particle track and the positions where the Čerenkov photons released first reflect from the tank walls. The upper right plot shows the positions of the second photon reflections. Reflections continue until the photons have been absorbed in the water or by the tank lining material; all reflection positions after the second are shown in the lower left plot. The distribution of reflection positions over the detector top surface integrated over all reflections is quite uniform. At lower right a density map of the detector top surface is shown.

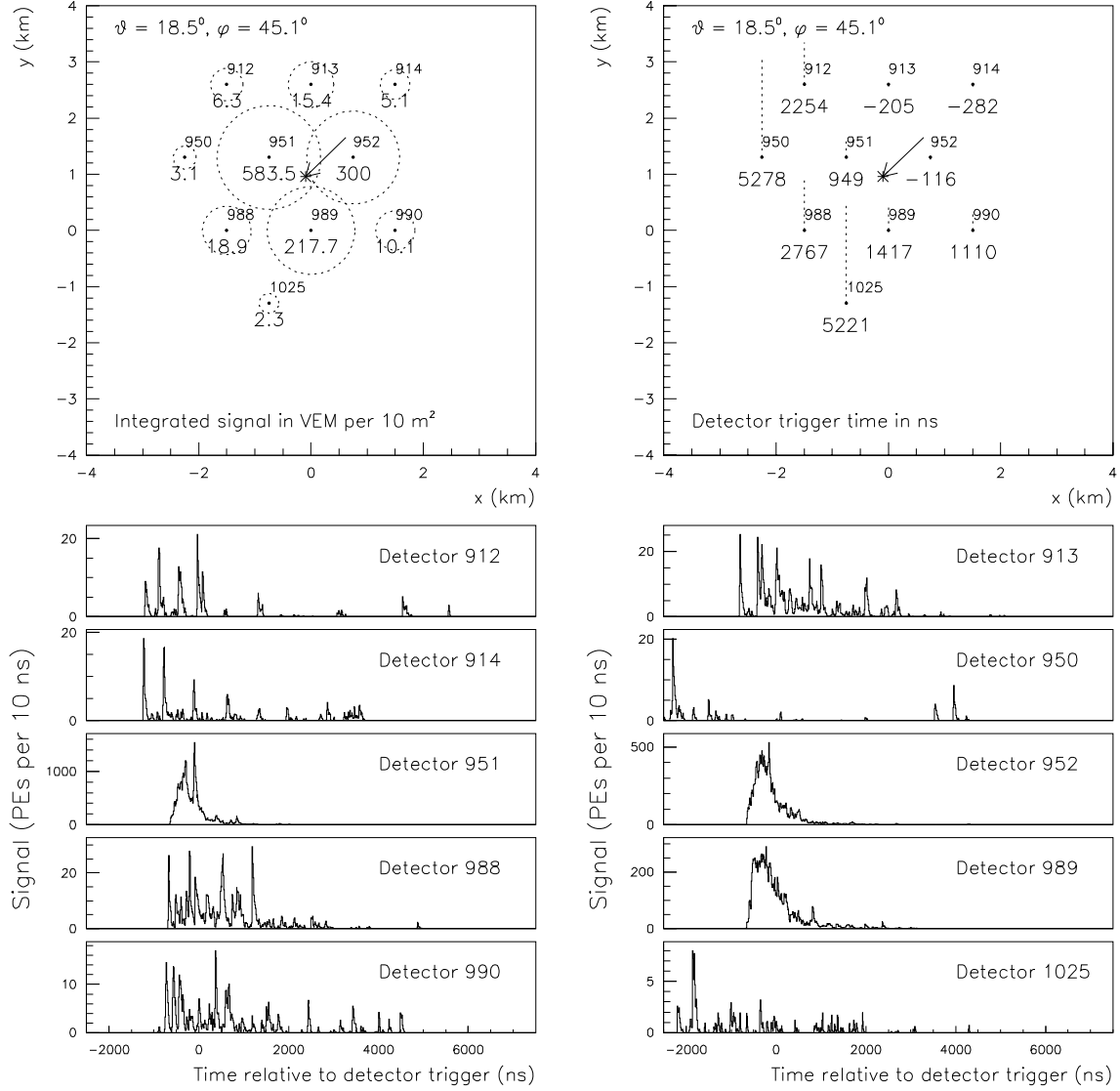


Figure 5.10: Illustration of a simulated EAS event falling on the reference design Auger Observatory water Čerenkov surface array. The shower was initiated by a 6×10^{19} eV iron nucleus incident at a zenith angle of 19° . The top left plot shows a ground plane signal density map, the radius of the circles being proportional to the logarithm of the time integrated signal. At top right is a map showing detector trigger times, the length of the vertical lines indicating the time relative to shower core impact. The lower part of the plot gives the time/amplitude signal profiles for each triggered detector — note the differing vertical scales.

Sets of showers have been run for various primary types and zenith angles using the procedures described above. Each of the Monte Carlo data sets presented in this section is the product of such a run. Event reconstruction errors have not been included at this point, the exact core distance being used to analyze the simulated measurement of particle lateral distributions. Note that one should not expect perfect agreement between the simulated events and the Haverah Park data since the simulated detector unit is not the same size and shape as the Haverah Park units. However, for the present case these effects will contribute second order discrepancies only.

Lateral distribution shape

In the last chapter (section 4.3.1), the lateral distribution function observed by the Haverah Park experiment was described. To review, a good fit to that data was empirically found to be a modified power law function:

$$\rho(r) = kr^{-(\eta + \frac{r}{4000})}, \quad (5.1)$$

where shower core distance r is in meters, k is a normalization parameter, and η is given by

$$\eta = 3.49 - 1.29 \sec \theta + 0.165 \log \left(\frac{E}{10^{17} \text{ eV}} \right) \quad (5.2)$$

where θ is the shower zenith angle, and E is the shower energy.

The signal density $\rho(r)$ is expressed in units of vertical equivalent muons per square meter (VEM m⁻²), obtained by dividing the total observed signal by the average value from a vertical through-going muon. Use of this density unit allows simple calibration of water Čerenkov detectors using background muons. The slope parameter η is a function of zenith angle θ and, to a minor extent, shower energy.

For the highest energy showers, Equation 5.1 is replaced at $r > 800$ m by the modified expression

$$\rho(r) = kr^{-(\eta + \frac{r}{4000})} \left(\frac{r}{800} \right)^{1.03}. \quad (5.3)$$

Equations 5.1–5.3 were seen to do an excellent job of describing data over the the entire measurement range (in the last chapter, Figure 4.6).

Figure 5.11 compares sets of Monte Carlo events with the Haverah Park experimental parameterization. Two cases are shown here, one for proton and the other for iron primaries. Each set was incident vertically and had primary energy of 10^{19} eV. The lateral distribution shape given by Equations 5.1 and 5.2 has been used in fitting the normalization constant k in the region $400 < r < 800$ m. For $r > 800$ m the flattened extension given by Equation 5.3 is shown, but this data was not used in the fit. The qualitative agreement in the shape is good, particularly for the iron primary simulations. This is shown on the right side of the figure where the ratio of the simulation points to the Haverah Park function is given. (Note that there is a slight overall normalization offset in the ratio plots; see the discussion of the parameter r_k in the next part of this section.)

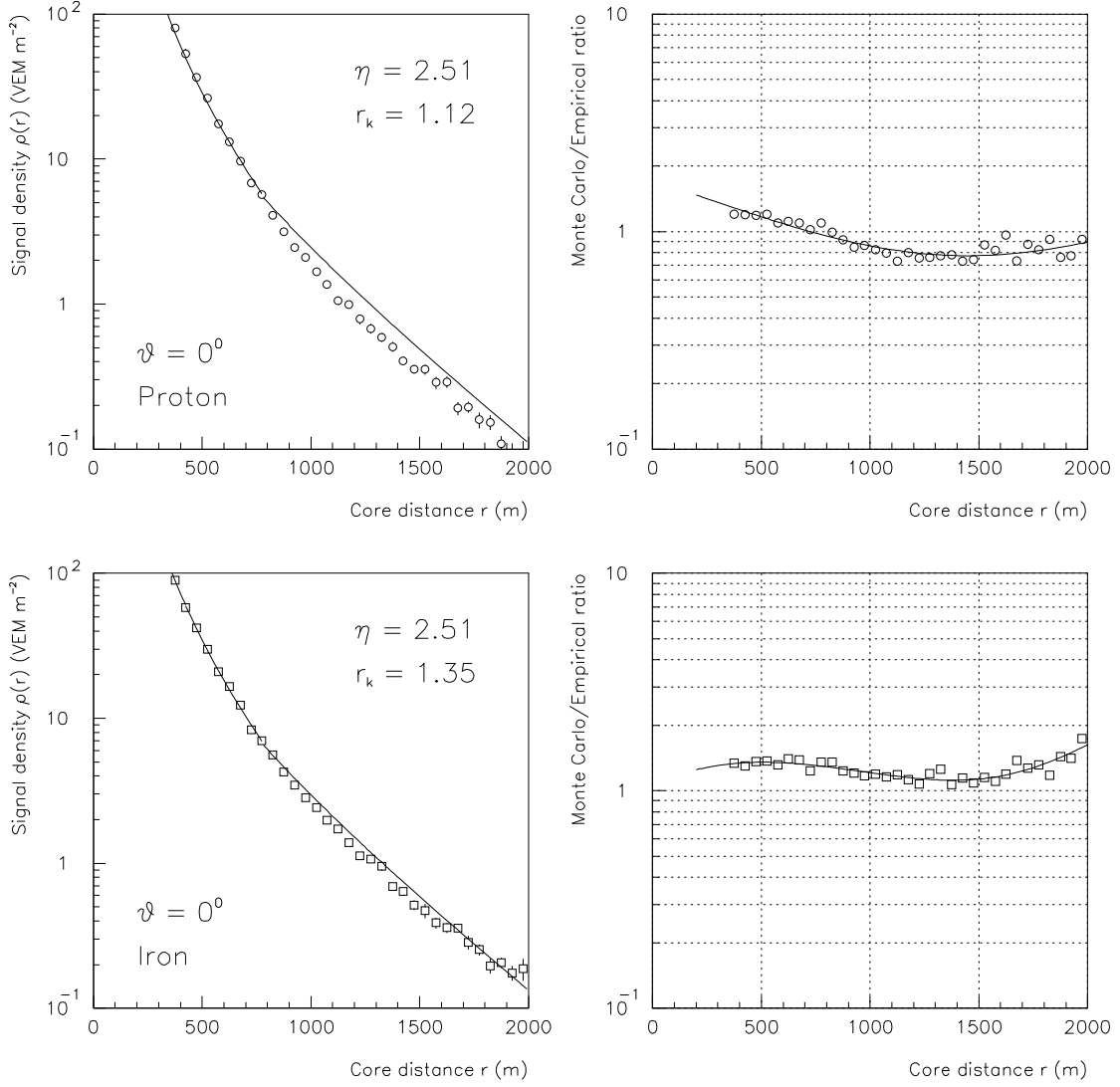


Figure 5.11: Left, comparison of simulated lateral distribution against measurements from the Haverah Park array. The points are Monte Carlo predictions for 10^{19} eV EAS, the lines experimental parameterizations given by Eqns. 5.3-5.2 in the text. The lateral distribution functions were computed using the indicated values for the slope parameter η and normalization correction r_k (see text and Table 6.1). On the right side, the ratio of the simulated points to the function; here, the lines are only to guide the eye.

As in the previous figure, Figure 5.12 shows comparisons for iron and proton primaries, except here the results are given at various zenith angles. The shower-plus-detector Monte Carlo reproduces the change in slope parameter η with increasing zenith angle θ . When showers are observed at increasing angles from the vertical, and hence at greater atmospheric depth, the lateral distribution “ages” or flattens, i.e. the slope parameter η decreases. Note that at large zenith angles protons and iron showers of a given energy produce very similar lateral distribution shapes. This is expected since the electromagnetic cascade has been almost entirely absorbed. The shape of the muon distributions in the two kinds of shower increasingly resemble one another as showers age beyond their maxima. The ability of the simulations to reproduce so well the change of η with zenith angle is a very encouraging result.

It is also seen in Figure 5.12 that the Haverah Park lateral distribution function appears to show slightly better agreement with the simulated iron showers than with the proton ones. This may be interpreted as a feature of the shower Monte Carlo rather than a real physical result. As discussed earlier, the number of muons at the ground is affected by the choice of hadronic model. This effect is not enormous but variations in the modeling may be sufficient to produce a better fit for proton primaries; further investigation is required. It is to be stressed that the effects of model assumptions do not seriously alter our calculations concerning the design of the array, but should be examined when performing detailed analyses of cosmic ray composition.

Lateral distribution normalization

The normalization constant k in Equations 5.1 and 5.3 is a function of shower energy and zenith angle. To account for the attenuation of a shower through the atmosphere, define a new density parameter $\rho_\lambda(600)$ by the relation $\rho(600) = \rho_\lambda(600)e^{-(\sec\theta-1)1018/\lambda}$, appropriate for the 1018 g/cm² atmospheric depth of the Haverah Park location. The measured value of the attenuation length λ at $r=600$ m was 760 ± 40 g/cm².

In the Haverah Park experiment shower energy is expressed in terms of $\rho_\lambda(600)$. When fitting experimental shower data with a free slope parameter, such as η , and using relatively few measurement points, errors in core location and slope parameter are interdependent. However, it turns out that the associated error in function normalization is on average minimal at a distance from shower core close to the array spacing distance (which for the Haverah Park system was typically 600 m). Simulations also suggest that shower-to-shower fluctuations produce smaller variations in density with increasing core distance, and that density dependence on primary particle mass is minimal near 600 m.

The relationship between primary energy, and lateral distribution normalization can only be determined from detailed calculations of shower development. Early Monte Carlo simulations by A. M. Hillas lead to the adoption of the relation $E = 7.04 \times 10^{17} \rho_\lambda(600)^{1.018}$ eV (where ρ_λ is in units of m^{-2}), for the Haverah Park array. This relationship is sensitive to experimental details, and so will differ somewhat from that obtained, for example, from Akeno data.

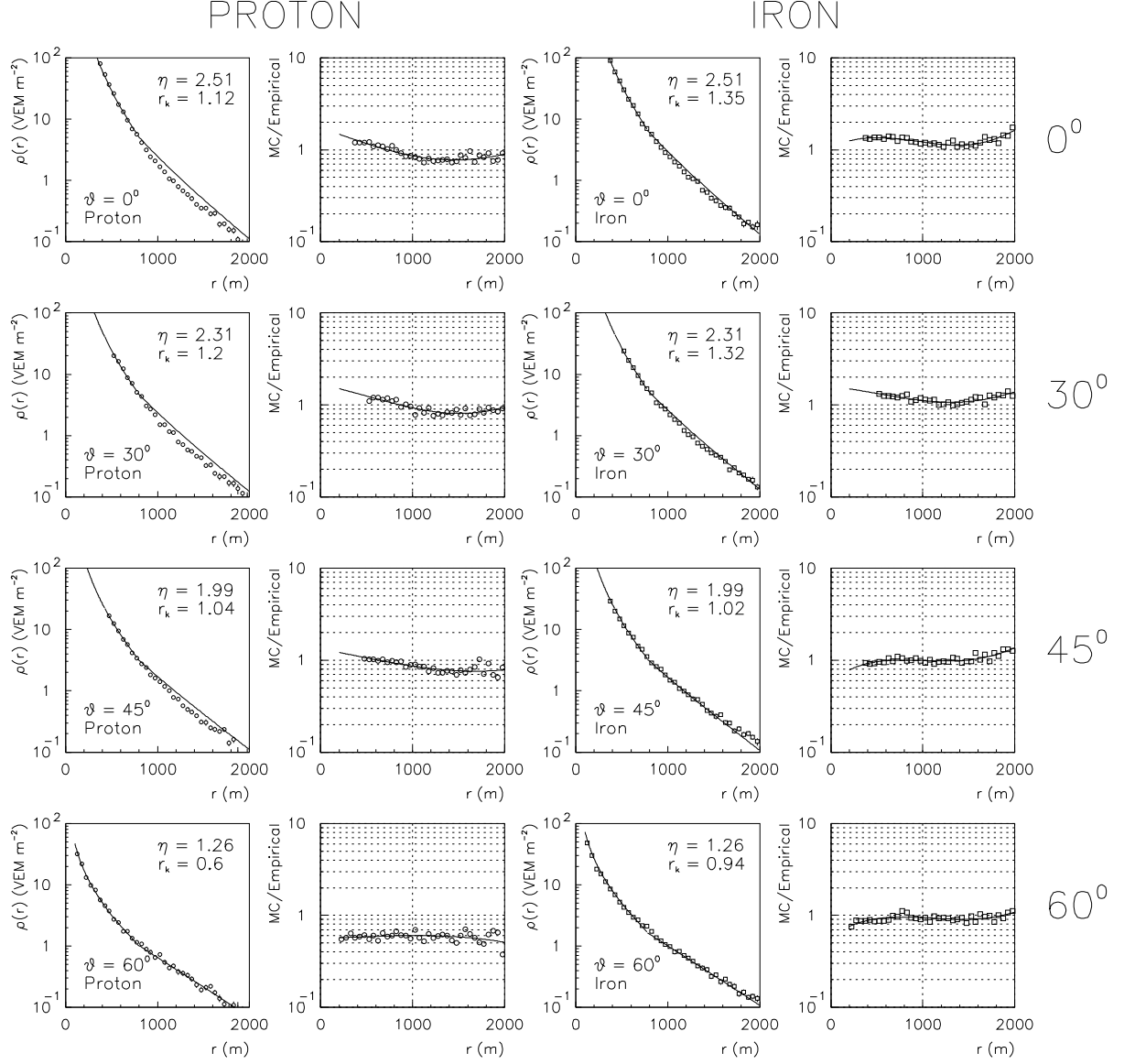


Figure 5.12: Comparison of simulation lateral distributions against measurements from the Haverah Park array, as in the previous figure. Here, simulated iron and proton showers at various zenith angles are shown.

Zenith angle (deg)	r_k (p)	r_k (Fe)
0	1.12	1.35
30	1.20	1.32
45	1.04	1.02
60	0.60	0.94

Table 5.1: Ratio of the fitted k parameter in normalization of the lateral distribution to the predicted value. Separate fits of the Monte Carlo data in the region $400 < r < 800$ m were done for protons and iron primaries at various zenith angles.

The above two relationships allow calculation of the expected value of the normalization constant k in Equation 5.1 for given shower energy and zenith angle. The quantity r_k (shown above in Figures 5.11 and 5.12) is the ratio of the k value determined by fitting the expected lateral distribution shape to the Monte Carlo data in the region $400 < r < 800$ m relative to the predicted value of k . For vertical showers the absolute normalization is the same to $\leq 35\%$. This is no more than saying that the new Monte Carlo reproduces the result of the old. However, the atmospheric attenuation with increasing zenith angle is also relatively well reproduced; Table 5.1 shows the values of r_k for proton and iron initiated showers at four different zenith angles. Note that the attenuation coefficient used is only known to be correct for $\theta < 45^\circ$.

Shower front rise time

The timing structure of a shower front is greatly affected by muons. In a water Čerenkov detector at large distances from the shower core a significant fraction of the total signal is due to muons. (The simulations predict $\approx 20\%$ at 0.5 km rising approximately linearly to 50% at 1.5 km, increasing somewhat with primary particle mass and zenith angle.) Muons scatter less than the electromagnetic particles and so tend to arrive earlier. So muons will also tend to dominate the signal if one considers only the earliest arriving particles. From simple geometry alone, if a shower is approximated as a line source of muons, then in a shower developing high in the atmosphere the path length differences between muons from the top and bottom of the hadronic cascade will be smaller than for showers lower in the atmosphere, leading to a smaller dispersion in their arrival times. Note also that showers initiated by primaries of higher mass are expected not only to be on average higher in the atmosphere, but also to have a larger ratio of muons to electromagnetic particles, and hence a greater muon signal fraction (recall Figures 5.6 and 5.7). All of the above effects produce a correlation between signal rise time and primary particle mass at a given core distance.

At Haverah Park the water Čerenkov detector output pulses were integrated, displayed on oscilloscope screens, and recorded photographically. It was straightforward to measure not only the total time integrated amplitude, but also the arrival time dispersion of the air shower signal. The parameter chosen was called t_{10-50} , defined as the time taken for the trace to rise from the 10% to the 50% levels relative to the eventual total.

Figure 5.13 shows a comparison of the Monte Carlo predictions of t_{10-50} against actual data from the Haverah Park archives using the cuts indicated. The qualitative agreement is good, particularly for the simulated iron showers. However, the same caution which applies to interpretation of the lateral distribution shape agreement also applies here. The disagreement at $r < 600$ m for the showers at $\theta = 60^\circ$ is partly due to bandwidth limitation effects in the Haverah Park electronics.

As a final comment, the differences in rise time between iron and proton showers is greatly reduced if one instead considers the majority (say, 90%) of the particles instead of only the first 50%. This effect is described later (Chapter 8) in relation to constructing an event trigger which is unbiased with respect to composition.

5.2.5 Reconstruction of simulated events

Analysis of the simulated events is done to estimate the ability of the Auger Observatory's detectors to achieve the physics goals. Given below are results of work on estimating the trigger efficiency, the accuracy of energy and direction reconstruction, and the separation of proton and iron induced showers.

Triggering

Schemes for triggering an array of water Čerenkov detectors have been implemented in the simulation. As mentioned before, the signals of photomultipliers are carefully simulated, including the digitizing electronics. One specific feature incorporated in the triggering simulation is that the muon signals are “clipped”, i.e., the magnitude of the largest pulses are not permitted to exceed modest levels in the formation of alerts. This will allow the detectors to register the time dispersed signals expected from large showers far from their cores without contamination from the high rate of fast, large pulses from random single cosmic ray muons. The motivation is to have only those ground stations with activity beyond noise levels contribute to the formation of shower triggers. This scheme has been used successfully by many experiments (such as CASA-MIA). Hardware for this purpose is incorporated in the electronics and is described in Chapter 9. This detector alert condition is done in hardware within individual stations and does not involve communication with neighbors.

It is useful to impose a *minimum* time requirement on the formation of an alert in a ground station in order to combat detector noise. The signal must not only be large enough, it must also *not* be very short in duration. The time width of a signal grows with the primary energy, so very low energy showers (the source of much of the detector noise) tend to have rather short signal durations. The rate of random alerts in individual stations can be several kHz due in part to lower energy ($\geq 10^{14}$ eV) air shower particles. MOCCA simulation of lower energy showers indicates that the time width of the shower front near the core of these showers is very much less than the μsec widths of useful (10^{19} eV) showers at core distances of order a kilometer. If one requires that the particles in a station arrive over a time *longer* than 200-500 nsec, alerts arising from air showers with energy $< 10^{16}$ eV are effectively

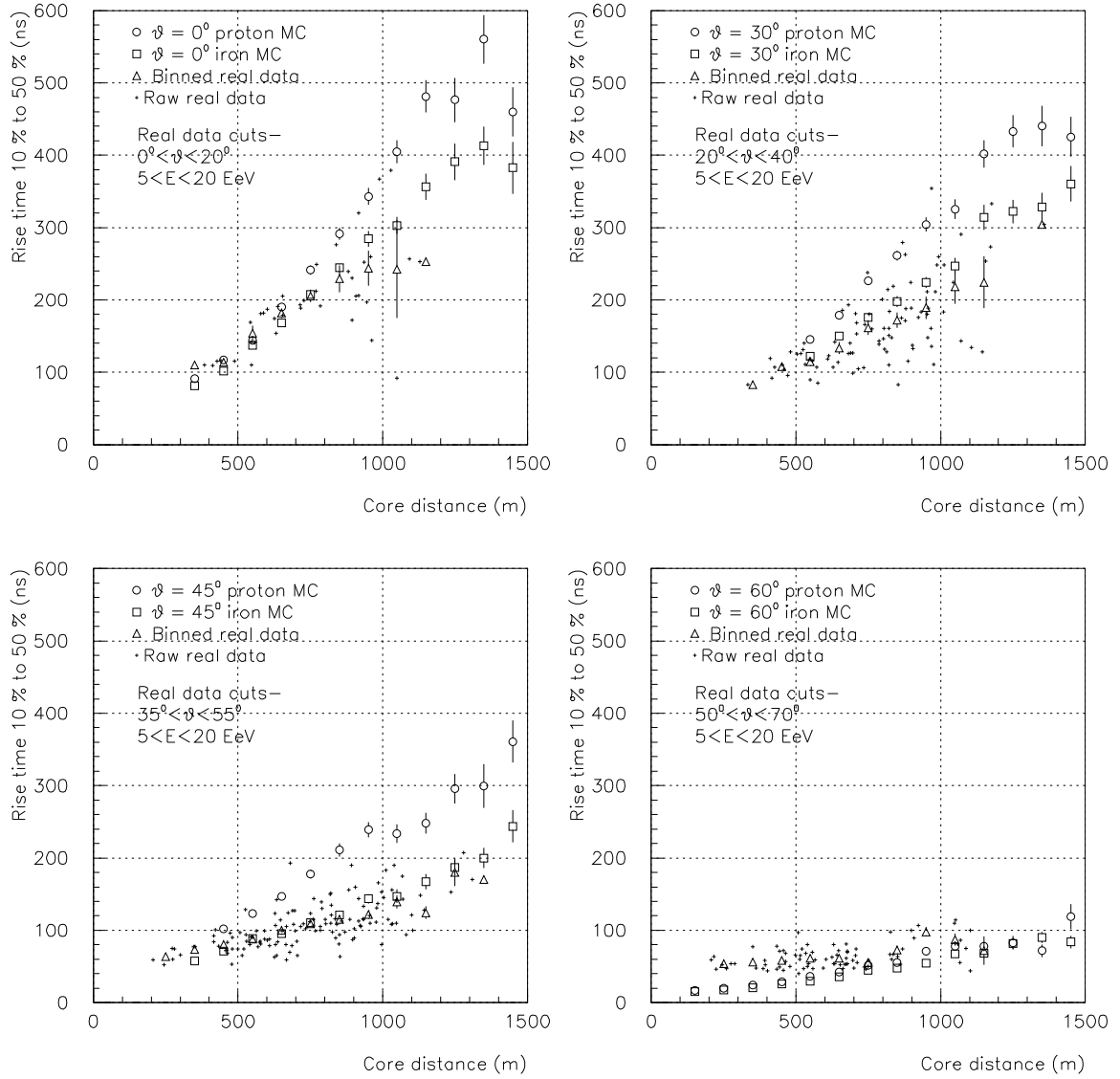


Figure 5.13: Comparison of simulated rise time against real data from the Haverah Park experiment. Comparisons are shown at zenith angles of 0, 30, 45 and 60 degrees. The “raw, real” observations have been extracted from the Haverah Park archives applying the data cuts indicated.

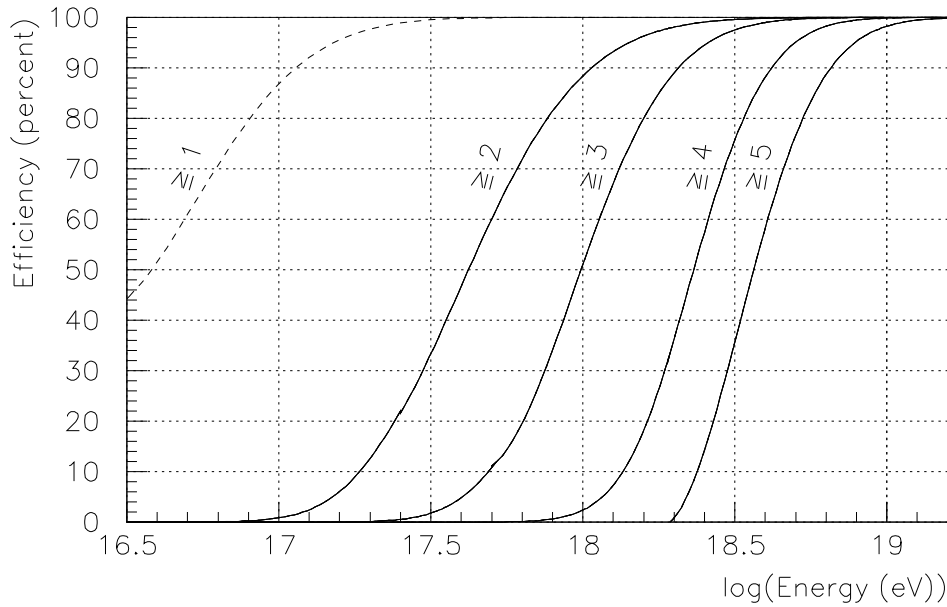


Figure 5.14: Trigger efficiency versus primary energy for vertical proton showers from MOCCA. Various alerted station multiplicity requirements are shown. Lower levels (and consequently lower energy) will be possible using additional constraints, such as separate triggers from the optical detector.

eliminated and so random noise is substantially reduced.

The shower trigger is formed by requiring some minimum number of stations to report coincident alerts within a minimum time. Figure 5.14 shows the efficiency at which vertical proton showers of various energies will trigger the array. Requiring 5 or more alerted stations within 20 μsec gives good efficiency at 10^{19} eV. Also shown are the efficiency curves at lower multiplicity requirements. While such low levels tend of course to eventually become noise-dominated, it will be possible to retain events with the additional constraint of requiring a separate trigger from the fluorescence detector. The reduced energy threshold of the ground array at the lower multiplicity levels (between 10^{17} eV and 10^{18} eV) is well matched to optical detectors such as those described in subsequent chapters.

Most showers recorded by the array will not be vertical. Figure 5.15a shows the 5-fold trigger efficiency and mean alert multiplicity for more typical events (30° from the zenith).

Direction Reconstruction

The determination of the arrival direction of a primary cosmic ray is done by reconstructing the resultant air shower geometry. Particles arrive at the ground in a shower front with a conical shape and a thickness of a few μsec (recall Figure 5.3 and Figure 5.4). If more than three ground stations report hits then the shower front geometry can be fit from the recorded arrival times.

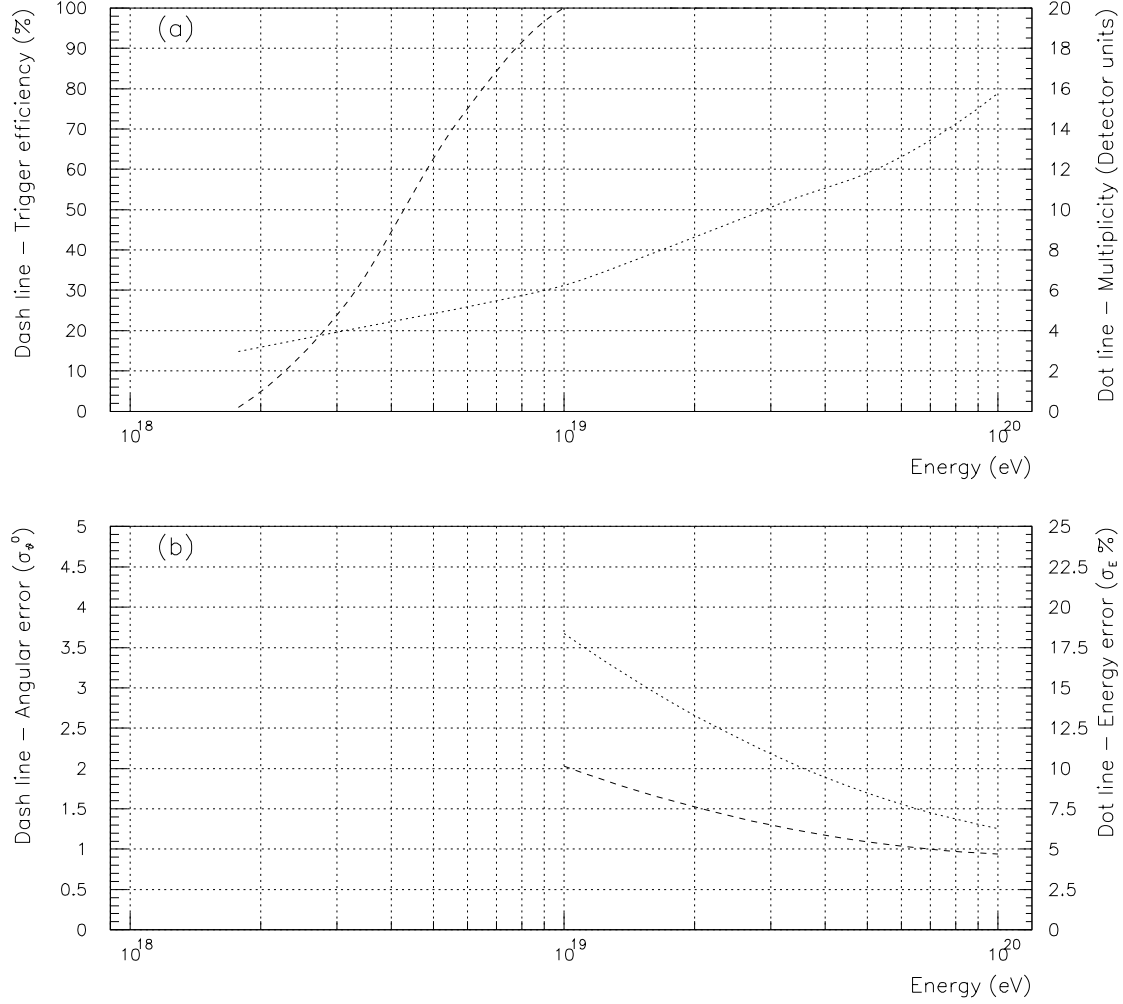


Figure 5.15: Summary of Auger Observatory water Čerenkov surface array performance as determined by reconstruction of simulated events. The upper plot shows the detector unit multiplicity and array trigger efficiency if 5 fold events are demanded, for proton showers at 30° (compare to last figure which used vertical showers). In the lower plot, expected reconstruction accuracy of direction and energy for vertical proton showers. The energy error plotted is only the random component due to detector physics and statistics. The estimated shower-to-shower fluctuations contribute 10% to the energy resolution, which should be added in quadrature with the values shown. The assumption of primary particle type results in a systematic shift of at most 25%. This systematic shift can be substantially corrected using rise time measurements, muon counting, and X_{max} measurements. The corrections can be calibrated and confirmed using hybrid data.

The detector simulation described above is used to provide realistic timing information (including the intrinsic dispersion in the shower front) for alerted ground stations. The precision of the signal digitizing electronics and GPS systems is taken as 5 nsec. The times are those of the first particle to strike each detector. The fit itself is a least-squares minimization of the difference between the recorded times and those expected from the arrival of a plane whose orientation is varied. A conical geometry should properly be used to fit the times, but if the core of the shower is not near the array boundary a plane fit works nearly as well and is insensitive to the location of the core.

The accuracy of the fit is determined by comparing a vector normal to the best-fit plane to the true direction of the shower. Under the assumption that the probability of observing some angle between these vectors is distributed as a symmetric two dimensional Gaussian function, Figure 5.15b shows the resulting σ obtained from our simulations. Alternatively, define the parameter σ_{63} to be the space angle with respect to the true direction within which 63% of events have been reconstructed. This parameter is commonly quoted as the “angular resolution” of an experiment since it is closer to the optimum signal-to-noise acceptance cone when searching for a point source in the presence of a uniform background. Note that σ_{63} can be easily computed without having to fit an assumed error distribution function. If the error distribution happens to be Gaussian, then $\sigma_{63} = \sqrt{2}\sigma$. We find that $\sigma_{63} = 3.0^\circ$ for vertical 10^{19} eV proton showers. The accuracy improves to about 1.3° at 10^{20} eV.

The geometry of water Čerenkov detectors is such that longer track lengths and consequently larger individual muon signals occur for showers away from the vertical. This causes the angular reconstruction accuracy to actually improve at large zenith angles. At 60° , for example, $\sigma_{63} = 1.3^\circ$ at 10^{19} eV and 0.5° for 5×10^{19} eV.

Reconstructions of iron showers at similar energies and zenith angles show slightly better angular resolution than proton showers. This presumably arises because the fitting procedure uses the times of the first arriving particles at each detector. Muons tend to be the earliest arriving particles in any air shower. Iron showers have more muons than proton showers of the same total energy, and so appear “bigger” when measured this way, with a corresponding improvement in reconstruction accuracy.

Energy Reconstruction

Algorithms for reconstructing the energy of the air shower have been developed using fits to the observed signal density at a specific core distance (600 m). Event reconstruction is done using standard least square fit methods. The Haverah Park experimental parameterization of the water Čerenkov lateral distribution given by Equations 5.1–5.3 is used. The Haverah Park attenuation coefficient is also used to predict normalization shift at increasing zenith angle. Using a maximum likelihood technique, the energy of the shower is computed using a fitted size-energy relation obtained previously from an independent set of analyzed MOCCA showers.

Firstly, assume that the nature of the primary composition is known so that proton showers are fitted according to relations appropriate for protons. The error distribution of

the reconstructed energy of the detectors is found to have a log-normal distribution (i.e., the distribution of $\log(E)$ has a Gaussian shape), with a standard deviation shown in Figure 5.15b. Note that the standard deviation of the distribution of $\log(E)$ is equivalent to the relative error in the energy, σ_E/E .

The reconstruction accuracy shown under these assumptions reflects only the random component from the sampling statistics of the detectors. This approach is relevant for showers with a single nuclear component or where the nature of the primary can be determined by other means, either from optical detector measurements or muon measurements. To avoid this requirement, the fits are also performed using an average of the lateral distribution functions of protons and iron. The accuracy of this method will depend on the true composition of the primary cosmic rays.

By means of a simple numerical exercise, estimates have been made as to whether the energy reconstruction will be sufficiently accurate to achieve the goal of identifying features in the cosmic ray energy spectrum. This is neither a detector nor a shower simulation, but rather an exercise to see the effects of “smearing” energies drawn from an assumed parent distribution. In particular, it investigates the degree to which energy resolution will distort the features of a spectrum which is, overall, steeply falling.

Shower energies are generated according to an input spectrum having an $E^{-2.5}$ power law character and a GZK cutoff [132]. The effects of triggering are estimated by accepting a fraction of the generated events according to the probability that five or more surface stations are alerted (from Figure 5.14). Each accepted energy is then altered according to a Gaussian distribution of $\log_{10}(E)$ to approximate the effects of reconstruction. The variance of this distribution includes both random errors as described above and another term corresponding to uncertainty in the primary composition which is assumed to be equal parts iron and protons. The two effects are added in quadrature. The net smearing of $\log_{10}(E)$ is equivalent to a relative error ($\delta E/E$) of about 25% at 10^{19} eV, improving to about 20% at 10^{20} eV. Note that the procedure is conservative and would overestimate the energy smearing of a sample of events which are dominated by a single nuclear type.

The “reconstructed” energy spectrum is compared with the input. Figure 5.16 indicates how well an assumed cosmic ray energy spectrum can be measured in this way. In this plot, the total number of events corresponds to about 1.7 years of operating the full Auger Observatory. It is clear that this level of resolution will permit the observation of the GZK cutoff. Rough inspection of the reconstructed spectrum suggests that changes in the power law slope of as small as 0.2 or features (bumps) greater than about 30% of the baseline power law can be discerned in this sample.

Also note that a significant number of events below 5×10^{18} eV will be obtained, despite low trigger efficiency, because of the steep spectrum of cosmic rays.

Composition Sensitivity

The simulated signal timing-amplitude profiles have been analyzed to determine the muonic signal fraction, and hence to separate showers on the basis of primary particle type. Large

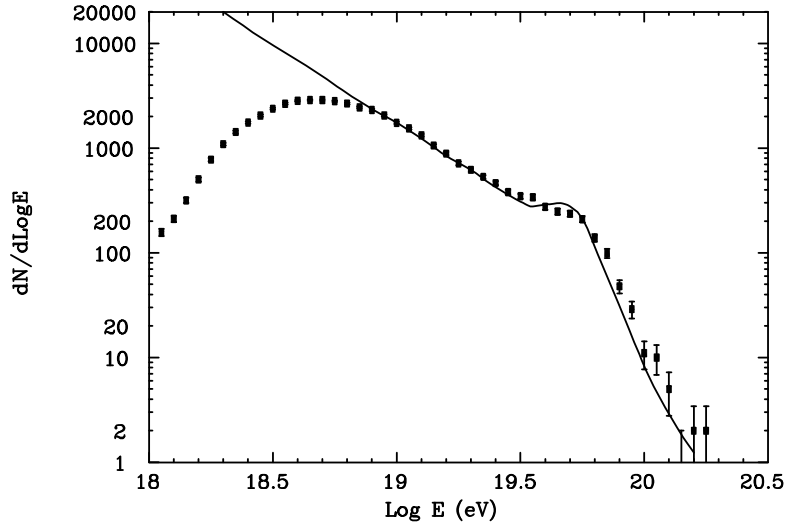


Figure 5.16: Reconstructed energy spectrum of cosmic rays, assuming an input spectrum shown with the solid line, an $E^{-2.5}$ power law and GZK cutoff. The points are from simulation corresponding to about 1.7 years operation of the Auger Observatory.

narrow pulses in the simulated detector signals are identified using a pulse height threshold criterion in the analysis (recall Figure 5.10). The fraction of the integrated signal contained therein is taken to represent the ratio of muons to electrons. The discussion in the last chapter illustrated an example of this technique. It is likely that this can be improved, either through optimizing the selection technique or perhaps by increasing the tank depth from 1.2 m to about 2 m.

Estimates of the nuclear composition as described in the last chapter could be made by constructing the $\mu:em$ parameter for events and comparing them to the curves shown. Also, considering that the composition may not be dominated by a single nuclear type, the *width* of the $\mu:em$ distribution for a sample of data can also be calculated and compared to the prediction of the simulation. This technique gives information on whether the composition is in fact mixed or pure and whether it is heavy or light. Such an approach has been employed previously by the Fly’s Eye group.

Note that the muon/electron ratio measurements for the purpose of studying composition are relatively insensitive to changes in the physics models of the simulation at extreme energy. As mentioned earlier (Figure 5.1), most ground-level particles originate from the lower energy interactions in the shower where the modeling has been well calibrated by accelerator experiments.

Again, caution must be applied when evaluating these reconstruction results. Although statistical and detector-imposed fluctuations are included in the simulation procedure, the shower-to-shower fluctuations caused by variations in depth of first interaction, etc., have been averaged out by the process used to overcome the “thin sampling” limitations of MOCCA. Some results may also be optimistic due to the lack of simulated events at the

“edges” of the array. Work is on-going on more realistic simulation.

5.3 Hybrid Detector Simulation

The simulation methods employed to evaluate the performance of a Hybrid detector are described here. The term “Hybrid” refers to the combination of a ground array and an atmospheric fluorescence detector. Advantage has been taken of the experience and existing detector simulation code from two groups - the ground array simulation code of the AGASA experiment, and the HiRes detector Monte Carlo. Both simulations have been developed over long periods, and have been refined using results from observations. Elements from both sources have been combined to first study the geometrical reconstruction accuracy of a Hybrid detector, using the ground array shower arrival time as a constraint in the fluorescence detector determination of the shower direction and core. The various elements of the simulation are described, from the shower generation through to detector modelling.

A three-eye fluorescence system is investigated. For the most part, showers are viewed by a single fluorescence detector in conjunction with the ground array, although at the highest energies some showers will be viewed by two or three eyes. Each eye images the sky up to an elevation angle of approximately 30° with 1.5° diameter pixels.

It will be shown that a shower viewed by a combination of a single fluorescence site and the ground array will be reconstructed with an accuracy equivalent to that given by a stereo fluorescence system, where showers are viewed by two fluorescence detectors without a ground array. (The latter technique, called “stereo” reconstruction, is the method employed by the HiRes detector). Based on the solid footing of good geometrical reconstruction, the energy and depth of maximum resolution of the Hybrid detector will be discussed.

Generic fluorescence and ground array detectors have been used in this study. For example, the fluorescence detector uses mirrors and phototubes in the classic Fly’s Eye approach, and the ground detector consists of an array of scintillators with the characteristics of the AGASA detectors, though with each detector having a larger area. Variants on these designs (i.e. for example replacing the scintillator detectors with water detectors of the same area and on the same grid spacing) will have only a small effect on the geometrical reconstruction accuracy, and hence a small effect on the fluorescence detector determination of energy and depth of maximum.

5.3.1 Methods

In our simulations of the Hybrid aperture, geometric reconstruction, and energy and X_{max} resolution, parametrizations of the longitudinal and lateral structure of the showers were used. Fluctuations were introduced where appropriate. Each parametrization is discussed in turn.

Longitudinal Profile

Each simulation was performed at fixed energy. For each energy, the *mean* depth of shower maximum was determined from simulations [133]. Results appropriate to a proton primary beam have been used, with a X_{max} of 780 g cm^{-2} at 10^{19}eV and an elongation rate of 55 g cm^{-2} . Such a composition is consistent with the Fly’s Eye data above 10^{19}eV .

Variations in the depth of maximum were simulated simply by introducing fluctuations in the depth of first interaction X_0 . A mean interaction length of 70 g cm^{-2} was assumed at all energies. This is clearly not accurate, though it is sufficient for our investigation of detector aperture, geometrical reconstruction and energy and depth of maximum resolution.

The primary energy determines the shower size at maximum, N_{max} [134]. Given N_{max} , X_{max} and X_0 , the complete longitudinal profile was described by the Gaisser-Hillas function [135].

Charged Particle Lateral Distribution

The AGASA lateral distribution function has been used to determine the particle counts in the ground detectors. The function is given in [15] and has a dependence on shower zenith angle. The shape of the function has no energy dependence, since none has been detected in the AGASA data.

The shower size at ground level (the normalization of the lateral distribution) is determined from the longitudinal profile discussed above, and the shower zenith angle. In this way the development fluctuations introduced in the fluorescence simulation are passed onto the ground array simulation.

Shower Front Timing Structure

To handle the shower front curvature and thickness, data tables of the delay of shower particles behind an imaginary plane shower front have been constructed using an ensemble of MOCCA-generated vertical proton showers at 10^{19}eV . These include the response of standard AGASA-type scintillators to low energy gammas and electrons. These tables are embedded into a subroutine which, given the core distance, assigns a particle an arrival time with respect to a plane shower front. In other words, both the curvature and the thickness of a shower front are simulated in a reasonable way.

5.3.2 Simulation of Fluorescence Detector Response

Three eyes are placed on the vertices of an equilateral triangle, 32.7 km on a side. A total of 1596 ground array detectors are arranged over an area defined by a “superman” outline (Figure 5.17). Each eye views the sky up to an elevation angle of 30° over the full azimuth range. There are 45 mirror units per eye, 23 in the lower ring and 22 in the second ring.

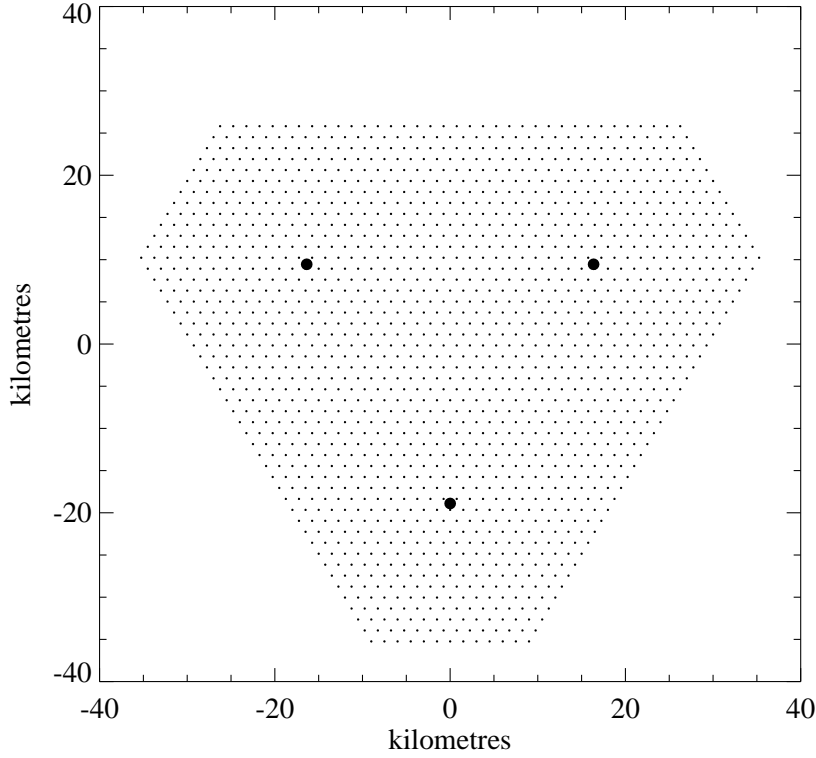


Figure 5.17: The positions of the three fluorescence detectors and the 1596 ground array detectors in the Superman arrangement.

Each mirror has an unobscured area of 1.54 m^2 (actual diameter 1.5 m) and each images the sky onto a cluster of 121 hexagonal photomultipliers (pmts). A single pmt views a solid angle equal to that of a circular pixel with diameter 1.5° . There are 5445 pmts in each of the three eyes.

The fluorescence simulation code is based on the HiRes Monte Carlo program. The phototube triggering thresholds are set by comparing the expected night sky noise level with that seen by HiRes. Given that the sky background light scales with the product of mirror area A and the solid angle viewed by a phototube Ω , the noise scales as $\sqrt{A\Omega}$ for AC-coupled electronics. Thus comparing the sky noise in the 1.5° pixel system with HiRes,

$$\frac{N_{1.5^\circ}}{N_{\text{HiRes}}} = \frac{\sqrt{A_{1.5^\circ}\Omega_{1.5^\circ}}}{\sqrt{A_{\text{HiRes}}\Omega_{\text{HiRes}}}} = \frac{\sqrt{1.54 \times (1.5^\circ)^2}}{\sqrt{3.75 \times (1^\circ)^2}} = 0.96$$

Thus, in the simulation individual pmt triggering thresholds are set at 96% of the HiRes levels.

The calculations are performed for an atmospheric depth of 860 g cm^{-2} . An outline of the simulation follows. Details of some of the methods used here can be found in [8, 136].

1. For a chosen energy determine the shower depth of maximum. Randomly choose shower arrival direction (zenith angle less than 60°) and core location. The core location must lie within the physical area of the ground array.
2. Calculate light emitted from the shower along its track. Both fluorescence and Cerenkov light is calculated. The pressure and temperature dependence of the fluorescence yields are taken into account.
3. Calculate the light yield arriving at the detector site. Rayleigh and Mie scattering processes are simulated, with full account taken of the spectral characteristics of the light. The isotropically emitted fluorescence light, as well as direct and scattered Cerenkov light, is propagated. Night sky background noise is added to the signal.
4. Mirror area and reflectivity are used to determine the light falling on each phototube cluster. Optical filter transmission and phototube quantum efficiency factors are folded with the light spectrum to give the photoelectron yield in each tube, due to signal and noise.
5. For each tube viewing the shower, the photoelectron yield, the pulse width and an estimate of the time at the midpoint of the pulse are recorded. These parameters are calculated assuming that the mirror produces a Gaussian-profile light spot in the focal plane with a fixed standard deviation of 0.25° . The mid-pulse time is calculated, then fluctuated, using experience with the FADC system currently being constructed for HiRes. The uncertainty of the mid-pulse time is a function of the pulse width and the number of photoelectrons.
6. A phototube is said to trigger if its instantaneous photoelectron current (taking into account the time constant of the circuitry) is greater than the 4σ night sky noise level. A mirror will trigger if it contains a sufficient number of firing tubes. Here we demand that the track length of firing tubes within a mirror exceeds 9° .
7. A trigger in at least one mirror defines an accepted event. The data from all firing tubes in the detector (even in mirrors not satisfying the track-length requirement) are recorded.

5.3.3 Simulation of Ground Array Response

The main steps of this procedure are taken from the AGASA detector Monte Carlo [15]. The array consists of 10 m^2 detectors made of 5cm plastic scintillator arranged on a triangular grid of spacing 1.5 km. The procedure is as follows,

1. Energy, shower direction and core location come from the fluorescence section of the simulation.
2. Determine the shape of the lateral distribution, a function of zenith angle.

3. Determine the ground level shower size from the profile used in the fluorescence calculation. In this way, fluctuations in the depth of maximum are translated into shower size fluctuations at the array. The shower size provides the normalization for the lateral distribution, which is used to calculate the particle count n_i in each detector.
4. Determine the number of particles registered by each detector by sampling from the Poisson distribution with mean n_i .
5. Each particle is assigned an arrival time relative to a plane shower front, using the data tables discussed earlier. The time of arrival of the first particle is recorded, as well as the mean arrival time and time dispersion of all the particles. It is assumed that each detector is equipped with FADC-like electronics with a sample rate of 40 MHz. (A systematic study of the effect of finite array timing resolution on hybrid reconstruction has been performed. It appears that there is little effect on reconstruction until sample rates fall below 10 MHz [137]).
6. Detector resolution is folded into the particle density. This is based on results from Akeno detectors in the 1 km² array.
7. For an event to trigger the array, it is required that at least three stations register a particle count greater than 3. (For simulations at 10¹⁸eV and 3×10^{18} eV the station requirement is relaxed to two, provided that a coincident fluorescence detector trigger is present). No pulse width discrimination is applied. Once a trigger is established, record data from stations with particle counts of at least one particle. This approximates a possible real trigger scheme.

5.3.4 Hybrid Geometric Reconstruction Method

A reconstruction method using the fluorescence detector alone is presented below, followed by a method of adding ground array information to constrain the fluorescence fit.

Fluorescence Detector Geometric Reconstruction

The standard single-eye fitting procedure for the shower core location and direction starts with the determination of the plane containing the shower axis and the center of the eye. This shower-detector plane (SDP) fit uses tube pointing directions, together with signal integrals. Tube timing information is not used at this stage, except to discard noise tubes.

The SDP fitting procedure as used with the HiRes detector is described in detail in [142]. Briefly, trial planes are compared with the pointing directions of fired phototubes, with the fit weighted by the signal amplitudes. Pulse width information, which would be available with Flash ADC electronics, has not been exploited. The pulse width would help determine the crossing point of the shower image across each tube and constrain the plane fit even further.

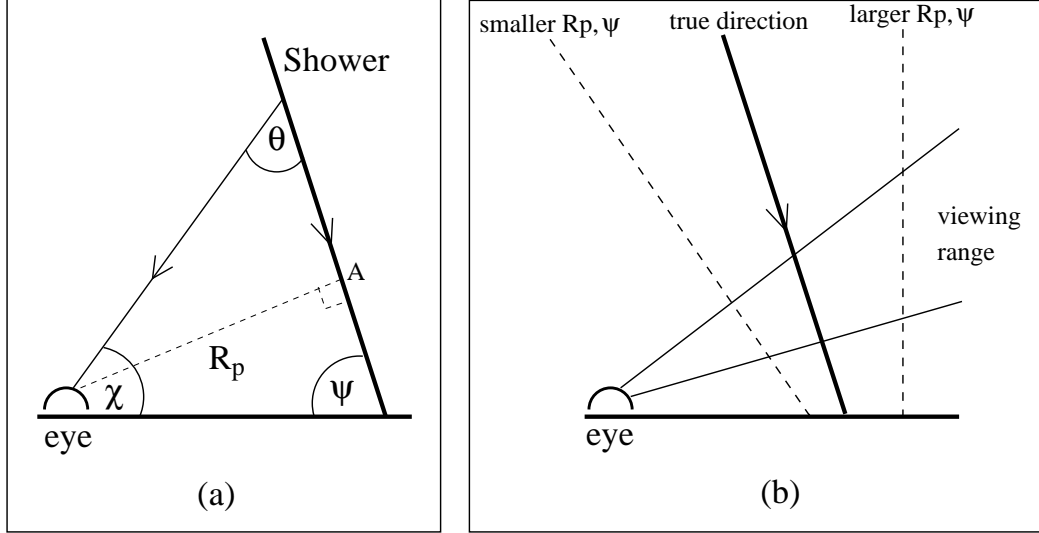


Figure 5.18: (a) Geometric reconstruction within the shower-detector plane. A phototube views the shower at an angle θ with respect to the axis. (b) Ambiguity in the position of the shower within the SDP for short tracks (highly exaggerated). Each of the three shower tracks shown would pass through the detector's field of view with similar (and approximately uniform) angular velocity.

Once the SDP is determined, the firing times of the tubes are used to determine the orientation of the shower axis within that plane. The times used here are estimates of the time at which the tube integral reaches 50% of its full value. This is our estimate of the tube-centre crossing time. Figure 5.18(a) shows the geometry within the SDP. For a given geometry, the arrival time of light at a tube viewing the axis at an angle θ_i is

$$t(\theta_i) = \frac{R_p}{c} \tan\left(\frac{\theta_i}{2}\right) + t_0$$

where t_0 is the time at which the shower reaches point A on the diagram, and $\theta_i = \pi - \psi - \chi_i$. A fit is done for R_p and the ground angle ψ . Together with the SDP, these parameters fully define the event geometry.

There is a problem with these timing fits, especially for short (i.e. distant) shower tracks. This has long been recognised, and is one reason the stereo Fly's Eye technique was pursued as an alternative to mono observations. With short tracks it is often the case that the range of θ_i sampled is not large enough to detect significant curvature in the tangent function in the above equation. In other words, the shower appears to pass through the field of view with *constant angular velocity*. Unfortunately, this leads to ambiguity in the fit, with a family of possible (R_p, ψ) values (Figure 5.18(b)).

Hybrid Geometric Reconstruction

This ambiguity can be resolved by using other information, for example a SDP from another fluorescence detector, or information from a ground array. The most promising ground

array parameter is the arrival time of the shower at the ground [143]. It is obvious from Figure 5.18(b) that if all eye and ground array times are measured with a common clock, then the ground array times will constrain the timing fit within the SDP.

The full Hybrid geometrical reconstruction proceeds in the following way:

1. The SDP is determined in the standard way, using fluorescence information only. Typically, the plane orientation is known to better than 0.25° , which corresponds to a distance of at most 60m on the ground at a distance of 15km. Thus ground array information is of limited use at this stage of the fit.
2. From this point on it is assumed that the shower core is contained on the line forming the intersection of the SDP and the ground. The timing fit is performed, minimizing a χ^2 which includes the standard fluorescence timing term and an array timing term. The fluorescence timing term is

$$\chi_1^2 = \frac{N_t}{\sum p e_i} \sum \frac{(t_i - t_{expected})^2}{\sigma_{ti}^2} p e_i,$$

where t_i is the estimate of the pulse mid-point time, and σ_{ti} is the mid-point time uncertainty for each tube. The elements of the sum are weighted by $p e_i$, the signal in each tube. The sum is multiplied by N_t , the number of firing tubes, to give the appropriate weight to this term of the χ^2 when the array component is added.

3. The array component of the χ^2 may take one of three forms.
 - (a) **Method 1:** The first method uses a single array detector to define the shower arrival time. The detector with the largest particle count is chosen, and a model of the curvature of the shower front is used to calculate the expected time in this detector for each trial geometry. The shower front curvature parametrization is the same one used in the generation of the data, but because this detector is close to the core, the dependence on details of the curvature is not strong. (In any case, it is expected that measurements of curvature will be one of the first tasks of the array). The χ^2 term is then

$$\chi_2^2 = \frac{(t_i^* - t_{expected})^2}{\sigma_{ti}^{*2}}$$

where

$$\sigma_{ti}^* = \frac{\sigma_{0i}^*}{\sqrt{n_i^*}}$$

and t_i^* is the mean arrival time of particles at the detector with the largest particle count, σ_{0i}^* is the dispersion in the arrival time, and n_i^* is the number of particles detected.

- (b) **Method 2:** While the method above is conceptually simple, it does not use all of the available array data. In the second method the mean arrival time of all array detectors with particle counts greater than 10 is used. The expected times

are again calculated using the shower curvature parametrization used in the data generation.

The term is

$$\chi_2^2 = \sum \frac{(t_i - t_{expected})^2}{\sigma_{ti}^2}$$

where

$$\sigma_{ti} = \frac{\sigma_{0i}}{\sqrt{n_i}}$$

where the sum is over all detectors with particle counts greater than 10 particles. t_i is the MEAN arrival time of the particles at each detector, σ_{0i} is the dispersion in the particle arrival time, and n_i is the number of particles detected.

- (c) **Method 3:** What if the form of the shower front curvature is not known? The following method was also found to work well. Again, times from all array detectors with particle counts greater than 10 are used. But here the time of the FIRST particle in each detector is used, and the expected time is calculated assuming a PLANE shower front. Surprisingly perhaps, this method works very well. It is true that the first particle will arrive closer to a plane front than the majority of the particles, which will be delayed. However, the success of this method probably relies on there being time measurements on all sides of the core. The method may produce a systematic error in direction for showers landing near the edge of the array.

The form of the χ^2 term is the same as in Method 2, but here t_i is the arrival time of the FIRST particle at each detector. Again σ_{0i} is the dispersion in the arrival time of all the particles, and n_i is the number of particles detected.

4. The final χ^2 minimization is performed on the linear sum of the fluorescence and ground array components, with the ground array component taking one of the three forms discussed above. That is,

$$\chi^2 = \chi_1^2 + \chi_2^2$$

Results from Methods 2 and 3 will be given below. For examples of the effectiveness of Method 1 see [144], a study of the “Cyclops” configuration of the Auger Observatory, in which a single large eye stands at the centre of a 3000 km² array.

5.3.5 Energy and X_{max} Resolution

The ability of a fluorescence detector to make an accurate determination of a shower’s longitudinal profile depends critically on the stage of analysis already discussed, the geometric reconstruction. Once a good geometry is determined, the conversion of measured light intensities into a longitudinal profile relies on an understanding of the light propagation properties

of the atmosphere. The analysis assumes the same atmospheric parameters used in the generation of the simulated data. The model used is in excellent agreement with the “1976 US standard” atmosphere with a desert aerosol profile. It is assumed that the atmosphere at the observatory site (particularly the aerosol structure) will be monitored and characterised using lasers, in a way similar to that being used at the HiRes site.

The method used for profile reconstruction is that used in the Fly’s Eye and HiRes experiments (see [8] for a description). Essentially, it is the reverse of the process described in the simulation section above. Photoelectron counts in a particular tube are converted to a shower size at the shower axis by a process which takes into account the physical parameters of the detector, atmospheric transmission and shower light production (fluorescence light and Cerenkov light, both direct and scattered). Finally, the Gaisser-Hillas function is fitted to the measured profile to extract the shower size at maximum, N_{max} , the depth of maximum, X_{max} and the depth of first interaction X_0 . The energy is then determined by integrating the profile, and taking account of the small fraction of energy not carried by the electromagnetic portion of the shower.

5.3.6 Results

Figure 5.19(a) shows the Hybrid efficiency as a function of energy. Showers with random zenith angles up to 60° and cores within the bounds of the ground array were simulated, an aperture of $7069 \text{ km}^2 \text{ sr}$. At least one eye and the ground array were required to trigger for the event to be accepted. The event was also required to successfully pass through the reconstruction procedures. Figure 5.19(b) shows one advantage of a three eye system - at the higher energies, many showers trigger two or three eyes.

For the following reconstruction studies, a single eye was chosen and showers were simulated over an area larger than its triggering aperture, so as to give a realistic collection of triggering events. While some showers will trigger more than one eye, this extra information has not been exploited in the current study.

Beginning with the geometry determined by the fluorescence detector alone, the error distribution for the *normal* to the shower-detector plane (SDP) is shown in Figure 5.20. All showers triggering the Hybrid detector at 10^{19} eV are used, and the differential and integral forms of the error distribution are shown. It can be seen that 50% of the plane normal errors are less than 0.22° and 90% are smaller than 0.80° .

Within the shower detector plane, the fluorescence detector uses tube firing times to determine the impact parameter R_p and the ground angle ψ (see Figure 5.18). The resolution of these measurements is strongly dependent on the length of the shower track viewed by the eye. Results are given for R_p in Figure 5.21, again for 10^{19} eV showers triggering the Hybrid array. Only fluorescence information is used in reconstruction here. Results for the ground angle ψ are included in Table 5.2.

Array information is applied to the fits using two of the three methods described earlier. (For examples of the efficacy of Method 1, see results from the “Cyclops Eye” simulations in

Meth.	$\Delta\text{direc.}(^{\circ})$		$\Delta\text{Core(m)}$		$\Delta R_p(\text{m})$		$\Delta\psi(^{\circ})$		$\Delta E/E (\%)$		$\Delta X_{\text{max}}(\text{g cm}^{-2})$	
	50%	90%	50%	90%	50%	90%	50%	90%	50%	90%	50%	90%
10^{18}eV (median plane normal error 0.34°)												
2	0.54	1.71	35	183	20	90	0.32	1.17	8.6	43	32	135
3	0.49	1.85	35	188	18	101	0.27	1.29				
$3 \times 10^{18}\text{eV}$ (median plane normal error 0.31°)												
2	0.43	1.35	35	141	17	95	0.26	0.82	4.9	23	25	83
3	0.40	1.35	35	144	16	95	0.21	0.88				
10^{19}eV (median plane normal error 0.22°)												
0	2.5	19.8	350	5600	350	3300	2.5	19.7	9.4	55	31	158
2	0.35	1.03	29	98	15	74	0.21	0.71	4.2	18	17	60
3	0.31	1.08	29	101	13	68	0.17	0.55				
$3 \times 10^{19}\text{eV}$ (median plane normal error 0.21°)												
2	0.31	0.81	27	79	14	59	0.19	0.54	3.2	15	16	64
3	0.29	0.80	25	84	11	71	0.14	0.48				
10^{20}eV (median plane normal error 0.23°)												
2	0.36	0.87	29	90	14	71	0.22	0.69	2.5	17	15	70
3	0.29	0.70	28	80	12	60	0.16	0.46				
$3 \times 10^{20}\text{eV}$ (median plane normal error 0.22°)												
2	0.36	0.89	32	91	16	80	0.24	0.76	2.5	30	15	105
3	0.28	0.73	30	72	14	65	0.17	0.47				

Table 5.2: Reconstruction resolution values from various methods, for a single 1.5° pixel eye in a 3-eye system. The values of the error parameter bracketing 50% and 90% of the distribution are given. The energy and depth of maximum resolution was not calculated for Method 3. “Method 0” represents reconstruction using single-eye fluorescence information without ground array data.

[144]). Again for 10^{19} eV triggers, Figure 5.22 shows the impact parameter R_p distributions for (a) Method 2 and (b) Method 3. Note how the dependence on track length has dramatically lessened. Similar results are found for the ground angle ψ (Table 5.2). Both methods represent significant improvements over “fluorescence only” fits in the previous figure. A median R_p error of about 15 m is found using these methods.

The final core location and shower direction errors for events at 10^{19} eV are displayed in Figure 5.23 for Method 2 (Method 3 gives very similar results as seen in Table 5.2). The plots show a median core location error of 29 m and a median shower direction error of 0.35° .

Figure 5.24 and Figure 5.25 show results from the profile reconstruction for 10^{19} eV showers. As with all figures in this section, no quality cuts have been applied to the distributions. In Figure 5.24(a), the X_{max} error ($X_{max\ reconstructed} - X_{max\ true}$) is shown for showers analysed using the fluorescence information alone. Also shown are the results for the same showers analysed using Hybrid Method 2. Again, results from Method 3 are quite similar. Even with good geometrical reconstruction, it is clear that a long track length improves the reconstruction of the longitudinal profile. The poorer fits to X_{max} and energy are generally associated with short tracks.

Figure 5.25 shows the energy resolution $(E_{reconstructed} - E_{true})/E_{true}$ for 10^{19} eV showers analysed with (a) fluorescence information only and (b) Hybrid Method 2. Again the Hybrid method significantly improves the tails of the error distribution. Results from other energies are given in Table 5.2. The slight worsening of the energy and X_{max} resolution at the highest energy is a result of some near-vertical showers arriving at ground level before reaching their maximum size.

At an energy of 10^{18} eV the array described is not fully efficient. However, showers of this energy may trigger two or three array detectors. Figure 5.26 shows results for 10^{18} eV showers analysed using Method 2. The array triggering requirement has been relaxed at this energy to allow events to trigger with only two detectors at the 3-particle level (instead of three detectors). Method 2 uses array times from detectors with a particle count of at least 10. In some events this may mean that only one or two detector times are used in the fit. Despite this, good reconstruction appears possible for most showers. Results for Method 3 are given in Table 5.2.

A compilation of reconstruction resolution results from the various methods used is given in Table 5.2. In each case the value of the error parameter bracketing 50% and 90% of the distribution is given. Given the similarity of geometrical reconstruction for Methods 2 and 3, the energy and depth of maximum resolution is given for Method 2 only. Method 0 represents the reconstruction with fluorescence data alone. Some of these data are displayed graphically in Figure 5.27.

	10 ¹⁹ eV		10 ²⁰ eV	
	Surface	Hybrid	Surface	Hybrid
$\Delta\theta$	2.0°	0.35°	1.0°	0.36°
Δcore	80 m	29 m	40 m	29 m
$\Delta E/E$	18%	4.2%	7%	2.5%
ΔX_{max}		17 g/cm ²		15 g/cm ²

Table 5.3: Summary and comparison of reconstruction resolution for the surface array alone and for Hybrid data. Median errors are shown, from simulations of proton showers.

5.4 Summary of Reconstruction Resolution

Simulations of the surface array performance predict that the reference design will provide data which can be used to reconstruct the energy, direction, and nuclear composition of the highest energy cosmic rays. The resolution of the reconstructions is more than sufficient to interpret the data in the context of the scientific models described in Chapter 2.

The hybrid data set – those events which have been simultaneously recorded by the surface array and one or more of the fluorescence detector “eyes” – will yield a subset of events which are particularly well measured, having independent data on energy and direction. The hybrid data set reconstructions are significantly improved over that of the surface array alone. When coupled with determination of X_{max} , these will greatly enhance the analysis of cosmic ray composition.

Table 5.3 summarizes the median reconstruction errors for various quantities. The values shown display the resolution expected from analysis of surface data alone, and the improvement expected for hybrid events. This brief summary gives representative values, obtained from the tabulations and detailed summaries found earlier in this chapter (e.g., Figure 5.15 and Table 5.2).

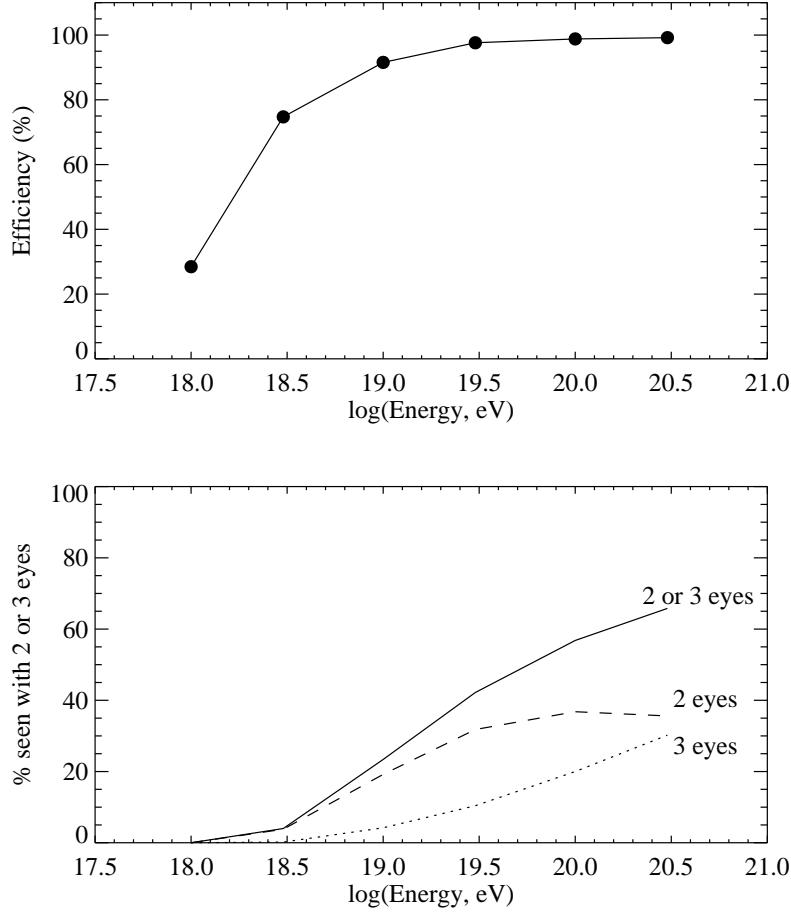


Figure 5.19: (a) Triggering/reconstruction efficiency as a function of primary energy. Showers were restricted to zenith angles less than 60° and cores within the 3000 km^2 area of the array. At least one of the eyes must have triggered in coincidence with the ground array. The fraction of triggering showers successfully passing through the reconstruction process has been included in the efficiency. (b) The fraction of showers triggering the array and exactly 2 eyes, exactly 3 eyes, and 2 or 3 eyes.

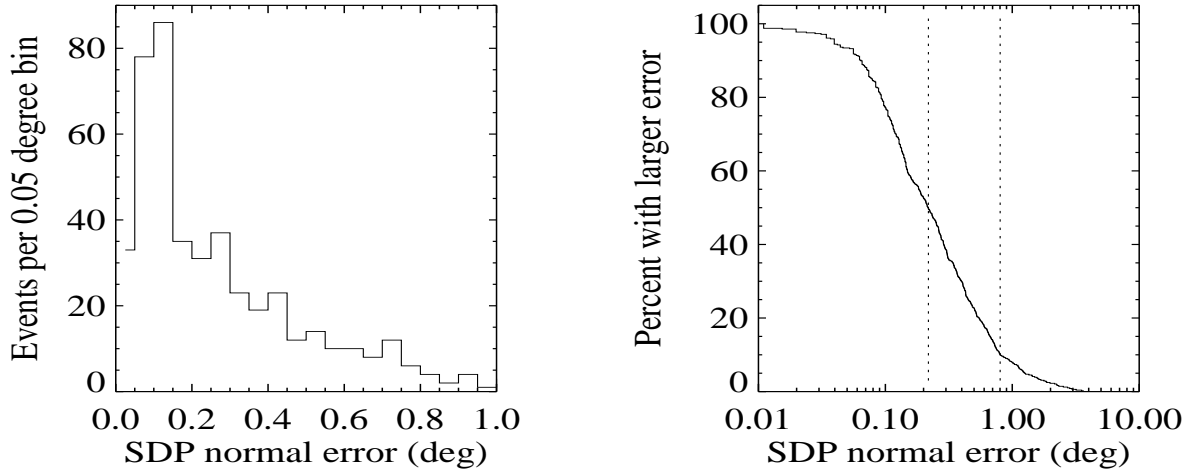


Figure 5.20: The error distribution for the *normal* to the shower-detector plane (SDP), for all showers triggering the Hybrid detector at 10^{19} eV. The differential and integral forms of the error distribution are shown. It can be seen that 50% of the plane normal errors are smaller than 0.22° and 90% are smaller than 0.80° .

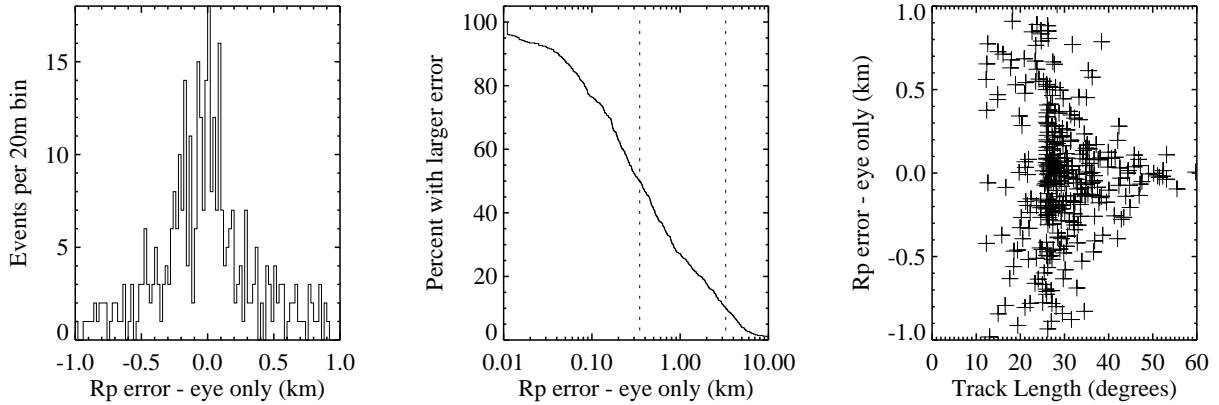


Figure 5.21: Reconstruction errors for the impact parameter R_p (see Figure 5.18). The resolution in this measurement (and that of the ground angle ψ) is strongly dependent on the length of the shower track viewed by the eye. Results shown for 10^{19} eV showers triggering the Hybrid array. Only fluorescence information is used in the reconstruction here.

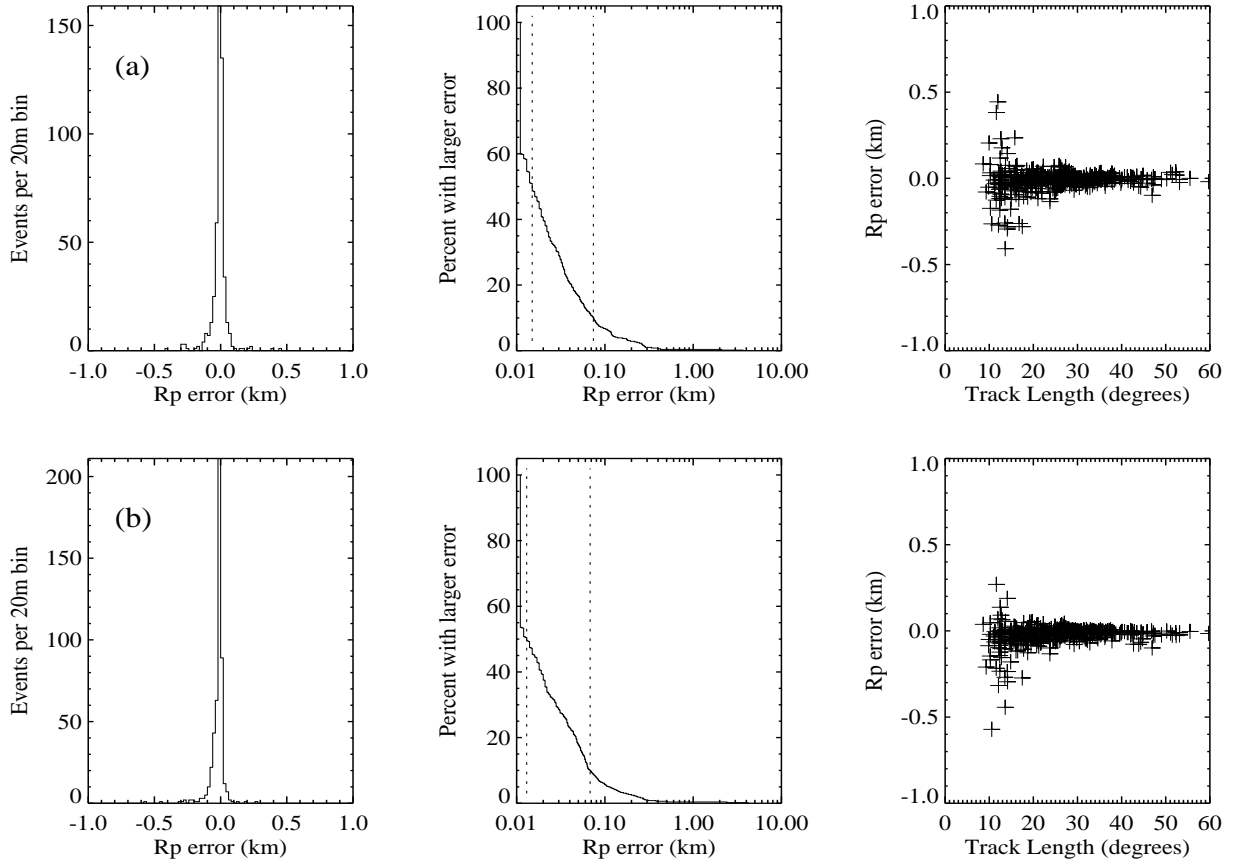


Figure 5.22: Impact parameter error distributions for (a) Method 2 and (b) Method 3 on 10^{19} eV triggered showers. The track length dependence of the error has dramatically lessened.

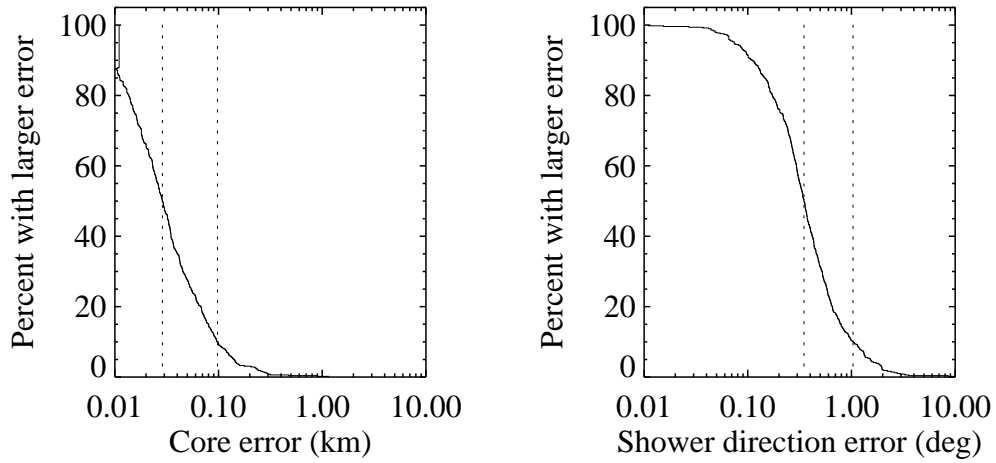


Figure 5.23: The final core location and shower direction errors for showers at 10^{19} eV analysed with Method 2.

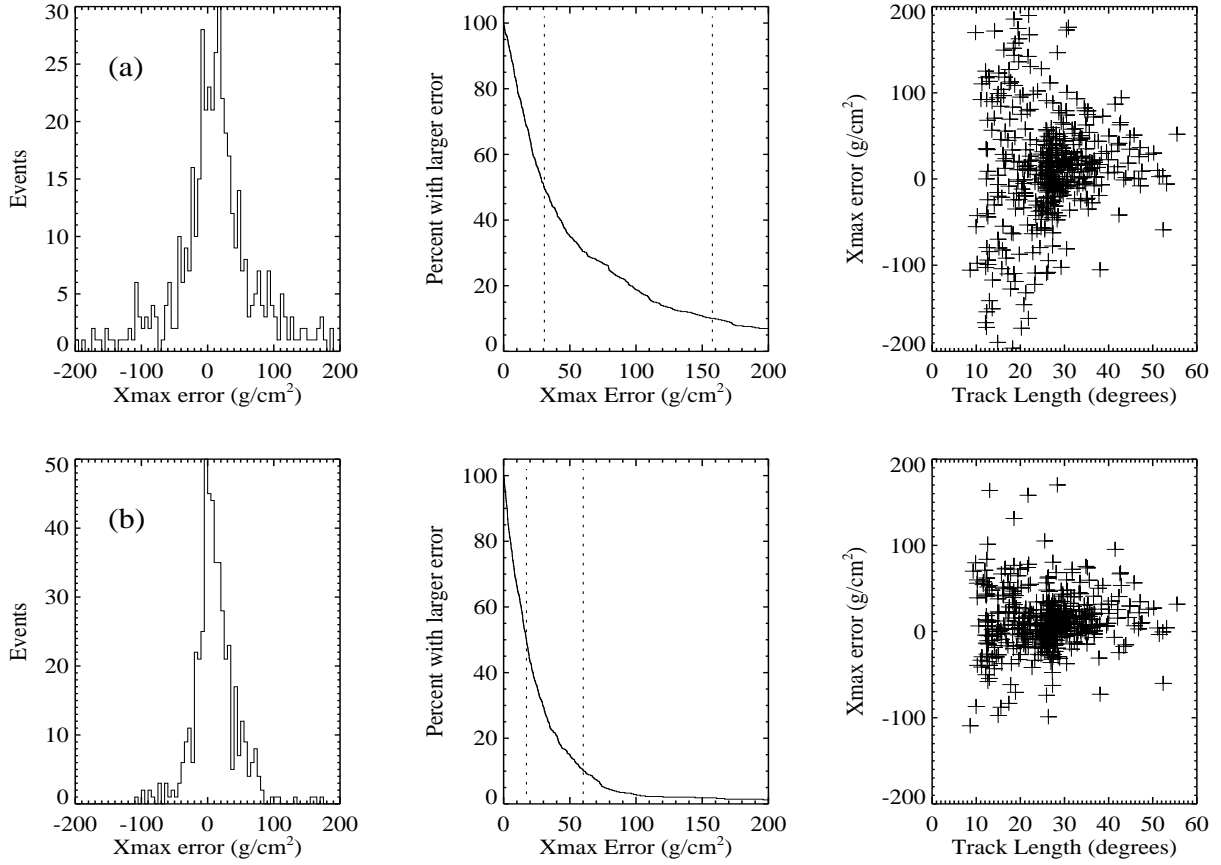


Figure 5.24: Profile reconstruction for 10^{19} eV showers. All showers triggering the Hybrid array have been included here. In (a) is shown the X_{max} error ($X_{max, reconstructed} - X_{max, true}$) for showers analysed using the fluorescence information alone. In (b) are shown the same showers analysed using Hybrid Method 2.

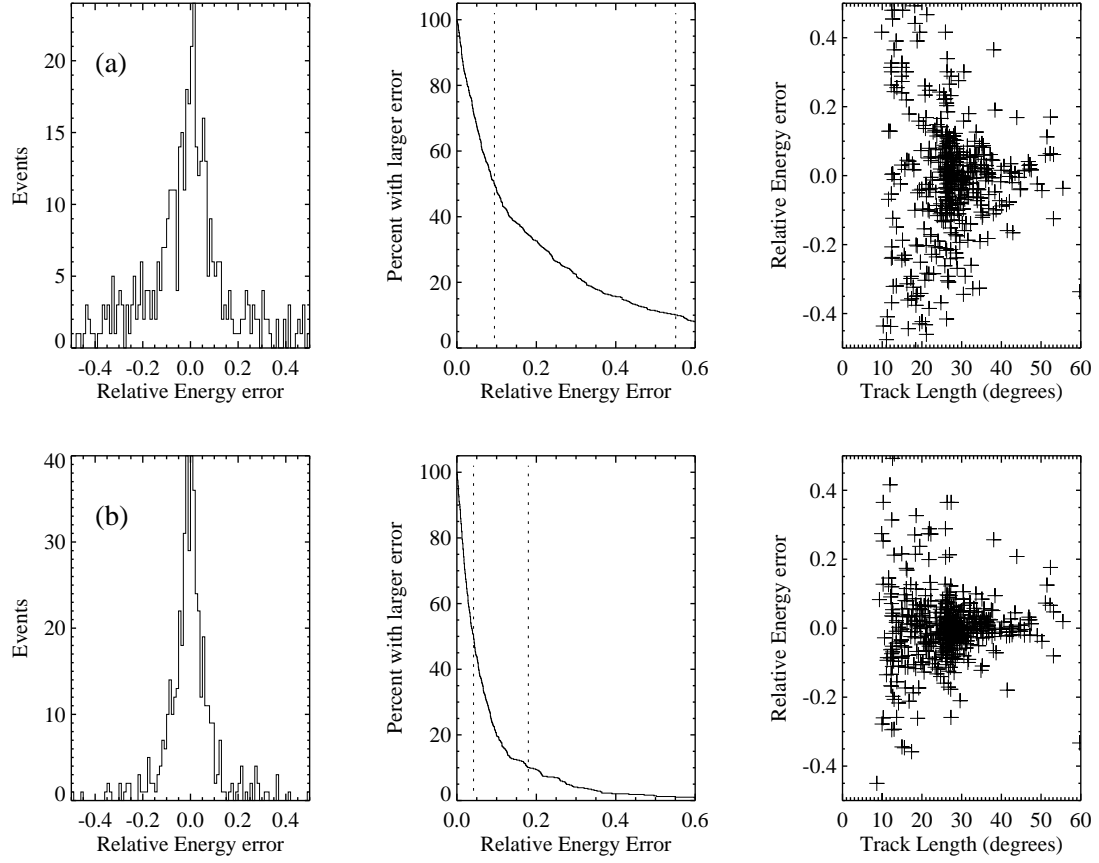


Figure 5.25: Energy resolution $(E_{reconstructed} - E_{true})/E_{true}$ for 10^{19} eV showers analysed with data from (a) the fluorescence detector only, and (b) with Hybrid data using Method 2.

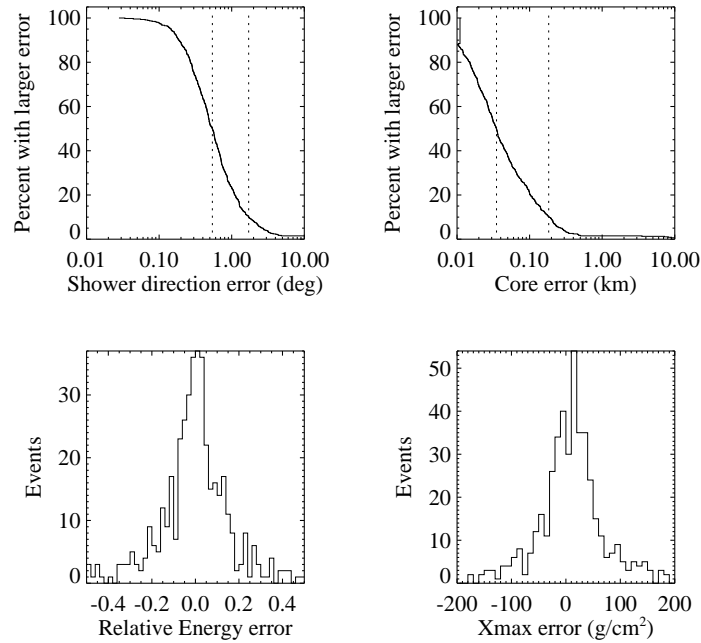


Figure 5.26: Reconstruction of lower energy (10^{18} eV) showers using Method 2.

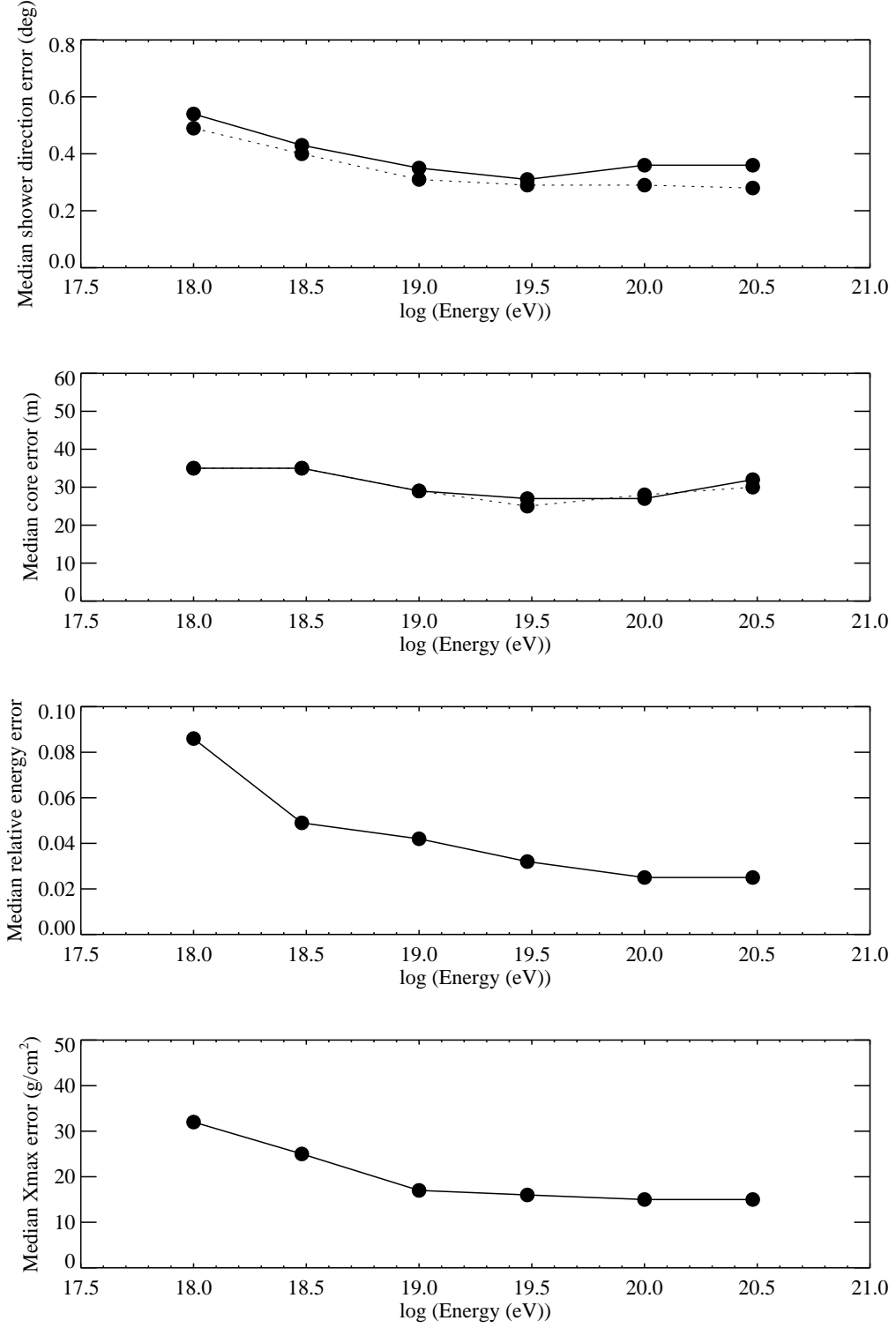


Figure 5.27: Hybrid median reconstruction errors for the three eye, 1.5° pixel system. The errors for the geometrical quantities (shower direction and core) are shown for Methods 2 (solid line) and 3 (dashed line), though the errors are almost identical. The energy and X_{\max} errors are shown for Method 2. A summary of these data, together with 90% errors, is given in Table 5.2.

Chapter 6

Surface Detector Array Design

Water Čerenkov detectors have been selected as the primary detector technology for the Auger ground array. A suitably designed water tank array can adequately address the physics requirements discussed in the previous chapters while proving cost effective and having demonstrated reliability. The reference design presented here calls for an array of 10 m² cylindrical detector units in a 1.5 km spaced triangular grid. In the sections which follow several aspects of the design and performance of the basic surface array units are discussed.

For 20 years a 12 km² array employing more than 200 water Čerenkov units was operated at Haverah Park in the UK[7] to study extensive air showers. The experience gained during that experiment provides much useful information for the Auger project and, in particular, demonstrates that an array based on this technique can operate for a long period with both high stability and low maintenance.

Alternatives to the water Čerenkov technique were considered for the surface detector array. Sandwich detectors, which consist of two thin particle detecting layers separated by a layer of electromagnetic converter such as lead, steel, or even concrete, have been investigated in detail. Both scintillation counters [173][174][175][176] and resistive plate counters (RPC's)[177] were studied. Although the sandwich detectors were found to have suitable performance for this application, water Čerenkov detectors were selected as the preferred design because of their inherent simplicity, the confidence inspired by their previous experimental success, and because the response of the detector to shower components provides advantages lacking in the sandwich detectors.

The altitude of the selected sites for the Auger Observatory, approximately 1400 m above sea level, puts the surface detector array beneath 880 g/cm² of atmosphere, which is near the shower maximum for vertical tracks in the energy range of interest. Because the amount of atmosphere that a shower passes through before reaching the ground increases with zenith angle, most of the showers will be beyond the shower maximum. In this regime the shower particle population can be approximated by an exponential decay in which the electromagnetic component attenuates much more rapidly than the muonic component. As a result, different types of detector produce different effective shower attenuation lengths

depending on their relative sensitivities to these two shower components. For the Haverah Park water Čerenkov array the attenuation coefficient for signal density at 600 m from the shower core was found to be 760 ± 40 g/cm² while for the Yakutsk scintillator array a value of 500 ± 40 g/cm² was derived[7]. (Both sites are very close to sea level.) These results suggest that the water Čerenkov array is less sensitive to atmospheric depth and hence to zenith angle than the scintillator array.

A detector with a large depth to lateral size ratio such as the water Čerenkov detector has another advantage: the projected area in the plane perpendicular to the shower axis falls much more slowly with increasing zenith angle than for a thinner detector. This geometrical effect, combined with the reduction in zenith angle sensitivity discussed in the proceeding paragraph, results in a greater collecting power per detector unit and a more uniform sky view in terms of declination angle. The experimental declination distributions from the Haverah Park and Volcano Ranch arrays which illustrate this point were shown in Figure 3.5.

6.1 The reference design

In its simplest form a water Čerenkov detector can be described as a volume of clear water acting as a Čerenkov radiator viewed by one or more sensitive light detectors. In this application the fact that the water also acts as a massive absorber and converter of the numerous shower gamma rays is very important.

Conceptually, the reference design proposed for the Auger ground array detector unit is a cylindrical volume of water viewed from above by three large (200 mm diameter) PMTs. The interior walls of the tank have a high diffuse reflectivity in the wavelengths of combined maximum Čerenkov light production, water transmissivity, and photocathode sensitivity. The water volume is 1.2 m deep and 3.6 m in diameter for a top surface area of 10 m². A conceptual drawing of the complete ground array detector station is shown in Figure 6.1.

6.2 Detector geometry and array spacing

The required detector area is a function of the array grid spacing and shower threshold energy desired. Since each station entails many fixed costs independent of the detector area (electronics, deployment, etc.), and for given array coverage the number of stations required is inversely proportional to the square of the array spacing, it is important that this spacing should be as large as possible. It is a requirement of the experiment that the array should be fully efficient for showers of energy 1×10^{19} eV and above. For a 1.5 km spacing a detector area of 10 m² will give adequate performance (see Chapter 5). With a spacing of 1.5 km the number of triggered stations will be large enough (15 to 20 units) at the very highest energies ($\geq 10^{20}$ eV) to allow high quality and unambiguous event reconstruction.

In the following we have assumed the dimensions of the reference design described in

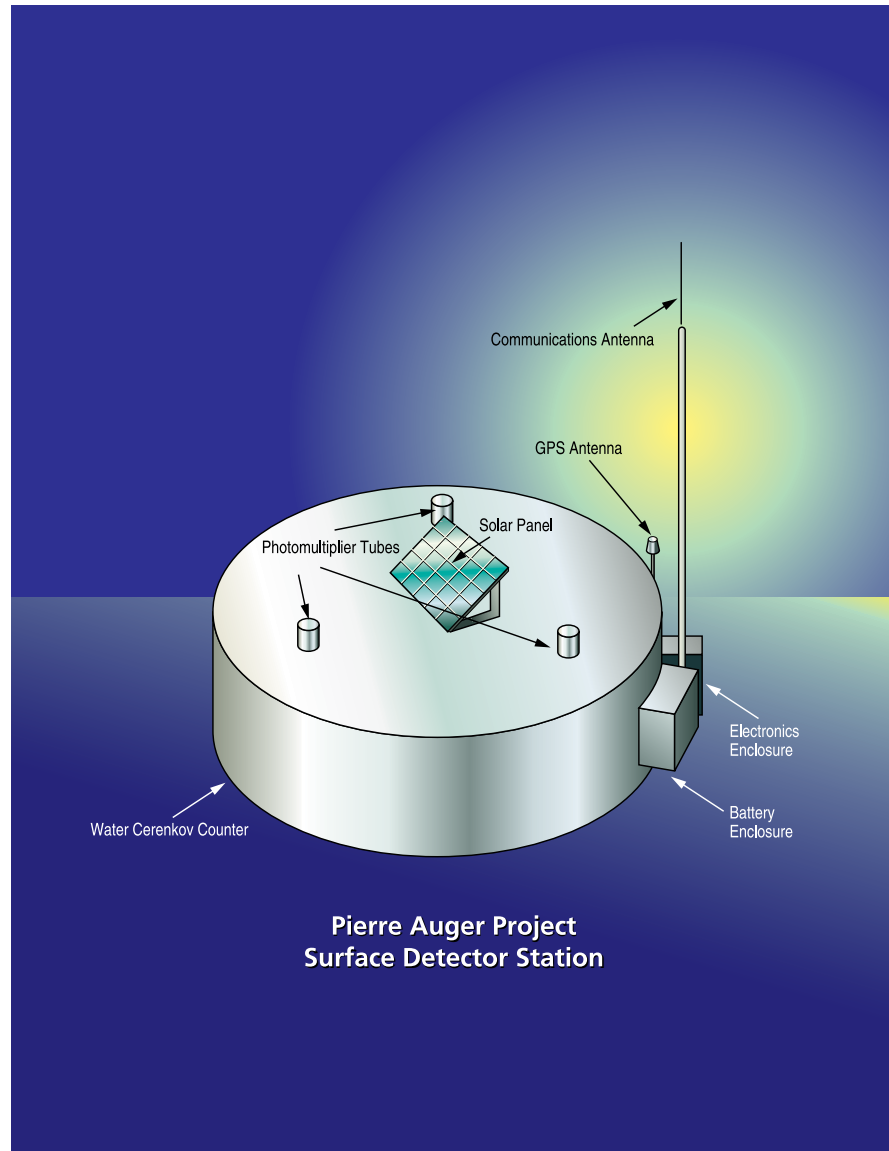


Figure 6.1: Concept for the Auger Project surface detector station.

the previous section. As discussed in Chapter 5, 3.5 radiation lengths of water is sufficient to absorb $\geq 90\%$ of the incident electromagnetic shower particles. A depth of 1.2 m was found to be optimum in some simulation studies[178], although other simulations[179] assuming different tank material properties suggest a slightly greater depth may be preferred to enhance the muonic content information which can be extracted from the differential time/amplitude signal profile.

A single unsegmented tank is also most efficient in terms of the photocathode area required for a given photoelectron yield, i.e., the ratio of photocathode to tank wall area must be maximized because the reflectivity of the tank wall is less than fully efficient. In addition, the cylindrical shape is favored as it is simple and has inherently uniform response to showers of given zenith angle incident from different azimuthal angles.

6.3 PMT positioning and detector uniformity

When reasonable values for the properties of the tank wall reflectivity, water clarity, and PMT performance are inserted in simulations the results indicate that three 200 mm PMTs will be sufficient for the $10 \text{ m}^2 \times 1.2 \text{ m}$ deep reference design detector. When the three PMTs are arranged looking downward from the top surface of the tank a mean photoelectron yield of 50 in response to a vertical through-going muon is easily obtained, which results in acceptable Poisson fluctuations. (When deionized water was used in a prototype tank at Fermilab with a Tyvek lining, yields exceeding 150 photoelectrons per vertical through-going muon were observed.) Very good proportionality between Čerenkov light produced and photoelectron yield is obtained when the PMTs are placed at 120° intervals on a circle of radius 1.2 m ($2/3$ of the detector radius.) The uniformity of response is shown in the upper part of Figure 6.2, representing a simulation of the reference design detector, and in Figure 6.3, which displays the results of measurements made with a $6.6 \text{ m}^2 \times 1.2 \text{ m}$ deep test tank operated at Fermilab. (The test tank differs from the reference design in that it had a slightly smaller area and had four 200 mm diameter PMTs arranged in a circle with a diameter $2/3$ that of the detector.) Measurements with the test tank[180] also demonstrated that the response was proportional to the track length through the detector for inclined tracks.

The uniformity of response would be seriously degraded if Čerenkov radiation were to impinge directly on the photocathode of any of the PMTs as would occur, for example, if the PMTs were mounted at the bottom of the water tank looking up. This is illustrated by the simulation results in Figure 6.2.

There are other ways in which the photocathodes can be directly illuminated with Čerenkov radiation and hence produce an anomalously large signal. The angle of Čerenkov emission in water does not exceed 42° but when a particle passes through the tank with a zenith angle greater than 48° direct illumination is possible. Use of plane-faced PMTs would completely suppress direct illumination up to the maximum 48° angle between particle trajectory and the zenith, and hence would be preferable to the more usual hemispherical design, although the manufacture of plane-faced PMTs may not prove to be cost effective in this large size. Particles with large angles relative to the zenith (our proposed accep-

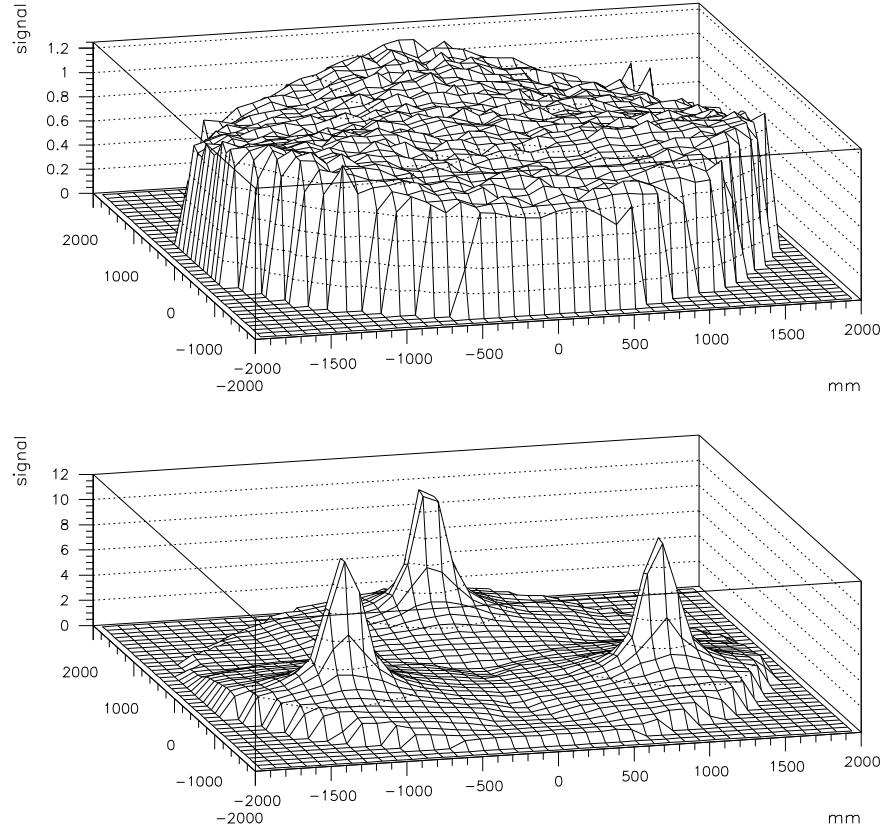


Figure 6.2: Simulated non-proportionality plot for the reference design water Čerenkov detector unit. The upper plot shows response with PMTs placed at the top looking down, and the lower plot is identical with the PMTs at the bottom looking up. Many 1 GeV muons were injected vertically at random positions over the detector top surface, and the resulting photoelectron yields averaged in 10 cm square bins. The vertical axis scales are relative to the overall mean signal in the down looking case.

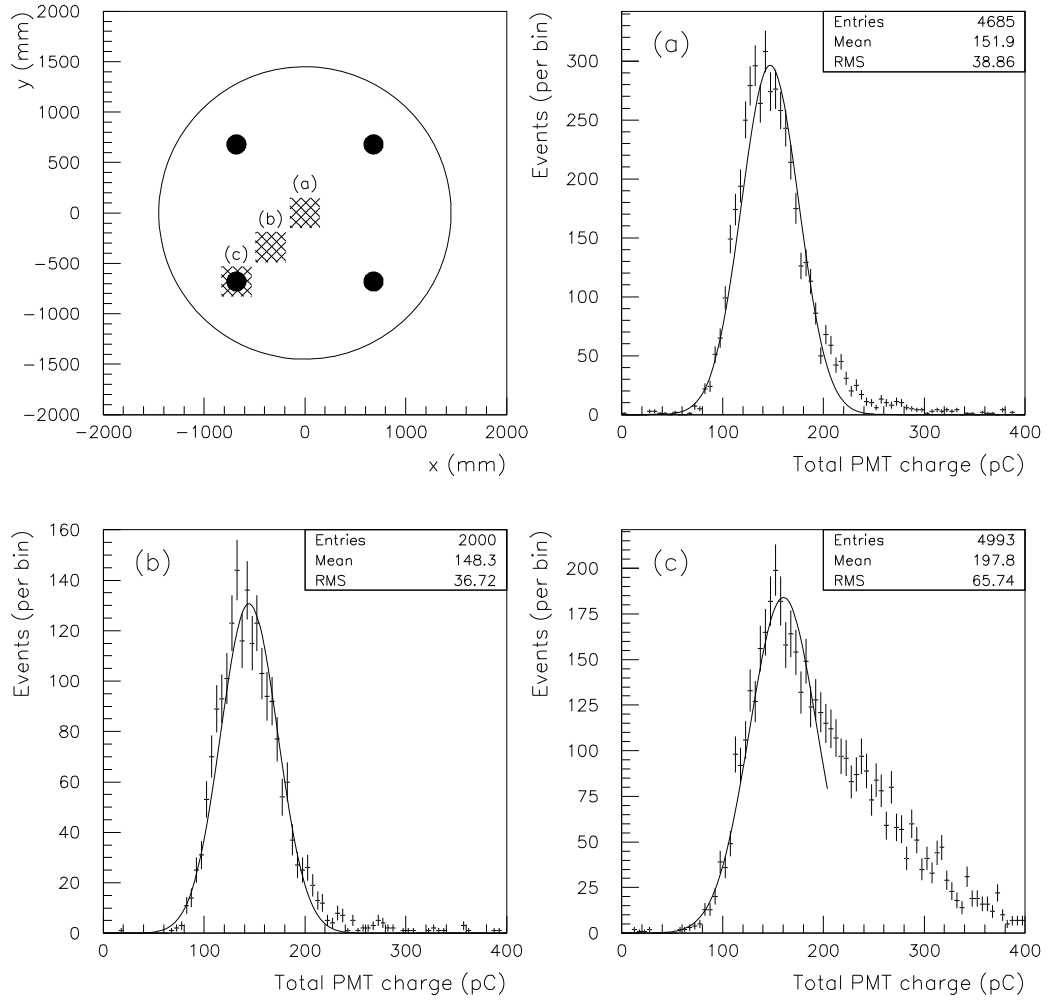


Figure 6.3: Test results from the cylindrical 6.6 m² × 1.2 m test water Čerenkov tank. The top left plot is a diagram of the detector top surface showing the positions of the 4 PMTs. Also indicated are the positions of scintillator paddles placed above and below the tank to trigger on through-going muons for the three calibration runs labelled (a), (b), and (c). The charge distributions shown are the analog sum of the signals from all 4 tubes. The high side tail of plot (c) is due to muons which pass through the tube itself.

tance extends to primaries with zenith angles up to 60°) will inevitably produce some direct Čerenkov illumination and hence some nonuniformity will necessarily be tolerated in these cases. In addition, decays of muons which stop in the detector tank volume will produce an unavoidable source of direct photocathode illumination.

Shower particles arrive with a large spread of angles relative to the shower axis although the high energy particles which produce significant Čerenkov radiant track lengths have a much smaller spread of angles. (Shower simulations indicate that particles with energy >10 MeV have median space angle deviation of $<20^\circ$ relative to the shower axis.) Particles do not scatter significantly away from their incident trajectory while passing through the water until the last few centimeters of the track, where little or no Čerenkov radiation is produced.

An increase in the number of photoelectrons would be possible if a water-soluble waveshifter such as 4-methyl umbelliferone[181][182] were added to the water. However, since the emission from a dissolved waveshifting material is isotropic, the “pseudo-direct” photocathode illumination due to a particle whose trajectory passes very close to a PMT would produce an anomalously large number of photoelectrons, leading to a degradation of the proportionality between total radiated Čerenkov light and detected signal.

Čerenkov radiation produced in the glass of the PMT face has not yet been simulated. The effect is minimized by positioning the PMTs looking downward and in direct contact with the water. The effect of muons passing through the PMT is evident in Figure 6.3c.

6.4 Mechanical realization and prototypes

The Haverah Park detectors were made from galvanized iron tanks of rectangular cross section ($1.85\text{ m} \times 1.24\text{ m} \times 1.29\text{ m}$ high) filled to a depth of 1.2 m. The walls (sides, top and bottom) were lined with a white diffusing PVC material supplied by ICI under the commercial name “Darvic.” The tanks were air tight and were opened only to replace defective photomultiplier tubes (on average once every five years). A single 100 mm diameter plane-faced PMT was positioned in the center of the top surface with the face dipped into the water. Only two tanks were refilled during the entire 20 year run of the experiment, and the loss of performance over this time was less than 10%. There were 225 tank units deployed in clusters of up to 34 m^2 total top surface area. Each cluster was housed in a heated, concrete floored wooden hut.

The Auger Project will require detector units which will withstand a harsh outdoor desert environment for 20 years with very little maintenance. They must withstand high winds, hail, temperature extremes, and casual vandalism. An important step in the Project is to develop a detector which meets these durability requirements as well as the performance requirements discussed earlier at a minimum cost. To this end, several prototype detectors have been built and operated and more are under construction. All of the prototype tanks have performed well as cosmic ray detectors and each one has been used to investigate different practical aspects of hardware.

A carbon steel tank was fabricated, fitted with three Hamamatsu R1408 200 mm PMTs

(the type used on all of the prototype tanks discussed here) and operated at Fermilab[183]. The perceived advantages of carbon steel are low cost and ease of fabrication by commercial processes as well as great durability and strength. The greatest challenge is seen as the need to provide a durable protection of the water from contamination by rust, so that the steel of the tank should will not come into contact with the water of the detector. A wave shifting epoxy paint was developed[184] for Fermilab which used the same paint technology normally used for water tanks in domestic and industrial water supplies, a technology which results in a paint lifetime of at least ten years in water tank service (and perhaps much longer life in the service planned here because the paint lasts longest when fully submerged, not when partially exposed to air as in more ordinary water tanks.) This paint increased the photoelectron yield by 70% over ordinary white epoxy paint in tests performed in a small (55 gallon drum) test water Čerenkov detector. (A careful quantitative extrapolation of the results to a tank the size of our reference design has not been performed.) Initial tests in the Fermilab prototype tank were made with the waveshifting paint on the inner surfaces. The photoelectron yield for a through-going muon was approximately 36 when the tank was filled with domestic water treated only by filtration through a one micron absolute filter.

An even more effective reflector of light in the important 300-400 nm wavelength range is Tyvek, a fibrous polyolefin manufactured by Dupont for various industrial and commercial purposes. The diffuse reflectivity was shown in Figure 5.8. When the Fermilab prototype tank was lined with Tyvek the number of photoelectrons per vertical through-going muon increased to about 56. Later tests in which the water was deionized by passing through ion exchange resins produced photoelectron yields exceeding 150. Tyvek is promising as a reflective inner surface on the tank wall or as the inner lining of a bag which would contain the water. A bag might be fabricated from a lamination of Tyvek and polyethylene. In the case of a bag system, the tank structure need only support and protect the bag and other detector components and this may lower the overall cost of the detector because the structure would not be required to be corrosion-free or even to be completely water tight. Perhaps a tank structure based on corrugated, galvanized steel would be cost effective. Test laminations of Tyvek and polyethylene have been made with encouraging results.

A prototype tank has been operating at AGASA[185] which has the same geometry as the reference design described herein and also uses a Tyvek lining. The tank structure in this case consists of a relatively light, nonrigid plastic structure supported by a steel frame, a technology commonly used for water storage systems in Japan. When AGASA triggers on a giant air shower, the signals from the three tank photomultipliers are recorded by a FADC system. Shower reconstructions are available from AGASA for each event so it is possible to compare the prototype tank's data with simulations. A sample event is shown in Figure 6.4. The time dispersed signature of the giant air shower far from the core is clearly visible with correlated late pulses seen in all three PMTs. It is clear that individual particles are being recorded. The data are in good agreement with the predictions of the simulations described in earlier chapters. Studies with this unique prototype arrangement are continuing.

A prototype detector has been fabricated and operated at the Tandem Laboratory in Buenos Aires[186]. The tank for this detector is 0.68 mm thick type 304 stainless steel welded by an automated fusion welding process. The very thin wall was selected to minimize material

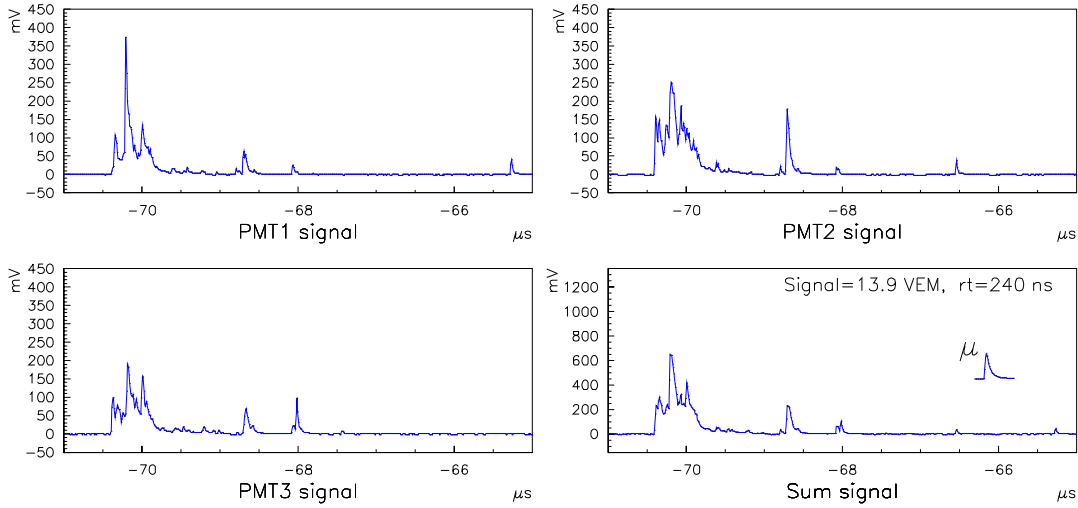


Figure 6.4: An extensive air shower event observed at a core distance of ≈ 1 km by the prototype Auger tank at the AGASA array in Japan. The signals from each of the three PMTs are shown, together with their sum. The shape of an average single muon is also shown on the same plot. The integrated shower signal is about 14 vertical equivalent muons.

costs, but otherwise this is a common technology for domestic water tank fabrication. The water depth and PMT positions may be varied to study the effect of these parameters on performance, and measurements have been made with the bare polished stainless interior and with a Tyvek lining. Although rusting was seen at the welds of the early Fermilab 6.6 m² stainless steel test tank due to chromium carbide precipitation in the weld zone, no rusting has been observed either on the inside or outside surfaces of the Tandar tank, suggesting the careful temperature control of the automated welding process has eliminated this potential problem. Because of the potential for chloride-induced stress corrosion cracking in the salty desert environment in which the detectors will be installed, further careful alloy selection or a protective finish may be required, or an installation which minimizes exposure to salt may be appropriate. This would not be important, however, if the Tyvek lined bag were to be selected as the water container with the stainless steel tank serving only as a protective support.

Additional prototype tank designs under consideration include two types of polyethylene tank: one type would be made by rotational molding and the other would be made by the extrusion welding process. These technologies are being considered because they are resistant to corrosion, have expected lifetimes without maintenance that are more than adequate for the Auger Project, are very robust (with wall thicknesses of 12-18 mm), and may prove to be cost effective. While either type of polyethylene tank construction could accommodate the Tyvek bag liner discussed above, the type made with the extrusion welding process could be formed of polyethylene plates which already had the Tyvek laminated to the inner surface, eliminating the need for the bag. Studies of these possibilities are continuing in the United States, Brazil, Mexico (especially tank technology) and China (especially Tyvek bag technology).

6.5 Water purification and stability

During the construction of the Auger surface detector arrays about 20000 tons of suitably pure water will be needed at each site. The Haverah Park tanks were filled with untreated water from a nearby borehole in magnesium limestone. That water proved to be adequate. Suitable sources of natural water are available near the Auger Observatory sites and, if required, the local water can be treated with standard industrial processes to suitable purity. (The water used in ordinary power plants is typically no less pure than that required for the Auger Project, and there exists a large industry which can supply that water.) The transport of water to each individual detector site represents a straightforward challenge, probably requiring substantial tanker trucks capable of carrying the 12 ton water load for each detector tank. For the Observatory locations selected in Argentina and the United States, truck access to most of the detector sites during most of the year should not be particularly difficult.

Some preliminary tests of water purification via filtration were conducted at Fermilab using a 55 gallon drum adapted for use as a small water Čerenkov tank. One Hamamatsu R1408 200 mm diameter hemispherical PMT was mounted in the center of the top surface. The tank interior was lined with Tyvek and the tank completely filled with water. A trigger on through-going muons was established with a scintillation counter telescope. The tank was successively filled with distilled water, unfiltered water from the Fermilab domestic water supply, domestic water filtered with a 3 μm absolute filter and domestic water filtered through a 1 μm absolute filter.

Figure 6.5 shows the average time versus amplitude profiles for sets of 100 muon tracks for each grade of water. Repeatability was checked for each fill of water and also for refills of the same type of water. The filtered water results were found to be fully reproducible but some drums of distilled water from the Fermilab stockroom gave better results than others, a result suggestive of contamination in some of the distilled water containers. Two examples are shown, one being little better than the 1 μm filtered water.

The tests conducted earlier with the Fermilab prototype tank showed the number of photoelectrons tripling when the 1 μm filtered water was deionized. This very large increase in performance is not necessarily inconsistent with the results shown in Figure 6.5 because the extrapolation to a full size tank would be expected to show a greater dependence on water clarity due to the increased path length for the average Čerenkov photon. The water in the Tandar Laboratory prototype tank was treated by reverse osmosis (less effective but less expensive than ion exchange resin treatment) and the water in the AGASA prototype tank was untreated domestic water. All prototypes had acceptable performance (defined as at least 50 photoelectrons per vertical through muon), suggesting water purity will not be a critical issue.

The stability of the water, however, is critical for the successful long term operation of the experiment. There are two sources of contaminant to be considered: chemical activity and biological activity. The former is typified by rust, known to have a strong adverse impact on light transmission in the water. This can be controlled by material selection,

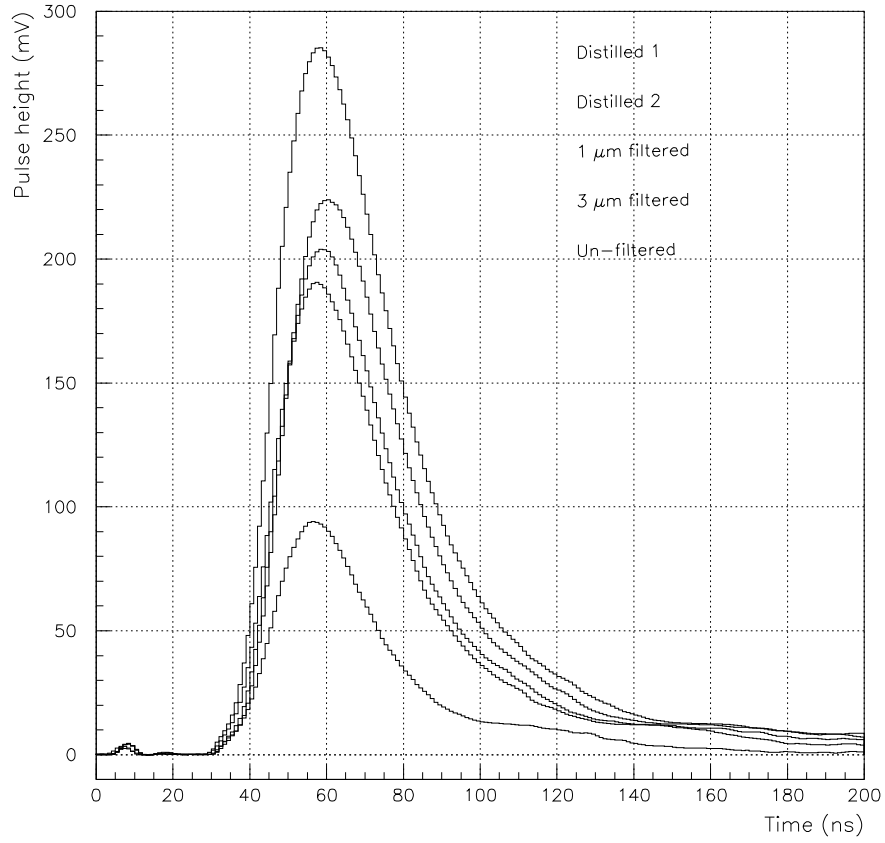


Figure 6.5: Water filtration test results. The time/amplitude profiles shown are each the average of 100 vertically penetrating muon events recorded on a 400 mega sample per second (MSPS) digital oscilloscope. (A cut has been made to remove multiple muon air shower events).

separating any rusting component from the water by using either a plastic barrier (e.g., a Tyvek-polyethylene bag) or a paint barrier (e.g., the epoxy-based paints.)

Biological activity in the water is being studied carefully [186][187], even though Haverah Park took no special precautions, and had no difficulties during the lifetime of that experiment. Bacterial activity can be suppressed by controlling the chemical impurities in the water (essentially depriving the bacteria of nutrients and a hospitable environment), by adding a biocide to the water, by sterilizing the water before installing it in the sealed detector tanks, or by a combination of these techniques. The choice of techniques will depend on the details of the water available at the selected sites and on the results of ongoing studies of bacterial growth in water.

Chapter 7

Fluorescence Detector Design

The primary role of the fluorescence detector is to measure the longitudinal development profiles of air showers in the atmosphere. The longitudinal profile gives a direct measure of the electromagnetic shower energy, and, for a given total energy, the depth of maximum shower size is correlated with the mass of the primary. The set of showers measured by the combination of both the surface array and the fluorescence detector (hybrid showers) will be the basis for the most reliable energy spectrum and composition determination. It is important to maximize the fraction of the surface array showers which are measured also by the fluorescence detector. The Fly's Eye experience demonstrates that operating the detector in clear, moonless conditions limits the duty cycle to 10%. To ensure that the hybrid shower set is not an even smaller subset of the surface array showers, it is essential that the fluorescence detector measure every shower accepted by the surface array. It is therefore required that its aperture include the entire aperture of the surface array.

The design of the fluorescence detector is guided by this aperture requirement together with specifications for the quality of longitudinal profile measurements. At any fixed energy, the expected depths of maximum span a range of approximately 100 g/cm^2 as the nuclear mass varies from proton to iron. A resolution of 20 g/cm^2 in the depth of maximum X_{max} is achievable and highly desirable for analyzing the primary mass distribution. Energy resolution of 10% is achieved by signal-to-noise requirements which have been shown previously (cf. 4.4.3) to lead to a 20 g/cm^2 X_{max} resolution.

These aperture and sensitivity requirements have been used to develop the reference design. Essential design parameters include the number of eyes, the elevation angle coverage, the pixel angular size, the light collecting area, the waveform time resolution, and the trigger conditions. The arguments for the chosen design parameters have been given in technical notes and will only be summarized briefly here. The design is based upon proven principles implemented in the High Resolution Fly's Eye (HiRes)[120].

Detailed simulation of the reference design has been done, and the results are summarized in chapter 5. Further details can be found in [137]. The reference design has been shown to meet the aperture and sensitivity requirements.

7.1 The site layout

At each of the two Auger Observatory sites there will be multiple separate optical detector stations or “eyes”. A layout with just a single eye, though capable in principle of achieving good shower reconstruction, suffers from the fact that it must be able to detect showers out to the edge of the array (31 km distant). This is approximately 3 horizontal attenuation lengths. Although adequate light signals could be collected with large enough mirrors, inferring the shower size from the small fraction of remaining light is subject to uncertainty due to uncertainty in the attenuation. Because of the exponential attenuation, the fractional uncertainty in the shower size is given by the fractional uncertainty in the atmospheric attenuation length *times the distance to the shower measured in attenuation lengths*. It has not been demonstrated that the aerosol density distribution can be monitored with sufficient precision to allow profiles to be measured with our required accuracy at a distance of 30 km. To ensure a robust design, it is worth a small additional cost to build multiple eyes and reduce the typical viewing distance. The hardware costs are not significantly greater for 3 moderate eyes than for a single far-sighted eye with smaller pixels and larger mirrors.

The specific arrangement of the eyes has not been definitively determined and may be based partly on land topology at the chosen sites. There is an advantage in building the eyes on elevated terrain so that they look up through less of the aerosol mixing layer. Two suitable arrangements are shown in Figure 7.1 and in Figure 7.2. The “Superman” configuration has 3 identical eyes, each viewing 360 degrees in azimuth. The “filled hexagon” configuration would use the same set of telescopes as the Superman configuration, but two of the eyes would be divided into 3 segments, each of 120 degrees azimuth coverage. The six partial eyes would be placed at the vertices of a regular hexagon, looking inward. One full (360-degree) eye would be at the hexagon’s center. The filled hexagon option offers more redundant coverage of the Auger array area [140]. Compared to the Superman configuration, there are more showers measured by 2 eyes, 3 eyes, etc. The highest energy showers might be measured by all 7 eyes. With this configuration, the fluorescence detector wastes very little aperture on showers landing outside the surface array, and even at threshold shower energies there is a significant multi-ocular viewing aperture. The Superman configuration, on the other hand, obtains some stereo fluorescence aperture for showers outside the periphery of the surface array [141]. It therefore extends the total aperture for well reconstructed fluorescence events. It also requires less site preparation and operation than the filled hexagon arrangement.

In either case, the telescopes will be arranged to cover an elevation angle range from 2° to 30° . This is adequate for measuring the longitudinal profiles of showers with cores distant enough so that the scintillation light is not dominated by direct Čerenkov light. A 360-degree eye will be made up of 45 telescopes, 23 viewing a low elevation altitude ring and 22 an upper elevation ring. Each mirror unit will have a field of view of $16^\circ \times 14^\circ$.

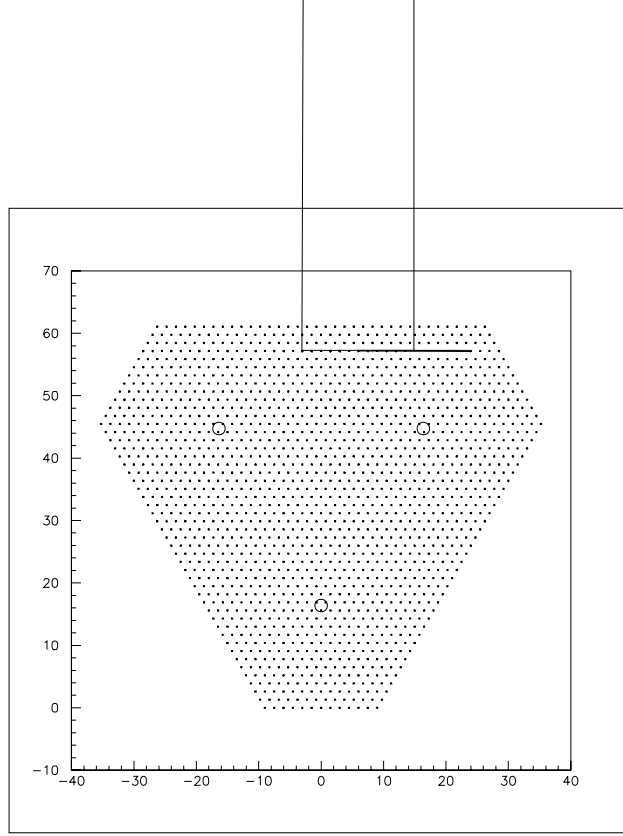


Figure 7.1: Superman layout. The long edge is 52.5 km, the short edge 18 km. There are 1596 ground stations enclosing an area of 2970 km^2 . The three eyes (circles, not to scale) are separated by 32.74 km. Each eye is expected to measure showers at least to a distance of 17.8 km.

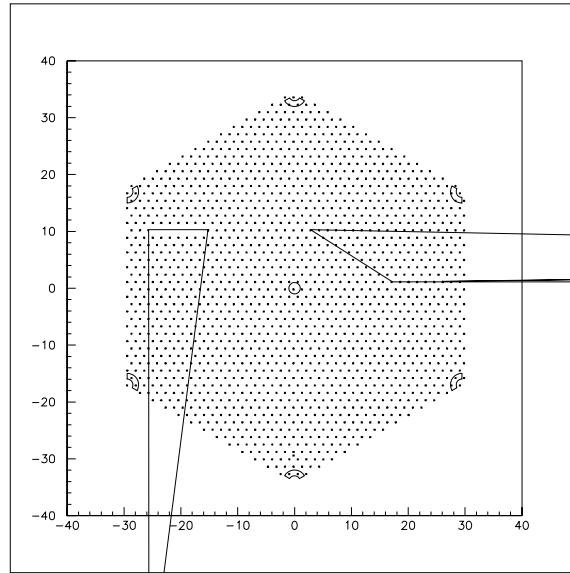


Figure 7.2: Filled Hex layout. The edges are 33.9 km in length. The central detector views a full 360° of azimuth. The detectors at the vertices each view 120° azimuthal regions centered on the central detector.

7.2 The telescope design

Primary design parameters for the telescope are the mirror area and the pixel solid angle. To achieve the S/N sensitivity imposed by the longitudinal profile resolution criteria, it is possible to trade one against the other, since

$$S/N \sim \frac{\text{mirror diameter}}{\text{pixel angular diameter}}.$$

A fundamental constraint is that the pixel size should not exceed a 1.5-degree diameter. Otherwise the angular resolution (finding the shower-detector plane) is insufficient for converting the measured light flux from the different parts of the shower into a longitudinal profile of the required accuracy. The simulations reported in chapter 5 demonstrate that 1.5-degree pixels are adequate.

There are good reasons to make the pixel size as large as the geometric reconstruction allows. A major reason is cost. Over the range of interest, it is less expensive to increase S/N with larger mirrors than by increasing the number of pixels. Even if cost were not a consideration, however, big pixels are desirable. As long as the shower axis geometry is known, the fluorescence light flux measured as a function of time gives the shower size as a function of atmospheric depth. It is advantageous to minimize detector complications in recording the light flux as a function of time. If the focused spot of light remains within the active region of a single PMT for an extended time, that is better than constantly crossing PMT boundaries. These considerations have led to the pixel size of 1.5 degree diameter.

With 1.5-degree pixels, the longitudinal profile resolution requires mirrors of 1.5 m diameter. Each is to be a spherical concave $f/1$ mirror with an associated camera at its focus. The camera will house a hexagonally packed array of 121 (11×11) pixels. Each hex-shaped pixel will have the equivalent area of a 1.5° diameter circular pixel. This will be accomplished with phototubes of the prescribed size and shape or with smaller phototubes augmented with Winston cones or Fabry lenses. Optical filters, chosen to remove most of the light outside the nitrogen fluorescence bands, will be placed ahead of the phototube faces.

Each pixel element will be attached to integrating flash ADC electronics which will digitally measure its signal every 100 ns. This time slice is smaller than the light pulses in individual PMTs, which can vary from about 100 ns for nearby showers approaching the eye to about $4 \mu\text{s}$ for the most distant showers going away from the eye (cf. Sec.4.4.3). In most cases, this time slicing will provide measurements of the pulse duration and pulse shape which are useful for the timing information used in the geometric reconstruction as well as augmenting the amplitude information in fitting the shower detector plane. To achieve good trigger sensitivity to the low amplitude distant showers, a running sum of perhaps $2 \mu\text{s}$ duration will be used to discriminate pixel “hits.” For at least some part of almost any track, the pixel pulse duration will be less than $2 \mu\text{s}$. The system will be designed to recognize, in real time, the temporal and spatial patterns of phototube hits characteristic of real cosmic ray showers. It should also be noted that a shower traverses less than 4 g/cm^2 of atmosphere in 100 ns, yielding a very fine segmentation of the longitudinal profile (if the S/N is high enough to take advantage of such fine segmentation).

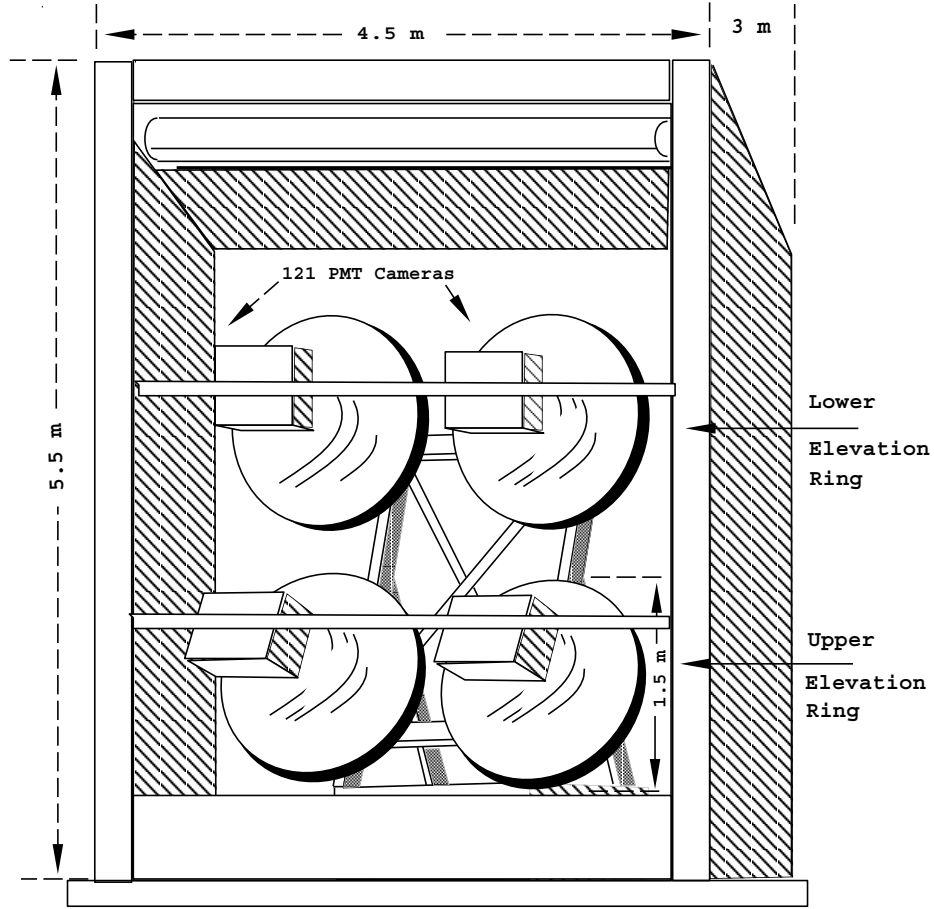


Figure 7.3: Possible Optical detector enclosure. Such a configuration contains four mirror units, two with a high altitude view, two with a low altitude view.

Several trigger levels will be implemented in each eye. The simplest, a sequence of hit phototubes in a linear pattern, will cause the associated data to be held locally for a time long enough to be available if trigger information comes either from the surface array or from another eye. The next level trigger, which utilizes the results of a rudimentary trajectory fit, will result in the information being broadcast to the other eyes and the surface array for possible confirmation. If still stronger criteria are satisfied, the data will be saved as a probable track, even in the absence of corroborating information.

At each 360-degree eye there will be 12 mirror buildings or enclosures and a central triggering and communication facility. 11 of the mirror buildings will house mutually mounted sets of 4 mirror units. One building will house a single mirror unit. The combined mirrors in each mirror building will observe both the upper and lower elevations for two side-by-side 16° azimuthal intervals. A conceptual drawing of a possible building is shown in Figure 7.3. Such structures with automatic roll doors have been successfully implemented by the High Resolution Fly's Eye (HiRes) project.

A sophisticated atmospheric monitoring system will be an integral part of the fluores-

cence detector system. In order to adequately characterize the volume of atmosphere above the surface array one must make periodic measurements of both the particulate distribution and cloud cover. This system will include multiple steerable LIDAR stations, an array of vertical Xenon flashers and several high-powered steerable UV lasers.

7.3 Alternative Designs

The reference design described above is based on techniques which have been well tested by the Fly's Eye and the HiRes prototype detectors. It is a conservative design which is certain to produce the required resolution. Some variations on this technology have been proposed for the Auger fluorescence detector but are not part of the reference design because they have not yet been demonstrated in practice. The modifications may offer better performance at reduced cost.

7.3.1 The Dual Mirror Concept

A novel detection scheme presently being studied is the *dual-mirror* system[138]. In this scheme, instead of a single telescope viewing any portion of the sky, there are two telescopes with almost identical fields of view. If each telescope has 2.5-degree wide pixels, say, then their fields of view would be offset from each other by 1.25° in elevation and 1.25° in azimuth. The overlapping views of the two mirrors A and B are illustrated in Figure 7.4. The instantaneous image of a shower will be seen in each mirror in one of its 2.5-degree pixels, but the overlap of the two pixels will isolate the position of the shower spot to a $1.25^\circ \times 1.25^\circ$ region of the sky at that instant. Such a system has been proposed because it provides 1.25° resolution with only 72 pixels instead of the 144 which would be needed with a single telescope. The cost is significantly reduced. Enhanced trigger efficiency is also expected since the mirrors, operating in coincidence, automatically reject most noise triggers. This method of suppressing noise triggers has been exploited extensively in atmospheric Čerenkov astronomy. In addition, an important advantage of this technique is that the spot of light from the shower front is almost always cleanly contained within some physical pixel's field of view, and the light flux is measured by each PMT for a longer duration. Pixel boundaries are less problematic in obtaining a reliable light flux as a function of time.

7.3.2 Wide angle Schmidt telescopes

The number of buildings and supporting equipment for the telescopes can be reduced if the field of view of each mirror is extended from approximately 15×15 degrees to 30×30 degrees. For a simple spherical reflector, such wide angle observations have unacceptably large coma aberration. A way to eliminate the coma is to use a diaphragm at the mirror's center of curvature[139]. The area of the diaphragm is then the light collecting area. The mirror must be much larger than the diaphragm to receive all the light which comes through the

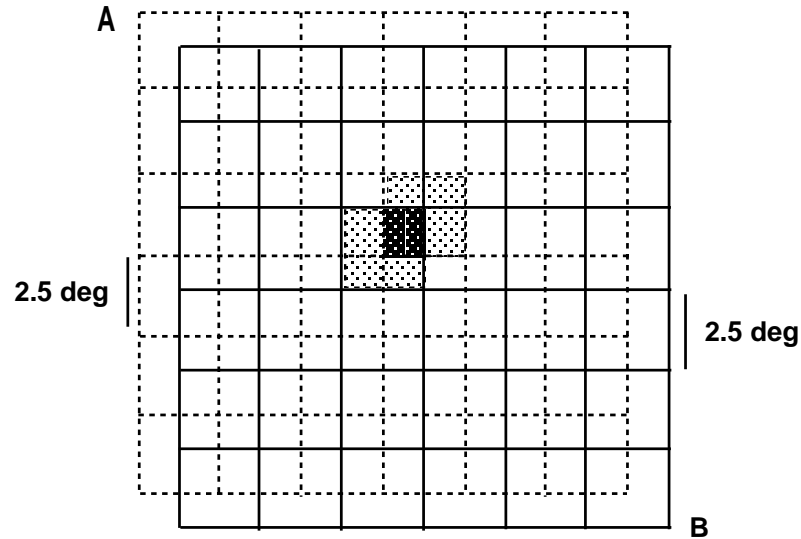


Figure 7.4: The fields of view for dual mirrors A and B. Each mirror has 72 pixels in its focal surface, each pixel having a 2.5° width. The fields of view are displaced from each other by 1.25° in azimuth and 1.25° in elevation. The signal can be localized to a 1.25° square by the intersection of a pixel in mirror A with a pixel in mirror B.

diaphragm over the large range of arrival directions. The focal surface must be part of a sphere which is concentric with the mirror at approximately half the radius. This method offers several important advantages: (1) Coma aberration is eliminated, and the spot is almost uniform even over the larger field of view. (2) The reduction in the number of buildings, electronics crates, calibration devices, etc., can reduce the cost of each eye. (3) The opening to the outside is only the diaphragm, so the building doors can be smaller and therefore less expensive and more reliable. (4) By covering the diaphragm with UV transparent material (like thin mylar), it may be possible to keep dust and dirt out of the telescopes and maintain them at nearly constant temperature, thereby eliminating important causes of sensitivity variation.

Chapter 8

Electronics Systems and Software

This chapter of the report deals with the electronics systems and associated software for the experiment, focusing on the ground array. These systems acquire data from the detectors, process the information, generate an event trigger, transport the data to a central site, archive it, and make it accessible to the collaboration. The optical fluorescence detector electronics and the lower levels of the fluorescence detector trigger will not be discussed in this chapter. They are briefly discussed in Chapter 7.

We begin with a discussion of the electronics located at each station, and follow the data flow back to the central site. Interspersed through the text we will introduce the various components of the multi-level triggering scheme and then tie that information together in a section dedicated to triggering. Figure 8.1 shows the block diagram of the station electronics. Each of the blocks will be discussed in more detail in the following sections.

8.1 Station Electronics Packaging

A careful balance must be kept between modularity, to allow each component of the electronics to be optimized, and a requirement for exceptional reliability, which demands a minimum of interconnections and modules. For example, in order to keep the mean failure rate less than 1 station per day per site, a mean time between failures of 5 years for the station electronics system is required.

The electronics logically splits into four main components: front end, station controller, timing, and communications. It will be powered by solar power through DC-DC power converters. To save the power consumption inherent in bus drivers the front end and communications boards will be incorporated into the final design as daughter boards of the station controller or a motherboard. For reliability we envision that these may be soldered in place. Provision will be included in the final design to allow the insertion of diagnostic modules and for future expansion. For example, the electronics for an air Čerenkov detector could be plugged into one of the spare slots.

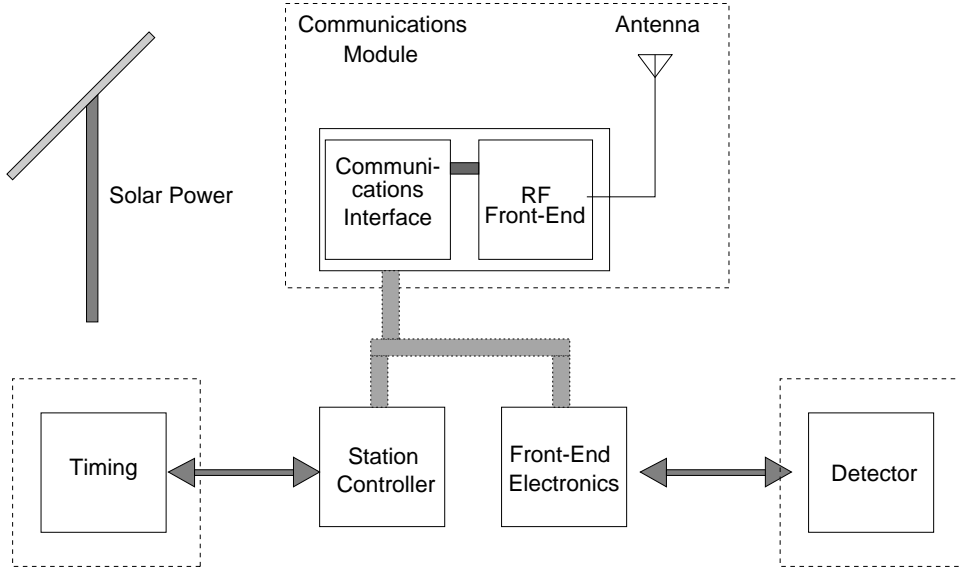


Figure 8.1: Block diagram of ground detector station electronics.

The electronics for each station will be housed in an environmental enclosure in thermal contact with the Čerenkov detector water tank to minimize thermal excursions. The PMT high voltage supplies will be integrated with the tube bases. The solar power system batteries will be housed in a separate enclosure, with a gas-tight electrical connection to the remainder of the electronics. Interconnections between the PMT housings, electronics enclosure, battery enclosure, etc. will be armored to prevent damage by animals and the elements.

8.2 Front End Electronics

The front end electronics at each station must both prepare the raw data for inclusion in a data event, and provide a level 1 trigger. Figure 8.2 shows the block diagram for the water Čerenkov detector front end board.

This board generates level 0 and 1 triggers. These triggers provide a first level of discrimination against single muons and small showers. The cosmic ray particle flux impinging on a 10 m^2 detector is about 2.5 kHz. PMT noise will add another few kHz rate. We will refer to this as the level 0 trigger, which fires any time there is a PMT signal above threshold. The level 1 trigger reduces this several kHz level 0 rate to less than 100 Hz. In practice there will be several level 1 trigger channels, each optimised for particular circumstances, which may be enabled in various combinations via a trigger mask.

There are two main functions of the primary level 1 trigger. One is clipping muon signals to reduce trigger sensitivity to the primary composition. The other is using the integrated time dispersion of the signal to bias against small showers close to the station which deposit signal over a very short time spread. The first function is motivated by the strong dependence of the muon content on the primary species. Suppressing the peak

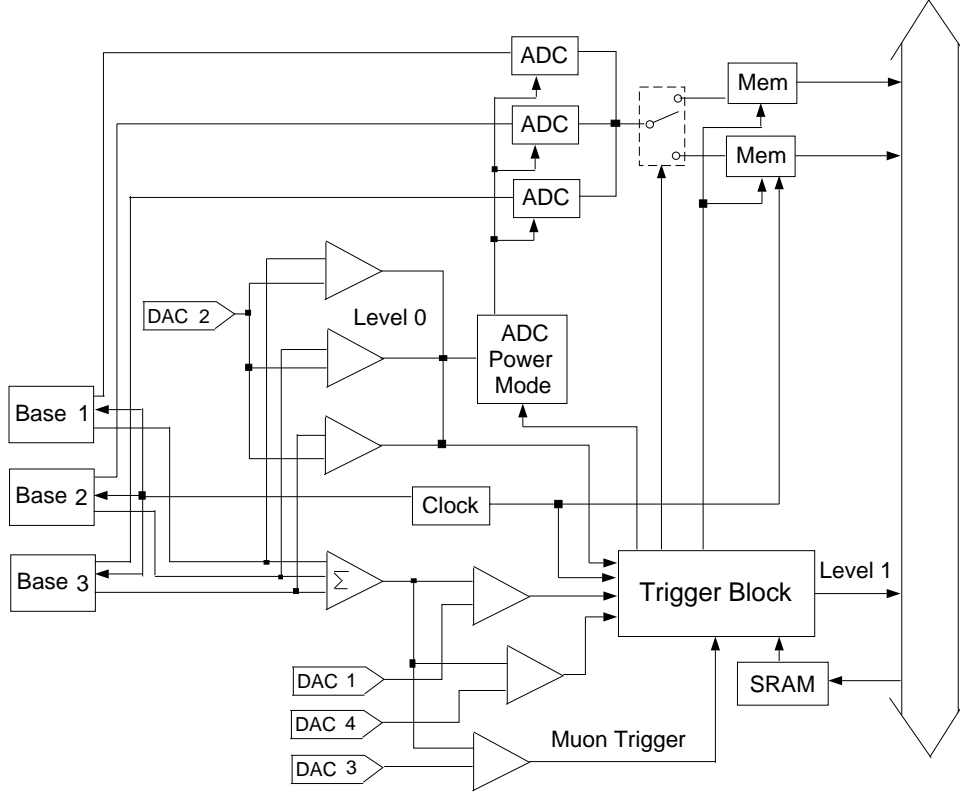


Figure 8.2: Block diagram of a possible front end board.

of the signal pulse generated by a through-going muon before integrating the remaining signal produces a trigger which is less dependent upon the primary particle composition. The second function is motivated by the increase in the time duration of the signal (e.g. the width of the shower front) as one gets farther from the shower core, as indicated in Figure 8.3. Note that the 10-90% rise-time plotted in Figure 8.3 shows little distinction between proton and iron showers, a desirable characteristic for the trigger, whereas in Figure 5.13 the 10-50% rise-time shows a clear distinction. This is because the 10-90% rise-time is dominated by the electromagnetic component of the shower, which arrives late, and depends only weakly upon the primary composition. The 10-50% rise-time, on the other hand, is mainly influenced by the muon content of the shower, which arrives early, and depends strongly upon the primary composition. Requiring that the signal be distributed in time biases the trigger against the abundance of smaller showers which land near the stations. While we want to reject triggers from small showers landing near a station, a variation of this trigger with a larger signal threshold and shorter time duration constraint will be implemented to trigger stations near the core of larger showers.

A “muon” trigger based upon the total light collected will be selectable to facilitate calibration of the PMTs on through-going muons. This muon trigger can be set globally or for a specific set of PMTs, to minimize the trigger bias on muon calibration pulse height distributions. These distributions have been nicely demonstrated using a test tank at AGASA. The feasibility of a special “muon-decay” trigger involving an isolated muon-like signal fol-

lowed by a delayed electron-like signal is being studied. A random noise trigger will also be incorporated as an additional diagnostic tool.

To record information useful in searching for Gamma Ray Bursts, a scaler will accumulate a count of GRB level 1 triggers (a clean “electron” signal well above PMT noise) occurring during 0.1 s intervals. This count will be read by the station controller and regularly passed along to the central facility, along with other accumulated data.

The level 1 triggers are sent (except for the GRB triggers) to the timing system and station controller via a dedicated interrupt line, causing the time of each level 1 trigger to be latched and generating an interrupt to the station controller to read out the captured waveform. As an option, the level 1 trigger can be set to disable itself upon formation, valuable for triggering on isolated muons as a calibration and diagnostic tool.

The 100 Hz limit of the level 1 trigger is imposed by dead-time considerations in the electronics. What does this mean in terms of the level 1 trigger condition? Using Poisson statistics, a 5 kHz level 0 trigger rate and a 20 μ s trigger aperture (this will be justified later in this section), implies a 450 Hz random doubles rate, and a 23 Hz random triples rate of uncorrelated level 0 triggers. The additional rate of level 1 triggers due to correlated level 0 triggers from small showers can easily be reduced to a few Hz or less using the rise-time constraint. This has been measured at Havarah Park using an 8.9 m² water Čerenkov detector and a waveform digitizer. The detector outputs were measured (described in terms of rise-time from 10% to 50%) whenever the signal was above 3.7 particles (vertical equivalent muons). The spectrum was strongly peaked towards fast, bandwidth limited, rise-times. A rise-time cut of >100 ns reduces the rate by a factor of 1000. Our simulations exhibit a similar sharp reduction in the trigger rate when a rise-time cut is applied. The 100 Hz design rate limit for the level 1 trigger is comfortably above what is expected for triggers comparable to those used in the simulations.

Our simulations indicate that a dynamic range of ≥ 14 bits and a sampling rate of ≥ 40 Mhz is advisable to make optimum use of the PMT signals. The large dynamic range facilitates reconstruction of the lateral profile of the showers while the fast sampling facilitates extracting parameters related to the muon component of the shower. Fortunately, only modest precision (8-10 bits) is required and the large dynamic range is not required at the fast sample rate. We are investigating several options, including multiple ADCs with overlapping ranges, analog compression of the signals, and switched capacitor arrays [152] with multi-range digitization. CMOS parts can be used for almost all of the components, minimizing power consumption. The front end board will have buffering for at least 2 events, minimizing the dead time incurred transferring the recorded waveforms to the station controller.

With careful design, power requirements for the front-end electronics can be kept reasonably low. Two factors contribute to this: the timing resolution requirements are modest enough to be met with fast CMOS, and the duty cycle for cosmic ray events is low so that most logic can remain quiescent most of the time. Judicious use of ASIC circuits can also help to reduce power consumption and increase reliability.

How long does the FADC record need to be? A conservative approach would be to

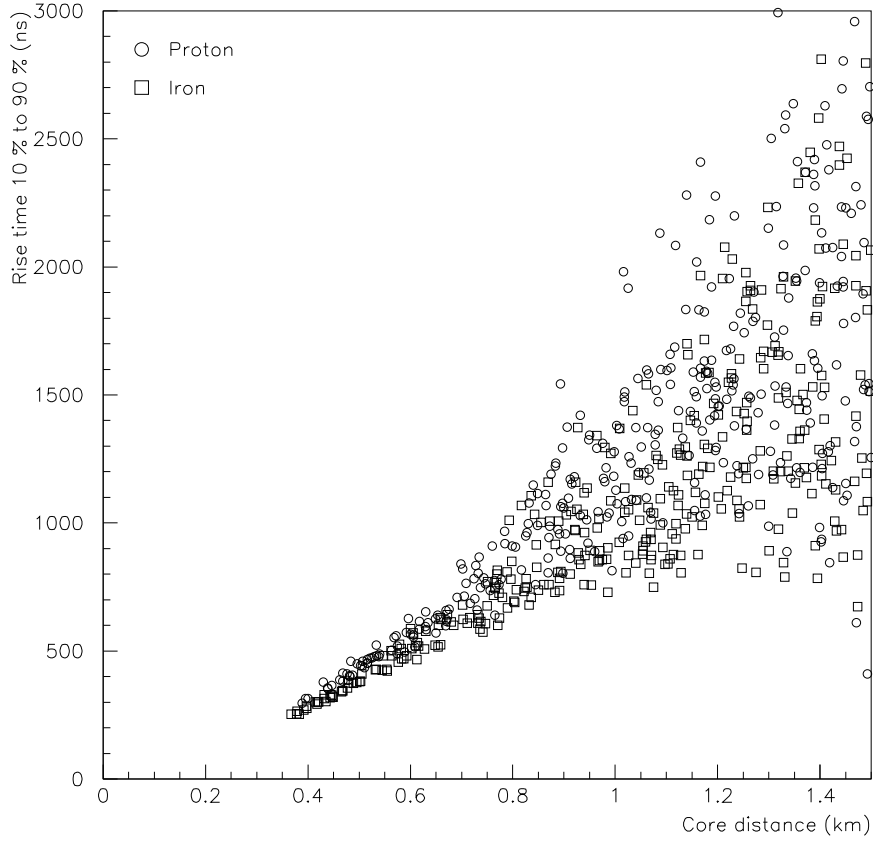


Figure 8.3: Distribution of 10-90% “rise-time” as a function of distance from the shower core for a sample of 100 simulated 10^{19} eV proton and iron showers. (*Cf.* Figure 5.13 where the 10-50% rise-time is displayed.)

have the record long enough to handle the full waveform of the very largest events one might expect to see. If they exist, showers with energies $\geq 10^{21}$ eV might be detected at a rate of 1 per several years. These showers will trigger stations out to about 5 km from the shower core. At this distance from the shower core a $20 \mu\text{s}$ window is required to catch $\approx 95\%$ of the particles. If we run the FADC system for $20 \mu\text{s}$ each time a $\sim 1/2$ photo-electron discriminator level is crossed (~ 5 kHz level 0 trigger), the system will be active only 10% of the time. Only the front-end amplifiers, comparators, and the clock crystal need to be operating in the intervening 90% of the time. This can reduce the power consumption of the front-end significantly. For example, the estimated power consumption was reduced from 12 W to 2.6 W in one design exercise. The FADC window will be extended for $15 \mu\text{s}$ after any level 1 trigger, so that the tail end of the waveforms is not lost even for events in which the FADC was started on a random signal. See Figure 5.10 for an example of the operation of such a trigger in a simulated air shower event.

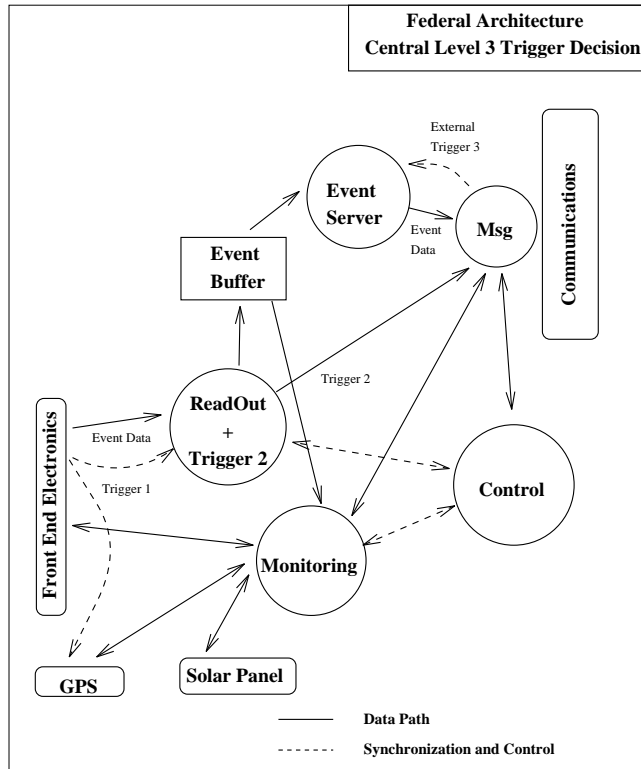


Figure 8.4: Block diagram of station controller code.

8.3 Station Controller

The station controller provides the local intelligence at each detector station. It performs a large number of tasks: controlling the PMT HV supplies, monitoring HV, solar panel performance, battery state, etc., reading data from the front end electronics, reading the time tag for each event from the timing system and applying necessary corrections, performing one or more levels of trigger logic, transferring data to the central data acquisition system, and local detector monitoring. In order to perform these tasks, the station controller will use a real time operating system such as OS-9. The station controller board will integrate these functions onto a compact low power board utilizing a highly integrated low power microcontroller, such as the IBM PPC403. We have benchmarked major elements of the station controller code and verified that this processor, which has extremely low power consumption (0.25 W) is fast enough for our purposes, with a comfortable factor of 10 safety margin. Figure 8.4 shows the block diagram for the station controller code.

It will not, in general, be possible to reset a misbehaving station remotely. Therefore, the station controller code must be robust and must monitor itself for satisfactory operation, automatically restarting itself as necessary. Similarly, it will not be feasible to change EPROMs in over 1600 stations scattered over 3,000 km² in order to install updated station controller operating code. Operating code and run conditions must be down-loadable through the communications network.

Only a minimal, very thoroughly tested and debugged, core program will be stored in the PROM. The primary function of the core program will be to reset PMT high voltages to a safe state, and to interact with the communications network to download operating code. The operating code will contain modular links so that selected portions of the code can be updated via the communications network, minimizing the frequency that the entire program needs to be transmitted when program updates are installed. The entire program, including operating parameter storage, will reside in less than 0.25 Mb of memory.

The station controller implements the level 2 trigger in software. It analyzes the digitized waveforms from the three PMTs in order to tag muons, determine the total signal magnitude, and characterize the time distribution of the signal. Using this information it generates the level 2 trigger, reducing the trigger rate from ≤ 100 Hz to ≤ 20 Hz per station.

The waveforms are highly compressible. The amount of compression depends upon the amount of low level noise present in the signal and the complexity of the compression algorithm. Our most pessimistic simulations indicate that a compression factor of 3 is easily achievable. Thus 4 Mb of buffer memory can store ~ 100 seconds of level 2 triggers. Implementing this amount of buffer memory is quite feasible, and is comfortably longer than the 10 second maximum trigger formation time.

To minimize the number of boards, many of the miscellaneous interfaces will be incorporated on the station controller board. The station controller board will incorporate sampling ADCs for monitoring the status of the solar power system and PMT high voltages. It will contain DACs to control the PMT high voltage supplies and incorporate a GPS interface with a ≥ 2 event FIFO.

8.4 Timing

Each station needs an accurate time base to 1) match level 2 trigger data with its neighbors, 2) allow shower directions to be reconstructed, and 3) provide a time base for the communications system. In the reference design the timing system is based upon Global Positioning System (GPS) receivers. The Leeds group has demonstrated that 10 ns relative timing can be obtained using inexpensive off-the-shelf scientific GPS receivers. Power consumption is less than 1W.

To allow cross-matching of cosmic ray event times for on-line shower recognition and off-line direction reconstruction it is crucial that data acquisition at each detector station be synchronized. We have simulated the effect of clock synchronization error on the angular resolution of the detector. Our simulations indicate that 15 ns synchronization error will contribute $\sim 0.15^\circ$ to the direction resolution. Given that our intrinsic angular resolution may in some cases be less than 0.5° (see Chapter 5), this is a reasonable requirement for the timing system.

The GPS is a US government satellite constellation which continuously disseminates position and time information worldwide by means of coded 1.5 GHz radio broadcast signals. The system is now fully operational and expected to remain so for several decades.

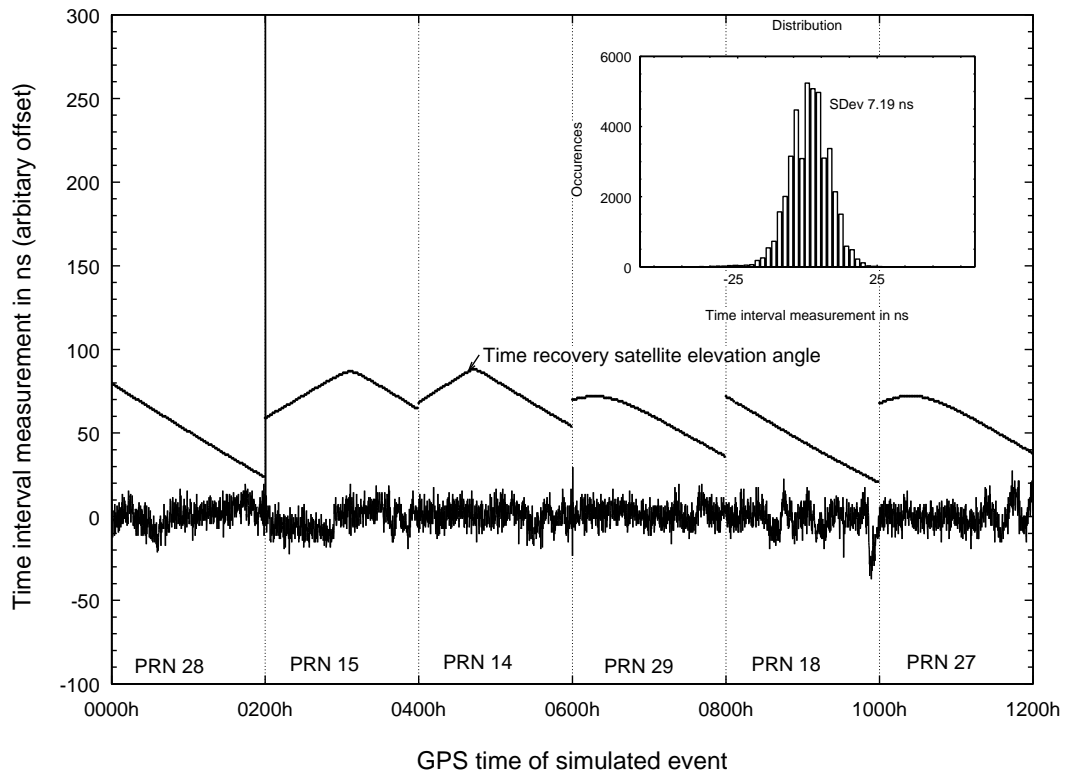


Figure 8.5: Apparent event time difference with the time-tagging systems separated by 11.2 km on the morning of 26/1/95. The upper line of the main graph shows the elevation angle of the satellite being used for time recovery, its PRN code being given at the bottom of the figure. The inset graph shows the distribution of the time interval errors shown in the main graph.

Unrestricted civilian access to the deliberately degraded Standard Positioning Service (SPS) is allowed. By the use of a simple technique known as “scheduled common view” the effect of this degradation can be eliminated when only relative accuracy is required.

The prototype design is very simple and has demonstrated excellent results[149]. The basic technique is to exploit a commercial GPS receiver module, in conjunction with a custom designed 100 MHz twin channel counter latch assembly. These are both interfaced with a computer. In the final design the interface will include a multi-event FIFO for the event trigger latch, and incorporated on the station controller board.

One of the latch triggers is fed from the GPS receiver 1 pps output, and the other from the event trigger source. By reading the latch values as they occur, in conjunction with information from the GPS receiver, the computer can calculate event time stamps by simple linear interpolation. In effect the GPS 1 pps is used to continuously calibrate the local counter time frame.

To remove the effect of the deliberate SPS accuracy degradation the scheduled common view technique referred to above is employed. The control computer instructs the GPS receiver to base the 1 pps output on information from a single satellite, which is periodically changed since the satellites remain visible for less than six hours at a time. Each system in

the network uses the same satellite simultaneously by means of a pre-determined tracking list.

Initially two prototype systems were constructed which were tested under two circumstances: (a) at the same location and (b) separated by 500 m using a high bandwidth cable link. The time interval measurement error distribution had a standard deviation of 6 ns, with a systematic error of 5 ns. The maximum errors observed during 8 days of operation, with 800,000 test triggers, were +21ns and -35ns.

The same two systems were tested over an 11 km baseline using a microwave link which form part of the MERLIN radio telescope interferometer centered at Jodrell Bank, UK. Figure 8.5 shows the results of this test, in which the time interval measurement had a standard deviation of 7 ns. It was not possible to measure directly the systematic error in this test. However, due to the variable geometry which occurs in the GPS system it is very hard to envisage a fixed source of error scaling with distance of separation. The largest EAS so far observed have footprint diameters of only 5-10 km. Even the largest showers will not have level 2 triggered stations more than about 5 km from the shower core.

Two more sophisticated systems based on the same technique have recently been deployed at the South Pole to allow cross-matching of the SPASE and AMANDA experimental data streams.

8.5 Communications

The communications system is used to correlate data from different detector stations to form an event trigger, transfer event data from detector stations to a central site, and transfer control and diagnostic information bi-directionally between the detector stations and the central site. The bandwidth required of the communications system depends not only upon the station trigger rate, but also on the topology chosen for the data links, and the level of local multi-station coincidence selected. The communications system design is based upon a maximum mean level 2 trigger rate of 20 Hz. We have chosen a wireless RF communication system for the reference design. Since the performance of the communications system is critical for the operation of the experiment, we will devote a number of pages to discussing the design considerations. For additional information refer to Refs [147] and [153].

Fully wired systems (copper or fiber optics) are easily rejected on the basis of cost considerations. For example, the length of copper or fiber (and trenches) needed to connect the stations is 7,200 km per site with 6 connections per station, or 3,600 km with only 3 connections per station (with minimal redundancy in case of link failure). The installed cost of copper or fiber is about \$10K/km. This is dominated by the installation cost and depends somewhat on site conditions. Even so, at an estimated cost exceeding \$72M, we need not consider this option further. However, the utilization of a fiber backbone may be advantageous. Further studies are ongoing.

8.5.1 Licensing Issues

Any RF transmitter must comply with regulatory requirements in the site countries. This becomes a complex issue, as the regulations unfortunately vary from country to country. For example, in the US several of the ISM (Industrial, Scientific, Medical) bands are attractive to consider for the station transceivers, as these bands allow operation (of type-certified equipment) without purchasing a license for each station. In the US, the 902-928 MHz, 2400-2483.5 MHz, and 5725-5850 MHz bands are the most appropriate. FCC regulations part 15.247 [150] limit the maximum peak transmitter output power to 1 Watt, and the maximum equivalent isotropic radiated power (EIRP) to 4 Watts (36 dBm) in these bands. In addition, the transmitted signal must be spread in bandwidth. The regulations in Argentina are essentially identical to those of the US in those bands. This makes it attractive to consider them for the reference design. A drawback of the ISM bands is that anyone can use them. This is not a problem for a controlled access site where we could restrict the use of other devices which might interfere with our communications system, but is a concern if the general public has access to the site. We will continue to investigate the use of other bands as we explore various options for the communications hardware.

8.5.2 Propagation

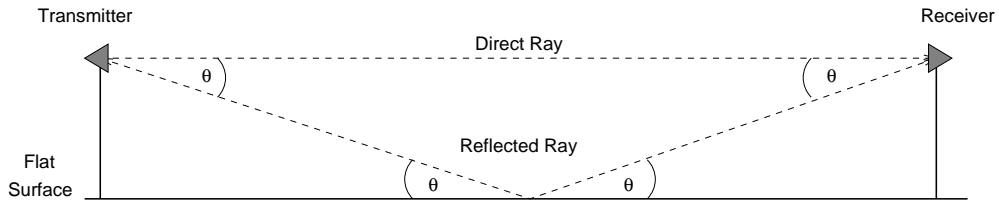
A critical parameter for the communication system is the strength of received signals relative to the noise. This will be function of the transmitter power, the transmitter and receiver antenna gains, propagation path loss, and atmospheric attenuation. Fortunately, atmospheric attenuation is less than 1 dB/km at frequencies below 3 GHz even in the heaviest rainfall, and thus is not a serious concern for propagation over 1.5 km distances.

Radio wave propagation in free space is given by the Friis equation[151]. For the case where the transmitting and receiving antennas are aligned and polarization matched, this equation reduces to

$$\frac{P_r}{P_t} = \left(\frac{\lambda}{4\pi D} \right)^2 G_t G_r \quad (8.1)$$

where

- P_t = power at output of transmitter,
- P_r = received power at input to receiver,
- D = distance between transmitting and receiving antennas (in meters),
- λ = wavelength of the radio signal (in meters),
- G_t = gain of transmitting antenna, and
- G_r = gain of receiving antenna.



Geometry of Multipath Interference

Figure 8.6: Multipath interference of radio waves.

However, reflection of the radio waves from the ground and subsequent interference with the direct waves is an important factor which cannot be neglected. This is depicted in Figure 8.6.

A further complication is that the ground will not be precisely flat, but will have some undulations in it. Figure 8.7 displays the calculated propagation loss versus distance between two 8 m high vertical full wave dipole antennas at 2450 MHz. The shaded area indicates the loss for a perfectly flat terrain. Each solid curve represents a different randomly generated terrain. The envelope does not vary strongly with terrain variations, as long as line of sight between the 2 antennas is maintained. The 8m antenna height is near optimum at 2450 MHz. At lower frequencies the received signal strength continues to increase for higher antennas.

The points where a bad fade occurs are problematic. One effective technique that is often used to combat bad fades is *antenna diversity*. That is, use multiple receiving antennas and pick the one that gives the strongest desired signal. We have simulated a two antenna receiver, where the second antenna is placed vertically below the first. The height of the second antenna is chosen such that the phase of the direct and reflected waves from a flat earth is changed by 90° . The calculated propagation losses are displayed in the right plot in Figure 8.7.

Another technique that is often used to combat fading is *frequency diversity*. That is, spread the signal over multiple frequencies (or a wide bandwidth) to mitigate the effects of a bad fade at one frequency. This will be effective if the path length for the interfering reflected signal is many wavelengths longer than the direct path. This can be the case for reflections from objects not in the plane of the two antennas. However, these effects are not fully modeled in our current simulations, which only include reflections in the plane of the antenna systems.

Spot checks of these simulations were made in 1995 at Woomera, Australia. At 900 Mhz a handful of measurements were made with 1.5 km spacing between antennas at different locations. The measurements agree within a few dB in the mean to that predicted by our simulations. At 2.4 Ghz measurements were only made at 2 locations. Both are ~ 10 dB below the predicted mean, but are within the envelope of expected path loss. These measurements confirm that there are no gross errors in the simulation, but with only a handful of measurements it is not possible to confirm the details of the predicted path loss distribution. Further radio survey measurements at the selected sites are planned.

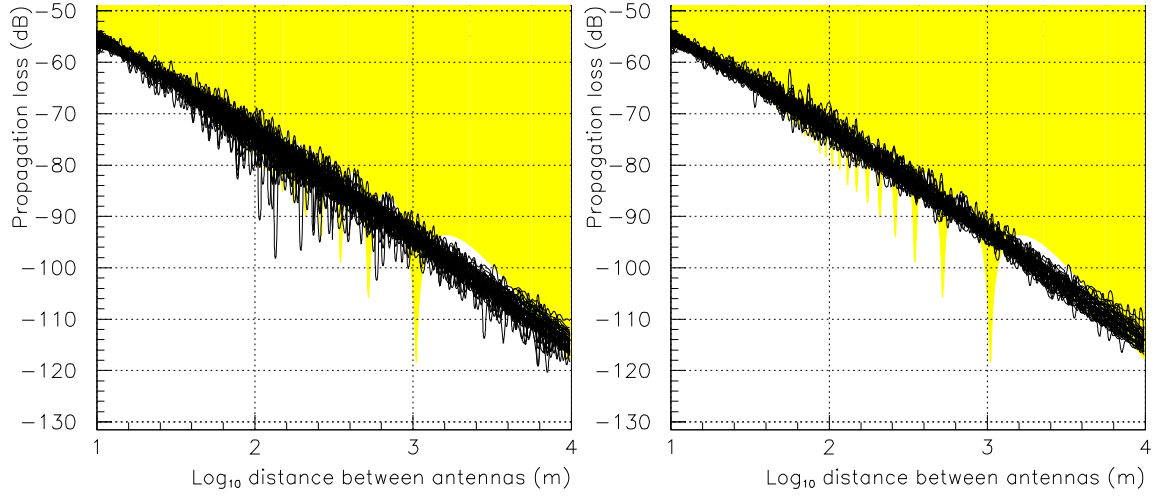


Figure 8.7: Calculated 2450 Mhz radio wave propagation loss for 8 m high full wave dipole antennas. The shaded curve is for an ideal flat plane. The solid lines show simulation results for 100 different random terrains with up to ± 4 m hills). The left plot depicts the case where one receiving antenna is used. The right plot depicts the case where the strongest signal from one of two vertically separated antennas is used.

The distribution of received signal strength in communications systems where there is a strong direct signal in the presence of a number of reflected signals (called multipath) can be shown to follow a Rician distribution. S_i , the received signal strength (Watts) from antenna i , has the (Rician) probability density function

$$f_1(s) = \frac{1}{2\sigma^2} \exp\left(-\frac{s + \alpha_i^2}{2\sigma^2}\right) I_0\left(\frac{\sqrt{s}\alpha_i}{\sigma^2}\right) \quad (8.2)$$

The distribution function is

$$F_1(s) = 1 - Q\left(\frac{\alpha_i}{\sigma}, \frac{\sqrt{s}}{\sigma}\right)$$

where $Q(a, b)$ is called the Marcum Q function and is given by

$$Q(a, b) = \int_b^\infty \exp\left(-\frac{a^2 + x^2}{2}\right) I_0(ax) dx.$$

The receiver measures S_1 and S_2 to determine which antenna has better signal-to-noise ratio (assuming the noise power and signal distributions are the same at both antennas). If we let $S = \max(S_1, S_2)$ then the density of S is

$$f(s) = 2f_1(s)F_1(s) \quad (8.3)$$

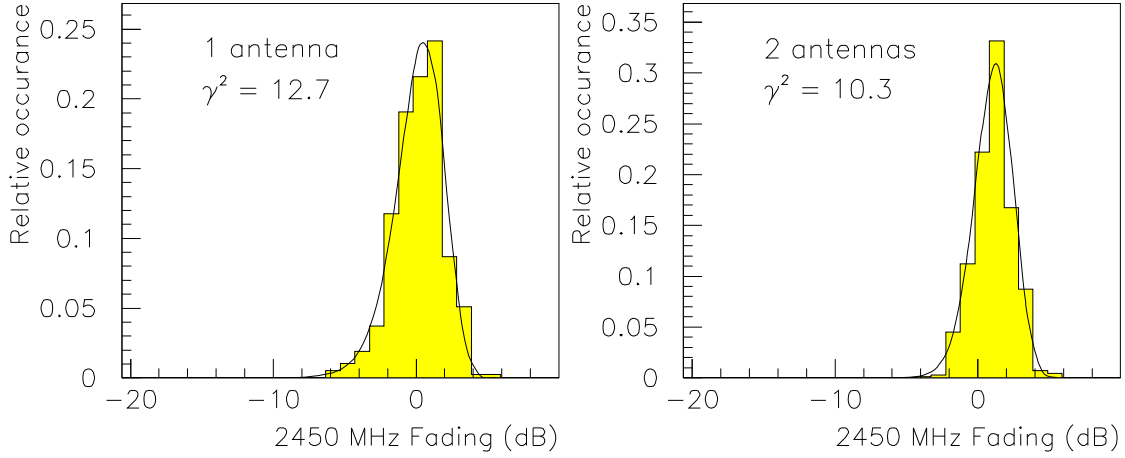


Figure 8.8: Calculated distribution of received signal strength relative to free space for 2450 Mhz radio wave propagation between 8m high full wave dipole antennas separated by 1.5 km. The histograms display the simulation results for 100 random terrains. The curve in the left figure is a least squares fit to Eqn. 8.2. The curve in the right figure is a fit to Eqn. 8.3.

The ratio $\gamma^2 = \alpha^2/(2\sigma^2)$, which is the ratio of received power in the direct path to that in the faded path, is important when determining the performance. The total average received energy is $\Gamma = E(\alpha_i^2 + 2\sigma^2)$, where E is the received energy in the direct path. The error probability shown in later figures is plotted as a function of Γ/N_0 , where N_0 is the noise power density.

The calculated distributions of propagation losses are displayed in Figure 8.8, along with least squares fits to $f_1(s)$ (left plot) and $f(s)$ (right plot). As expected by the assumption that the signals at the two receiving antennas have the same probability distribution, the fits produce the same value of γ^2 within errors, with a mean value of $\gamma^2 = 11.5$.

8.5.3 Performance Analysis of Frequency-Hopped Spread Spectrum.

In this section we will analyze the link level performance of a particular data communications system to demonstrate the feasibility of our communications links, using as an example the Plessey DE6003 transceiver [148]. This is a frequency-hopped 2.4 GHz ISM band spread spectrum transceiver with two antenna inputs. A typical frequency-hopped spread spectrum system consists of a data source followed by an error control encoder. The error control encoder adds redundant bits to the data stream to protect against errors. The encoded data is then modulated using binary frequency-shift-keying (BFSK). The modulated signal is frequency-hopped over a set of frequencies. One goal in transmitting information at

different frequencies is that the fading statistics will be different at different frequencies. Thus a given multipath situation will yield a particular fading statistic at one frequency but a different (and independent) fading statistic at another frequency. If a small percentage of the frequencies result in poor performance then an error correcting code will be able to correct the errors that occur when transmitting at those frequencies. The receiver consists of a dehopper/demodulator followed by the error control decoder.

There are several types of codes that could be used. These include convolutional codes and block codes. The convolutional codes are easier to decode with reliability information from the channel (eg. the received signal strength). The block codes have a larger variety of code rates (number of information symbols per channel symbol) available and are slightly easier to analyze. We will only consider the use of Reed-Solomon block codes (used in CD players) in this report.

In a block code (such as a Reed-Solomon code) a number of information symbols k is protected by transmitting not only the information symbols but in addition transmitting $n - k$ redundant symbols. These redundant symbols depend on the information symbols so that if an error occurs during transmission and several symbols are received erroneously the correct information can still be determined. Reed-Solomon codes operate on non-binary symbols typically of size 32 to 256 bits. These usually are called bytes. A non-binary symbol is formed by grouping together bits. For example, in a Reed-Solomon code with symbol size 32, each symbol consists of sequences of 5 bits. The encoder groups information symbols into blocks for the purpose of encoding. For the Reed-Solomon codes considered here $k \cdot m$ bits are grouped together. First m bits are grouped and called a code symbol. Based on k information symbols, $n - k$ redundant symbols are determined. The codeword then consists of the k information symbols followed by the $n - k$ redundant symbols. The decoder can correct any pattern of $e = \lfloor (n - k)/2 \rfloor$ errors.

The codeword generated by the Reed-Solomon encoder can be transmitted using BFSK. Usually there are a large number of bits transmitted during each frequency hop. However, a well designed system would transmit only one code symbol per hop. In order to transmit many bits per hop, and only one code symbol per hop, interleaving is required. Interleaving works as follows: instead of generating a single codeword at a time, L codewords are generated (from different data symbols) simultaneously. Then only one code symbol from each of the L codewords is transmitted during a particular hop. Thus there are $L \cdot m$ bits transmitted per hop.

It is very important to know what the correlation is between the amplitude of the fading at two different frequencies. If the fading amplitudes are independent then error control coding can significantly improve the performance by correcting the errors due to the occasional bad fade at a particular frequency. If, on the other hand, the fading amplitudes are highly correlated between different frequencies, then error control coding will not be effective in reducing the error probability. As we do not yet have survey measurements or simulation results that can accurately estimate this correlation, we consider the two extreme cases: 1) different frequencies are independently faded and 2) different frequencies are identically faded (completely correlated).

The conditional error probability for making an error in determining the value of a received data bit, given a particular signal strength, is given by

$$P_e(S) = \frac{1}{2} \exp -\frac{ES}{2N_0}$$

The average error probability is given by

$$\bar{P}_e = \int_0^\infty f(s) P_e(s) ds$$

For coding purposes we are interested in the probability of error in a code symbol which consists of m consecutive bits transmitted at the same frequency and having the same fading value (not only the statistics are the same but the realization is the same). The conditional symbol error probability is given by

$$P_s(S) = 1 - (1 - P_e(S))^m$$

The average symbol error probability is given by

$$\bar{P}_s = \int_0^\infty f(s) P_s(s) ds$$

Given that the different code symbols are transmitted on different hops, the probability that a Reed-Solomon codeword is decoded incorrectly is the probability that there are more errors than can be corrected by the code. The error correcting capability is $e = \lfloor (n - k)/2 \rfloor$. The probability of error is then

$$\bar{P} = \sum_{l=e+1}^n \binom{n}{l} \bar{P}_s^l (1 - \bar{P}_s)^{n-l}.$$

It is usually the case that a Reed-Solomon decoder will fail to decode when there are more errors than can be corrected, rather than put out an incorrect codeword. This means that decoder errors will (with high probability) be detected.

Finally we consider the case where all code symbols experience the exact same fading amplitude. For this case the codeword error probability is given by

$$\bar{P} = \int_0^\infty f(s) \sum_{l=e+1}^n \binom{n}{l} P_s(s)^l (1 - P_s(s))^{n-l} ds.$$

Later we show the large difference between coding for independently faded channels and identically faded channels.

8.5.4 Link Budget

In this section we consider the link budget for a system using a 20 dBm (100 mW) transmitter with stations separated by 1.5km. The transmitter and receiver have antennas which each

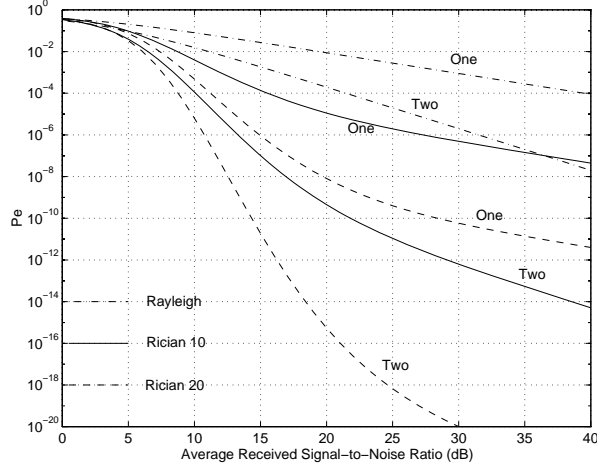


Figure 8.9: Bit error probability for fading without coding with one and two antennas.

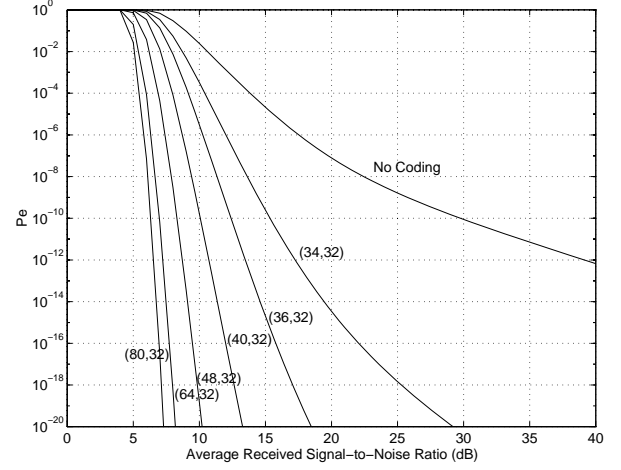


Figure 8.10: Block error probability for Rician fading with coding and symbols independently faded ($\gamma^2 = 10.0$).

provide 3 dB antenna gain. The loss due to free space at frequency 2.45 GHz is 103.7 dB. Thus the transmitted signal power is reduced by 97.7 dB. For a 100 mW transmitter the received power in the direct path is 16.8×10^{-12} W. The data rate considered (that used in the Plessey DE 6003) is 625kbps. From this the (direct path) energy per bit is given by $16.8 \times 10^{-12} / (625 \times 10^3) = 2.7 \times 10^{-17}$ joules/bit. In addition there is the energy from the multipath components. Based on simulations the ratio of the energy received from direct path and multipath components ($\gamma^2 = \alpha^2 / (2\sigma^2)$) is 11.5. The total received energy is then $\Gamma = 2.7 \times 10^{-17} (1 + 1/11.5) = 2.9 \times 10^{-17}$ joules/bit. The noise level (from the DE6003 data sheet) is $N_0 B_{IF} = -103\text{dBm}$, where B_{IF} is the bandwidth of the IF filter (1.5 MHz for the DE6003). Thus the noise power density $N_0 = 3.3 \times 10^{-20}$ W/Hz. The average received signal-to-noise ratio is $\Gamma / N_0 = 29.5\text{dB}$. There are potential implementation losses which reduce the effective signal-to-noise ratio. Plessey estimates these to be of the order of 5dB for the DE6003. Thus the effective received signal-to-noise ratio of 24 dB may be appropriate (in the absence of other interfering signals). Although our simulations indicate $\gamma^2 \approx 11.5$, we will use a more conservative $\gamma^2 = 10$ below.

Interference from other transmitting stations must also be considered, as this may raise the noise. We are considering using a 7 slot time division multiple access (TDMA) scheme with about 237 stations transmitting simultaneously. In a frequency hopping system with 79 or more adjacent channels (like the DE6003) there would be three stations transmitting on each channel at the same time, and an additional six stations transmitting on neighboring channels. With fixed station positions we can arrange the frequency hopping sequence to maximize the distance between interfering stations. In that case, interference from other transmitting stations will typically be 20 dB below the desired signal.

The bit error probability for an uncoded system with one or two antennas is plotted against the average received signal-to-noise ratio in Figure 8.9. In the case of two antennas

the receiver is assumed to be able to select whichever antenna has the largest signal. It is clear from this figure that significant gains can be achieved by using two antennas. The three sets of curves correspond to the case of no direct path (Rayleigh, pessimistic), a direct path and faded path with $\gamma^2 = 10$ (Rician 10, realistic) and with $\gamma^2 = 20$ (Rician 20, optimistic).

The codes we considered all operate with the same number of information bits (256) grouped into 32 8-bit bytes. In the uncoded case we just transmit these 32 symbols without any extra redundant bits. The codes have different block lengths n but the same number of information symbols (32). The (48,32) code has $n - k = 16$ and can correct 8 errors in the block of 48. The (64,32) code has $n - k = 32$ and can correct 16 errors in a block of 64. In Figure 8.10 the block error probability is shown for the case where each symbol is independently faded, and the power in the direct path is ten times the power of the faded path (Rician 10). In this case the block error rate may be as low as 1 part in 10^{14} . However, if the fading is identical at different frequencies, the error coding is much less effective at reducing the error probability, reducing it by only a factor of two.

Radio surveys of the selected sites will permit us to refine these calculations, but at present it appears that commercial transceivers like the Plessey DE6003 will provide a satisfactory block error rate level when combined with error correcting codes.

Thus we are comfortable that a radio communications network poses no intrinsic technical roadblocks. The actual implementation will undoubtedly differ in the details. In the next section we will consider in more general terms the requirements for Auger.

8.5.5 Network Topology

Once we establish reliable radio links which provide a path via one or more hops between each station and the control center we have, in principle, the means to transfer the information necessary to operate the project. This is trigger information, data packets, software downloads, etc. The network topology and protocols are primarily implemented in software that operates on the communications hardware. It will be advantageous to conform to international standards, such as the ISO/OSI 7 layer model, as much as possible.

Critical parameters for the communications network are the user data rate and the allowable station to central collection point latency. The data rate from each station is dominated by level 2 trigger packets and monitoring data. Our 20 Hz level 2 trigger rate limit requires 480 bits/second mean rate from each and every station. Adding a 220 bits/second estimate for monitoring data gives us a 700 bits/second user data rate transmitting from each station. It should be noted that the bandwidth required to read out triggered events is totally negligible for these considerations. The bit rate for data from the central collection point to each station is dominated by the constraint that the (infrequent) software downloads should not take an excessively long time. 600 bits/second is adequate here, but this is admittedly a softer number than the requirement for the other direction. The communications system implementation should have provisions for upgrades that increase the data bandwidth by a factor of 2 to allow the addition of later enhancements to the ground array. Additional rate is required for packetizing and forward error correcting coding. In

many schemes additional headroom is required to avoid packet loss due to congestion. These latter are highly dependent upon the details of the implementation, hence are difficult to specify in general.

There is a trade off between maximum network latency and the amount of memory required in the ground array stations and fluorescence detector electronics to buffer data while awaiting a trigger decision. A 5 second maximum latency specification in each direction yields buffer memory requirements which can be reasonably achieved in both the ground stations and the fluorescence detector. It can also be met by many of the communications schemes we have studied.

It is desirable for most stations to have line-of-sight communication with its six nearest neighbors. In many implementations, this provides alternative communication links in case of station failures, a prerequisite for a fault-tolerant network. Occasional obstacles (e.g. hills) can be tolerated.

We have considered two general classes for the network topology: the “flat” or “fraternal” architecture where the level 3 trigger decision is performed by the station controllers; and the “hierarchical” or “federal” architecture where local stations send all level 2 trigger data to a central system via concentrators.

Because of the possibility of “exotic” physics which we may not fully anticipate at the present time, there is a strong motivation to process as many of the trigger levels as possible at a central point, where information from the entire array can be included in the trigger pattern recognition. Therefore, we have chosen the federal network topology. One example of a hierarchical network topology is depicted in Figure 8.11.

In each lowest level cell the concentration may be either by point-to-point links or TDMA global collecting down to the six “first ring” stations surrounding the local base station (see Figure 8.12).

Higher bandwidth is required as the data is concentrated towards the center. This is satisfied with a hierarchy of directional microwave links or fiber backbones. Other implementations of this basic scheme are currently under study.

The concentrator network will not only carry the data from the ground array stations, but also provide links between fluorescence eyes, and between the eyes and the control center.

8.6 Solar Power

The ground array stations will operate from solar power (photovoltaic, PV). The power budget for each station shown in Figure 8.13. The PV system must provide regulated power to the station electronics with minimal maintenance over the expected lifetime of the experiment. Each station will have its own PV array, battery bank, charging regulator, low battery voltage disconnect, and control/monitoring system as shown in Figure 8.13. The orientation of the PV array will be fixed at an angle which maximizes the solar exposure during the winter.

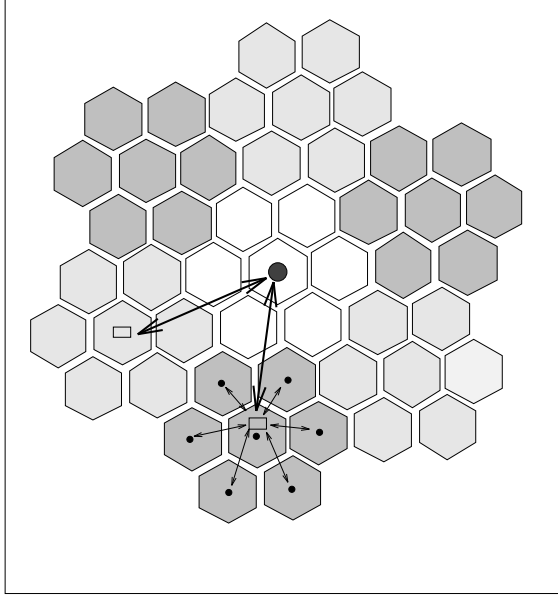


Figure 8.11: Cell configuration in the 2-level hierarchy. Each of the small hexagons represents one cell of stations depicted in Fig. 8.12. A base station at the center of each such cell communicates with a microwave repeater at the center of each cluster of 6 cells. These repeaters in turn communicate with microwave transceivers at the center of the array.

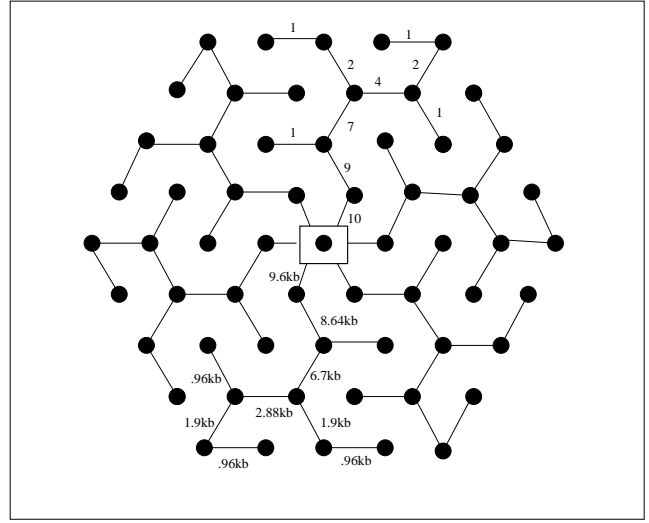


Figure 8.12: Communication links and data flow rates in a level-2 mini-cell. Each dot represents a detector station. The lines indicate the radio communication links between stations. At the center is a base station which communicates with a microwave repeater (see Fig. 8.11).

The number of required solar panels and size of the battery bank are estimated from a knowledge of the daily power requirements, the estimated availability of solar radiation at the site, and the percentage of down time due to insufficient power that can be tolerated. The statistical nature of the event data means that pushing for much less than 2% outage due to insufficient solar power is probably not warranted if it adds substantial cost to the system. However, as it turns out, this goal appears to be easily achieved.

For planning purposes we have sized the system for a site with the solar radiation characteristics of Dugway, Utah. Both of the selected sites have better characteristics than this. A simple but conservative analysis has led us to propose the use of two 53 peak Watt (Wp) silicon solar panel arrays for power collection and two 12 volt gel-cell lead-acid batteries for power storage. This provides sufficient Wp capacity such that with average insolation at Dugway (minimum of 3 hours Wp mid-winter) the batteries never discharge to 50%. The battery capacity is sufficient to power the system for more than 10 days without sun, discharging to 50%. The technology of both of these components is mature and their commercial use is common.

Although the outage probability has not yet been accurately estimated, this system is expected to perform much better than the design goal of less than 2% outage probability per station. A more detailed analysis of the system sizing and outage probability will be

Station Power Budget	
System	Power Rqd (W)
High voltage	1.0
Front end	2.6
Station controller	2.5
GPS receiver	0.85
Communications transceiver	0.83
Transceiver interface	0.5
Total	8.3
Converter losses	$\times 1.2$
Total	9.9

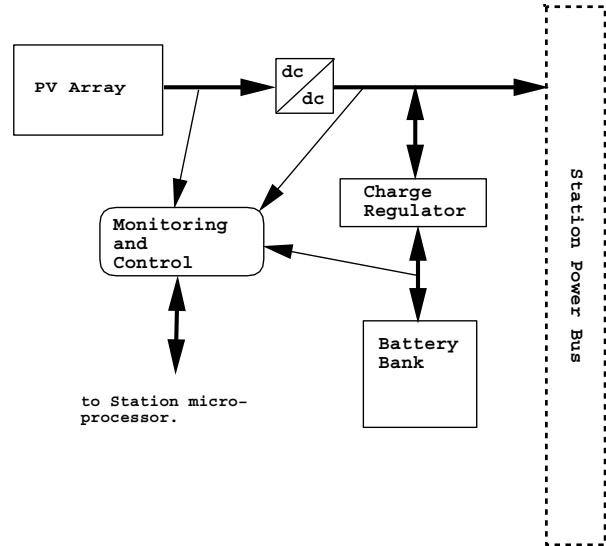


Figure 8.13: Block diagram of the solar power system for each station

performed using accumulated insolation data for the two sites in due course.

8.7 Data Acquisition and Archives

The collection of data at the central site will be handled by Unix workstations. Figure 8.14 shows the block diagram for the control center data acquisition (DAQ) code.

The philosophy of the DAQ is the following. The ground array and the fluorescence detector have their separate acquisition hardware and computers. For each detector, there are two servers: one for the data acquisition (trigger, event-building) and archiving, the other for the monitoring, calibration and slow control tasks. The computing resources required are modest by present day standards and can easily be handled by low cost workstations. Each would have ~ 128 Mb of central memory, a ~ 4 Gb system disk, ~ 8 Gb of temporary data storage space, and an output device (e.g. DAT tape or CD-ROM) where the data is permanently and locally stored. Software and licences were also considered (including FORTRAN, PASCAL and C compilers).

A relatively high speed Internet access (>1 Mbit/s) to the site will be provided via fiber optic link or satellite link. This will allow collaborators to monitor the experiment from anywhere in the world and transfer moderate amounts of data. The full data sets will be transferred over this link to a primary distribution center in each hemisphere which will make the data available to the collaboration.

The data acquisition hardware can only be outlined at present. We envisage a few VME crates. Absolute time reference will be obtained from GPS.

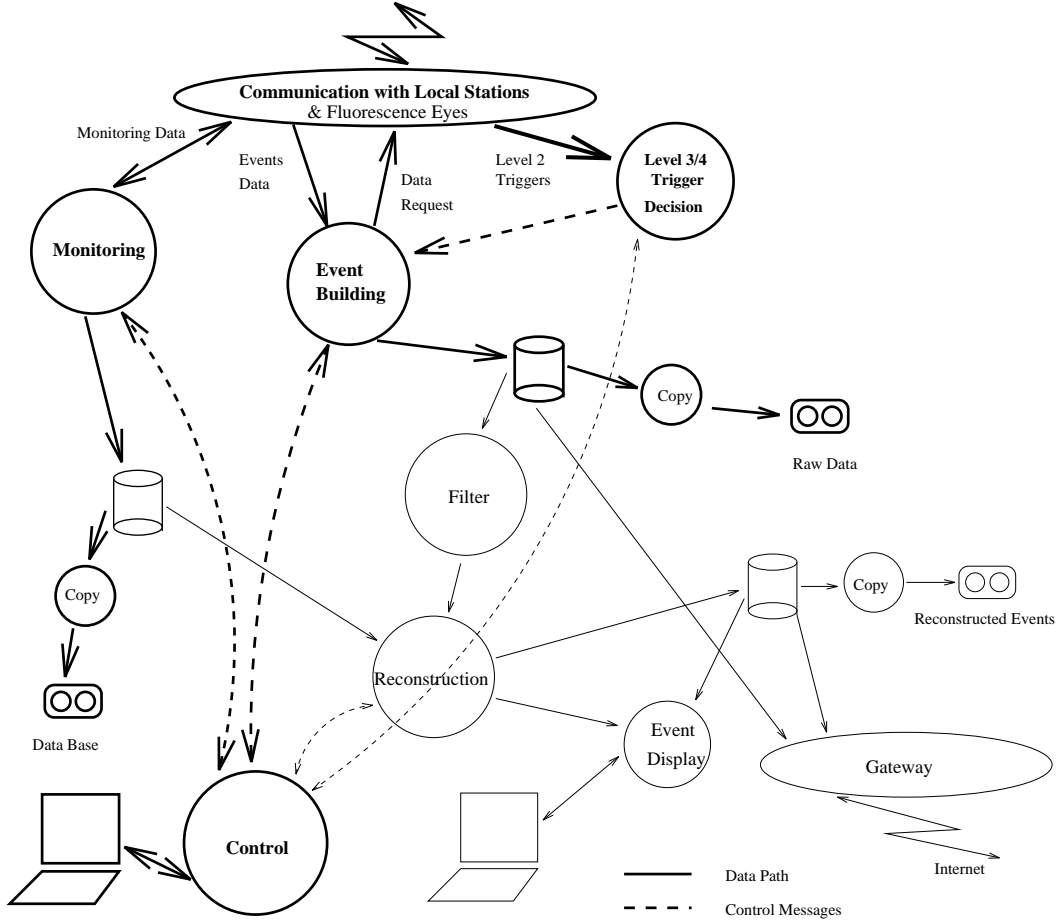


Figure 8.14: Block diagram of central station data flow.

8.8 Trigger

We conclude this chapter with a discussion of the trigger, which must select interesting physics events from a large background of random coincidences of small air showers. In order to accomplish this we have adopted a multi-level trigger design which is distributed both between hardware and software, and geographically. Table 8.1 summarizes the trigger levels and associated rates at each level for the ground array. This rate is compared to the rate of $\geq 10^{19}$ eV showers.

The level 1 trigger selects potentially interesting data from a background of several kHz of single muons, small showers, and PMT dark noise. This trigger is implemented in hardware on the front end board (see Section 8.2).

As it will take about 1 ms to transfer the FADC waveforms to the station controller memory, negligible ($< 1\%$) dead time will be incurred if trigger rate has been reduced to less than 100 Hz by the level 1 trigger and the FADC board is double buffered. The station controller then applies software algorithms to analyze the FADC waveforms to refine the level 1 trigger and produce the level 2 trigger. The level 2 trigger rate will be less than 20

Trigger level	Where	How	Condition	Rate	Triggers /Shower	Randoms (%)
0	Station	Hardware	Single μ + small showers + PMT noise	≈ 5 kHz per station	8×10^{10}	100
1	Station	Hardware	Limited/integrated energy	100 Hz per station	1.6×10^9	100
2	Station	Software	Level 1 + FADC info	20 Hz per station	3×10^8	100
3	Central	Software	3 fold level 2 in $20\mu\text{sec}$ window	0.2 Hz	1.5×10^3	100
4a	Central	Software	Level 3 + 1 additional level 2 in $1\mu\text{sec}$ window	15 / day	1.5	33
4	Central	Software	Level 3 + 2 additional level 2 in $1\mu\text{sec}$ window	10 / day	1	0.7

Table 8.1: Ground array trigger summary. In the last 2 columns the trigger rate is compared to the rate of $\geq 10^{19}\text{eV}$ showers. Level 3-4 rates are for the whole array.

Hz. This rate limit is imposed by the communications system, and is high enough that we will not be cutting out interesting physics events. Level 2 triggers are transmitted to the control center for further trigger processing.

The level 3 trigger nominally correlates information from nearby stations (e.g. 3 in any 7 station cell within a $20 \mu\text{s}$ coincidence window) or nearby stations plus an external level 2 trigger (e.g. optical fluorescence plus two stations). However, since the trigger is formed centrally in software, other variations can be implemented which are more sensitive to possible exotic phenomena. The level 3 trigger contains the minimum information required to reconstruct a shower. For example, a shower direction cannot be reconstructed from less than three ground stations. However, the background from random coincidences of single muons and small showers (estimated using binomial statistics and the 20 Hz level 2 rate constraint) is 1500 times larger than the rate of $\geq 10^{19}\text{eV}$ showers. Thus, level 3 triggers are in general not useful for physics analysis without additional constraints. Nevertheless, due to their low rate (0.2 Hz per site), all level 3 triggers will be archived and made available for further offline analysis. Once a level 3 trigger is formed the ground array and the fluorescence eyes are informed and the data from level 2 triggered stations is read out.

One should note that there is a high degree of symmetry in the trigger formation between the ground arrays and the fluorescence eyes. Level 2 and higher triggers from all components are incorporated into all higher level trigger decisions. Thus there are variations of the level

3 and higher triggers which contain only ground array data, contain a mixture of ground array and fluorescence detector data, or contain only data from 1 or more fluorescence eyes. For clarity, table 8.1 includes only purely ground array triggers.

The level 4 trigger further reduces the background contamination. This will be used as the basis for the on-line analysis of data. For the ground array a level 3 trigger, plus 2 additional level 2 triggers (from the 19 station cell centered on the level 3 trigger) occurring within a $1\ \mu\text{s}$ window around the shower front defined by the level 3 trigger will reduce the background to less than 1% of the triggers. In Table 8.1 we note (in line 4a) that one additional level 2 trigger is not sufficient in this scenario; $1/3$ of the triggers would be random coincidences.

Chapter 9

Site Survey

This chapter describes the work of the Site Survey Group and the candidate sites. The Auger Collaboration voted in November 1995 to select Nihuil, Argentina as the Southern Hemisphere site, and in September 1996 selected Millard Co., Utah, USA, as the Northern Hemisphere location.

9.1 Introduction

The Survey Group's task was to identify and characterize candidate sites — both in the Northern and Southern Hemispheres — suitable for construction of the Auger Cosmic Ray Observatories. Towards this end, and in consultation with members of the collaboration, a set of desirable site criteria was established. Contacts were initiated with interested parties in Argentina, Australia, China, Mexico, Russia, South Africa, Spain, and the USA. A summary of the site selection criteria was circulated to these groups, and they were asked to nominate candidate sites based on their knowledge of the respective areas.

Site visits to Argentina, South Africa, and Australia were completed in the first half of 1995 (a second visit to Argentina was made in September 1995). Visits to candidate sites in Spain and in Russia and Kazakhstan took place in the second half of 1995. During the first half of 1996 a site in northern Mexico and a number of sites in the western United States were investigated.

The following sections outline the criteria used in site selection, describe site visits and the data being collected as part of the survey effort, and summarize the results of these site visits.

9.2 Site Requirements

Discussions were held with members of the Fluorescence, Surface Detector, and Communications Groups to identify desirable site characteristics. These discussions led to a set of selection criteria: some motivated by physics considerations and others by more practical concerns. In the absence of a detailed detector design these requirements should be viewed as guidelines; a site failing to strictly meet these criteria would not necessarily be excluded from further consideration.

The selection criteria included:

- a latitude between 30° and 45° North or South of the equator;
- an area of about 3000 square kilometers;
- an altitude between 500 and 1500 meters above sea level;
- cloud cover less than $\sim 15\%$ with little ground fog and moderate temperatures;
- good visibility, and no significant nearby sources of light pollution.

Among the practical concerns were:

- that suitable infrastructure (e.g. power supply, freight access, telecommunications, and “goods and services”) should exist;
- the site should be relatively level with a mean slope less than 1% and not in excess of 2% to 3% over distances of a few hundred meters (i.e. both locally and globally flat);
- the vegetation, soils, and topography should not significantly impede array installation and maintenance.

Beyond the physical attributes of the sites under consideration the level of interest and support of the local scientific and civilian communities as well as of the governments, Provincial/State and Federal, concerned is of the utmost importance.

9.3 Site Visits and Relevant Data

Visits by the Site Survey Group have generally begun with a review of the materials collected by the host institution(s). These data include:

- “civil” maps indicating the location of roads, highways, railways, and airports; cities and towns; power and telecommunications links;

- topographic maps with elevation contours suitable for verifying access within the array;
- long term weather records including cloud cover, precipitation (both rain and snow), and high, low, and mean temperatures;
- an indication of the level of infrastructure present at or near the site (e.g. technical support services; industrial properties for off-site assembly and storage; facilities for vehicle maintenance; access to housing, fuel and food, etc.);

On-site visits themselves have typically been for a period of two to five days depending on the weather encountered. During this period an effort was made to traverse the sites on existing roads wherever possible. No off-road travel was undertaken and ease of access within any given site remains to be determined. Nearby towns which might provide the goods, services, and housing required by the project have also been visited.

Photometric (UBV) observations of selected stars were made at each site (see Figure 9.1). These data, taken in drift-scan mode throughout a range of zenith angles, yield both the background sky brightness and the apparent magnitude of the star under observation (the absolute magnitude diminished by wavelength dependent atmospheric absorption and scattering). It must be noted, however, that the limited time frame associated with these observations cannot provide a decisive indication of the optical quality of the sites; nor can the relative sensitivity of these measurements from site to site be guaranteed. Nevertheless, these observations do provide the best available measure of the relative atmospheric clarity and background sky brightness levels.

9.4 Argentina

Prior to the Survey Group's initial visit nearly a dozen sites were identified as possible candidates in Argentina. Due to time constraints however, only a few had been examined in significant detail. Of these sites three were selected for further investigation: Laguna Blanca, La Humada, and Monte Coman.

Subsequent to the first site visit, two additional candidates were identified — Nihuil and Somuncura. Work performed by the host institutions in Argentina together with results from a follow-on visit by the Site Survey Group led to the selection of Nihuil as the preferred candidate in Argentina.

9.4.1 Laguna Blanca:

The village of Laguna Blanca (41.5° S, 65° W, 1000 m.a.s.l.) is north of Jacobacci and approximately 200 kilometers east of San Carlos de Bariloche. It was known *a priori* that the site was in fact too small. However, the area is believed to be representative of much of the Province of Rio Negro in terms of the night sky background and atmospheric clarity.

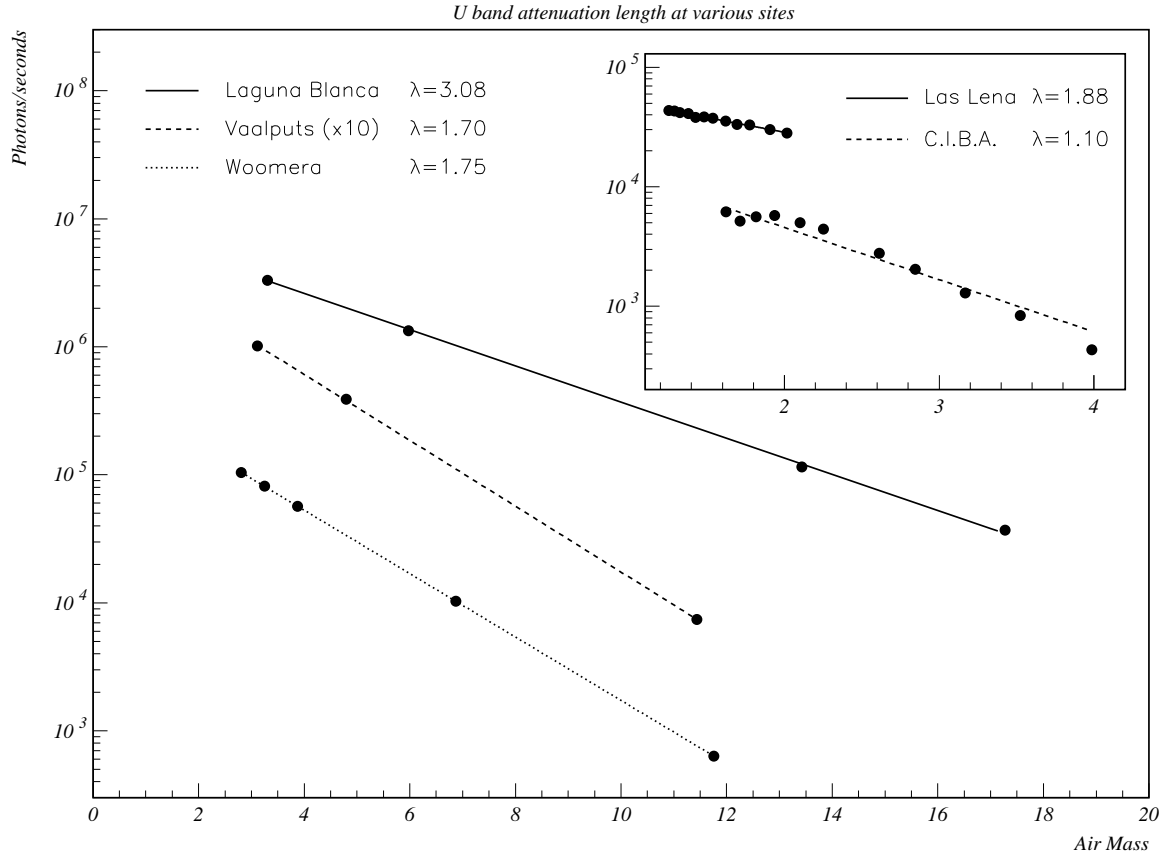


Figure 9.1: Rate vs Air Mass (g/cm^2) for U band (365 nanometers) observations at Laguna Blanca (solid line), Vaalputs (dashed line), Woomera (dotted line) and in the smaller frame Las Lena (solid line) and C.I.B.A. (dashed line). The measured $1/e$ attenuation distances in units of air mass range from 3.08 (Laguna Blanca) to 1.1 (CIBA). Measurements in the B and V bands are consistent with the above results.

Typically higher and more arid than other Provinces, Rio Negro has the potential for providing a very favorable site (see Somuncura below). On-site observations do indeed confirm that visibility is excellent and the sky extraordinarily dark.

9.4.2 La Humada:

The site near La Humada (36.2° S, 68° W, 750 m.a.s.l.) is 40 kilometers southwest of the small town of Santa Isabel. Santa Isabel, while a major crossroads in the Province of La Pampa, has itself somewhat limited infrastructure (e.g., it is not connected to the national power grid — electrical power is locally generated).

The La Humada site is more than adequate in size, both level and flat, and at an altitude suitable for the use of any of the detector technologies now under consideration. However, the infrastructure in the area is very limited — no power, water, or telecommunications links exist in or near the site. Access is via a single gravel road of good quality. The surface is composed of fine clay soils which are likely to be incompatible with fluorescence or other optical detector. The latter factor, together with the absence of infrastructure, has eliminated La Humada from further consideration.

9.4.3 Monte Coman:

The site (34° S, 67.5° W, 400 m.a.s.l.) is 40 kilometers northeast of the town of Monte Coman and occupies the southern portion of a uniformly flat area of nearly 20,000 square kilometers. Monte Coman is itself 60 kilometers east of San Rafael, one of the principal cities within the Province of Mendoza.

Physical Characteristics

The site is large, level, and with the exception of a few consolidated dunes, extraordinarily flat. The average elevation is 450 meters trending very slightly (0.1%) down towards the east. The surface is composed of compacted sedimentary material mixed with sand. Low vegetation (≤ 2 meters in height) covers much of the area. The Diamante River forms the southern boundary of this extended region while to the east and west the land rises substantially.

Climate

While the area is classified as “arid” the annual precipitation approaches 400 millimeters. Mean monthly rainfall in January (summer) is nearly 70 mm, while in July it falls to 20 mm; the relative humidity is typically 60%. The average nocturnal cloud cover, based on the ISCCP data, is 35% (peaking in July). Temperatures are moderate, averaging 16°C with a mean maximum of 31°C and a mean minimum of 1°C.

Infrastructure

Substantial infrastructure is present in the area. The cities of San Rafael (population 95,000) and San Luis (110,000), and to a lesser degree Monte Coman, provide most of the amenities required by the project. Regular domestic flights connect San Rafael and San Luis to Buenos Aires. Excellent rail and highway access as well as electrical power and water are available at the site's periphery. A good tarred road crosses its southern edge and dirt tracks exist within the site itself.

9.4.4 Nihuil:

Nihuil (35.2° S, 69.2° W, 1400 m.a.s.l.) lies near the center of the Province of Mendoza, 80 kilometers west of San Rafael. Malargüe (population 10,000), which supports the nearby resort of Las Leñas and a small oil processing facility, is near the site's southwestern border. In the western portion of the proposed site some oil extraction is being undertaken.

Physical Characteristics

The site is largely circular in shape encompassing an area of 3100 square kilometers and having a mean slope of less than 0.5%. Incorporating regions in which the slope approaches 1.5% increases this area to more than 3400 square kilometers. The Salado and Atuel rivers enter the site from the west and form an extremely broad and nearly flat alluvial fan composed of well consolidated soil, sand and gravel. At the edge of the fan shallow surface water may be present seasonally. The Salado River joins the Atuel in the western portion of the site and crosses from west to east. In the west it has formed a number of shallow channels extending laterally (that is, north to south) for approximately one kilometer. Across much of the site the river is contained in a single channel whose depth and breadth may exceed 5 and 20 meters respectively — fording will not be feasible and a bridge will be required. Grasses grow throughout the area and though relatively sparse (nowhere exceeding 70% coverage) across the alluvial fan they form an irregular surface — high clearance vehicles may be required.

Climate

Like Monte Coman, Nihuil is classified as “arid”. However, the annual precipitation is considerably lower, at 280 millimeters, and nearly uniform through the year. The estimated nocturnal cloud cover is similar to Monte Coman (35%, peaking in July at nearly 50%). As expected for the higher elevation, temperatures are cooler. The mean annual temperature is only 12°C, mean maximum 20°C, and the mean minimum of -2°C; the mean winter temperature is approximately 4°C with frost occurring 90 or more days per year.

Infrastructure

Nihuil is serviced by good tarred roads from San Rafael and Malargüe. Both cities can provide most of the necessary support facilities. High voltage transmission lines lie along the site's north and western borders. Water is readily available from the Atuel River and from underground aquifers.

9.4.5 Somuncura:

Somuncura (41.5° S, 67.4° W, 1200 m.a.s.l.) is near the southern border of the Province of Rio Negro and is the most southerly of the proposed Southern Hemisphere sites. Even by Argentine standards Somuncura is remote and sparsely inhabited; the settlements which do exist are on its periphery. Los Menucos, 70 kilometers to the north, lies on Route 23 and the rail-line which connects San Carlos de Bariloche to the deep water port at San Antonio Oeste.

Physical Characteristics

The Somuncura Plateau is an extensive basaltic highland totaling nearly 12,000 square kilometers. Elevations extend from 650 to 1350 meters above sea level. The proposed site encompasses 4000 square kilometers at an elevation of 1200 meters and is reported to be extremely level with a few isolated hillocks which are volcanic in origin and typically 100 meters in height.

Climate

Local climatic conditions must be inferred from meteorological stations at some distance from the site. The estimated precipitation is 160 millimeters per year with a cloud cover similar to that observed at Monte Coman and Nihuil. The mean annual temperature is 9°C, mean maximum 15°C, and the mean minimum 3°C. Frost is observed typically 130 days per year.

Infrastructure

The area is virtually devoid of infrastructure with no electrical power, tarred roads, telecommunications or other amenities. Serviceable gravel roads connect the site to Los Menucos. Tracks provide limited access within the site. Underground rain-fed aquifers provide the only available water. In Los Menucos, wells drilled to a depth of 100 meters supply 90 cubic meters per hour while nearby sources produce perhaps one-third this amount.

9.5 South Africa

Only a single site was selected for investigation in South Africa. It is in many respects the best of the sites visited.

9.5.1 Vaalputs:

The site is in the North Cape Province approximately 300 kilometers north of Cape Town and extends to the northeast from Vaalputs (29.8° S, 18.8° E, 950 m.a.s.l.). Vaalputs is operated by the Atomic Energy Corporation and is home to South Africa's low and intermediate level radioactive waste repository. The facility's primary mission is to receive waste from South Africa's civilian nuclear reactor program, verify the integrity of the casks in which it is transported, and to inter these in clay-lined pits.

The main building at Vaalputs contains three crane equipped high-bay areas for off-loading waste shipments, a small machine shop, a service bay for heavy vehicle maintenance, and administrative offices. The "Camp", located 8 kilometers from the main building, provides comfortable hotel style accommodation for 35 and includes a large communal kitchen, a lounge, and conference facilities.

Physical Characteristics

The proposed site is roughly rectangular in shape extending 45 kilometers to the east and 85 kilometers to the north of Vaalputs. Deviations from the average elevation are everywhere less than 20 meters and slopes are less than 0.5%. The site is bounded in the east by the Koa Valley depression, a relic drainage which seasonally contains a few flooded pans. To the west the land rises slightly becoming quite uneven; this is the uplifted edge of the South African escarpment.

Vegetation over the entire area is limited to grasses and widely scattered low shrubs; the soil is compacted sedimentary material, gravel, and some wind-blown sands.

Climate

Vaalputs maintains an automated meteorological station. Based on these and other records (from Springbok and Pofadder) the annual precipitation is estimated to be less than 40 millimeters per year. The mean annual temperature is 21°C, mean maximum 37°C, and the mean minimum 10°C; temperatures can exceed 40°C in summer. No immediately relevant ground-based cloud cover data is available. However, the atmospheric conditions at Sutherland, an astronomical observatory in the Karoo approximately 150 kilometers south of Vaalputs and sharing much the same weather, rival those of other well known astronomical observatories.

Infrastructure

The infrastructure in South Africa is, in the main, excellent. Even in the sparsely populated North Cape Province tarred roads connect most of the significant communities. To the east of the Koa Valley a heavy rail-line connects iron mines in the northeast of the Province with the coast at Saldanha. The site, which is primarily utilized for grazing, is criss-crossed by a network of well-maintained gravel roads (the personnel at Vaalputs commute daily 120 kilometers to Springbok on these roads). Numerous dirt tracks afford access within the grazing lands themselves.

Two power lines, servicing Vaalputs in the southwest-west and an air navigation beacon to the north-east, extend some 20 kilometers into the site. Both lines could be economically upgraded to 400 KVA. Other than in the seasonally flooded pans, no surface water exists in the area. However, as part of the preparatory work for the waste disposal facility, staff geologists at the Atomic Energy Corporation have thoroughly investigated the area's geo-hydrology. Substantial quantities of fossil water have been identified at depths of 60 meters at several points within the site. This water is highly mineralized and may require filtering and/or treatment by reverse osmosis.

Much of the economy of the North Cape Province is based on mineral extraction. Springbok provides most of the support required by the surrounding mining communities. Housing, industrial properties, and freight handling facilities are among the numerous services available at Springbok.

9.6 Australia

Australia has a long history of involvement in all aspects of ground based particle astrophysics. In particular, the University of Adelaide until recently operated an air shower array at Buckland Park and continues today to be involved in the design, construction, and operation of several atmospheric Čerenkov detectors at Woomera. Several individuals now at Adelaide have been members of the Fly's Eye collaboration in the past and bring with them a thorough understanding of all aspects of the Auger Project having to do with fluorescence detectors.

9.6.1 Woomera

The site is located in the south-east portion of the Woomera Prohibited Area (WPA; 31.1° S, 136.8° E, 150 m.a.s.l.), north and west of the town of Woomera which is itself 450 kilometers north of Adelaide. The WPA is operated by the Australian Department of Defense whose activities in the area are mainly directed to munitions testing. Most of the land, however, is leased for grazing and access is relatively unrestricted.

Physical Characteristics

The site is bounded in the south by seasonally flooded Lake Hart and in the east by uneven terrain and Lake Torrens. Topographic maps indicate that a significant fraction of the northern portion of the site is covered by consolidated dunes with heights of 2 to 5 meters. Aerial photos confirm the presence of the dune field. Further, they suggest that the dunes run mostly east-west with level areas interleaved between adjacent dunes. Far to the west, though still within the proposed site, trees with heights up to 4 meters are present. Though not dense, over distances of a kilometer or more they do significantly obscure the line-of-sight.

Though for the most part flat, small pans and associated drainages are present within the site. These can rapidly flood making access difficult if not impossible. Soils outside the dune fields or pans are principally “gibber”. This surface is characterized by myriad small pebbles or stones on top of a fine soil. While wind-blown dust is not a concern, mobility over the surface following any significant rainfall is reported to be extremely difficult.

Climate

In a climatic sense Woomera is midway between the coastal zone and the continental interior. Temperatures are moderate with a mean annual temperature of 21°C, and mean maximum and minimum temperatures of 32°C and 8°C respectively. Rainfall annually averages 140 millimeters. The University of Adelaide has initiated a sophisticated program of atmospheric monitoring using a technique similar to that used by the Site Survey Group. Observations by the Adelaide group agree with those made concurrently by the Survey Group.

Infrastructure

At present Woomera has 1300 inhabitants. In the past the population has been as high as 5000 and the facilities are commensurate with that number. Electrical power, potable water, housing, and industrial space are all readily available. The Stuart Highway and a railway connect Woomera to Adelaide and ports on the Spencer Gulf. Pimba just to the south of Woomera has a rail spur and unloading facilities.

Woomera’s infrastructure extends well into the site itself. Power, water and communications are present at “Range E” 45 kilometers northwest of Woomera, at “Range G”, site of Adelaide’s Čerenkov telescopes, and at the so-called “Stack Frag” facility. A number of surfaced and gravel roads pass through the site.

9.7 Spain

Initially three sites were under consideration in Spain: Tierra de Campos in Castilla y Leon, Castilla La Mancha northwest of Albacete, and Los Monegros east of Zaragoza. All three are located approximately 250 kilometers from Madrid and are readily accessible via the

federal highway system. All three are well serviced by an existing infrastructure network (e.g. roads, electrical power). In the end, however, only Tierra de Campos was selected for further consideration — both La Mancha, a heavily cultivated and somewhat irregular region, and Los Monegros, an area of significant vertical relief, were judged to be unsuitable.

9.7.1 Tierra de Campos

Tierra de Campos (41.8° N, 4.9° W, 780 m.a.s.l.) lies some 40 kilometers north of the city of Valladolid (population 400,000). The proposed site is bounded by Medina de Rioseco and Sahagun to the north and south respectively and by Paredes de Nava and Majorga in the east and west.

The University of Valladolid includes departments of Physics, Meteorology, and Telecommunications (within the Engineering School). The Meteorological Institute operates “CIBA” (Centro de Investigaciones de la Baja Atmosfera) an experimental station near the southern edge of the site. CIBA’s facilities include atmospheric monitoring equipment (e.g. acoustic sounding, nephelometers for measurement of atmospheric scattering) and 350 square meters of combined office, laboratory, and living space.

Physical Characteristics

The proposed site occupies a portion of the Castilla y Leon region which covers some 6000 square kilometers in total. The terrain is broadly flat with a mean slope from north to south downwards of 0.65°C. Shallow valleys in the southwest and northeast associated with the Valderaduey and Sequillo rivers cross the area; rolling hills are present in some areas, particularly in the north.

Approximately 80% of the land is either fallow or used in the production of cereal crops. The population density, low by European standards, is between 5 and 10 individuals per square kilometer. Within the site there are 4 or 5 villages of ten to fifteen thousand and an additional half dozen with populations between one and five thousand. (In contrast, the population density within the three southern hemisphere sites is significantly less than 0.1 per square kilometer.)

Climate

The climate in Tierra de Campos is classified as “semi-arid” with a mean annual precipitation of 450 millimeters. Monthly rainfall peaks in the winter at 55 millimeters, falling to typically 10 millimeters during the summer months. Cloud cover, based on estimates of the annual available sunshine, is 35%. The mean annual temperature is 12°C. Mean maximum (summer) and minimum (winter) temperatures are 28°C and 0.5°C respectively.

Infrastructure

As is expected, in association with the relatively high population density, the infrastructure is particularly well developed. The site is served by two highways and a network of national and regional roads (all tarred). In addition, a large number of well established (though untarred) roads provide ready access throughout the cultivated lands. A rail-line connects the area to Valladolid in the south (and hence on to Madrid) and to Leon in the north. Electrical power is available throughout the site from a number of high voltage transmission lines and from a network of low voltage distribution lines which serve the inhabitants of the immediate area. Water is readily available from domestic (municipal) supplies and from underground aquifers.

The industrial sector in Castilla y Leon is extensive and includes both heavy and high-technology manufacturing.

9.8 Mexico

In consultation with a group of geologists with extensive experience in the area a number of candidate sites were identified in northern Mexico. However, most were south of latitude 30°N and would provide only limited northern sky coverage. The preferred candidate, El Barreal, lies just south of the international border between Mexico and the United States.

9.8.1 El Barreal

The proposed site is approximately 100 kilometers west-south-west of the cities of Ciudad Juarez and El Paso (population > 1,000,000) and within the “tax free” border zone (31.3° N, 107.2° W, 1200 m.a.s.l.). Land use is principally grazing (30 – 40 ranches) though a few thousand hectares are under irrigated cultivation.

In addition to the scattered ranches two small villages, Las Palomas and Rodrigo Quevedo, lie within or immediately adjacent to the site; the population on-site is estimated to be less than 3000.

Physical Characteristics

The total land area at El Barreal is in excess of 6000 square kilometers; thus, several siting options are available. A regular hexagon containing no significant line-of-sight obstructions could be accommodated in the eastern portion of the area. However, the surface there is primarily consolidated dunes 1 to 3 meters in height — access would to a degree be impaired. In the north, northwest, and western sections the soils are basaltic and/or calcareous (i.e. of a much firmer nature). While generally flat this area does contain some high ground. The higher locations are typically 200 – 300 meters above the surrounding terrain, limited

in extent, and are generally accessible (excepting some steep terrain in a portion of the southwest).

Vegetation throughout the area is limited to low scrub, grasses, and some cacti.

Climate

The area is best described as “semi-desert”. The mean annual temperature is 25°C. The mean maximum (summer) temperature is 35°C, with a mean minimum in winter of -1°C. Annual precipitation averages 220 millimeters with more than 60% of the total falling in the months of July, August, and September. Between 180 and 220 days per year are cloudless; only 80 days are classified as cloudy (more than 50% cloud cover).

Infrastructure

Infrastructure at El Barreal is somewhat limited. A good tarred road crosses east to west across the northern portion of the site (connecting Juarez to Ascension southwest of the site). A second tarred road runs north to the border crossing at Rodrigo Quevedo near the western edge of the site. All other access throughout the site is via gravel roads of only moderate quality.

Electrical power is available only in the western portion of the site west and north of Las Palomas. An optical fiber connects Juarez and Ascension and a (presently) disused rail-line crosses the center of the site. Supplies and accommodation are available in Ascension and Rodrigo Quevedo.

9.9 United States of America

More than a dozen sites in the southwestern United States were considered as potential candidates for the Northern Auger Observatory (one in Nevada; three each in Arizona, Colorado, and Utah; five in New Mexico). After visits to each of the sites and following a careful review of the available data (e.g climatological, topographic), and in consultation with representatives from each State, four sites were selected for more detailed investigation.

9.9.1 Engle, NM:

The center of the site lies approximately 30 kilometers east of Truth or Consequences (33.1° N, 106.9° W, 1500 m.a.s.l.). The site is bounded in the east by White Sands Missile Range and the San Andreas Mountains, in the southwest by the Caballo Mountains, and in the northwest by the Fra Cristobal Mountains. Las Cruces (New Mexico State University) is roughly 80 kilometers south of the site; Albuquerque lies 150 kilometers to the north.

Physical Characteristics

The site deviates significantly from the “ideal” hexagonal configuration; its north-south extent is roughly three times that of its east-west dimension. (Dividing the site into fifths north to south, its east-west dimensions are 40, 27, 32, 40, and 42 kilometers respectively).

The mean elevation of the site is 1500 meters. However, very little of the land is level. Rather, it trends downward from the east and west towards a mid-valley line running north-south at an elevation of 1400 – 1450 meters. While numerous east-to-west and west-to-east drainages exist they are not generally deep. Elevated locations (up to 1750 meters) overlooking the site are accessible on the flanks of the Caballo, Fra Christobal, and San Andreas Mountains.

Approximately 70% of the land is State or Federal. The balance is held by a small number of individuals and lies principally in the north and northwest. Land cover is primarily grass and scrub. No significant areas of sand dunes or mud flats exist; some volcanic outflows are present in the far northern portion of the site.

Climate

The mean annual rainfall (at Truth or Consequences) is 240 millimeters. Precipitation is less than 0.5 millimeters per day excepting the period July through September when it increases roughly four-fold. During this period the likelihood of rainfall on any given day is 15% to 30%. Mean maximum and minimum temperatures in January (the coldest month) are 12°C and -3°C. The record maximum (minimum) temperature is 41°C (-21°C).

Infrastructure

An excellent tarred road connects Truth or Consequences to Engle. North and south from Engle are gravel roads of good quality (in the south connecting to the Interstate Highway near Hatch, New Mexico). Both a rail-line and a high voltage transmission line run north to south. A rail siding exists at Engle.

9.9.2 Grand Canyon, AZ:

The site is located on the Coconino Plateau just to the south of the Grand Canyon (35.8° N, 112.4° W, 1700 m.a.s.l.). Flagstaff lies 90 kilometers to the southeast beyond the San Francisco Mountains.

Physical Characteristics

The site is roughly elliptical in shape (30 by 75 kilometers) and extends from east of Valle, AZ to the Hualapai Reservation in the west and is bounded in the north by the Havasupai

Reservation and the Kaibab National Forest. The elevation increases to 1800 meters in all directions except north. A number of particularly high points lie along the southwest (long) edge of the site (e.g. Long Point which stands 200 meters above the site). Cataract Canyon, though narrow, bisects the site from southeast to northwest and forms a formidable barrier across the northern one-third of the site.

Approximately 45% of the land is held by the State of Arizona, 28% is owned and managed by the Navajo Tribe, and 27% by the Babbitt Ranches. Both the Babbitt Ranches and the Director of the Navajo Division of Natural Resources have expressed strong support for the project. The land cover is primarily grass with very little scrub; above 1800 meters elevation pinyon-pine is dominant.

Climate

The nearest National Weather Station is in Flagstaff 90 kilometers to the southwest and 400 meters higher — climate data there may not be representative of the site. Nevertheless, annual rainfall at Flagstaff is 580 millimeters (plus 2760 millimeters of snow). The mean rainfall is 2 millimeters per day decreasing significantly April through July; the “Percent of Possible Sun” is typically 75%, peaking in mid-June at 95%. The record maximum and minimum temperatures in Flagstaff are 36°C and -30°C respectively. The mean high (low) in January is 6°C (-9.3°C).

Infrastructure

Flagstaff and Williams (population 2500; 60 kilometer to the south) provide most of the required goods and services. State Highway 180 connects Grand Canyon Village to Flagstaff via Valle. Highway 64 connects Valle directly to Interstate 40 at Williams. No other tarred roads exist within the site. However, a number of good quality gravel roads enter the site from the south, southwest, and west; a paved road which serves the Hualapai reservation lies along the western boundary of the site. An electrical transmission line crosses the site east to west near Valle. A rail-line connects Williams to the South Rim of the Grand Canyon and a siding exists at Valle.

9.9.3 Lamar, CO:

The center of the proposed site lies near Highway 287 midway between Lamar and Springfield (37.7° N, 102.5° W, 1300 m.a.s.l.) The precise location is flexible due to the site’s size and overall uniformity. A hexagonal or “superman” configuration would be readily accommodated.

Physical Characteristics

The land slopes slightly from 1370 meters in the southwest portion of the site downwards to the north and east to an elevation of 1220 meters. Shallow drainages cross the area. Twin Buttes, at 50 meters above the surrounding terrain, is the only high point within the site. No other particularly significant topographic features exist.

Virtually all the land is privately held; the estimated number of land holders is 150. Local municipal and county officials believe that access is unlikely to be a significant concern. Land use is primarily grazing though up to 20% is under irrigated cultivation.

Climate

The mean annual rain and snow fall are 282 and 673 millimeters respectively. Precipitation is low October through April, typically 0.5 millimeters per day, increasing roughly three fold May to September. The mean maximum and minimum temperatures in January are 6°C and -10°C respectively.

Infrastructure

Lamar (population 8343) and Springfield (population 1475) lie 40 kilometers to the north and south respectively. Both are primarily farming communities. Pueblo, the nearest large community, is some 200 kilometers west of Lamar via the town of Las Animas.

The site is bisected by Highway 287 and bounded in the south at Springfield by Highway 160. A very extensive network of roads (on a standard one mile grid) covers much of the area; most are gravel of good quality. A large number of electrical distribution lines cross the area and a rail-line runs through Springfield northwest to Las Animas.

9.9.4 Millard, UT:

The site lies in Millard County just to the south of Delta and west of Filmore (150 kilometers southwest of Salt Lake City); its center is 6 – 8 kilometers southwest of Pavant Butte a prominent landmark (39.1° N, 112.6° W, 1400 m.a.s.l.) Inclusion of some high ground (the Cricket Mountains) in the west permits a hexagonal array configuration. The site is bounded to the east and southeast by Interstate 15 and in the south by rising ground near the Twin Peaks.

Physical Characteristics

The northern half of the site is at an elevation of 1400 meters, sloping slightly upwards toward the south to 1450 meters. A number of peaks and ridges exist within the proposed

bounds of the site including: the northern portion of the Cricket Mountains, Pavant Butte, Beaver Ridge (Telegraph Point), and Black Rock.

The Cricket Mountains are probably the most significant impediment within the Milford site. However, while they extend into the site approximately 15 kilometers, their lateral dimension are typically only 2 kilometers. Peak elevations are near 1800 meters and microwave relay stations are present at two locations. Pavant Butte is a prominent volcanic cinder cone roughly 2.5 – 3 kilometers in diameter and with an elevation of 1750 meters.

Volcanic outflows cover an area of 50 – 60 square kilometers; access is limited due to the extremely rough surface. Seasonally inundated mud flats exist covering an area of 150 square kilometers.

Approximately 80% of the land is Federal or State, the balance is in private hands (some 200-300 landholders) and lies near Interstate 15 in the eastern portion of the proposed site. Public lands are used for grazing while the private lands are under irrigated cultivation. Land cover throughout most of the public lands area is grasses with very little scrub.

Climate

Long term climatic records are not available for Delta. The nearest reporting station is in Milford 80 kilometers to the south and 100 meters higher in elevation. At Milford, the mean annual rain (snow) fall is 249 (1221) millimeters. The “Percent of Possible Sun” ranges from 60% during the fall and winter to 75% during spring and summer. (There is little seasonal variation in precipitation.) Mean maximum and minimum temperatures in January are 3.4°C and -10.9°C respectively.

Infrastructure

Delta (population 2998) is some 15 kilometers north of the northern boundary of the site; The northeast, and east and southeast sides of the area are bounded by Highway 50 and Interstate 15 respectively. Numerous gravel roads cross the site and the high ground of the Cricket Mountains, Pavant Butte, and Black Rock are all accessible via gravel road. A power line crosses Beaver Ridge in the south and a high voltage transmission line passes east-west just north of Pavant Butte. A rail-line with numerous sidings parallels Hwy 257 as does a fiber optic telecommunications link.

The Intermountain Power Plant (IPP), a multi-gigawatt coal burning facility, lies approximately 20 kilometers northeast of Delta. Assets at the IPP which may be available to the Auger Project include high-bay fabrication areas, office space, computing access, and industrial scale ultra-pure water production facilities.

Chapter 10

Central Station

In this short chapter we describe a model for the central station which we have used primarily to estimate costs. The estimated costs will be brought together with those of the detectors in the next chapter.

10.1 Central Station

We include in the Central Station a building containing office space and the central data acquisition system, a dormitory building and a shed to store material and assemble the detectors on the site. We assumed that the station should be able to house (office space and bedrooms) up to 10 people. Since the buildings are modular, the cost can easily be updated if other scenarios are envisaged. We include here the estimates of the civil-engineering and general equipment (details of the scientific equipment are given in the corresponding chapters).

10.1.1 The Office Building

We took as the basis of our proposal a barrack-type building of good quality available from a French firm. It has a total surface area of 153 m² obtained by using four identical modules each consisting of two office rooms, plus one specific module containing sanitary equipment and a kitchenette. The walls separating the individual office rooms can be suppressed to make larger rooms. Our proposal is to have 5 office rooms (including the kitchenette) and use the remaining space to install the data acquisition system and an electronics workshop. The office modules are 3 m wide, 10 m long (including a corridor separating the two face-to-face office rooms) and they can be added to or removed from the configuration we propose.

The building and equipment include all necessary comfort : thermal and acoustic insulation of roof and exterior walls, heating with thermostatically controlled electrical convection heaters, sanitary equipment, etc. The total cost given includes transport, labor and installation. The labor part of the cost would be around 25%. The furniture is included.

Four office rooms will be configured to contain the data acquisition system, terminal room and an electronics workshop. The latter would occupy the equivalent of one office room, and be equipped with standard laboratory instruments such as oscilloscopes, power supplies and pulse generators. A space equivalent to three offices would be devoted to the data acquisition system equipment and terminal rooms. The servers and electronic crates may be separated from the rest by an insulated partition wall to make a small air-conditioned room of about 10m². The air-conditioning clearly depends very much on the local climatic conditions. We were given upper and lower limits for the cost on the basis of 15 m² office space. We foresee much more powerful air-conditioning for the small room housing the electronics crates and the servers.

The fire safety installation consists of a general alarm (that can be computer monitored) and two extinguishers for each of the three buildings. A 200 kVA uninterruptable power supply will provide clean power to the electronics.

10.1.2 The Dormitory

The dormitory building is also modular and consists of 6 modules of 3×11.2 m², out of which five are pairs of rooms (hence a total of ten bedrooms) and one provides space for two rooms : one is a kitchen and the other may be used as a laundry. The building is delivered with the following equipment included (apart from those mentioned for the office building) : 1500 W thermostatically controlled convection heaters, sanitary facilities (showers, WC in all bedrooms), water heater and equipped kitchenette. The total cost includes transportation and installation.

10.1.3 The Shed

The shed has a surface of 680 m² to house an assembly area for the detectors before they are transported to the assigned local station position. The (included) thermal insulation of the shed (if needed) represents 30% of the cost. There is a rather complete mechanical workshop inside the shed.

10.2 Civil Engineering

This is the strongly site and country dependent part. To have a realistic cost estimate, we asked (through the Civil Engineering Department of the French National Research Council, CNRS) a few firms to work on the following scenario. We need to bring electricity, telephone lines, water and a road to the central station. The distance over which all these items are required is 35 km, roughly that from the border of the array to the center. It is not excluded that the facilities are accessible much closer to the central station, so the cost estimates on those items should be considered as very indicative. The ground is supposed to be flat and easy to dig. No rocks or other hard-to-cross obstacles are to be removed. There are no

Equipment	Cost (k\$)
Deployment and engines	424
Office building	375
Dormitory building	285
Shed/Assembly area	413
Roads	4359
Electrical and telephone lines	5213
Water	611
EDIA for access to site	1175
DAS (without Fly's Eye) and networks	276
Total	13131

Table 10.1: Central station and DAS overall cost estimates (per site).

construction works such as bridges, tunnels or viaducts. All raw materials are assumed to be close to the site, so that no transportation cost is included.

On the site itself, the civil engineering work comprises the concrete slabs for the three buildings (including parking places) and the sewers. The slab for the shed is thick enough to stand heavy loads (trucks). The others are thinner. The labor is estimated at approximately 50% of the total cost.

The road is 35 km long and 3.5 m wide with an asphalt surface. Every 2 km a 40m×4m crossover area is installed. The work includes the clearing of the ground, earth moving (embankments, hard core) and digging two lateral ditches (one of them containing the pipework for water and cableways for electricity and telephone). The asphalt surface lies on foundations.

Both electricity and telephone are transported between two main stations 35 km apart. In each case, three substations relay the lines. The main cost (\$100/m, i.e. 87% of the total) comes from the electrical cables. Installing underground cables (the situation envisaged here because of environmental impact issues) is much more expensive than aerial cables on poles. Depending on site details, the latter solution, if used, brings substantial economies on this item. The cold water is transported over the 35 km through 3 pumping sub-stations.

Chapter 11

Organization, Cost, and Schedule

11.1 Introduction

The Pierre Auger Project is a broad-based international endeavor to design, construct, and operate two giant ultra-high energy cosmic ray detectors, in the Northern and Southern hemispheres. The two detectors, to be located in the United States and Argentina, will operate as a single instrument: the Pierre Auger Cosmic Ray Observatory. The diverse nature of the collaboration, combined with the separation of the detectors, necessitate a clear management structure to meet its objectives.

11.2 Organization

An undertaking such as the Auger Project requires a multinational organization, a corporate entity, to act as its financial and legal agent. Since most contributions to the project will be in-kind, the funds held and dispersed by the corporation would be those funds needed to purchase materials and services which no participating country can provide, i.e. common funds. We envisage that the corporation would have a board of directors composed of the members, or a subset thereof, of the Auger Collaboration Board. Our intention is either to establish an international organization or use the services of an existing organization. CERN has indicated its willingness to host the Auger Organization.

Project tasks and contributions from each of the collaborating institutions will be negotiated by the Spokesman and the Project Manager. A Memorandum of Understanding between the Auger Project and each collaborating institutions will detail the scope of work, deliverables, the level of contribution to the common fund, the work schedule, and funding arrangements.

The organization of the Auger Project is indicated in Figure 11.1. The Collaboration Board is the principle governing body of the collaboration. The scientific and technical direction of the project is invested in the Spokesperson by the Collaboration Board. The

Figure 11.1: Pierre Auger Project Organization Chart.

Project Manager is responsible for construction and operation of the Auger Cosmic Ray Observatory. The Project Manager is supported by the Technical Board and by a staff which includes engineering, budget, and administrative personnel. Each site has a Site Manager who directs construction and operations on-site and who reports directly to the Project Manager. Task leaders are responsible for the major components of the detectors.

A description of the duties and responsibilities of each of the Collaboration Offices follows:

- **Spokesperson:** The Auger Project Spokesperson is elected by the Collaboration and is the representative of the Collaboration in scientific, technical, and management concerns; the Spokesperson speaks and negotiates on behalf of the Collaboration. He or she is responsible for establishing the scientific goals and for securing the means for the Collaboration to pursue those goals. The Spokesperson is also expected to assist in the identification of resources needed by the Auger Project and to seek the commitment of same. These resources come from the members of the Auger Collaboration, and their supporting agencies and institutions. The Spokesperson serves a renewable three-year term.
- **Site Spokesperson** — Each site will have a designated site spokesperson. The site spokesperson will be a member of the collaboration. He or she will act as liaison between the Project Spokesperson and the host country.
- **Collaboration Board** — The Collaboration Board, whose membership consists of one representative selected by each collaborating institution, deals with issues which concern the Collaboration as a whole. These include the governance of the Collaboration, the policy on admission of new members and institutions, and publication policy.
- **Project Manager** — The Project Manager is responsible for the design and fabrication of the detectors. The Project Manager defines and carries out project tasks, and is responsible for meeting cost, performance, and schedule goals for the project. He or she is responsible for managing the technical efforts set forth in the Memoranda of Understanding with each of the participating Project institutions. The Project Manager is assisted by personnel of the Project Office with the following tasks:
 - **Cost and Schedule** — The cost and schedule officer is responsible for budget, schedule development and tracking. He or she assists the Project Manager in developing contracts and Memoranda of Understanding for all Auger Project tasks.
 - **Systems Engineering and Integration** — The Project Engineer is responsible for technical requirements and the engineering quality of the technical interface among participating institutions, vendors and task leaders.
 - **Quality Assurance** — The Quality Assurance Officer develops and maintains a Quality Assurance Program to ensure the performance and reliability of the detector systems. He or she will assist the Project Engineer in developing production

quality control travelers and shop procedures for production of detector components.

- **Technical Board** — The technical Board consists of scientists and engineers involved in leadership roles in the various technical areas of the Auger Project. The members of the Technical Board are task leaders and others appointed by the Spokesperson and the Project Manager. The Technical Board is chaired by the Project Manager. The Technical Board reviews and makes recommendations to the Spokesperson and the Project Manager on all major technical decisions relevant to the Auger Project.
- **Site Managers** — The Site Manager is responsible for operations at the site both during construction and subsequent operation.

11.3 Construction Cost Estimate

The project cost estimate was developed using a variation of Work Breakdown Structure (WBS). The WBS is a “bottom-up” estimate in which an attempt is made to identify in detail all components, materials, services, and labor for the construction and installation of the project. The basic units for the cost estimate are mirror units for the fluorescence detector and detector stations (tanks) for the surface array. The materials, labor, and EDIA (engineering, design, inspection, and administration) are detailed for each unit. EDIA has been allocated as half of the total to each site. Labor costs have been estimated using standard US labor rates. Actual expenditures will be at local prevailing labor costs. Direct labor disbursement will be through the leading institution for each of the two sites.

Contingencies are applied to each line of the cost estimate according to a graded scale of the quality of the estimate.

Cost estimates do not include the labor, support, or travel expenses of the physicists or postdoctoral fellows; these costs are assumed to be covered by the collaborating institutions.

The intention of the collaboration is to maintain the total project cost below \$100M US (1996 dollars). A summary of the construction cost estimate is shown in Figure 11.2. The dollars summary is a rollup to the highest levels of the current WBS. The WBS will continue to evolve as detector development continues. For example the exact balance between the fluorescence detector and the surface detector necessary to achieve project objectives is not yet firm. Similarly, the level of in-kind contributions is not known.

11.4 Operating Cost

In estimating the Pierre Auger Observatory operating costs we have made the following assumptions:

- There will be two sites of approximately 3000km², each with approximately 1500 Water Cerenkov Detectors.
- Each site will include three Fluorescence Detectors.
- The project will operate for 20 years.
- Batteries in the surface detector power supply will require replacement twice during the period of operation.
- Each site will be equipped with five vehicles for maintenance and operations support.
- There will be a professional staff at the site to operate and maintain the observatory. These include:
 - a site manager,
 - an administrative clerk,
 - a computer systems professional,
 - three electronics technicians,
 - three electro-mechanical technicians,
 - three MS-level “observers,”
 - two general maintenance personnel.

A computer professional will be required for maintenance of the computer systems for both the surface array and the fluorescence detectors: including trigger systems, on and off site communications, and data acquisition. Auger’s detectors are comparable to astronomical observatories. Hence the presence of three MS-level physicists who will act as “observers” who will assist, as time permits, with detector diagnostics and software and hardware maintenance. Based on experience, two technicians will be required for maintenance of the fluorescence detectors; the remainder will be required by the surface detector systems. A crew of two will maintain the roads, pathways, and building and grounds on the site. The salaries including benefits indicated in Table 11.1 are based on information provided by the University of Utah and the Millard County Economic Development Office.

Estimated operating costs other than labor are summarized in Table 11.4. It is assumed that about 5% of the detector systems (other than tanks and buildings) would need to be replaced each year. The cost of leasing private land is uncertain at this time. Our most conservative estimate of \$90,000/year is shown in the table. Estimates are made for other expenses. The total operating cost for each site is estimated to be \$3M/year.

We have assumed that operating costs for the Southern site will be the same as the Northern site for estimating purposes only.

Pierre Auger Project Cost Estimate

November 11, 1996

W.B.S	WBS Name	Total M&S K\$	Total Labor K\$	Total EDIA K\$	Total Cont. K\$	Total Sites K\$	Total Project K\$	
	COMPLETE PROJECT	65,373.0	8,483.0	6,456.6	17,817.5	98,130.2	98,130.2	
	SOUTHERN SITE	32,776.0	4,241.5	3,347.8	8,986.5	49,351.8		
	NORTHERN SITE	32,597.0	4,241.5	3,108.8	8,831.1	48,778.4		
								0
1.0	FLUORESCENCE DETECTOR	9,817.3	426.6	1,127.5	1,825.1	13,196.4	26,392.8	26392.84
								0
1.1	Detector System	7273.2	374.4	780.0	990.4	9418.0		18835.92
								0
1.1.1	Camera System (mirror station)	3,672.0	277.2	280.0	484.4	4,713.6		9427.12
1.1.2	Camera Readout System	2,445.6	54.0	150.0	325.4	2,975.0		5949.92
1.1.3	Mirror System	504.0	43.2	100.0	75.4	722.6		1445.12
1.1.4	Mirror housing building (4 per)	651.6	0.0	250.0	105.3	1,006.9		2013.76
1.2	Calibration System	458.4	48.0	75.0	60.2	641.6		1283.28
1.3	Atmospheric Monitor	312.0	.1	100.0	31.2	443.3		886.62
1.4	Power Distribution	133.8	4.1	5.0	41.4	184.2		368.41
1.5	Fluorescence eye controls	368.6		51.5	110.6	530.6		1061.23
1.5.1	Building	168.0		50.0	50.4	268.4		536.8
1.5.2	Furniture	3.5			1.0	4.5		8.97
1.5.3	Workshop	57.3			17.2	74.5		148.98
1.5.4	HVAC	1.8		0.5	0.5	2.8		5.68
1.5.5	Fire Safety	4.5		1.0	1.4	6.9		13.7
1.5.6	Computer facility	133.5			40.1	173.6		347.1
1.6	Fluorescence Eye Trigger	471.3		16.0	141.4	628.7		1257.38
1.6.2	Level 2 trigger	144.0		5.0	43.2	192.2		384.4
1.6.3	Level 3 trigger	84.0		1.0	25.2	110.2		220.4
1.7	Shipping (to site)	800.0		100.0	450.0	1350.0		2700
2.0	SURFACE DETECTORS	18,192.8	2,564.5	1,490.0	5,730.8	27,978.0	55,956.0	55955.972
2.1	Detector System	5576.0	328.0	325.0	1354.8	7583.8		15167.6
2.1.1	Cerenkov Radiator Tank	4,776.0	168.0	320.0	1,114.8	6,378.8		12757.6
2.1.2	Radiator	800.0	160.0	5.0	240.0	1,205.0		2410
								0
2.2	Readout	5,088.0	300.0	233.0	987.7	6,608.7		13217.4
								0
2.2.1	Photomultiplier tubes	4,080.0	60.0	50.0	431.0	4,621.0		9242
2.2.2	Tube bases	384.0	168.0	63.0	186.7	801.7		1603.4
2.2.3	Phototube Assembly	480.0	36.0	110.0	313.0	939.0		1878
2.2.4	Phototube High voltage	144.0	36.0	10.0	57.0	247.0		494
2.3	Electronics	4,085.6	611.8	736.0	1,631.6	7,065.0		14129.932
2.3.1	Front End & calibration	720	166	206	358	1450		2900
2.3.2	Control, DAQ & Monitor	800	22	200	506.7	1529.2		3058.4
2.3.3	Timing	512.0	40.0	50.0	76.2	678.2		1356.4
2.3.4	Communications (Federal Sys.)	1,253.6	41.3	140.0	320.0	1,754.9		3509.732
2.3.5	Mounting/card cage/backplane//	480	22.5	70	171.7	744.2		1488.4

Figure 11.2: Summary of the Cost Estimate.

Pierre Auger Project Cost Estimate

November 11, 1996

W.B.S	WBS Name	Total M&S K\$	Total Labor K\$	Total EDIA K\$	Total Cont. K\$	Total Sites K\$	Total Project K\$
	2.3.6 Electronics enclosure	320.0		70.0	39.0	429.0	858
	2.3.7 Electronics Package Testing		160.0		80.0	240.0	480
	2.3.8 Installation		160.0		80.0	240.0	480
							0
2.4	Solar Power System	1,763.2	480.0	60.0	426.3	2,729.5	5459.04
							0
	2.4.1 Power system	1,763.2		50.0	181.3	1,994.5	3989.04
	2.4.2 Battery Enclosure		320.0	10.0	165.0	495.0	990
	2.4.3 Installation		160.0		80.0	240.0	480
							0
2.5	Shipping (to site)	1600.0		100.0	850.0	2550.0	5100
							0
2.6	Deployment	80.0	844.7	36.0	480.3	1,441.0	2882
							0
	2.6.1 Site preparation	80.0	304.0	24.0	204.0	612.0	1224
	2.6.2 Installation	0.0	220.7	7.0	113.8	341.5	683
	2.6.3 Station check out		320.0	5.0	162.5	487.5	975
							0
3.0	CENTRAL STATION	2,247.0	0.5	387.3	647.0	3,281.8	6,563.6
							6563.5806
							0
3.1	Office Building	685.7	0.5	71.5	109.3	867.1	1734.1296
							0
	3.1.1 Concrete Slab(thin)	30.0		7.5	9.0	46.5	93
	3.1.2 Building and gen. equipment	130.0		32.0	26.5	188.5	377
	3.1.3 Furniture(5 office rooms)	10.9			1.1	11.9	23.87
	3.1.4 Air conditioning	47.6		5.0	14.3	66.9	133.7496
	3.1.5 Fire Safety	6.0		1.5	1.8	9.3	18.6
	3.1.6 Terminal Room	34.9		5.0	3.5	43.3	86.692
	3.1.7 LAN	1.4	0.5	0.5	0.7	3.1	6.218
	3.1.8 Machines for deployment	425.0		20.0	52.5	497.5	995
							0
3.2	Housing	282.5		61.8	39.9	384.2	768.487
							0
	3.2.1 Concrete slab (thin)	22.5		5.0	6.8	34.3	68.5
	3.2.2 Building and gen. equipment	210.0		50.0	21.0	281.0	562
	3.2.3 Air Conditioning	33.4		4.5	10.0	47.9	95.775
	3.2.4 Fire safety	1.2		0.3	0.6	2.1	4.2
	3.2.5 Furniture	15.5		2.0	1.5	19.0	38.012
3.3	Assembly Area/Shop	454.6		84.0	112.4	651.0	1302.024
							0
	3.3.1 Concrete slab (thick)	200.0		50.0	60.0	310.0	620
	3.3.2 Building	85.0		20.0	16.5	121.5	243
	3.3.4 Utilities	10.0		2.5	5.0	17.5	35
	3.3.5 HVAC	53.5		5.0	16.1	74.6	149.204
	3.3.6 Electronics Workshop	68.0		5.0	6.8	79.8	159.6
	3.3.7 Mechanical workshop	32.1			5.0	37.1	74.22
	3.3.8 Fire safety	6.0		1.5	3.0	10.5	21
3.4	Data Acquisition	95.0		20.0	26.9	141.9	283.8
							0
	3.4.1 Computer (array)	95.0		20.0	26.9	141.9	283.8
							0
3.5	Telecommunications	163.8		50.0	49.1	262.9	525.88
							0
	3.5.1 External links	8.8		15.0	2.6	26.4	52.88
	3.5.2 Internal links	155.0		35.0	46.5	236.5	473
							0
3.6	Acquisition Hardware	61.5			9.0	70.5	140.9

Figure 11.3: Summary of the Cost Estimate.

**Pierre Auger Project
Cost Estimate**

November 11, 1996

W.B.S	WBS Name	Total M&S K\$	Total Labor K\$	Total EDIA K\$	Total Cont. K\$	Total Sites K\$	Total Project K\$
							0
3.6.1	Array controller	61.5			9.0	70.5	140.9
							0
3.7	Office Equipment	3.8			0.4	4.2	8.36
							0
3.7.1	Furniture	3.8			0.4	4.2	8.36
3.8	Water Supply for Surface Det.	500.0		100.0	300.0	900.0	1800
4.0	SITE SPECIFIC COSTS	4,359.0	1,200.0	447.0	1,411.8		7,417.8
							0
4.1	Southern Site	2,269.0	600.0	343.0	783.6	3,995.6	7991.19997
							0
4.1.1	Roads	1,606.0		239.0	553.5	2,398.5	4796.99997
4.1.2	Electrical & Telephone lines	633		100	219.9	952.9	1905.8
4.1.3	Water	30.0		4.0	10.2	44.2	88.4
4.1.4	Site Management		600.0			600.0	
4.2	Northern Site	2,090.0	600.0	104.0	628.2	3,422.2	6844.4
							0
4.2.1	Roads	1,660.0		50.0	498.0	2,208.0	4416
4.2.2	Electrical & Telephone lines	400.0		50.0	120.0	570.0	1140
4.2.3	Water	30.0		4.0	10.2	44.2	88.4
4.2.4	Site Management	0.0	600.0			600.0	
5.0	PROJECT MANAGEMENT	500.0	1,300.0				1,800.0
							0
5.1	Personnel		1,300.0				
5.2	M&S	500.0					

Figure 11.4: Summary of the Cost Estimate.

Personnel	Annual Cost (k\$)
Site Manager	100.0
Administrative Clerk	34.1
Computer Sys. Manager	90.0
Electro-mech. Techs. (3)	158.0
Electronics Techs. (3)	158.0
Physicist/Observers (3)	180.0
General Maintenance (2)	74.8
Total	794.9

Table 11.1: Estimated salaries for on-site Project personnel including fringe and benefits.

Task	Cost (k\$)
Detector Maintenance	1450.0
Land Maintenance	90.0
Battery replacement	91.0
Upgrade stations	160.0
Facilities maintenance	20.0
Road maintenance	50.0
Vehicle maintenance	40.0
Vehicle acquisition	25.0
Utilities	62.5
Custodial services	50.0
General materials and services	200.0
Total	2238.5

Table 11.2: Estimated annual operating costs (excluding salaries).

11.4.1 Project Schedule

The Auger Observatory design is already well underway. There are no known barriers to successful construction of the observatory. The basic methodology uses techniques which have become the standard in the field over thirty years. Many of the scientists who pioneered these techniques are Auger collaborators.

Most aspects of the detector have been studied well enough to begin preliminary design of components of the detectors. Development of this design will continue while funding is being secured. A formal preliminary design review (PDR) will be held during 1997. Detailed design of components will be completed in the first year of project support. This will culminate in a critical design review (CDR), and detector construction will begin. In parallel with the design effort, necessary infrastructure improvements to the site will begin, and the central facility will be constructed.

We estimate the detector will be fully operational in five years. A schedule of project milestones is included in Table 11.3. Data taking will begin in the second year.

Table 11.3: Commissioning and Preliminary Data Taking.

Year 1 1998	Design activities and critical design review. Construction of central facility. Civil construction at fluorescence site 1. Field testing of prototype water Cerenkov detector. Construct first batch of 100 water Cerenkov detectors. Begin construction of components for fluorescence detectors.
Year 2 1999	Install first 100 water Cerenkov detectors. Fluorescence site 1 fully operational. Complete and install fluorescence site 1. Civil construction at fluorescence site 2.
Year 3 2000	Install 600 water Cerenkov detectors. Fluorescence sites 1 and 2 fully operational. Complete and install fluorescence site 2. Civil construction at fluorescence site 3.
Year 4 2001	Install 600 water Cerenkov detectors. Fluorescence sites 1 and 2 fully operational. Complete and Install fluorescence site 3.
Year 5 2002	Install last 300 water Cerenkov detectors, including those in areas with different access. All fluorescence sites fully operational. Transition to observatory operations.

Appendix A

Auger Project Participants

A.1 Auger Collaboration Membership

The Auger Collaboration was formally established during a meeting in Paris at UNESCO headquarters in November 1995. The official list of collaborators and institutes (as of January 1997) is given here. In the following list, Group Representatives (Collaboration Board members) are indicated by a "*" and their e-mail addresses are indicated for the group. The (S) indicates the PhD students.

Argentina

Country contact : Alberto Etchegoyen.

- **Comisión Nacional de Actividades Espaciales (CONAE) - Instituto de Astronomía y Física del Espacio (IAFE)**
Address : C.C. 67, Suc. 28, 1428 Buenos Aires
Fax : (+54)1 7868114
E-mail : rcolomb@conae.gov.ar
Raul Colomb*, Eduardo Colombo, Adrian Rovero.
- **Centro Regional de Investigaciones Científicas y Tecnología (CRICyT)** Address : Bajada de Cerro s/n, Parque Gral. San Martin, CC 131 - 5500 Mendoza
Fax : (+54)61 287370
E-mail : cricyt@planet.losandes.com.ar
Richard Branham*, Beatriz Garcia, Enrique Miranda, Juan Weisz.
- **Universidad Nacional de La Plata**
Address : Facultad de Ciencias Exactas, Departamento de Física, C.C. 67 - 1900 La Plata
Fax : (+54)21 252006
E-mail : dova@venus.fisica.unlp.edu.ar

Luis Anchordoqui (S), Maria Teresa Dova* (Shower simulation coordinator), Luis N. Epele, Pablo E. Lacentre (S), Hugo Lorente, Sergio J. Sciutto.

- **Instituto Argentino de Radioastronomia (IAR)**

Address : C.C. 5, 1894 Villa Elisa, Pereyra Iraola, Provincia de Buenos Aires

Fax : (+54)21 254909

E-mail : romero@venus.fisica.unlp.edu.ar

Ismael Azcarate, Esteban Bajaja, Santiago Perez-Bergliaffa, Jorge A. Combi, Gustavo E. Romero*, Jose Bava, Aurelio Juan Sans

- **Laboratorio TANDAR-CNEA**

Address : Departamento de Física, Comisión Nacional de Energía Atómica, Av. del Libertador 8250, (1429) Buenos Aires.

Fax : (+54)1 754 7121 (TANDAR) ; (+54)1 7827647 (FCEyN)

E-mail : afaf@tandar.cnea.edu.ar

Alberto Etchegoyen (Southern site Spokesman), Jorge Fernandez-Niello, Armando Ferrero, Alberto Filevich* (Southern site Manager), Armando Ferrero, Carlos Guerard, Frederico Hasenbalg, Ricardo Piegaia, Diego Ravignani, Pablo Bauleo, Julio Rodriguez, Miguel Mostafa.

- **Centro Atómico Bariloche e Instituto Balseiro (CNEA - Universidad de Cuyo)**

Address : 8400 S.C. de Bariloche

Fax : (+54)944 45299

E-mail : masperi@cab.cnea.edu.ar

Alberto Ceballos, Andres Garcia, Luis Masperi*, Rafael Montemayor, Guillermo Silva(S), Guillermo Zemba.

Armenia

Country contact : Ashot Chilingarian.

- **Yerevan Physics Institute**

Address : Alikhanian Brothers Str.2, Yerevan 36

Fax :

E-mail : chili@crdlx3.yerphi.am

Ashot Akhperjanian, Ashot Chilingarian*, Gagik Hovsepian, Eduard Mnatzakanian, Vardan Sahakian, Samvel Ter-Antonian.

Australia

Country contact : Roger Clay.

- **University of Adelaide**

Address : Department of Physics and Mathematical Physics, University of Adelaide
(South Australia) 5005

Fax :

E-mail : rclay@physics.adelaide.edu.au

David Bird, Roger Clay*, Bruce Dawson (Detector simulation coordinator).

Bolivia

Country contact : Carlos Aguirre.

- **University of La Paz**

Address : Instituto de Investigaciones Fisicas, Universidad Mayor de San Andres, PO
Box 8635, La Paz

Fax : 591 2 792622

E-mail : rticon@fumsa.bo

Carlos Aguirre, Rolando Ticona*, Alfonso Velarde, Francisco Zaratti.

Brazil

Country contact : Carlos Escobar.

- **University of Campinas (UNICAMP)**

Address : CP 6187 CGI, 13083-970 Campinas

Fax : (+55)192 394717 E-mail : turtelli@ifi.unicamp.br

Biral (S), Carola Dobrigkeit, Jose Chinellato, Anderson Fauth, Marcelo Guzzo, Kemp
(S), Leigi (S), Mengotti (S), Nogima (S), Santos (S), Edson Shibuya, Armando Turtelli*.

- **University of Sao Paulo**

Address : Instituto de Fisica, Universidade de Sao Paulo (CP 66318), 05389-970 Sao
Paulo, SP

Fax : (+55)11 211 2742 E-mail : escobar@if.usp.br

Carlos Escobar* (Chairman of the CB), Philippe Gouffon, Miguel Luksys, Nikolai Ku-
ropatkin, Renata Zukanovich.

- **CBPF-Lafex**

(Catholic University, Rio -PUC- represented by CBPF)

Address : Rio de Janeiro

Fax :

E-mail : shellard@lafex.cbpf.br

Gilvan Alves, Luiz Mundim, Anselmo Paschoa (PUC), Maria Elena Polme, Ronald
Shellard* (Analysis software coordinator), Moacyr de Souza.

- **Physics Institute - Federal University**

Address : Instituto de Fisica, Universidade Federal do Rio de Janeiro, Cidade Universitaria - CT/Bl. A, Ilha do Fundao, 21945-970 Rio de Janeiro (RJ)

Fax : (+55)21 280 76 93

E-mail : marechal@if.ufrj.br

Miriam Gandelman, Bernard M. Maréchal*, Leandro de Paula.

Chile

Country contact : Patricio Häberle.

- **Universidad Técnica Federico Santa Maria (UTFSM)**

Address : Departamento de Física, UTFSM, Casilla 110-V, Av. Placeres 401, Valparaíso

Fax :

E-mail :

Gastón Agüero, Rolando Esparza, Patricio Häberle*.

China

Country contact : Ma Yuqian.

- **Institute of High Energy Physics (IHEP)**

Address : High Energy Astrophysics Lab, P.O.BOX 918-3 - Beijing 100039

Fax : (+86)10 68213374

E-mail : mayq@heal2.ihep.ac.cn, mayq@astrosv1.ihep.ac.cn

Ma Yuqian*, Bai Xinhua, Jiang Yinlin, Zhang Chengmo, Xu Chunxian, Sheng Changquan, Sheng Peiruo, Dai Yifang, Shao Xiaohong, He Huilin, Gao Xiaoyu.

France

Country contact : Murat Boratav.

- **Ecole Nationale Supérieure de Télécommunications de Paris (ENST)**

Address : 46 rue Barrault, 75634 Paris Cedex 13

Fax : (+33)(0)145804036

E-mail : roux@elec.enst.fr

Marie-Laure Boucheret (ENST - Toulouse), Emmanuel Boutillon*, Nicolas Demassieux, Denis Roux (Electronics department) ; Claude Rigault (Networks department) ; Robert Vallet (Communications department).

- **Groupe Temps-Fréquence de l'Observatoire de Besançon**

Address : 41bis Avenue de l'Observatoire (BP 1615), 25010 Besançon Cedex

Fax : (+33)(0)381666944

E-mail : fmeyer@obs-besancon.fr

François Meyer*, Philip Tuckey, François Vernotte, Michel Vincent.

- **Laboratoire de Physique Corpusculaire du Collège de France**

Address : 11 Place Marcelin-Berthelot, 75231 Paris Cedex 5

Fax : (+33)(0)143546989

E-mail : jmb@cdf.in2p3.fr

Jean-Michel Brunet*, Jean-Noël Capdevielle, Bernard Courty, Pierre Frenkiel, Laurent Guglielmi, Corentin Le Gall (S), Gérard Tristram.

- **Laboratoire de Physique Nucléaire et de Hautes Energies, Université Paris 6 (LPNHE)**

(Orsay University and Meudon Observatory represented by LPNHE.) Address : LPNHE - Université Paris 6 (Boîte 200), 4 Place Jussieu, 75252 Paris Cedex 05

Fax : (+33)(0)144274638

E-mail : antoine@lpnpsc.in2p3.fr

Pierre Billoir, Murat Boratav (Secretary of the CB), Sylvie Dagoret-Campagne, Antoine Letessier-Selvon*, Zaharia Strachman.

- **Individuals** (represented by LPNHE)

Alain Cordier (Orsay), Paul Eschstruth (Orsay), Bernard Merkel (Orsay), Patrick Peter (Meudon), Philippe Roy (Orsay).

Germany

Country contact : Karl-Heinz Kampert.

- **University of Karlsruhe - IK3 Forschungszentrum**

Address : Forschungszentrum Karlsruhe (IK3), P.O.Box 3640, D 76021 Karlsruhe

Fax :

E-mail : kampert@ik1.fzk.de

Hartmut Gemmeke, Ralph Glastetter (S), Karl-Heinz Kampert*, Hans Klages, Johannes Knapp (Shower simulation coordinator), Peter Steinhäuser.

Greece

Country contact : Emmanuel Fokitis.

- **National Technical University of Athens**

Address : NTUA, Physics Department, Zographos 15780

Fax :

E-mail : fokitis@vxcern.cern.ch

Anastasios Filippas, Emmanuel Fokitis*, Leyteris Kayafas, Victor Kytopoulos, Stavros Maltezos, Kassiaty Manolatu (S), Nick Uzunoglu.

Institute for Electronic Structure and Lasers - Crete (represented by NTUA) : Address :
Materials Research Group, IESL, Science and Technology Park of Crete, PO Box 1527
Voutes, Heraklion 71110, Crete

Fax : (+30)81 239735

N.Garawal (S), Giorgos Kyriakidis, C.Moshovis, S.Nikolaki, G.Vasiliou, Ch. Xirouhaki.

Japan

Country contact : Motohiko Nagano.

- **Institute for Cosmic Ray Research (ICRR)**

(Yamanashi and Osaka City Universities represented by ICRR.)

Address : University of Tokyo, 3-2-1 Midoricho, Tanashi-shi, Tokyo 188

Fax : (+81) 424 62 3096

E-mail : mnagano@asun2.icrr.u-tokyo.ac.jp

Naoaki Hayashida, Ken Honda (Yamanashi), Saburo Kawakami (Osaka City), Motohiko Nagano*, Masahiro Teshima (TA coordinator), Shigeru Yoshida.

Mexico

Country contact : Arnulfo Zepeda.

- **Benemerita Universidad Autonoma de Puebla (BUAP)**

Address :

Fax :

E-mail :

Eduardo Cantoral, Alberto Cordero Davila, Lorenzo Dias Cruz, L. Guillermo de Ita, German A. Munoz Hernandez, Arturo Fernandez*, Andrey S. Ostrovsky, Alfonso Rosado, Humberto Salazar, Alexandre Zemilak.

- **High energy experimental physics, Centro de Investigacion y de Estudios Avanzados del IPN (CINVESTAV)**

Address :

Fax :

E-mail : zepeda@titan.ifc.uv.es

Umberto Cotti, Hector Mendez, Arnulfo Zepeda*.

- **Universidad Nacional Autonoma de Mexico (UNAM)**

Address : IGf/UNAM, Ciudad Universitaria, 04510 Mexico D.F.

Fax :

E-mail : jfvaldes@tonatiuh.igeofcu.unam.mx

Juan Carlos D'Olive, Lorenzo Martinez, Arturo Menchaca, Jose F. Valdes*.

- **Individuals** (represented by CINVESTAV)

Alberto Carraminana Alonso (Instituto Nacional de Astrofisica, Optica y Electronica -INAOE-), Arturo Gonzalez Vega (Universidad Autonoma de Guanajuato -UAG-), Celso Gutierrez (INAOE), Antonio Morelos Pineda (Universidad Autonoma de San Luis Potosi), Luis M. Villasenor Cendejas (High energy experimental physics, Universidad Michoacana de San Nicolas Hidalgo -UMSNH-).

Russia

Country contact :

- **Moscow State Engineering Physics Institute (MEPhI)**

Address : NEVOD, MEPhI, Kashirskoye shosse, 31, Moscow 115409

Fax : (+7)095 3242111

E-mail : PETRUHIN@nevod.mephi.msk.su

Vladimir Aynutdinov, Rostislav Kokoulin, Anatoli Petrukhin*, Igor Yashin.

Slovenia

Country contact : Danilo Zavrtanik.

- **Institut Jožef Stefan**

Address : Jamova c. 39, 61111 Ljubljana

Fax : (+38)6 611252017

E-mail : danilo.zavrtanik@ijs.si

Andrej Filipčič, Danilo Zavrtanik*, Marko Zavrtanik.

Spain

Country contact :

- **Telecommunication Engineering School - Polytechnical University of Madrid (ETSIT-UPM)**

Address : ETSI Telecomunicacion-UPM, Ciudad Universitaria s/n, 28040 Madrid

Fax : (+34)1 336 7350

E-mail : javier@gaps.ssr.upm.es

Francisco Javier Casajus Quiros*, Pedro Olmos (CIEMAT), Jesus Cid Sueiro, Maria Soledad Torres ; Pedro Ladron de Guevara (CIEMAT).

United Kingdom

Country contact : Alan A. Watson.

- **University of Leeds**

Address : Physics Department, Leeds LS2 9JT

Fax : (+44)113 233 3900

E-mail : phy6je@phys-irc.novell.leeds.ac.uk

Paul Clark, Jeremy Lloyd-Evans*, Alan Watson (Co-Spokesman).

USA

Country contact : Paul Mantsch.

- **Enrico Fermi Institute - University of Chicago**

Address : 5640 South Ellis Avenue, Chicago - IL 60637

Fax : (+1)312 7026645

E-mail : gibbs@uchepp.uchicago.edu

James W. Cronin (Spokesman), Brian Fick, Kenneth Gibbs*, Clement Pryke, Jonathan Rosner, Simon Swordy.

- **Colorado State University**

Address :

Fax :

E-mail : harton@lamar.ColoState.EDU

John Harton*, Phil Kearney, Russel Malchow, James Sites, David Warner, Robert Wilson.

- **University of Colorado**

Address : Department of Physics, Boulder, CO 80309-0390

Fax : (+1)303 492 5119

E-mail : tonyb@colohe.Colorado.EDU

Anthony Barker*, Jeffrey Brack, Carl Gelderloos, Uriel Nauenberg, Stephen Pollock, Robert Ristinen, Chris Zafiratos, Ellen Zweibel.

- **Fermilab**

Address : Fermilab, MS 343 - Box 500, Batavia, Illinois 60510

Fax : (+1)708 840 8032

E-mail : mantsch@fnal.gov

Mike Albrow, Mary Anne Cummings, Tom Droege, Tom Groves, Carlos Hojvat (Deputy-Manager), Hans Kautzky, Paul Mantsch* (Project Manager), Peter Mazur, Lou Voyvodic.

- **University of Michigan**

Address : Dept of Physics, Randall Laboratory, Ann Arbor, MI 48108

Fax : (+1)313 936 1817

E-mail : jamesmm@umich.edu

Bob Ball, John Mann, James M. Matthews* (Detector simulation coordinator), Colleen Murphy, David Nitz (Telecom coordinator), Wayne Stark.

- **New-Mexico State University (NMSU)**
 Address :
 Fax :
 E-mail : stochoj@nmsu.edu
 Steve Stochaj*, Bill Webber.
- **University of New Mexico**
 Address : Physics Department, Albuquerque, NM 87131
 Fax : (+1)505 2772077
 E-mail : johnm@nmhepb.phys.unm.edu
 Byron Dieterle, Michael Gold, John A.J. Matthews*, Sally Seidel.
- **Northeastern University**
 Address : Department of Physics, 110 Forsyth Street, Boston, Mass. 02115-5096
 Fax : (+1)617 373 2943
 E-mail : swain@hex.neu.edu
 John Swain*.
- **Pennsylvania State University**
 Address : Dept of Physics, 104 Davey Laboratory, University Park, PA 16802
 Fax : (+1)814 865 3604
 E-mail : jjb@phys.psu.edu
 Steven Beach(S), James Beatty*, Michael DuVernois.
- **University of Utah**
 Address : Department of Physics 201 JFB, Salt Lake City, UT 84112
 Fax : (+1)801 581 6256
 E-mail : sommers@mail.physics.utah.edu
 David Kieda, Gene Loh, Paul Sommers* (FE coordinator).

Vietnam

Country contact : Tran Huu Phat.

- **Dalat Nuclear Research Institute - Vietnam Atomic Energy Commission**
 Address : 1 Nguyen Tu Luc street, Dalat, Lamdong
 Fax : (+84)63 8 21107
 E-mail : vnchnd1@csetdaco1.vn@csercc.ait.ac.th
 Huynh Dong Phuong*, Do Thanh Thao, Huynh Ton Nghiem.
- **Hanoi Institute of Nuclear Science & Technique - Vietnam Atomic Energy Commission**
 Address : P.O. Box 5T-160, Nghiado, Tuliem, Hanoi
 Fax : (+84)4 8 363295
 E-mail : thphat@csetdaco1.vn@csercc.ait.ac.th
 vkhkthn@csetdaco1.vn@csercc.ait.ac.th
 Tran Huu Phat*, Vo Van Thuan*, Hoang Dac Luc, Nguyen Hao Quang.

A.2 Auger Project Contributors

Many individuals have participated in the numerous workshops on the Auger Project as well as the work of the Design Group. Some of those who have made significant and important contributions, and who are not on the official collaboration list above, are acknowledged with gratitude here. This list is arranged by the country of the individual, and their institutional affiliation during the time of the work of the Auger Design Group.

Australia

Telstra Applied Technologies
Geoff Kelly

Brazil

LAFEX/CBPF
Alberto Santoro

Bulgaria

Institute for Nuclear Research
L. Popova

Peoples Republic of China

Institute of High Energy Physics
Jian-Zhong Wang

France

Laboratoire de l'Accelérateur Lineaire - Orsay
Boris Dudelzak

Observatoire de Besançon:
Alain Vincent

LURE - Orsay
Roger Bosshard

Germany

Gottingen
K. Mannheim

University of Heidelberg
T. Kutter

M-P-I fur Kernphysik, Heidelberg
F. A. Aharonian

M-P-I fur Fysik, München
Eckhart Lorenz

M-P-I fur Radioastronomie, Bonn
P. L. Biermann

India

Tata Institute of Fundamental Research, Bombay
B. V. Sreekantan

Italy

INFN, laboratory Nazionali del Gran Sasso
V. S. Berezinsky

University of Rome
Paolo Lipari

University of Torino
Gianni Navarra

Japan

Nagoya University
Y. Matsubara

Yamanashi University
K. Hashimoto
K. Honda
N. Kawasumi
I. Tsushima

Netherlands

Philips Photonics
Esso Flyckt
Wayne Seemungal

Russia

Inst. of Terrestrial Magnetism, Ionosphere and Propagation of Radio Waves
V. Ptuskin

Moscow State University
Boris Khrenov
G. B. Khristiansen
Vyacheslov Vashkevich

South Africa

Space Research Unit, Potchefstroom
B. Christo Raubenheimer

Spain

Univ. of Santiago Complutense
Enrique Zas

Sweden

Uppsala University
Hector Rubinstein

United Kingdom

University of Leeds
M. Gallagher
A.M. Hillas

United States

Columbia University
John H. Boyer
Eric J. Mannel

University of Delaware - Bartol Research Institute
T.K. Gaisser
T. Stanev

Fermilab
Rocky Kolb
Andrew Shih
Merle M. Watson

Johns Hopkins University
Robert Fletcher
Colin Norman

Los Alamos National Laboratory
Stirling Colgate

Moorhead State University
Joseph Gress

NASA, Goddard Space Flight Center
Floyd Stecker

Institute for Advanced Study, Princeton
Eli Waxman

Texas A&M University - Kingsville
Daniel J. Suson

University of Arizona
J. R. Jokipii

University of California, Irvine
Gaurang Yodh

University of Chicago
Fausto Cattaneo
Angela Olinto
Rene Ong
G. Sigl

University of Michigan
Lawrence W. Jones

University of Utah
J. Ball
Hongyue Dai
R. Koehn
A. Pantziris

University of Wisconsin
Lori A. Gray
Francis Halzen

University of Washington
D. Wilkerson

Bibliography

- [1] An overview with references of the early history of cosmic ray research can be found in M.S. Longair, “High Energy Astrophysics”, Vol.1 (Cambridge: Cambridge Univ. Press, 1994).
- [2] P. Auger et al., Comptes Rendus **206**, 1721 (1938), P. Auger, Rev. Mod. Phys. **11**, 288 (1939)
- [3] J. Linsley, Phys. Rev. Lett. **10**, 146 (1963)
- [4] D.J. Bird et al., Astrophys. J. **441**, 144 (1995).
- [5] N.N. Efimov et al., Proc. ICRR International Symposium on the Astrophysical Aspects of the Most Energetic Cosmic Rays (eds. M. Nagano, F. Takahara), p. 20 (1991).
- [6] N. Hayashida et al., Phys. Rev. Lett. **73**, 3491 (1994).
- [7] M. A. Lawrence, R. J. O. Reid and A. A. Watson, J. Phys. **G17**, 733 (1991).
- [8] R.M. Baltrusaitis et al Nucl. Inst. Methods **A240**, 410 (1985).
- [9] N. Hayashida et al., J. Phys. **G21**, 1101 (1994).
- [10] D. J. Bird et al., Astrophys. J. **424**, 491 (1994); D.J. Bird et al., Phys. Rev. Lett. **71**, 3401 (1993).
- [11] A.A. Penzias and R.W. Wilson, Ap.J. **142**, 419 (1965).
- [12] K. Greisen, Phys. Rev. Letters **16**, 748 (1966).
- [13] G.T. Zatsepin and V.A. Kuz'min, JETP Letters **4**, 78 (1966).
- [14] S. Swordy, private communication. The points are from published results of the LEAP, Proton, Akeno, AGASA, Fly's Eye, Haverah Park, and Yakutsk experiments.
- [15] S. Yoshida et al., Astroparticle Physics **3**, 105 (1995).
- [16] M. Nagano et al., J. Phys. **G18**, 423 (1992).

- [17] An excellent recent overview of the acceleration and propagation of cosmic rays is that of R.J. Protheroe, preprint astro-ph/9612212, to appear in the Proceedings of the 10th Course of Int'l School of Cosmic Ray Astrophysics, Erice, Sicily (World Scientific, 1997).
- [18] E. Fermi, Phys. Rev. **75**, 1169 (1949).
- [19] C.F. Kennel et al., J. Geophys. Res. **91**, 917 (1986). See also the discussion in M.S. Longair, "High Energy Astrophysics", Vol.2, p. 357 (Cambridge: Cambridge Univ. Press, 1994).
- [20] L.O'C. Drury, Rep. Prog. Phys. **46**, 973 (1983); L.O'C. Drury, Contemp. Phys. **35**, 231 (1994); see also the excellent discussion by T.K. Gaisser in "Cosmic Rays and Particle Physics", (Cambridge: Cambridge Univ. Press, 1990), Chapter 11, and references therein.
- [21] P.O. Lagage and C.J. Cesarsky, Astron. Astrophys. **118**, 223 (1983).
- [22] J.R. Jokipii, Ap. J. **313**, 842 (1987).
- [23] A.M. Hillas, Ann. Rev. Astron. Astrophys. **22**, 425 (1984).
- [24] R.W. Clay et al., Proc. Adelaide Design Workshop on Techniques for the Study of Cosmic Rays above 10^{19} eV - Jan. 1993, p.1 (Adelaide: University of Adelaide, 1995).
- [25] C.J. Cesarsky, Nucl. Phys. B (Proc. Suppl.) **28B**, 51 (1992).
- [26] C.J. Cesarsky and V. Ptuskin, Proc. 23rd ICRC (Calgary) **2**, 341 (1993).
- [27] V.S. Berezinsky et al., Astrophysics of Cosmic Rays, Chapter IV (North-Holland, 1990).
- [28] Stirling Colgate, talk at the opening workshop of the Auger Study, Fermilab, January 31, 1995. There is also a discussion of related mechanisms in Ref. [27] above, based on the work of R.V.E. Lovelace, Nature, **262**, 649 (1976) and R.D. Blandford, Mon. Not. R. Astron. Soc. **176**, 465 (1976) and **179**, 433 (1977).
- [29] R.J. Protheroe and P. Johnson, Astropart. Phys. **4**, 253 (1996).
- [30] J.W. Elbert and P. Sommers, Astrophys. J. **441**, 151 (1995); J.L. Puget, F.W. Stecker and J.H. Bredekamp, Astrophys. J. **205**, 638 (1976); W. Tkaczyk et al., J. Phys. **A8**, 1518 (1975).
- [31] J. W. Cronin, Nucl. Phys. **28B** (Proc. Supp.), 213 (1992).
- [32] F.A. Aharonian and J.W. Cronin, Phys. Rev. **D50**, 1892 (1994).
- [33] S. Yoshida and M. Teshima, Prog. Theor. Phys. **89**, 833 (1993).
- [34] G.R. Farrar, Phys. Rev. Lett. **76**, 4111 (1996).

- [35] P.P. Kronberg, Rep. Prog. Phys. **57**, 325 (1994).
- [36] S. Lee, G. Sigl, and A. Olinto, Astrophys. J. **455**, L21 (1995).
- [37] G. Cocconi, Nuovo Cimento **3**, 1433 (1956).
- [38] C. A. Norman, D. B. Melrose and A. Achterberg, Astrophys. J. **454**, 60 (1995).
- [39] H. Kang, D. Ryu and T.W. Jones, Astrophys. J. **456**, 422 (1996).
- [40] P.L. Biermann and P.A. Strittmatter, Ap.J. **322**, 643 (1987).
- [41] D. Fichtel et al., Ap. J. (Suppl.) **94**, 551 (1994).
- [42] M. Punch et al. Nature **358**, 477 (1992), J. Quinn et al., IAU Circular 6178 (1995).
- [43] K. Meisenheimer et al., Astron. Astrophys. **219**, 63 (1989).
- [44] K. Meisenheimer et al., Astron. Astrophys. **307**, 61 (1996).
- [45] J. Rachen and P.L. Biermann, Astron. Astrophys. **272**, 161 (1993).
- [46] J. Rachen, Todor Stanev and P.L. Biermann, Astron. Astrophys. **273**, 377 (1993).
- [47] P.L. Biermann, Topical Review in J. Phys. **G23**, 1 (1997).
- [48] G.E. Romero et al., to appear in Astropart. Phys. (1996).
- [49] D. Hartmann et al., in preparation (1996).
- [50] T. Stanev et al., Phys. Rev. Lett. **75**, 3056 (1995).
- [51] E. Waxman, K.B. Fisher, T. Piran, preprint (submitted to Astrophys. J., 1996).
- [52] N. Hayashida et al., Phys. Rev. Lett. **77**, 1000 (1996).
- [53] C. A. Meegan *et al.*, Nature **355**, 143 (1992); B. Paczyński, Nature **355**, 521 (1992); T. Piran, Astrophys. J. **389**, L45 (1992); J. P. Norris *et al.*, Astrophys. J. **423**, 432 (1994).
- [54] P. Mészáros and M. Rees, Mon. Not. Roy. Astron. Soc. **269**, 41P (1994); T. Piran, in *Gamma-ray Bursts*, eds. G. Fishman *et al.* (AIP 307, NY 1994); P. Mészáros, to appear in Proc. 17th Texas Conf. Relativistic Astrophysics, NY Acad. Sci. (1995).
- [55] E. Waxman, Phys. Rev. Lett. **75**, 386 (1995)
- [56] M. Vietri, Astrophys. J. **453**, 883 (1995).
- [57] E. Waxman, Astrophys. J. **452**, L1 (1995)
- [58] E. Cohen, & T. Piran, Astrophys. J. **444**, L25 (1995)
- [59] E. Waxman, & P. Coppi, Ap. J. *Letters*, in press (1996) (astro-ph/9603144)

- [60] M. Milgrom, & V. Usov, *Astrophys. J.* **449**, L37 (1995)
- [61] M. Vietri, *Mon. Not. R. Astron. Soc.* **278**, L1 (1996)
- [62] J. Miralda-Escudé, & E. Waxman, *Ap. J. Letters*, in press (1996) (astro-ph/9601012)
- [63] C. T. Hill, *Nucl. Phys. B* **224**, 469 (1983); C. T. Hill, D. N. Schramm, and T. P. Walker, *Phys. Rev. D* **36**, 1007 (1987); P. Bhattacharjee, *Phys. Rev. D* **40**, 3968 (1989); P. Bhattacharjee and N. C. Rana, *Phys. Lett. B* **246**, 365 (1990); G. Sigl, *Space Sc. Rev.* **75**, 375 (1996).
- [64] P. Bhattacharjee, C. T. Hill, and D. N. Schramm, *Phys. Rev. Lett.* **69**, 567 (1992);
- [65] P. Bhattacharjee and G. Sigl, *Phys. Rev. D* **51**, 4079 (1995).
- [66] A. J. Gill and T. W. B. Kibble, *Phys. Rev. D* **50**, 3660 (1994).
- [67] G. Sigl, K. Jedamzik, D. N. Schramm, and V. Berezhinsky, *Phys. Rev. D* **52**, 6682 (1995).
- [68] C. E. Fichtel *et al.*, *Astrophys. J.* **217**, L9 (1977); D. J. Thomson and C. E. Fichtel, *Astron. Astrophys.* **109**, 352 (1982).
- [69] S. W. Digel *et al.*, *Astrophys. J.* **441**, 270 (1995).
- [70] J. L. Osborne, A. W. Wolfendale, and L. Zhang, *J. Phys. G* **20**, 1089 (1994).
- [71] S. Lee, preprint, submitted to *Phys. Rev. D*.
- [72] G. Sigl, S. Lee, and P. Coppi, preprint, to be submitted to *Phys. Rev. Lett.*
- [73] G. Sigl, S. Lee, D. N. Schramm, and P. Bhattacharjee, *Science* **270**, 1977 (1995).
- [74] F. A. Aharonian, P. Bhattacharjee, and D. N. Schramm, *Phys. Rev. D* **46**, 4188 (1992).
- [75] G. Sigl, S. Lee, and P. Coppi, in preparation.
- [76] M. Cvetič and P. Langacker, *Phys. Rev. D* **54**, 2570 (1996).
- [77] N. A. Porter, *Nuov. Cim.* **16** 958 (1960).
- [78] T. W. Kephart and T. J. Weiler, *Astropart. Phys.* **4**, 271 (1996).
- [79] E.N. Parker, *Astrophys. J.* **160**, 383 (1970).
- [80] For a review see T.K. Gaisser, F. Halzen and T. Stanev, *Phys. Rep.* **238** (1995) 173.
- [81] F.W. Stecker, C. Done, M.H. Salomon and P. Sommers, *Phys. Rev. Lett.* **66** (1991) 2697.
- [82] F. Halzen and G. Jaczko, Univ. of Wisconsin-Madison Preprint MADPH-96-929, *Astro-ph/9602038*, and references therein .

- [83] L. D. Landau and I. J. Pomeranchuk, Dokl. Akad. Nauk. SSSR **92**, 535 (1953), and Dokl. Akad. Nauk SSSR **92**, 735 (1953) (These papers appear in English in L. D. Landau, Collected Papers, Pergamon Press (1965)); A. B. Migdal, Phys. Rev. **103** 1811 (1956).
- [84] L.K. Ding et al., Astrophys. J. **474**, 490 (1997).
- [85] Z. Cao et al., Phys. Rev. **D54**, 6674 (1996); Z. Cao et al., Phys. Rev. **D53**, 6608 (1996); Z. Cao et al., Phys. Rev. Lett. **75**, 1268 (1995).
- [86] J. Miralda-Escudé, & E. Waxman, preprint Astro-ph/9607059, (1996).
- [87] S.M. Astley et al., Proc. 17th ICRC (Paris)**2**, 156 (1981).
- [88] N.N. Efimov et al., Proc. 18th ICRC (Bangalore)**2**, 149 (1983).
- [89] P.V.J. Eames et al., Proc. 19th ICRC (LaJolla) **2**, 254 (1985).
- [90] A.W. Wolfendale and J. Wdowczyk, J. Phys. G. **10**, 1453 (1984).
- [91] V.S. Berezinsky and A.Yu. Smirnov, *Astrophys. Space Science* **32** (1975) 461.
- [92] M. Nagano et al., J. Phys. Soc. Japan 30 (1971) 33; S. Mikamo et al., Lett. al Nuovo Cimento 34 (1982) 273.
- [93] P. Kiraly, M.G. Thompson and A.W. Wolfendale, J. Phys. A: Gen. Phys. 4 (1971) 367; M. Nagano et al. J. Phys. G: Nucl. Phys. 12 (1986) 69; E. Zas, F. Halzen and R.A. Vazquez, Astropart. Phys. 1 (1993) 297; G. Parente, R.A. Vazquez and E. Zas, Proc. 24th ICRC (Rome), **1**, 377 (1995).
- [94] M.C. González-García, F. Halzen, R.A. Vázquez and E. Zas, Phys. Rev. D49 (1994) 2310.
- [95] G. Parente, A. Shoup and G.B. Yodh, Astropart. Phys. 3 (1995) 17.
- [96] F. Halzen and E. Zas, Phys. Lett. B289 (1992) 184.
- [97] G. E. Allen et al., Proc. 24th ICRC (Rome), **1**, 321 (1995).
- [98] M. Aglietta et al, Phys. Lett.**B333** (1994) 555.
- [99] J.W. Cronin, G. Parente and E. Zas, to appear in Proc. of the High Energy Neutrino Workshop, Venice, March 1996.
- [100] S. Yoshida et al., Proc. 24th ICRC (Rome) Vol. **1**, 793 (1995).
- [101] A.D. Martin, W.J. Stirling and R.G. Roberts, Phys. Lett.**B354** (1995) 155.
- [102] M. Glück, E. Reya and A. Vogt, Zeit. Phys.**C67**, 433 (1995).
- [103] J. Ralston et al., preprint Astro-ph/9607059 (1996), to appear in Proc. of the High Energy Neutrino Workshop, Venice, March 1996.

- [104] K. Asakimori et al., Proc. 24th ICRC (Rome) **2**, 707 (1995).
- [105] J. Linsley and L. Scarsi, Phys. Rev. **128**, 485 (1962).
- [106] Catalogue of highest energy cosmic rays No.1 (Volcano Ranch and Haverah Park), World Data Center C2 for Cosmic Rays, Tokyo (1980)
- [107] D.J. Bird et al., Proc. 24th ICRC (Rome), Vol.**3**, 560 (1995).
- [108] F. Kakimoto et al., Proc. 24th ICRC (Rome), Vol. **1**, 1047 (1995); F. Kakimoto et al., Nucl. Instrum. and Meth. **A372**, 527 (1995).
- [109] A.A. Watson, Nucl. Phys.**22B**(Proc.Supp.) , 116 (1991).
- [110] S.S. Al-Dargazelli et al., J.Phys.**G22**, 1825 (1996).
- [111] J.P. Vallée, Ap.J.**366** 450 (1991).
- [112] E.N. Parker, Proc. 22nd ICRC (Dublin), Vol.**5**, 38 (1991). Parker estimates the characteristic extension of the halo fields beyond the disk to be between 0.6 and 2 kpc, which is related to the gas density in the halo. See also A.J. Owens and J.R. Jokipii, Ap.J. **215**, 677 (1977).
- [113] X. Chi and A.W. Wolfendale, 1992, J. Phys. G **18** 539.
- [114] A.M.Hillas, Proc. 12th ICRC, Hobart, **3**, 1001 (1971).
- [115] K. Greisen, Proc. 9th ICRC (London), Vol.**2**, 609 (1965).
- [116] G. Cavallo, Astron. Astrophys., **65**, 415 (1978).
- [117] P. Sommers, Astroparticle Physics **3**, 349 (1995).
- [118] M. S. Longair, High Energy Astrophysics, 2nd Edition, Cambridge Univ. Press 1992.
- [119] Y. Mizumoto, Proc. Tokyo Workshop on Techniques for the Study of Extremely High Energy Cosmic Rays (ed. M. Nagano), p.194 (1993).
- [120] D.J. Bird et al., 23d ICRC (Calgary) **2** (1993) 450.
- [121] A. Borione et al., Nucl. Inst. and Meth., **A346** (1994) 329.
- [122] J. Phys. **G14**, 793 (1988).
- [123] M.Nagano et al., J. Phys. **G10**, 1295 (1984)
- [124] D. Ravignani and C. Hojvat, Auger Technical Note GAP-96-032 (1996).
- [125] Gaisser, T.K. & Hillas, A.M., *Proc. 15th Int. Cosmic Ray Conf.* (Plovdiv), **8**, 353 (1977).
- [126] A.M. Hillas, Proc. 19th ICRC (La Jolla) **1**, 155 (1985).

- [127] T.K. Gaisser, “Cosmic Rays and Particle Physics”, (Cambridge: Cambridge Univ. Press, 1990), Chapter 17.
- [128] R.S. Fletcher et al., Phys. Rev. **D50**, 5710 (1994).
- [129] J. Engel et al., Phys. Rev. **D46**, 5013 (1992). Further discussion on the validity of the assumptions underlying the superposition model can be found in T.K. Gaisser et al., Phys. Rev. **D47**, 1919 (1993)
- [130] S. Yoshida et al., J. Phys. **G20**, 651 (1994).
- [131] R. C. Smith and K. S. Baker, Appl. Optics **20**, 177 (1981).
- [132] F. Aharonian and J.W. Cronin, Phys. Rev. **D50**, 1892 (1994).
- [133] T.K.Gaisser et al. Phys. Rev. D **47**, 1919 (1993)
- [134] R.M. Baltrusaitis et al. Proc. 19th ICRC, La Jolla **7**, 159 (1985)
- [135] T.K.Gaisser and A.M. Hillas, Proc. 15th ICRC, Plovdiv **8**, 353 (1977).
- [136] H.Y. Dai, in “Tokyo Workshop on Techniques for the Study of Extremely High Energy Cosmic Rays” (ed. M. Nagano, F. Takahara), p. 133, (Tokyo: ICRC, 1993).
- [137] B.R. Dawson, “Hybrid Simulations of a 3 Eye System with Dual Mirrors”, Auger Project Technical Note GAP-96-18 (1996).
- [138] P. Sommers, Auger Technical Notes GAP-96-035 and GAP-96-010.
- [139] A. Cordero et al., Auger Technical Note GAP-96-039.
- [140] R. Biral et al., Auger Technical Note GAP-97-001.
- [141] B.R. Dawson et al., Auger Technical Note GAP-96-047.
- [142] J.W. Elbert, in “Tokyo Workshop on Techniques for the Study of Extremely High Energy Cosmic Rays” (ed. M. Nagano, F. Takahara), p. 158, (Tokyo: ICRC, 1993).
- [143] P.Sommers, Astropart. Phys. **3**, 349 (1995).
- [144] B.R. Dawson, H.Y. Dai, P. Sommers and S. Yoshida, Astropart. Phys. **5**, 239 (1996).
- [145] P. Sokolsky, Proc. Tokyo Workshop on Techniques for the Study of Extremely High Energy Cosmic Rays, ed: M. Nagano, p.280 (1993).
- [146] J. Boyer et al., “A Flash ADC Electronics System for the HiRes Detector,” Proc. 24th Int. Cosmic Ray Conf. (Rome) **3**, 750 (1995).
- [147] Auger Project Technical Note GAP-95-025 (1995)
- [148] DE6003 Digital Radio Tranceiver, GEC Plessey Application Note DS3506-6.3 (1994)

- [149] C. Pryke et al., Nucl. Inst. Methods **A354** 560 (1995)
- [150] Code of Federal Regulations, Title 47, Parts 0-19, Office of Federal Register, National Archives and Record Admin. (1994)
- [151] Donald E. Kerr, Propagation of Short Radio Waves, Dover Publ. (1951)
- [152] Auger Project Technical Note GAP-96-014 (1996).
- [153] Auger Project Technical Note GAP-96-026 (1996).
- [154] D. B. Kieda, *Astropart. Phys.* **4**, 133 (1995).
- [155] D. B. Kieda and D. J. Suson, *Nucl. Inst. Meth. in Phys. Res.* **A 374**, 381 (1996).
- [156] D. B. Kieda, in Proc. Intnatl. Symp. on Extremely High Energy Cosmic Rays: Astrophysics and Observatories (Tanashi, Tokyo Sept 1996) (M. Nagano, ed., ICRR, Japan) (to be published, 1997).
- [157] G. K. Garipov, B.A. Khrenov, and V.V. Prosin, preprint “EAS Cerenkov Radiation Detector for Operation in the Presence of High Light Noise”.
- [158] W. J. Willis and V. Radeka, Nucl. Inst. and Meth. **A120**, 221 (1974).
- [159] P. R. Barker, W. E. Hazen, and A. Z. Hendel, Phys. Rev. Lett. **18**, 51 (1967); W. E. Hazen, *et al.*, *ibid.* **22**, 35 (1969); **24**, 476 (1970).
- [160] H. R. Allan, in *Progress in Elementary Particles and Cosmic Ray Physics*, v. 10, edited by J. G. Wilson and S. G. Wouthuysen (North-Holland, Amsterdam, 1971), p. 171, and references therein; V. B. Atrashkevich et al., *Yad. Fiz.* **28**, 366 (1978).
- [161] K. Kadota *et al.*, Proc. 23rd International Conference on Cosmic Rays (ICRC-23), Calgary, 1993, v. 4, p. 262; Tokyo Workshop on Techniques for the Study of Extremely High Energy Cosmic Rays, Tanashi, Tokyo, 27 – 30 Sept. 1993.
- [162] C. Castagnoli *et al.*, Proc. ICRC-23, Calgary, 1993, v. 4, p. 258.
- [163] P. I. Golubnichii, A. D. Filonenko, and V. I. Yakovlev, *Izv. Akad. Nauk* **58**, 45 (1994).
- [164] R. Baishya *et al.*, Proc. ICRC-23, Calgary, 1993, V. 4, p. 266.
- [165] F. D. Kahn and I. Lerche, Proc. Roy. Soc. **A 289**, 206 (1966); S. A. Colgate, *J. Geophys. Res.* **72**, 4869 (1972).
- [166] R. R. Wilson, Phys. Rev. **108**, 155 (1967); R. A. Roussel-Dupré, A. V. Gurevitch, T. Tunnell, and G. M. Milikh, Los Alamos National Laboratory report LA-12601-MS, November, 1993.
- [167] R. Gall and K. D. Green, UMC-CASA note, Aug. 23, 1996 (unpublished).

- [168] M. Atiya, M. Ito, J. Haggerty, C. Ng, and F. W. Sippach, Nucl. Inst. Meth. A **279**, 180 (1989).
- [169] D. Bryman, J. V. Cresswell, M. LeNoble, and R. Poutissou, IEEE Trans. **NS-38**, 295 (1991).
- [170] RICE Project, D. Z. Besson *et al.*, proposal to National Science Foundation; G. M. Frichter, J. P. Ralston, and D. W. McKay, "Toward radio detection of PeV neutrinos on the cubic kilometer scale," report astro-ph/9606008, to be published in Proceedings of the 7th International Symposium on Neutrino Telescopes, Venice, Feb. 27 – Mar. 1, 1996.
- [171] D. J. Bird et al., Proc. 24th ICRC (Rome), Vol.**2**, 760 (1995).
- [172] Clay R.W. and Dawson B.R., Eds., Adelaide Design Workshop, Final Report, Univ. of Adelaide (1995) 66.
- [173] B. Dudelzak et al., LAL Orsay, Report 95-01 (1995)
- [174] M. Boratav et al., Proc. 24th ICRC (Rome), **Vol.1**, 954 (1995)
- [175] K. Hashimoto et al., Auger Technical Note GAP-95-017
- [176] P. Mantsch, Auger Technical Note GAP-95-008 (1995)
- [177] P. O. Mazur, Proc. Int'l Workshop on Resistive Plate Chambers and Related Detectors, Universita degli Studi di Pavia, Scientifica Acta **XI**, 331 (1996)
- [178] C. Pryke, Auger Technical Note GAP-96-008 (1996)
- [179] P. Bauleo et al., Auger Technical Note GAP-96-029 (1996)
- [180] M. A. Cummings, Auger Technical Note GAP-97-010(1997)
- [181] M. Takiue et al., Nucl. Inst. Meth. **227**,571 (1984)
- [182] N. A. Porter, Il Nuovo Cim. **5**, 526 (1957)
- [183] D. Ravignani et al., Auger Technical Note GAP-96-033 (1996)
- [184] Series 69-B2697, Tnemec Company, Inc., North Kansas City, Mo., USA
- [185] M. Sakaki and M. Nagano, Proc. Int'l. Symposium on Extremely High Energy Cosmic Rays, Tokyo (1996) to be published
- [186] A. Etchegoyen et al., Auger Technical Note GAP-96-040 (1996)
- [187] O. A. Bernaola et al., Auger Technical Note GAP-96-036 (1996)